



UNIVERSITÀ  
DEGLI STUDI  
FIRENZE

PhD in  
Chemical Sciences

CYCLE XXXVI

COORDINATOR Prof. Papini Anna Maria

Optimization of the sample selection procedure for radiocarbon dating  
of historical mortars

Academic Discipline (SSD) GEO/05

**Doctoral Candidate**

Dr. Calandra Sara

**Supervisor**

Prof. Garzonio Carlo Alberto

**Co-Supervisors**

Dr. Cantisani Emma

Prof. Mariaelena Fedi

**Coordinator**

Prof. Papini Anna Maria



UNIVERSITÀ  
DEGLI STUDI  
FIRENZE

PhD in  
Chemical Sciences

CYCLE XXXVI

COORDINATOR Prof. Papini Anna Maria

Optimization of the sample selection procedure for radiocarbon dating of historical mortars

Academic Discipline (SSD) GEO/05

**Doctoral Candidate**

Dr. Calandra Sara

**Supervisor**

Prof. Garzono Carlo Alberto

**Coordinator**

Prof. Papini Anna Maria

*The consultation of the thesis is free. Unless a specific authorization is obtained from the author, the thesis can be, however, downloaded and printed only for strictly personal purposes related to study, research and teaching, with the explicit exclusion of any use that has – even indirectly – a commercial nature.*

## Table of contents

1	Introduction.....	8
2	Historic mortar .....	13
2.1	Definitions and type of mortars .....	13
2.2	Production of historical lime mortar .....	17
2.2.1	Production of aerial mortar.....	19
2.2.2	Production of hydraulic mortar .....	23
2.3	Raw materials and technologies in building Heritage.....	27
3	Mortar dating by radiocarbon.....	29
3.1	Principles of radiocarbon dating .....	29
3.2	Advantages and challenges of applying <sup>14</sup> C dating to mortars .....	31
3.3	Review of recent strategies on sampling, characterization, and selection of datable fraction in mortar radiocarbon dating .....	34
3.3.1	Sampling .....	35
3.3.2	From macro to micro mortar characterization .....	36
3.3.3	Pre-treatment of lime mortar .....	39
4	Research aim .....	45
5	Analytical strategies for a comprehensive characterization of mortars .....	49
5.1	Mineralogical, petrographic and chemical characterization of mortar.....	49
5.1.1	Carbonation test .....	49
5.1.2	Optical microscope .....	50
5.1.3	Scanning Electron Microscopy with Energy-Dispersive X-ray Spectroscopy .....	54
5.1.4	X-ray powder diffraction .....	56
5.1.5	Thermogravimetric analysis.....	57
5.1.6	Fourier Transform Infrared Spectroscopy.....	58
5.1.7	Cathodoluminescence .....	59
5.2	Application of advanced techniques to mortar characterization.....	61
5.2.1	FPA-FTIR.....	62
5.2.2	μXRPD.....	65

6	Non-destructive characterization on selected portions of sample .....	69
6.1	Selection of geogenic and anthropogenic/standard samples .....	70
6.1.1	Preparation of samples .....	70
6.1.2	Characterization of chosen samples .....	71
6.2	Study for the identification of calcites using ATR-FTIR .....	74
6.2.1	Previous FTIR spectroscopy studies on calcite mortar .....	74
6.2.2	Infrared measurements .....	75
6.2.3	Results and discussion .....	77
6.3	Study for the identification of calcites using micro-Raman .....	81
6.3.1	Previous Raman spectroscopy studies on calcite mortar.....	81
6.3.2	Raman measurements and statistical analysis.....	82
6.3.3	Results and discussion .....	84
6.4	Final remarks .....	96
7	Mortar dating at LABEC .....	97
7.1	Micro-sample preparation for the measurement.....	97
7.2	The acidification line.....	98
7.3	Graphitization line .....	100
7.4	Accelerator Mass Spectrometry .....	102
8	<sup>14</sup> C dating of natural hydraulic mortar in Florentine building .....	105
8.1	Literature background of Florentine mortar.....	105
8.1.1	Case studies of historical Florentine buildings.....	106
8.2	Castle of Trebbio.....	107
8.2.1	Sampling .....	107
8.2.2	Characterization of mortars to select the most suitable samples for in radiocarbon dating .....	111
8.2.3	Selection and characterization of calcite mortar powders .....	118
8.2.4	Pre-treatment and acid dissolution of selected mortar powders .....	121
8.2.5	AMS measurements.....	122
8.3	S. Felicita Church.....	125
8.3.1	Sampling .....	125

8.3.2	Characterization of mortars to select the most suitable samples for in radiocarbon dating .....	127
8.3.3	Selection and characterization of calcite mortar powders .....	135
8.3.4	Pre-treatment and acid dissolution of selected mortar powders .....	137
8.3.5	AMS measurements.....	138
8.4	Medici Riccardi Palace .....	140
8.4.1	Sampling .....	140
8.4.2	Characterization of mortars to select the most suitable samples for in radiocarbon dating .....	143
8.4.3	Selection and characterization of calcite mortar powders .....	154
8.4.4	Pre-treatment and acid dissolution of selected mortar powders .....	159
8.4.5	AMS measurements.....	160
8.5	The S. Giovanni Baptistery .....	163
8.5.1	Sampling .....	163
8.5.2	Characterization of mortars to select the most suitable samples for in radiocarbon dating .....	165
8.5.3	Characterization of calcite mortar powders .....	170
8.6	Final remarks .....	171
9	Feasibility study of bedding mortar dating in Pompeii .....	173
9.1	Literature background .....	173
9.2	The mortars of the public building in Pompeii.....	174
9.3	Characterization of mortars for sample selection in radiocarbon dating .....	179
9.4	Non-destructive characterization, pre-treatment and acid dissolution of selected samples .....	196
9.4.1	Selection and characterization of calcite mortar powders .....	196
9.4.2	Pre-treatment and acid dissolution of selected mortar powders.....	201
9.5	AMS measurements.....	202
9.6	Final remarks .....	204
10	Radiocarbon dating of organic fragments in the mortar mixture .....	207
10.1	The plasters of the St. Philip Church in Hierapolis (Turkey) .....	207
10.2	Characterization results of the plaster from the St. Philip Church.....	210

10.3	Mechanical selection and sample preparation of straw fragments.....	213
10.4	AMS measurements.....	215
11	Conclusion .....	218
	References.....	224
	Acknowledgements.....	244
	Appendix 1: The instrumentation and specific analytical methodology .....	246
	Appendix 2 Supplementary information.....	251
	Appendix 3: Published work on PhD topics.....	278
	Appendix 4: Published work on topics different from the PhD project.....	280

# 1 Introduction

Radiocarbon dating is one of the most widely used dating techniques in the field of archaeology and Cultural Heritage. This technique is used to typically date organic finds (such as charcoal, wood, bone, or tissue) but also inorganic material, such as carbonate compounds, i.e., lead white).

Among all the possible applications to inorganic carbon-based materials, the use of the radiocarbon method ( $^{14}\text{C}$ ) for dating ancient mortars was proposed as early as in the 1960s, applying the method to the inorganic binder. Mortar is an artificial product made and used by man since ancient times, consisting mainly of a binder, some aggregate and possible additives. In mortars, the inorganic radiocarbon-datable component is calcite, which is formed by the reaction of calcium hydroxide with atmospheric  $\text{CO}_2$  during the setting of the material (the so-called anthropogenic calcite). Aerial mortars are the most suitable for dating, because they set and harden completely, incorporating atmospheric  $\text{CO}_2$ . Since mortars are complex and heterogeneous materials, other sources of C can be present in the mortar samples, which may contaminate the  $^{14}\text{C}$  concentration. Contaminations can be due to the presence of:

- unburned carbonate rock fragments of stone for lime and carbonate aggregates present in the mixture (geogenic calcite). These two sources make the sample older than expected;
- (re)crystallized calcium carbonates of the binder and delayed hardening (the so-called secondary calcite). Secondary calcite forms after the initial hardening of the mortar, causing an apparent rejuvenation of the sample.

Moreover, the type of binder of the mortar sample may not be quite ideal, as there are historical mortars with not totally aerial lime binder.

Selection of the datable fraction and elimination of potential contamination is a challenge for the international radiocarbon community. Accurate sampling, complete mineralogical and chemical characterization of the mortars are the first steps. Complete separation of binder from the aggregate coupled with characterization of the



separated carbonate fractions is mandatory. Proactive identification of the origin of calcite allows reducing the possible contamination risk, thus obtaining accurate  $^{14}\text{C}$  measurement by accelerator mass spectrometer (AMS).

However, historical mortars in Italy often consist of binder ranging from weakly hydraulic binders, obtained from natural hydraulic binders or aerial lime with the addition of natural or artificial pozzolanic materials to moderately-properly hydraulic binder. This type of mortar is usually not entirely suitable for dating with the  $^{14}\text{C}$ .

In the Florentine area, historical mortars were typically made with natural hydraulic lime binders obtained by burning marly limestones. Setting and hardening occurred through both the carbonation of calcium hydroxide and the hydration of calcium silicates and calcium aluminates.

Roman mortars were usually made by mixing an aerial lime with materials having pozzolanic behaviour (i.e. pozzolana, cocchiopesto).

My PhD project aimed to optimize the sample selection procedure for radiocarbon dating of historic mortars. Within this framework, the project research has moved into two directions:

- developing a procedure to select the most suitable datable fraction in historic mortars, in case of both inorganic and organic materials. A multi-analytical characterization of the mortar fragments (i.e. optical and electron microscopy (OM, SEM-EDS), X-ray diffraction on powders (XRPD) and thermogravimetric analysis (TGA), infrared spectroscopy (FTIR)) and further characterization of the binder sample selected for dating was designed. New non-destructive technologies (XRPD, OM-cathodoluminescence, FTIR, micro-Raman) to identify the origin of calcite (geological calcite and anthropogenic calcite) were evaluated. A new experimental set-up for the collection of  $\text{CO}_2$  evolving from the selected calcite was installed, by integrating an acidification reactor into our so-called Lilliput graphitization reactors, which are optimized for microgram-sized samples. The graphitization line is used to obtain graphite samples whose residual  $^{14}\text{C}$  abundance is measured by AMS.

- Application of the selection procedure to mortars that are not completely aerial to evaluate the use of the  $^{14}\text{C}$  method. The feasibility of applying this method in new contexts, such as Pompeii and historic Florentine buildings (Trebbio Castle, S. Felicita Church, Medici Riccardi Palace, and S. Giovanni Baptistery) was investigated. In addition, the capability to date small sample masses has led us to consider the possibility of dating small straw inclusions in the plaster of the St. Philip Church (in the archaeological site in Hierapolis, Turkey).

Overarching challenge of this research is optimizing the radiocarbon dating procedure for complex, heterogeneous materials such as historic mortars. Selection of the datable fraction and removal of potential contamination require rigorous sampling, thorough mineralogical, petrographic, and chemical characterization, and identification of the calcite origin on selected sample for dating. With the development of innovative techniques and the use of advanced analytical techniques, there is an opportunity to extend the applicability of radiocarbon dating to not ideally contexts.

The present thesis deals with all the basic steps in optimization the sample selection procedure of historical mortars for radiocarbon dating, and it is organised thus:

- the next chapter describes mortars and their constituents, including binders, aggregates, and additives. It also explains the setting and hardening processes of both aerial, natural hydraulic and pozzolanic mortars, which are the focus of this thesis. This chapter emphasizes the importance of studying mortars for both relative and absolute chronology.
- The third chapter addresses the challenges associated with radiocarbon dating of mortars. After a brief explanation of the basic principles of radiocarbon dating ( $^{14}\text{C}$ ), the potential problems associated with dating mortars are highlighted. Consequently, a review of recent strategies for sampling, characterization, and selection of the datable fraction in radiocarbon dating of mortars is presented to evaluate the various approaches and developments used in the international radiocarbon community.

- In the fourth chapter, the research project for the development of the procedure based on characterization, selection and preparation of mortar samples for radiocarbon dating is presented.
- The fifth chapter describes the techniques selected for the initial characterization of mortars and the potential information that can be obtained from these techniques. It also explains the meaningful information that can be acquired by using advanced techniques for mortar characterization (FTIR microscope with FPA imaging detector and high-resolution 2D mapping XRPD at beamline ID13).
- In the sixth chapter, new analytical techniques for distinguishing the origin of calcite from different domain (geogenic and anthropogenic calcite) are evaluated. Standard samples of geogenic and anthropogenic calcite were selected to determine if ATR-FTIR and micro-Raman spectroscopy can distinguish calcite formed by different mechanisms. Various methods were used to validate the methods and the findings obtained.
- The seventh chapter deals with the optimization of the acidification line and the graphitization set-up for microsamples of carbonate mortar samples. It also contains a brief description of the measurement of radiocarbon concentration by AMS at the INFN-LABEC laboratory in Florence.
- The eighth chapter describes the feasibility study of radiocarbon dating of historic mortars in Florentine buildings, including the Castle of Trebbio, S. Felicita Church, S. Giovanni Baptistery, and Medici Riccardi Palace. Each procedural step is described for each building: sampling and historical background, mortar characterization, selection and characterization of calcite mortar powders, pre-treatment and acid dissolution of selected mortar powders and AMS measurements.
- The ninth chapter examines the feasibility of dating historical mortars in public buildings in Pompeii. Our procedure is applied, and each step is explained: sampling and historical background, mortar characterization, selection and

characterization of calcite mortar powders, pre-treatment and acid dissolution of selected mortar powders, and AMS measurements.

- In the tenth chapter, the feasibility of dating organic samples in mortar mixture is examined as an alternative approach when binder or lump selection is deemed inappropriate. This approach was applied to the mortars of the Church of St. Philip in Hierapolis, Turkey, which contain straw fragments in painted plasters.

## 2 Historic mortar

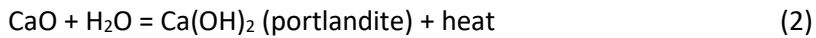
### 2.1 Definitions and type of mortars

Mortar is one of the oldest building materials. It is a human-made material that is widely used in construction thanks to its easy preparation and the availability of natural resources. These materials can harden and give a durable and cohesive product. For this reason, they have allowed extensive use in the architectural field, for bedding the elements of a masonry (bricks, stone blocks), as a filling of the core of the walls and as a support for wall paintings, mosaics or pavements and plasters to protect and / or decorate the walls (Moropoulou et al., 2005; Borges et al., 2014; Pecchioni et al., 2018). The main components of mortar are the binder, aggregates, the water and the additives, that allow to modulate the properties of the mortar according to its use. In order to define more clearly the components and properties of mortars, the Italian National Unification (UNI, Ente Nazionale Italiano di Unificazione) has created a clear legislative framework (UNI EN 10924, 2001) that defines a mortar as: “a mixture of inorganic or organic binder, aggregates, water and possible addition of organic/inorganic additives in such proportions as to confer to the mixture, in the fresh state, a suitable workability and, in the hardened state, suitable physical, mechanical, aesthetical characteristics together good durability when cured”. Mortars can be differentiated and classified according to their location, function and composition. Classification by composition is based on the type of binder, the type of aggregate, and the organic and/or inorganic constituents added to the recipe.

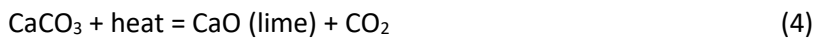
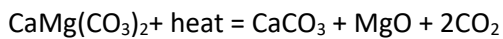
With regard to the binder, these main types of mortars can be distinguished:

- Aerial mortars: the binder of this mortar reacts with the CO<sub>2</sub> present in the air, forming a cohesive material. Historically, calcium and magnesium lime binders are used, depending on the composition of the limestone selected for lime production.

Pure limestone ( $\text{CaCO}_3 > 95\%$ ) is burned around  $850^\circ\text{C}$ , then calcic lime mortar sets and hardens through carbonation of calcium hydroxide  $[\text{Ca}(\text{OH})_2]$  with the formation of calcite, following these reactions:



Instead, the use of carbonate rock  $\text{CaMg}(\text{CO}_3)_2$  produces magnesian lime mortars. The different amount of magnesium in the stone (up to 10% in magnesium limestones, 50% in dolomitic limestone, 90-100% in dolostones) contributes to the results of the production processes. During the burning,  $\text{CaMg}(\text{CO}_3)_2$  dissociates into two phases (4): the decomposition of dolomite into  $\text{MgO}$  and  $\text{CaCO}_3$  at  $750^\circ\text{C}$ , followed by the dissociation of calcite into  $\text{CaO}$ . In some studies (Boynton, 1980), dolomite initiates dissociation starting at  $300^\circ\text{C}$ .



It sets and hardens through carbonation of calcium hydroxide and partial carbonation of magnesium hydroxide with formation of hydromagnesite. This involves compositional inhomogeneity and remnant phases of magnesium hydroxide  $[\text{Mg}(\text{OH})_2]$ , due to different carbonation rates of the magnesium phases, in comparison to calcium hydroxide.

Aerial mortars are produced by mixing an aerial binder, aggregates, and water, in such a proportion to make the mixture plastic and malleable. This type represents the most used mortars in ancient times, both for decorative and functional application, and indoor and outdoor finishing.

- Hydraulic mortars: these mortars set and harden in particular conditions, such as high humidity or even in an underwater environment. Hydraulic mortars can be produced using natural hydraulic lime binders, aerial binder with addition of materials providing hydraulic characteristics (historical production), and modern hydraulic binder (hydraulic lime, formulated lime, natural cement, white cement, (Arizzi and Cultrone, 2021)). Modern hydraulic binders are industrially produced by higher temperatures and with specific limestone properties. The setting occurs through a hydration reaction between water and calcium silicates and calcium aluminates.

Historical hydraulic mortars are produced by burning of marly/siliceous limestones to obtain natural hydraulic binder; and by reaction of hydraulicization components (pozzolanic materials, forging scoriae, crushed ceramics), and aerial binders to obtain the “pozzolanic” binder. The hardening process is composed of the carbonation of calcium hydroxide and the hydration of calcium silicates and calcium aluminates.

- Gypsum mortars: gypsum is the first binder produced by man and is obtained by burning gypsum rock ( $\text{CaSO}_4 \cdot 2\text{H}_2\text{O}$ ) at a low temperature (about  $200^\circ\text{C}$ ). Gypsum mortars harden quickly, due to the water evaporation and the consequent formation of gypsum crystals.
- Mixed binder mortar: is made by mixing several binders (historically i.e. calcitic lime, gypsum binder; now i.e. aerial and hydraulic binders) in varying proportions with a sandy or pozzolanic aggregate and water. The purpose of using such mortars is to reduce costs and improve adherence times or increase resistance to leaching and degradation produced by moisture. They are still used today and are known as cement-lime mortars (Alvarez et al., 2021).

Mortars can be enhanced with additives to increase their workability, strength, and durability (Centauro et al., 2017). Table 2.1 describes the effects and role of additives. The organic materials traditionally added to mortars can be divided into two groups. The first consists of the compounds used as filler or reinforcing materials, such as straw,

sawdust, other plant filamentous materials, and animal dung (mainly from horse and goat). The second group includes the so-called modifiers, which even in small quantities can adjust certain mortar properties. For example, they can change the water distribution in the fresh mortar and the speed of its setting, initiating crystallization and thus changing the properties of hardened mortar.

*Table 2.1 Organic additives in mortars and their classification by their effects on fresh and hardened mortars, as reported in (Kuckova et al., 2009).*

<b>Function</b>	<b>Effect</b>	<b>Material</b>
Accelerator	Accelerating firmness and increasing early firming	Egg white, blood, sugar, grease, curd, starch
Setting retarder	Extending workability time	Sugar, treacle, fruit syrup, blood, egg white, gluten
Plasticiser	Improving workability, consolidation of fresh mortar	Milk, egg white, fats, oils, sugar, colophony
Aerator	Improving permanency and frost proof	Malt, beer, urine
Sealing and hydrophobic additive	Providing waterproof character	Fats, oils, wax, asphalt, sugar
Adhesive	Improving cohesion	Colophony, gelatine, animal glue, casein
Firmer	Increasing firmness	Treacle, fruit syrup, fats, oils
Stiffening agent	Adjusting mortar consistency	Sour milk, casein, cheese, rye dough, gluten, plant gums, blood, collagen, gelatine

The next section describes the processes of preparation and hardening of historical mortars based on aerial and hydraulic lime binders, which are useful for the topic of the doctoral thesis.



## 2.2 Production of historical lime mortar

The mortars used until the end of the 18th century are called "ancient" and are represented by aerial mortar (calcic and magnesian lime binder), gypsum mortar and hydraulic mortar (aerial lime binder with addition of materials providing hydraulic characteristics and natural hydraulic mortar) (summarized in Figure 2.1); only later, the use of artificial hydraulic binders was established (Alessandrini, 1985). The historical considerations of ancient technologies are briefly reported, focusing on aerial mortars and the two types of hydraulic mortars. Their production methods are explained in 2.2.1 and 2.2.2, with each step described in detail.

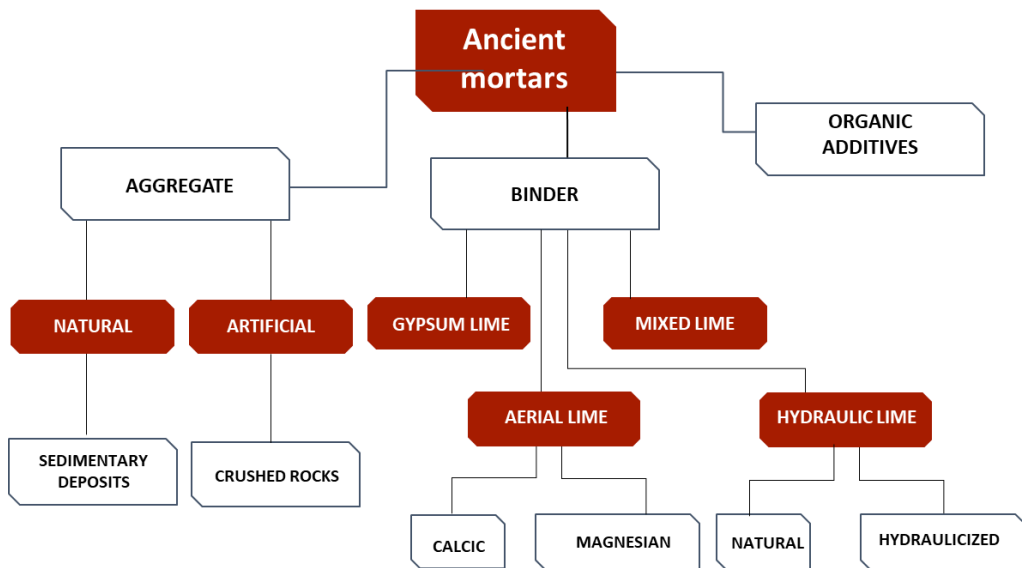


Figure 2.1 – Schematic representation of the ancient mortars.

The use of lime as a binder was probably accidental; there are many examples of the use of lime or mortar since prehistoric times. Its earliest use is documented in archaeological sites in Palestine and Turkey in 12000 BCE (Elert et al., 2002). Examples of the use of lime and stone are found in the pavement of the Southern Gallery at Yiftah (Israel), dating to 7000 BCE, and in the pavement of Lepenski Vir (Serbia), 5600 BCE

(Bensted, 1997). Other evidence is found in the archaeological sites of Jerash and Byblos, 5000-6000 BCE; in the construction of the pyramids and Great Wall in China, 2000-200 BCE; in the construction of Troia and Mikene in Mesopotamia, 5000-4000 BCE (Schiele and Berens, 1976; Secco et al., 2019); and in Ancient Egypt, 1400 – 1200 BCE (Davey, 1965). The Egyptians often used a gypsum binder; however, the use of lime-based mortar has been reported in a mural at Thebes (1950 BCE). The technology was passed on to the Greeks, who used it mainly as a support for paintings and wall cladding. The Greeks transmitted their knowledge to the Etruscans (from the 8th century BCE) and to the Romans. Since then, in addition to aerial lime, hydraulic materials have been used, whose development and diffusion was expanded by the Romans.

Although the Greeks were the first to use volcanic powder (Santorini earth) or crushed ceramics (since the 8th century BCE) (Colleparidi 1990), the Romans improved both the production technology and the quality of hydraulic mortars in the 3rd century BCE. These mortars were made by combining air-hardening lime with crushed bricks (cocciopesto) (Megna et al., 2010), pumice powder (pumex Pompeianus), scoriae (Izzo et al., 2018). The Romans realized that certain volcanic deposits combined with sand and lime could produce a mortar that could absorb water, just as the Greeks, Etruscans, and Phoenicians had done before them. The use of pozzolan<sup>1</sup> represented an advance in construction, because it could harden under water and carbonation was faster. The studies of Jackson et al. (2013) show that such mortars can provide high mechanical strength, durability, and structural integrity in earthquake-prone areas.

In the book "De Architectura," Vitruvius describes in detail the preparation and use of mortars in construction. He emphasizes the importance of the proper ratio of lime and sand in the various types of mortars and offers valuable insights into ancient building techniques. His work, widely recognized as a landmark from the Renaissance to the end

---

<sup>1</sup>The pozzolan known in Vitruvius' text as "sand of Cuma" is a brownish volcanic soil from Pozzuoli, Gulf of Naples, Italy, and he recommends mixing the powder with slaked lime in a ratio of two to one.

of the 19th century, remains an important reference for understanding the use of mortars in Roman architecture.

Since ancient times, natural hydraulic lime mortars have been used in masonry structures to bond the stone elements (Lanas et al., 2004; Maravelaki-Kalaitzaki et al., 2003; Zhang et al., 2018). Unlike hydraulic lime binders and aerial binder with added materials, Vitruvius does not mention lime binders derived from impure limestone. The slightly hydraulic character of natural hydraulic mortars obtained by burning impure limestones was found in the bridge of Narni in central Italy (3rd century CE), a very ancient example of this production (Cantisani et al., 2002). In certain periods and regions, the use of very white and pure limestones recommended by Vitruvius for lime production was abandoned and instead impure limestones with varying amounts of silica or aluminosilicate phases were inadvertently selected, leading to the production of binders with very different degrees of hydraulicity. The first written source comes from Palladio of the 16th century, who speaks of the production of these mortars. Palladio, an influential Italian Renaissance architect, probably discussed the use and properties of natural hydraulic mortar in his architectural treatises and designs.

### 2.2.1 Production of aerial mortar

To better understand the process of mortar hardening, it is important to analyse all the phases to realize the artifact itself, because each of them leads to a product with specific properties. The manufacturing process of an aerial mortar is shown in Figure 2.1.

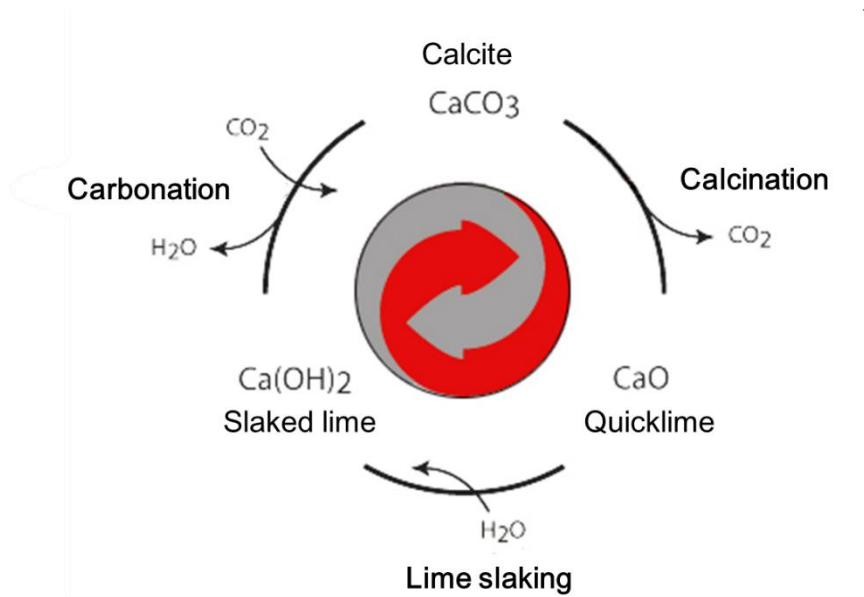


Figure 2.2 - The reactions and processes involved in the production of lime include the burning of geogenic carbonates (i.e. marble and limestones) to produce carbonation and hardening of slaked lime. This results in the formation of anthropogenic calcite, which acts as a binder in the mortar.

The process begins with the firing of natural carbonate rock (e.g. marble, pure limestone) and produces an artificial material, the binder, with the same calcitic composition as the starting product. This binder is also called anthropogenic calcite, which serves as a binder between the materials present in the mixture (aggregates, additives, etc.). For its production, it is preferable to use the purest possible carbonate rock, light in colour, free of alterations such as veins or patina, with a microcrystalline texture and fine grain size (according to Vitruvio's recipe).

Carbonate rock is crushed and heated at a temperature  $\sim 850^{\circ}\text{C}$  (Rodríguez-Navarro et al., 2009): this first step is called calcination and involves the thermal decomposition of a  $\text{CaCO}_3$  substrate to produce quicklime,  $\text{CaO}$  and gaseous  $\text{CO}_2$ . The result of the calcination process is a fine-grained, porous material with sufficient exposed surface area to properly perform the subsequent hydration and setting processes of the mortar.

The calcination degree is given by the complete leakage of the  $\text{CO}_2$ ; the more compact and coarse-sized is the starting limestone, the slower is this process. When decomposition is incomplete and  $\text{CO}_2$  remains in contact with the  $\text{CaO}$  crystals, a more compact and therefore less reactive product is obtained. In addition, if the fragments are too large, the dissociation of carbon dioxide will be difficult, causing a very slow calcination reaction with a less reactive  $\text{CaO}$ .

The firing temperature is another parameter which affects the lime quality/reactivity: calcite ( $\text{CaCO}_3$ ) typically dissociates into  $\text{CO}_2$  at  $898^\circ\text{C}$  at the pressure of 1 atmosphere (Elert et al., 2002). When temperatures below  $900^\circ\text{C}$  are reached, or if there are temperature differences in the cooking environment, as it can easily happen in the production of mortars according to traditional technologies, some parts of material may not complete the calcination process, resulting in unburned portions. To ensure complete calcination, even for larger fragments, the temperature can be increased above  $1100^\circ\text{C}$ , quicklime can be composed of large calcium oxide crystals and crushed limestone remains. The possibility that the generated  $\text{CO}_2$  will not easily volatilize out of the furnace is also a crucial point. If this occurs, the freshly formed  $\text{CaO}$  crystals may undergo a second reaction, generating lumps of  $\text{CaCO}_3$ . The remains of  $\text{CaCO}_3$  produced in the calcination, may represent a critical issue for the radiocarbon dating, as explained in the following paragraphs.

The hydration process (also called slaking) is a subsequent process, a highly exothermic reaction in which quicklime is slaked with water to yield hydrated lime,  $\text{Ca}(\text{OH})_2$ . When the  $\text{CaO}$  powder is mixed with an exact (i.e., stoichiometric) amount of water, a fine dry powder is obtained (dry hydration process). When the  $\text{CaO}$  powder is mixed with excess water, a smooth paste is obtained in a calcium hydroxide suspension in water (lime slaking process), which is called “slaked lime” or lime putty.

Historically, the aging of lime putty took place under water for a period of 6 to even more than 24 months. This process changed the crystal form of  $\text{Ca}(\text{OH})_2$  crystals (from prismatic to tabular) and improved the mechanical properties of the future mortar (Figure 2.2).



*Figure 2.3 – Vats for the maturation of quicklime. If the CaO powder is mixed with an excess of water, it forms slaked lime in the form of portlandite. This compound is then matured in dedicated vats to acquire plastic properties.*

For use in masonries or decorations,  $\text{Ca}(\text{OH})_2$  is added to silicate (e.g. quartz sand), carbonate (e.g. limestone pebbles) aggregates and/or rock fragments, to increase volume and enhance the mechanical stability and durability of the final product. The aerial mortar mixture set through the carbonation process, hydrated lime turns back to  $\text{CaCO}_3$ , usually in the form of calcite, upon incorporation of carbon dioxide ( $\text{CO}_2$ ) from air and evaporation of water (Boynton, 1980; Xu et al., 2015, 2016). The final product (mortar) is obtained very slowly, due to the effect of two phases: setting and hardening reactions. At first, as the mixture is set, loss of machinability, plasticity, and deformability as well as a contraction of the supplied mass can be recognized. Putty lime in solution starts to precipitate, while at the same time, free water is lost through evaporation (over a period of hours or days).

In the second phase, the calcium hydroxide is transformed into  $\text{CaCO}_3$  crystals, the process may take months or years depending on the conditions of exposure to  $\text{CO}_2$  and humidity. The hardening reaction involves an increase in volume of the solid part (about

12%), which fills a part of the pores previously occupied by the free water of the dough (Pecchioni et al., 2018). The atmospheric CO<sub>2</sub> absorption of calcium hydroxide allows the formation of secondary carbonate (anthropogenic), that acts as a binder between the inert materials of the mortar.

## 2.2.2 Production of hydraulic mortar

The group of ancient hydraulic mortars includes hydraulic lime binders obtained by firing of impure limestone and aerial binder with addition of materials providing hydraulic characteristics, of which the production phases will be deepened, as the subject of the research.

### *Aerial lime binder with addition of materials providing hydraulic characteristics*

Mixing lime binder with partially or fully reactive aggregate represents the transition from lime-based aerial mortar to hydraulic mortars (Artioli et al., in 2019). The reactive aggregate, which contains Si and Al-rich material, initiates the dissolution of silicate or aluminosilicate phases and the consequent formation of insoluble, Si-rich, hydrous phases when exposed to an alkaline environment (Hobbs and Siddall, 2011). This reaction between lime and aluminosilicate phases is commonly known as a “pozzolanic reaction” or a “hydraulic reaction”. When the presence of reactive aluminosilicate phases promotes the pozzolanic reaction in the binder, it is referred to as a 'hydraulic' or 'pozzolanic' binder mortar (Massazza, 1998). The hydraulic ability of pozzolanic mortar to set underwater is the result of direct reactions between the slaked lime and pozzolana. This eliminates the need to capture atmospheric CO<sub>2</sub> during the setting process. In fact, this type of mortar was primarily used for hydraulic works and external plastering to increase the resistance to moisture in buildings.

The chemistry involved in the setting of pozzolana binder is more intricate than that of slaked lime. Pozzolana is a fine, highly porous powder composed of weathered volcanic glass and silicate and hydroxide minerals rich in Al, Na, K, Mg, Ca, and Fe (Massazza, 2003). When slaked lime and pozzolana are mixed, the slaked lime creates an alkaline

environment for the pozzolana, promoting pozzolanic reactions due to the large surface area of the powder. In the equation (5), the pozzolanic reaction is shown. However, in the literature you can find information about other pozzolanic reactions involving aluminosilicates and other oxides (Dodson, 1990; Hobbs and Siddall 2011).



The strongly alkaline portlandite solution reacts with the surfaces of the scoriaceous pozzolan, causing volcanic glass and silicate minerals to dissociate, their alkali ions to dissolve in the liquid phase, and calcium to be adsorbed on the scoriae surfaces, forming the calcium silicate hydrate (CSH, where C = CaO, S = SiO<sub>2</sub>, and H = H<sub>2</sub>O). CSH indeed acts as the binder in pozzolana mortar. This notation is beneficial because it avoids the need to specify calcium silicate hydrate stoichiometry, which is not universally standardized (Dodson, 1990). In the above equation, we can observe that pozzolana sets through hydration, consuming water. Therefore, pozzolanic mortar can harden even in a humid environment or under water, but if these conditions are not present, it can harden even in the presence of air (Hobbs and Siddall, 2011).

#### *Natural hydraulic mortar*

Natural hydraulic mortar, as discussed by Palladio, is a type of mortar that has hydraulic properties due to the presence of certain natural minerals in the burned limestone. It sets and hardens when exposed to water, making it suitable for various construction applications, including masonry and architectural works. Mortars made of natural hydraulic lime are generally produced by heating marly limestone, which contains between 6% and 20% clay. These limestones, fired at temperatures around 900°C, produce calcium silicates and aluminates that react with water, giving the material moderate hydraulic properties. The calcination process is carried out on dry powdered material, resulting in a compound consisting mainly of quicklime, with smaller quantities of silicates, aluminates, and complex calcium ferrites. The best hydraulic properties are achieved at 900°C, as they require less water and time to set. Moreover, lower temperatures do not favour the alteration of the hydraulically active compounds (such



as aluminium hydroxylates from the original clays), which react with lime in the presence of water during the setting and hardening period. After the elimination of hygroscopic water, between 850 and 900°C,  $\text{CaCO}_3$  decomposes into  $\text{CaO}$ , which then reacts with  $\text{SiO}_2$  present in the clay minerals, forming dicalcium silicate  $2\text{CaO} \cdot \text{SiO}_2$  (C2S) without reaching the formation temperature of tricalcium aluminate.

Recently, furnaces operating in the temperature range of 1100–1500°C have been employed, as higher temperatures enhance the hydraulic properties of materials by forming higher concentrations of active calcium silicates and aluminates.

The next phase of slaking lime must be carried out with the appropriate amount of water; an insufficient amount would result in unhydrated lime in the product, which would slowly absorb water and cause swelling and subsequent fractures. Simultaneously, it is necessary to avoid an excess of water, as it could lead to rapid hydration (Mariani, 1976). The hydraulic hydrated phases are virtually insoluble and transform into gel-like substances or microcrystalline materials, unlike calcium hydroxide, which carbonates more quickly. The quenching of weak and moderately hydraulic limes is done in water baths, allowing them to mature slowly like aerial lime. Quenching times are evaluated according to the quicklime content (which is higher in low or moderately hydraulic limes), the percentage of the present clay minerals, and the calcination temperature. The weak exothermic process results in the formation of a kind of a putty with less greasiness and adhesive properties compared to what is produced by aerial lime. The setting process is partly aerial and partly hydraulic: the carbonation of calcium hydroxide is more significant due to the prevalence of quicklime in the mixture; however, even small portions of silicates and aluminate calcium hydrates contribute to the setting and hardening phenomenon.

Following the completion of the setting process, the hardening phase begins, with further hydration and the development of mechanical strength. The main differences observed when comparing hydraulic mortar with aerial lime are the higher mechanical strength and lower porosity characteristics.

The degree of hydraulicity can be assessed on the basis of the quantity of components constituting the raw material (such as silica, alumina, iron, etc.) and is determined by the Hydraulicity Index (HI), expressed as a percentage ratio of the present oxides (Boynton, 1980):

$$HI = \frac{SiO_2 + Al_2O_3 + Fe_2O_3}{CaO + MgO}$$

The above expression is the most used and provides a useful parameter for classifying the hydraulic binder used in mortar preparation (Table 2.2). It represents the ability of a mortar or hydraulic binder to set and harden in a shorter or longer period and to maintain its strength properties even in a humid or submerged environment (Pecchioni et al., 2018). The lime produced before the 19th century shows highly variable composition, resulting in a behaviour, which varies from weakly to moderately hydraulic due to low kiln temperatures (850-900°C). The determination of the hydraulicity degree and of the complicated dynamics of the production process can be quite challenging due to the fine-grained size of the original material and the heterogeneity of the microtexture (Riccardi et al., 2007).

*Table 2.2 HI values in relation to clay content and respective setting times (Menicali, 1992).*

<b>Lime</b>	<b>HI</b>	<b>% Clay</b>	<b>Setting Time (days)</b>
Weakly hydraulic	0.10-0.16	5-8	15-30
Moderately hydraulic	0.16-0.31	8-15	7-11
Properly hydraulic	0.31-0.42	15-19	4-7
Highly hydraulic	0.42-0.50	19-22	4
Boundary limes (Normal cements)	0.50-0.65	22-27	4

## 2.3 Raw materials and technologies in building Heritage

Building archaeology aims at establishing the chronology of historical buildings, often relying on the study of mortar and masonry in building heritage. In the absence of written records or other archaeological evidence, characterization of historic lime mortars provides valuable insight into the technologies and construction phases used in the past until you obtain important dating information.

Mortar can be a valuable resource for both relative and absolute dating in the field of archaeology and building Heritage. In relative dating, the analysis of mortar helps archaeologists and historians to establish the relative chronology of different construction phases within a building or site.

Mortars are complex and heterogeneous materials, the raw materials used in mortar and masonry construction are essential components to examine. The composition of mortar, such as the types and proportions of binders (e.g., lime, clay, or gypsum) and aggregates (e.g., sand or crushed stone) helps us understanding the availability of specific materials, the sources from which they were obtained, and the technological choices made by ancient builders. According to the historical period and the geographical location, different binders have been employed in the production of mortar throughout history (Elsen et al., 2012). The information found in the mortars enables one to recognize old "recipes" by identifying the key ingredients, such as aggregate and binder, the latter of which serves to give the paste "cohesion" and harden it. In this way, it is the primary element that can affect the functionality and longevity of these materials. By comparing the characteristics of mortars, it is possible to assess differences and similarities to conduct a relative dating of the sampled construction phases. This knowledge contributes to the preservation, restoration, and appreciation of our architectural heritage, ensuring its enduring legacy for future generations to admire and learn from. The analysis results guide restoration by identifying compatible materials and techniques that preserve the authenticity and structural integrity of the original construction. The possibilities to estimate the dating of structures aids in

establishing conservation priorities, identifying previous restoration interventions, and making informed decisions regarding the preservation and maintenance of historic buildings.

In absolute dating, Optically Stimulated Luminescence (OSL), Thermoluminescence (TL), and Radiocarbon dating ( $^{14}\text{C}$ ) can provide a specific chronological time frame for the construction of a building or wall structure. In principle,  $^{14}\text{C}$  and OSL can be applied to date a mortar. The  $^{14}\text{C}$  method can be used to determine when the lime binder carbonated, while OSL dating focuses on analysing the aggregates in the mortar to determine when they were last exposed to light before the mortar was embedded in a structure. The  $^{14}\text{C}$  dating can be also applied to organic materials present in the mortar, for instance as additives.

The OSL technique determines the time since the mortar was last exposed to sunlight, by measuring luminescence in quartz and feldspar grains (Goedicke, 2003; Panzeri et al., 2019).

This method was used in (Jain et al., 2002; Jain et al., 2004) for tests on building mortars. OSL dating is based on the assumption that quartz in the sand used to make mortar has been optically zeroed or "bleached" by light during mortar manufacture. The degree of bleaching is the main problem in OSL dating of mortars. Early results from mortars where the classic multigranular method was used are not accurate or precise (Goedicke, 2003; Goedicke, 2011). Many historic mortars contain grains with varying degrees of optical whitening, so they emit luminescence signals of varying intensity (Jain et al., 2004).

The instrumental upgrading of the "single grain" technique for OSL dating represents a significant advance in its application to mortars.

In addition, the OSL method is also applicable to other materials containing quartz or feldspar, such as brick fragments (Gueli et al., 2010; Panzeri et al., 2019).

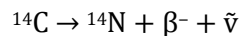
Each method has its advantages and limitations, and the choice depends on the properties of the sample and the desired dating accuracy.

## 3 Mortar dating by radiocarbon

### 3.1 Principles of radiocarbon dating

Radiocarbon dating is a radiometric technique based on the measurement of the residual concentration of a carbon isotope in certain materials. The main principles of this method were initially developed and published between 1947 and 1949 by a team of chemists at the University of Chicago led by Willard Frank Libby, who was awarded the Nobel Prize for this work in 1960 (Libby, 1964).

$^{14}\text{C}$  is a radioactive isotope of carbon, undergoing  $\beta^-$  decay through the following decay process:



is produced  $^{14}\text{N}$ , a  $\beta^-$  electron with a maximum energy of 156 KeV, and an antineutrino  $\bar{\nu}$  (Martini, 2002).

$^{14}\text{C}$  is produced by interactions between thermal neutrons, which are a byproduct of cosmic rays, and atmospheric nitrogen ( $^{14}\text{N}(n,p)^{14}\text{C}$ ). Atoms of the radioactive carbon isotope, along with stable carbon atoms, rapidly oxidize to  $\text{CO}_2$  and enter the life cycle of living organisms through photosynthesis and metabolic processes. The production of radiocarbon concentration in the atmosphere is continuous and constant ( $^{14}\text{C}/^{12}\text{C} = 1.18 \cdot 10^{-12}$  pMC (Olsson, 1968)), despite its radioactivity. Considering the fact that the exchange in the biosphere is continuous, the living organisms have approximately equal radiocarbon concentration in the atmosphere.

When the life cycle of an organism ceases, the absorption of radiocarbon stops, and the concentration of  $^{14}\text{C}$  begins to decrease, following an exponential decay equation, where at a given time  $t$ :

$$[^{14}\text{C}]_t = [^{14}\text{C}]_0 \cdot e^{-t/\tau}$$

where  $[^{14}\text{C}]_0$  is the radiocarbon concentration at the time of death of the organism and  $\tau$  is the mean life of  $^{14}\text{C}$  (Fedi, 2009). This equation can be used to determine the time

that has elapsed since the death of the individual to the present day;  $t$  is defined as the conventional radiocarbon age ( $t_{RC}$ ) by making certain assumptions, i.e. using the mean life proposed by Libby of 8033 years and considering  $[^{14}\text{C}]_0$  as the radiocarbon concentration in the atmosphere attributed to 1950.

Therefore, the conventional radiocarbon age is given by:

$$t_{RC} = \tau \ln \frac{[^{14}\text{C}]_0}{[^{14}\text{C}]_t}$$

The conventional radiocarbon age (expressed in years Before Present (BP)) is not an accurate representation of the true age of a sample because of approximations in the underlying assumptions. Calibration curves are used to adjust the conventional radiocarbon age and determine the true age of the sample.

These curves combine data from different dating methods and establish the relationship between conventional radiocarbon age and calendar date. The IntCal20 and Marine20 calibration curves (Reimer et al., 2020; Heaton et al., 2020), based on different calibration datasets, are commonly used in radiocarbon dating to 55,000 years ago. Calibration software such as OxCal, developed by the Oxford Radiocarbon Accelerator Unit, is commonly used.

Figure 3.1 shows a calibration curve depicting the relationship between calendar age and conventional radiocarbon age, along with the experimental error.

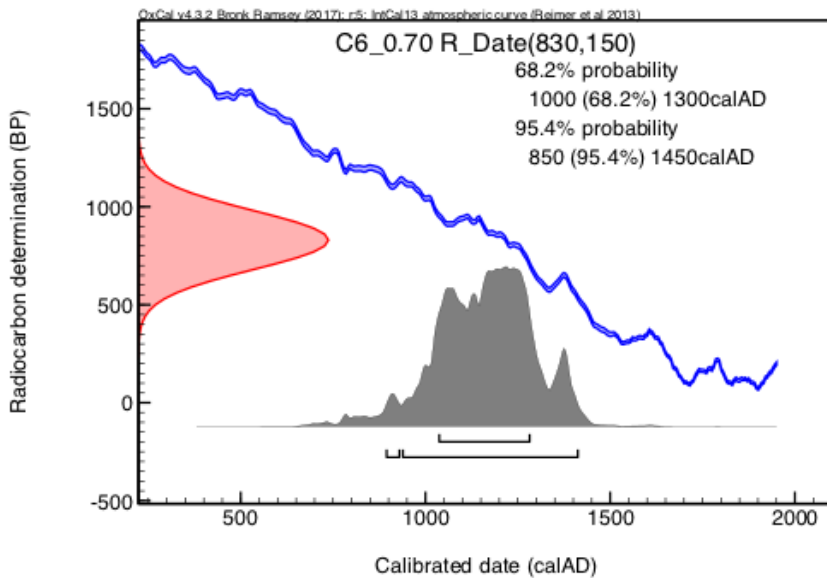


Figure 3.1 – Example of calibration of the radiocarbon conventional age of sample, using Oxcal.

These principle properties of the dating method can also be applied to the inorganic material of the mortar binder, since the incorporation of atmospheric CO<sub>2</sub> in the setting reaction of the mortar fixes the atmospheric radiocarbon in the calcitic lime binder at this time.

### 3.2 Advantages and challenges of applying <sup>14</sup>C dating to mortars

The possibility to reconstruct the chronology of historical buildings provides valuable information. Dating buildings by direct dating of lime mortars would be of great help; in principle, this can be done by radiocarbon dating. The dating of mortars is based on the absorption of atmospheric CO<sub>2</sub> by calcium hydroxide during the setting process. This forms CaCO<sub>3</sub>, which acts as a binder between the aggregate materials, fixing the atmospheric <sup>14</sup>C in the structure of the binder calcite.

The calcite in the binder represents the datable component of the mortar, also known as anthropogenic calcite, as its <sup>14</sup>C concentration remains in equilibrium with the

atmospheric concentration until the end of the hardening process. This method would be very useful because it would reconstruct the archaeological chronology and estimate the age of the construction. It is generally considered more reliable than dating charcoal that can be found in the inorganic matrix, since dating charred materials could provide aged dates not directly associated with the building's construction. Charcoal is a compound that is produced when wood is burned and therefore reflects the age of the wood. The problem arises from the type of wood used for the furnace. It can be a small branch, so I get the date when the branch was "dead". Or the wood may be from the inner ring of a very old tree, which is full of rings. Then the date measured may be much older than when the tree stopped living.

In addition, charcoal is not intentionally added to mortars; its presence is accidental and may result from the unintentional accumulation of carbonaceous residues from the fuel during the quicklime manufacturing process. Moreover, in general, the binder in a mortar is generally present in greater quantity than random fragments of charcoal.

As a proof of principle, anthropogenic carbonates such as lime plaster and lime mortar, which are man-made materials composed of calcium carbonate ( $\text{CaCO}_3$ ) produced through pyrotechnological processes (Weiner, 2010; Artioli, 2010), can be dated to estimate the construction phase of masonry. While general and widely accepted procedures have not yet been established, numerous papers discuss the feasibility of applying radiocarbon dating to mortars, highlighting the limitations of the method due to potential sources of contamination and suggesting experimental strategies to mitigate these sources (Hayen et al., 2017).

It can be challenging to isolate and date binder C from such a complex matrix when additional carbonate phases, such as aggregates or foreign carbonates, interact and alter the signature of the system. The primary sources of C that may lead to measurement bias are:

i) original unburned limestone fragments (calcination relics), resulting from incomplete burning of limestone during quicklime production, leading to an aging effect and potential age overestimation in radiocarbon dating;



- ii) geogenic carbonate from the aggregates, used as inert materials during mortar production, which can again lead to aging of the mortar dating;
- iii) (re)crystallized carbonates, derived from the interaction of the binder with current water or rain, including varying amounts of dissolved inorganic carbon. These carbonates can either cause general rejuvenation or accelerated aging, depending on whether the water source is groundwater or surface water;
- iv) delayed hardening, a complication wherein mortar may harden significantly later than the time of construction due to the slow uptake of atmospheric CO<sub>2</sub> (thick walls), leading to potential inaccuracies in dating.

Furthermore, radiocarbon dating is only applicable on certain types of mortars, specifically those that utilize atmospheric CO<sub>2</sub> during the hardening process. For example, in the case of pozzolana mortars, those hardened in conditions of high humidity or even under water environments do not acquire atmospheric CO<sub>2</sub> and are not recommended for radiocarbon dating. On the other hand, pozzolana that hardens in the presence of air has the potential for carbon dating, as the Ca(OH)<sub>2</sub> can react with atmospheric CO<sub>2</sub>, resulting in the production of datable CaCO<sub>3</sub>. The possibility of dating pozzolanic mortar can be evaluated according to their function. Generally used in hydraulic structures (such as aqueducts, cisterns, pavements) due to their properties, the conditions that make them suitable for dating see the continuous exchange with water.

Moreover, the sample that will be radiocarbon-dated should be viewed as a closed system, according to one of the fundamental principles of radiocarbon dating. This occurs for the mortar immediately following the binder has complete hardening because that is when ambient CO<sub>2</sub> absorption ceases. This need is not always followed, though, as dissolution and the subsequent recrystallization phenomenon could result from things like water percolation.

The complete carbonation of the mortar could take place in particularly long times, which are much larger than the experimental uncertainties of a radiocarbon measurement, making the measurement inaccurate.

The possibility of dating an archaeological mortar has been also explored, using lime lump dating. The first radiocarbon dating tests of lime lumps yielded positive results (Van Strydonck et al., 1992) because lime lumps offer the advantage of accurately representing the binder without the influence of aggregates (Lindroos, 2005; Pesce et al., 2009; Pesce et al., 2012). However, lime lumps need to be thoroughly investigated, taking into account the different types of lumps and their small size, which complicates their selection from mortar samples.

Given the above factors, radiocarbon dating of mortars presents a number of technical challenges, and considerable attention must be paid to both the sampling of the mortar and its characterization. Only through accurate analytical characterization of the collected materials is it possible to determine whether the selected samples are suitable candidates. Therefore, a complete separation of the binder from the aggregates is essential. The following paragraph will present sampling strategies, characterization techniques, and various procedures used to separate the binder from the aggregates.

### 3.3 Review of recent strategies on sampling, characterization, and selection of datable fraction in mortar radiocarbon dating

A considerable amount of time has passed since the first attempts to date mortars (Folk and Valastro, 1976). After the initial studies, Van Strydonck et al. (1983) and Heinemeier et al. (1997) proposed a more systematic approach to radiocarbon dating ( $^{14}\text{C}$ ) of mortars. Subsequently, several methodological developments were made over the years;  $^{14}\text{C}$  dating of mortars gained popularity, and new procedures or their modifications were evaluated (Nawrocka et al., 2009; Marzaioli et al., 2011; Michalska et al., 2017). At present, in the international community, there is not a unique and fully accepted way of mortar sample preparation to systematically obtain accurate results. Only recently has it become apparent that accurate analytical characterization of the collected materials is essential to determine whether the selected samples are suitable candidates. Good strategies and reference literature on sampling, characterization

methods, and preparation procedures are important steps that are briefly discussed below.

### 3.3.1 Sampling

Accurate dating of mortar in masonry requires a comprehensive approach involving collaboration between experts in mortar analysis, archaeologists and architects who understand wall stratigraphy. Precise sampling is crucial and begins with well-defined research questions related to chronology. For example, if the goal is to determine the age of construction, it is important to avoid sampling in areas where repairs or renovations have occurred. However, if the investigation is aimed at determining the period of use of the building, such areas may be of greater importance. When selecting a sample from a building unit, it is important to consider which structural elements are likely original and which are likely the result of subsequent repairs or renovations (Heinemeier et al., 2010; Ringbom et al., 2014).

Bedding mortar or core mortar is usually less altered and restored over time than plaster and is potentially less exposed to the elements (Boaretto, 2009). Mortar that is between stone blocks can be considered original if the stone block is overlying the mortar and not the other way around. If the mortar protrudes and is above the stone block, it indicates subsequent intervention after the masonry was originally constructed. It is strongly recommended that scattered mortar samples not be taken on the ground, as they may have been transported by different units or weathered by organic acids. This precaution is especially important with collapsed ruins and rubble. Obtaining a secure contextual sample is a critical first step in achieving successful  $^{14}\text{C}$  dating results in mortar, regardless of the specific chronological research objectives.

Samples subject to such complications may yield inconclusive results because the problems are many and may stem from the mortar itself (i.e., type of mortar, type of aggregate) or from interaction with the environment to date (i.e., state of preservation, recrystallization, delayed hardening).

To reduce secondary carbon sources, sampling sites should be carefully selected, favouring masonry areas less exposed to weathering over exterior surfaces or foundations and analysing samples from intermediate depths. Ambient water, which can influence mortar, can originate from various weathering sources such as rainfall, surface water, and groundwater. Rainfall and surface water can be absorbed by the sample, appearing younger than expected; whereas groundwater and soil moisture may contain dissolved geological carbonates, resulting in an apparent aging effect.

Mortar hardens through the absorption of atmospheric CO<sub>2</sub>, with the hardening process initiating at the surface and progressing inward through the diffusion of CO<sub>2</sub> from the surface. The hardening process slows down as it reaches the innermost parts, which can only be reached by diffusion through partially hardened mortar. Consequently, the inner parts of a thick wall may experience a delay in hardening compared to the time of construction, ranging from decades to centuries (Pesce et al., 2012). This can lead to inaccuracies in dating results, with the age appearing younger than the actual time of mortar placement. The optimal sample should be taken at a depth close to the wall's surface, deep enough to avoid recrystallization near the surface due to weathering, and potential future surface repairs or repointing, taking care of delayed hardening issues. The sample could contain carbonate aggregate, it can be identified by the presence of compact and tenacious white fragments. In such cases, the primary strategy during sampling should be to minimize the generation of splinters and therefore limit the dispersion of geological carbon in the sample. Confirmation and identification of geogenic calcite contamination is accomplished by examination of thin sections during petrographic analysis.

### 3.3.2 From macro to micro mortar characterization

The characterization of the mortars allows evaluating if the sample is suitable for dating. Typically, mortar samples or powders that have been mechanically separated from mortar samples are subjected to one or more preliminary characterization procedures.

These provide useful details about the constituents of a mortar sample and potential problems or contaminants. Based on Daugbjerg et al. (2021b) analysis of 56 publications (published between 1964 and 2020) aimed at dating pre-characterized mortars, it was possible to evaluate the most commonly used characterization methods for this type of study. The frequency histogram is shown in Figure 3.2.

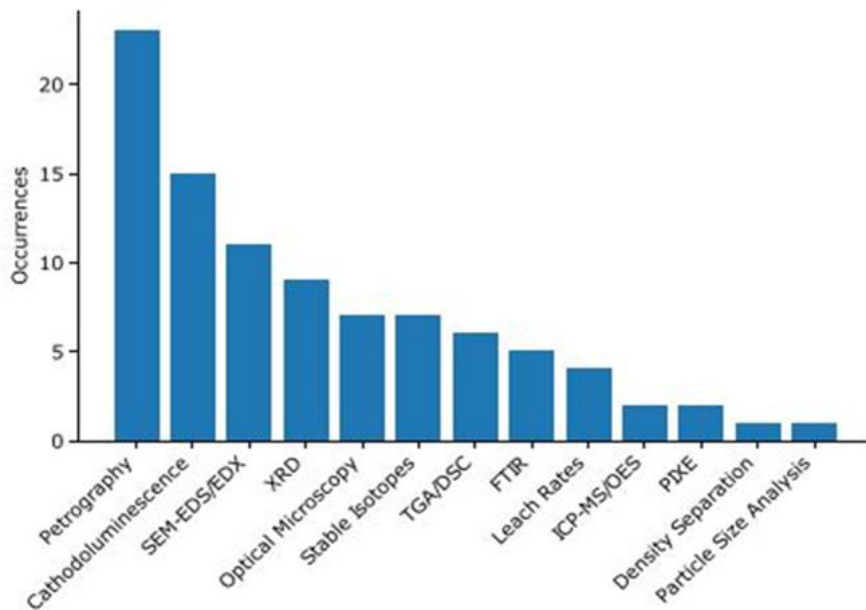


Figure 3.2 - Histogram of frequency of characterization techniques in 40 research on mortar dating conducted between 1964 and 2020 (Daugbjerg et al., 2021b).

The most common analytical methods used to examine mortars with the aim at dating are petrography, X-ray powder diffraction, cathodoluminescence, scanning electron microscope.

Since the 1980s, the investigation of historical mortars has relied on the examination of petrographic and mineralogical characteristics using a polarizing optical microscope, treating mortars as if they were natural rock-like materials (Martinet and Quenée, 2000; Pecchioni et al., 2020). Mineralogical and petrographic studies provide information on the nature of binder, aggregates, lump, possible additives/admixtures of the mortars

themselves. X-ray diffractometry on powders (XRPD) allows qualitative or semi-quantitative mineralogical analysis of polycrystalline components. XRPD analysis can be performed on both bulk samples and on separated lumps.

Mortar dating studies widely use cathodoluminescence (Figure 3.2), which allows the observation of minerals and sediments luminescent in thin section (30  $\mu\text{m}$ ) or in powdered form through polarized transmitted light. The observed phenomenon is represented by emission of visible lights of different wavelengths, produced by high-energy electrons interacting with a semiconductor crystal, where most of the energy is converted to heat. Luminescence centres can be categorized as intrinsic or extrinsic. Intrinsic centres arise from vacancies and lattice imperfections, while extrinsic centres result from ion substitutions. One example of an extrinsic centre is  $\text{Mn}^{2+}$ , which acts as an activator and gives rise to orange-red luminescence in carbonate rocks. It is worth noting that geogenic forms of  $\text{CaCO}_3$ , like limestone, often display orange-red luminescence due to the presence of  $\text{MnCO}_3$  sites within the calcite crystal lattice. Cathodoluminescence can allow us to discriminate, through different emission colours, the grains of limestone and dolomite with dead carbon from anthropogenic calcite (Lindroos et al., 2007; Toffolo et al., 2020; Ricci et al., 2022).

SEM (Scanning Electron Microscope) is a technique used to obtain morphological and chemical information (semiquantitative analyses), enabling the identification and characterization of various types of aggregates, lumps, and binders, including calcium-based, magnesium-based, and hydraulic binders (Cantisani et al., 2021).

Thermogravimetric analysis or/and differential scanning calorimetry (TGA/DSC), TGA and DSC are important techniques for mortar characterization. TGA measures weight changes during heating, revealing thermal stability, decomposition, and moisture content, helping identify binder types. DSC measures heat flow during temperature changes, providing insights into phase transitions and thermal behavior (Moropoulou et al., 1995; Bakolas et al., 1995). These techniques aid in understanding mortar composition, and thermal properties.

The Fourier-transform infrared spectrometer (FTIR) is used to analyse chemical composition and the origin of calcite in mortar. By comparing the FTIR spectra of the mortar sample with reference spectra of different sources of calcite, such as limestone or shell fragments, the origin of the calcite in the mortar can be determined (Chu et al., 2008; Regev et al., 2010). A recent study suggests that SEM-CL and laser-induced fluorescence (LIF) can integrate XRPD and FTIR analyses for assessing the structural order in  $\text{CaCO}_3$  crystals (Toffolo et al., 2019; Toffolo et al., 2020). The study compares the analyses on experimental lime plasters, mollusk shells, and precipitated crystals to produce a reference database.

Additional characterization methods used in mortar dating investigations, such as leach rates (Lindroos et al., 2007), density separation (Toffolo et al., 2020), and particle size analysis (Ortega et al., 2012), have also been successful in identifying potential contaminants.

### 3.3.3 Pre-treatment of lime mortar

The pre-treatment of mortar samples involves isolating the fraction of carbon dioxide ( $\text{CO}_2$ ) from the binder, using procedures aimed at removing various contaminants. Finding the most suitable preparation technique can be challenging as it often depends on the types of contaminants present in the sample. Numerous studies have suggested a possible experimental set-up, although general and widely accepted protocols have not yet been established.

The so-called **sequential dissolution** method is one of the most common approaches, developed in 1997 (Folk and Valastro, 1976), and related to the expected different solubility and reaction rate of the anthropogenic carbonate of the binder compared to other components of the mortar. As a first step, a mechanical separation is performed using a sieve with a grain size of 46 to 75  $\mu\text{m}$  to reject most of the aggregates and enrich the sample in binder. Then, the sample is placed in a vacuum line and dissolved using an 85% aqueous solution of  $\text{H}_3\text{PO}_4$ , to extract  $\text{CO}_2$  (as shown in scheme in Figure 3.3a).

Originally, hydrolysis was performed with hydrochloric acid (HCl). However, when comparative tests were performed between HCl and  $\text{H}_3\text{PO}_4$  on the same mortar samples, it was found that HCl had too much variability and was overly influenced by the type of mortar, while  $\text{H}_3\text{PO}_4$  gave more reliable and consistent results (Ringbom et al., 2014). The sample is dissolved, and several aliquots of  $\text{CO}_2$  are collected at different time intervals from the start of the reaction.

In principle, the first  $\text{CO}_2$  fractions collected in very short reaction times should reflect the age of the construction, as the bonds of anthropogenic carbonates are weaker and therefore easier to dissolve compared to the cohesive chemical structures that constitute geological carbonates. To evaluate the possible influence of contaminants, multiple  $\text{CO}_2$  fractions are collected at subsequent time intervals, and the radiocarbon content is measured for each fraction. The last fractions should indicate the possible presence of contaminations. However, these age profiles are often much more complicated, due to various factors influencing the trend of ages for sequential  $\text{CO}_2$  fractions, such as the presence of fine-grained carbonate aggregates that would react even faster than the binder. For this reason, the importance of characterizing the mortar before dating has recently been emphasized.

Mortars with moderate dead carbon, recrystallization, or alkalinity issues respond well to the sequential dissolution approach (Folk and Valastro, 1976; Lindroos et al., 2007; Michalska and Czernik, 2015). Sequential dissolution can be complicated by significant dead carbon contamination (Lichtenberger et al., 2015, for example). Furthermore, the method is extremely time consuming and expensive.

The **Cryo2SoniC** procedure is a mechanical separation method used before  $\text{CO}_2$  extraction from mortar samples. It is a modification of the initial CryoSoniC procedure, developed to improve the separation efficiency between binder and aggregate and enable its application to real samples (Marzaioli et al., 2011; Pesce et al., 2012).

The Cryo2SoniC process involves several steps (as shown in scheme in Figure 3.3b). Firstly, the sample is cooled with liquid nitrogen and subjected to cycles of heating and cooling. Subsequently, it is gently crushed to minimize the production of fine particles



not belonging to the binder. After crushing, the resulting fragments are sieved and immersed in deionized water. The suspension is then subjected to a first ultrasonic bath to remove more easily soluble phases, such as fine aggregates and carbonates resulting from secondary processes. Once sedimented, the suspension undergoes a second ultrasonic bath to separate the carbonates derived from the binder, theoretically free from contamination. The resulting "sand" and "susp" fractions are dried and subjected to acid attack to obtain CO<sub>2</sub>. Finally, the collected CO<sub>2</sub> fraction is graphitized and measured using AMS for radiocarbon analysis.

This method offers advantages, including a reduction in the number of radiocarbon measurements for each mortar sample. However, results from different sources in the literature vary: Cryo2sonic technology has been used in some works to successfully suppress dead carbon (Ortega et al., 2012; Nonni et al., 2018), whereas in other studies (Nonni et al., 2018; Ponce-Anton et al., 2018), dead carbon has remained.

An alternative approach to isolating CO<sub>2</sub> from mortar involves thermal decomposition of the sample.

**Ramped pyrolysis/oxidation** methods exploit the use of thermal decomposition properties of calcium carbonate in the mortar. This method involves ramped, continuous heating of a sample under oxygen or oxygen-free conditions, capturing CO<sub>2</sub> at different temperature intervals for later radiocarbon dating (as shown in scheme in Figure 3.3c). The process includes the insertion of material after pre-cleaning onto a quartz glass reactor with a bed of quartz wool. The sample is then progressively heated in a furnace with flowing helium gas, from 200°C up to 600°C. After holding at 600°C for 20 minutes to remove potential contaminants, the temperature is ramped from 600°C to 800°C over 1.5 hours.

Enhanced oxidation occurs as pyrolysis products are carried into a lower furnace with copper oxide, nickel, and platinum catalysts, converting them to CO<sub>2</sub> at targeted temperature ranges. Gas analysis is performed, and CO<sub>2</sub> is collected and graphitized for further analysis using the hydrogen reduction method. Various fractions of CO<sub>2</sub> are collected at temperature intervals that cover the decomposition range of calcium

carbonate in the sample. These CO<sub>2</sub> fractions will be subsequently analysed to obtain information about the dating of the sample. The number and width of the temperature intervals may vary depending on the dating material and specific characteristics of the analysed sample.

TGA characterization allows to establish the temperature range, in which the carbonates in the mortar release CO<sub>2</sub>. However, studies in the literature do not find a common temperature range: in (Toffolo et al., 2017; Ricci et al., 2020) the thermal decomposition of anthropogenic carbonate begins in the range 500-550°C, while in (Daugbjerg et al., 2021a) and others occur around 550-650°C. In this way, the first fractions include CO<sub>2</sub> from sample phases that thermally decompose at lower temperatures, while the next fractions contain CO<sub>2</sub> from sample phases that thermally decompose at higher temperatures, such as the organic phase up to 500°C, the hydroxides of dolomitic lime mortars around 500-550°C, the anthropogenic carbonates in the range of 500-650°C, and geogenic carbonates in the range of 700-800°C. The entire set-up and method have been described in detail in a publication by Keaveney et al., 2021 and have been applied to mortar samples in (Barrett et al., 2021; Barrett et al., 2023).

Recently, it has been discovered that aragonite (Toffolo et al., 2017) forms together with calcite in high temperature fired ashes, and in certain Israeli sites, these materials are found in distinct layers within the stratigraphic sequence. Aragonite appears to be easily recognizable and potentially an ideal material for radiocarbon dating. The separation of aragonite from calcite is achieved using the thermal decomposition method, which has resulted in accurate dating in some experiments (Toffolo et al., 2020).

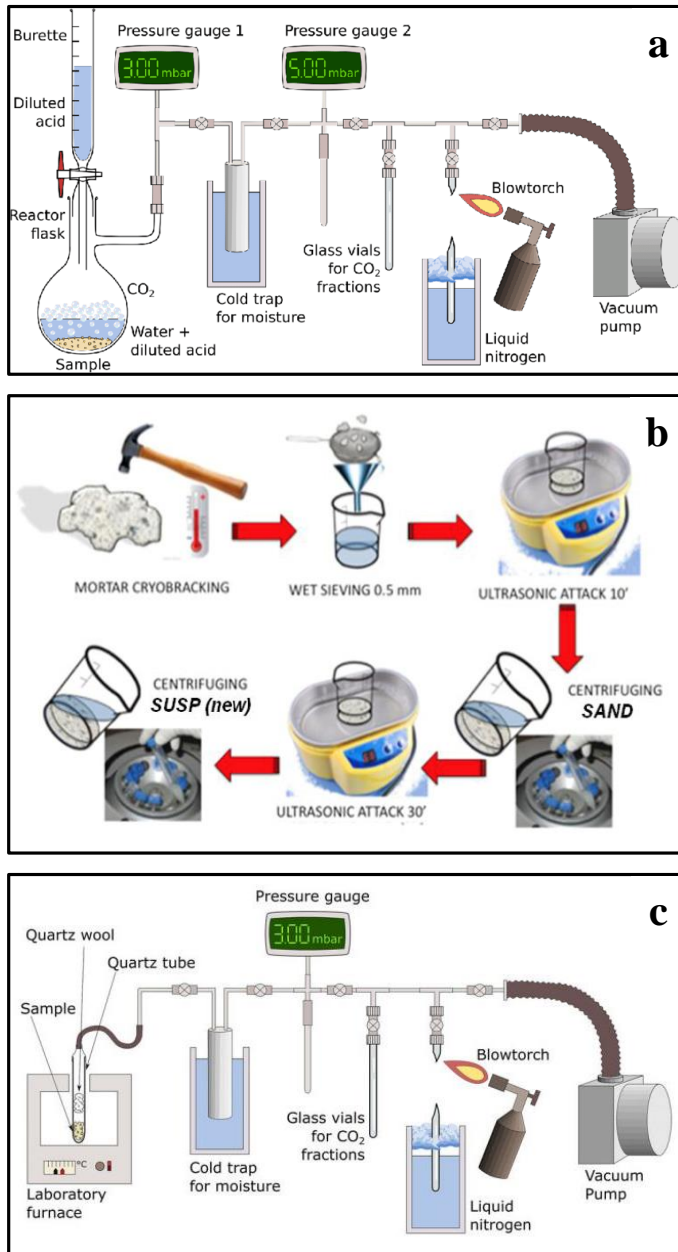


Figure 3.3 – Schematic representation of the pre-treatments of lime binder: a) sequential dissolution method (Ringbom et al., 2014); b) Cryo2SoniC procedure (Nonni, 2014); and c) thermal decomposition approach (Daugbjerg et al., 2021a).

The methods described above are currently used to process CO<sub>2</sub> from whole mortar samples or lumps. Bibliographic sources have highlighted that determining the <sup>14</sup>C

concentration in binder lumps leads to more homogeneous results compared to whole mortar samples, when treated with acid digestion (Lindroos et al., 2014). Lumps have been analysed in several studies (Van Strydonck et al., 1992; Heinemeier et al., 1997; Lindroos et al., 2014; Lubritto et al., 2015; Barrett et al 2023) and have generally shown ages consistent with the expected ones. Such inclusions can be considered free from any contamination, provided that lumps resulting from limited mixing of the binder with the aggregate are identified.

A study was proposed to evaluate the results obtained by applying various procedures of the same mortar samples in different laboratories, the project is named "Mortar Dating Intercomparison Study" (MODIS), implemented in 2017 and 2020 (Hajdas et al., 2017; Michalska et al., 2017; Artioli et al., 2024). In 2017, the samples were fractionated into appropriate carbon fractions for radiocarbon dating by seven different radiocarbon laboratories: Aarhus, CIRCE, ETHZ, Poznań, RICH, and Milano-Bicocca. Overall, the findings of this initial intercomparison offer critical insights on material selection and the likelihood of a fruitful mortar date. These findings demonstrate both the potential and limitations of  $^{14}\text{C}$  dating mortars, showcasing the difficulty involved in this research field.

## 4 Research aim

Radiocarbon dating is a powerful tool that allows us to measure the age of ancient materials, but it is crucial to understand that the accuracy and reliability of the results depend on the quality of the initial information. To ensure accurate mortar dating, a multidisciplinary approach promoting collaboration across various disciplines is mandatory. In such a way, challenges and complexities of dating historical mortars can be highlighted. In particular, the complete characterization of historical mortars before radiocarbon dating is an essential step to achieve accurate and meaningful results.

Figure 4.1 shows the workflow set up during this PhD project to deal with all the criticalities in the possible application of radiocarbon to mortar dating.

The procedure proposed in this PhD research begins with the study of historical sources and archaeological analysis of the masonry to perform a first selection.

The second step is a comprehensive characterization performed on all sampled mortars in order to determine the type of binder, aggregate, the presence of lumps, and to evaluate the feasibility of the application of radiocarbon to mortars dating. The application of optical and electron microscopy (OM, SEM), X-ray diffraction on powders (XRPD) and thermogravimetric analysis (TGA) represent the preliminary characterization phase for each sampled mortar, following a well-established approach. In this PhD project, for the first time,  $\mu$ XRPD (high lateral resolution 2D mapping XRPD on beamline ID13) and FPA-FTIR (FTIR microscope FPA-imaging detector) were employed to investigate ancient mortars. This approach demonstrated the complementarity of these high-resolution imaging techniques, which was essential for addressing controversial aspects regarding the stability of calcium carbonate polymorphs and crystalline and amorphous calcium silicate in the binder of ancient mortars (Chapter 5).

The third step regards the selection of portions of sampled mortars that can be dated. These portions can be represented by binder or lime lumps. After completion of the second step, a secondary selection is performed, focusing on the most suitable samples, which are then subjected to further diagnostic tests, finally leading to a refined selection. In this research project, we explore novel methods (ATR FTIR and micro-Raman spectroscopies) to effectively differentiate between calcites formed through different processes, such as the so-called geogenic and anthropogenic calcite. Geogenic calcite is mainly present in sedimentary and metamorphic rocks (e.g. marbles); while anthropogenic calcite is mainly found as a binder in ancient mortars and plasters. The goal is to enhance the characterization of the samples by integrating well-established techniques commonly used in dating with new methodologies developed during the project, aiming to fully comprehend the composition of the sample intended for dating.

In order to avoid any type of contamination, the procedure includes the characterization of the datable fraction using XRPD, cathodoluminescence by optical microscopy (OM-CL), infrared spectroscopy (ATR-FTIR), and micro-Raman spectroscopy, developed in the laboratory DST-LAM and ISPC-CNR.

This procedure was evaluated on standard samples and then applied to non-standard samples to determine whether each method could be added as a technique to the procedure, as discussed in Chapter 6.

To complete the treatment of the mortar samples within the network of collaboration with Florentine laboratories for the development of mortar dating, the experimental set-up for the pre-treatment and measurement of  $^{14}\text{C}$  concentration was designed and optimized at the LABEC laboratory (Chapter 7).

In summary, our approach includes: 1) documentation, historical research, and good sampling strategies; 2) initial characterization of all mortar samples to assess the feasibility of dating; 3) selection of the datable fraction (lump or/and bulk samples) and their non-destructive characterization. The proactive identification of the origin of

calcite present in the sample powder allows for the measurement of only anthropogenic calcite, thereby reducing the time and cost of Accelerator Mass Spectrometer (AMS) measurements. Therefore, utilizing a non-destructive method is crucial, assuming limited sample quantities.

Considering the different types of mortars and the principles on which the radiocarbon dating method is based, it is evident that the non-hydraulic mortar is the most suitable for dating, as it fully incorporates atmospheric CO<sub>2</sub> during its hardening process. However, historical mortars in the Italian territory often consist of hydraulic binders, both natural and aggregate-added hydraulic binders. The PhD project aim is to expand and evaluate the selection procedure and application of <sup>14</sup>C to various historical hydraulic mortars of Florentine historical buildings (Chapter 8) and the bedding mortars of public buildings in Pompeii (Chapter 9). The case studies of historical buildings in Florence (Castle of Trebbio, S. Felicita Church, S. Giovanni Baptistery, and Medici Riccardi Palace), as well as public buildings in Pompeii (Temple of Apollo, Eumachia, Tabularium, Temple of Genius Augusti), were processed following the two analytical steps outlined in our designed procedure (mentioned above). Our procedure applied on Florentine mortar samples, allowed us to select samples suitable for dating from a natural hydraulic binder. Satisfactory results were achieved through non-destructive studies, experimental set-up and <sup>14</sup>C measurements of unique, small samples.

In Pompeii cases, starting from the characterization, it was possible to evaluate possible issues and limitations of the method and develop critical material selection procedures. Nevertheless, even with good strategies and rigorous sampling and analysis procedures, we may encounter mortar with too many sources of contamination. In this case, we must accept the limitations of the method and exclude the possibility of dating the binder fraction or lumps and select organic additives, if present. For the optimization of the datable fraction selection for radiocarbon dating of historical mortars, we evaluated the selection of organic inclusions when we are sure that the binder or lump selection must be excluded. This approach was applied to the mortars of the Church of San Philip in Hierapolis (Turkey), as discussed in detail in Chapter 10.

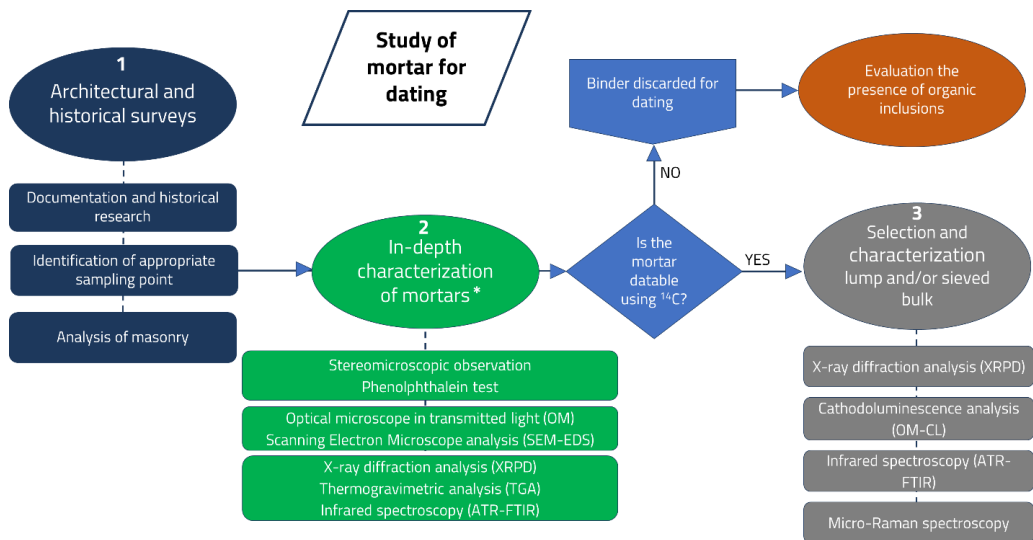


Figure 4.1 – Graphic workflow of the approach proposed in the PhD project. \*Application of advanced techniques to mortar characterization: FTIR microscope Focal Plane Array detector (FPA-FTIR), and  $\mu$ XRPD at the ID13 beamline in the European Synchrotron Radiation Facility (ESRF).



## 5 Analytical strategies for a comprehensive characterization of mortars

### 5.1 Mineralogical, petrographic and chemical characterization of mortar

To characterize mortars for dating purposes, it is essential to determine the composition of all the constituents of the mixture, their relative amounts (binder/aggregate ratio), the nature of the binder and aggregate, and the constituents within the binder, and to determine the degree of carbonation. For a comprehensive characterization, several investigations must be performed, each useful in reconstructing the overall picture and providing key information to select or exclude material for dating. The complementarity of multiple investigations is key to a correct and comprehensive understanding of the material.

The following techniques were employed for the initial characterization and assessment of the dating potential of mortar samples related to the case studies of this PhD thesis. The instrumentation and specific analytical methodology for each technique are detailed in Appendix 1.

#### 5.1.1 Carbonation test

At the sampling point or on the sample taken, the evaluation of the degree of carbonation of the mortar with the phenolphthalein test (UNI EN 14630, 2007) is the first obligatory characterization step. Phenolphthalein serves as a chemical indicator that undergoes a colour change depending on the pH of the environment, indicating the presence of calcium hydroxide in the mortar. Specifically, it turns purple when the pH is above 8.5, which is characteristic of alkaline conditions of calcium hydroxide. By observing the phenolphthalein colour change on the surface of the sample, the degree and depth of carbonation can be determined. Carbonation is considered incomplete if the sample exhibits a pinkish tint, and it is considered complete if it remains colourless.

A sample that is not fully carbonated must be excluded for  $^{14}\text{C}$  dating. The test can be performed in situ on masonry (Figure 5.1a) or in the laboratory on a sample (Figure 5.1b).

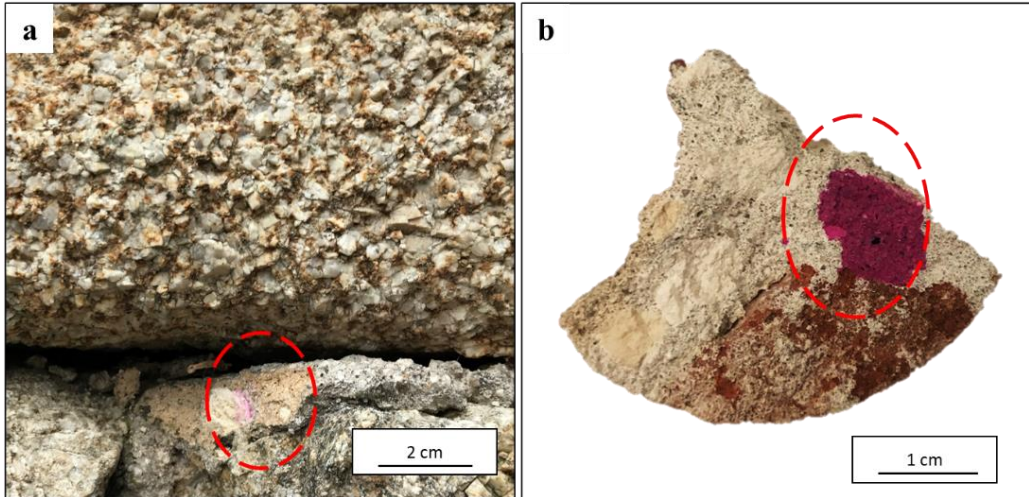


Figure 5.1 – Phenolphthalein tests: a) in situ on masonry; b) in laboratory on a sample.

### 5.1.2 Optical microscope

The observation of thin sections of mortar under the optical microscope in transmitted light (OM) provides a lot of information about the nature of the binder, the aggregates and the type of lumps (UNI 11176 (2006)).

For the binder, thin section observation provides information on texture (micritic, microsparitic, sparitic), mineralogical composition, birefringence colours, structure (homogeneous, in plagues, with lumps) and interaction between binder and aggregate. Calcium aerial lime binder has a homogeneous structure, is light brown, free of impurities and generally has a micritic texture consisting of calcite crystals smaller than  $10\ \mu\text{m}$ .

Magnesian aerial lime binder is heterogeneous with areas from micritic to microsparitic texture. This phenomenon is due to separation of the magnesian phase with respect to the calcic phase. Remnants of hydromagnesite (a partially carbonated phase of

magnesium hydroxide) with subspherical forms and a matte appearance are typically highlighted in OM.

Natural hydraulic binders exhibit a less uniform structure, brown colour, micritic texture, and impurities: widespread presence of small, dark neoformation phases composed of non-hydrated calcium/aluminosilicates (Figure 5.2a) (Cantisani et al., 2021; Cantisani et al., 2022; Calandra et al., 2022a; Calandra et al., 2022b). Binders with materials that provide hydraulic compounds exhibit a visible reaction rim between the binder, which consists of aerial lime (with micritic/microsparitic texture depending on the lime source), and the aggregate grains (i.e., pozzolanic or cocciopesto grains). This typical mix design was used in the Roman era (Figure 5.2b) (Miriello et al., 2010; Dilaria et al., 2022).

Moreover, from petrographic observation can be ascertained whether the binder displays a non-uniform appearance with zones of varying crystallinity. This phenomenon may be attributed to inhomogeneities in mixing or partial recrystallization due to circulating water within the masonry (Figure 5.2c). In Figure 5.2c the thin section of a sample from the foundations of the S. Giovanni Baptistery is shown, characterized by recrystallization of calcite in the pores, and a carbonate aggregate. These two features represent sources of contamination, and the sample has been excluded from  $^{14}\text{C}$  dating. So, the aggregate description is a fundamental step for evaluate the contamination sources: the particle size distribution (homogeneous, heterogeneous, banded), grain morphology (shape, sphericity, rounding, orientation) and size, mineralogical composition (assessing the relative abundance of each phase) are the main evaluated characteristics. Binder/aggregate ratio (B/A), expressed as the volume percentage of binder to aggregate; macroporosity (total porosity, shape and distribution); alteration products (surface, interlayer, voids, etc.) are other relevant characteristics. When the binder is predominant (i.e.,  $B/A < 1/3$ , fat mix), the sample, at equal mass, should contain a higher datable inorganic fraction. A well-prepared mortar should possess an appropriate amount of pores and few shrinkage fractures, allowing for proper carbonation (and thus effective  $\text{CO}_2$  diffusion in depth). In mortar samples where  $\text{CO}_2$

has not penetrated, a heterogeneous binder is observed, appearing dark in colour. If portlandite ( $\text{Ca}(\text{OH})_2$ ) is the predominant phase, the binder under OM exhibits low interference colours (birefringence 0.0270). This characteristic makes a carbonation defect easily recognizable (Figure 5.2d).

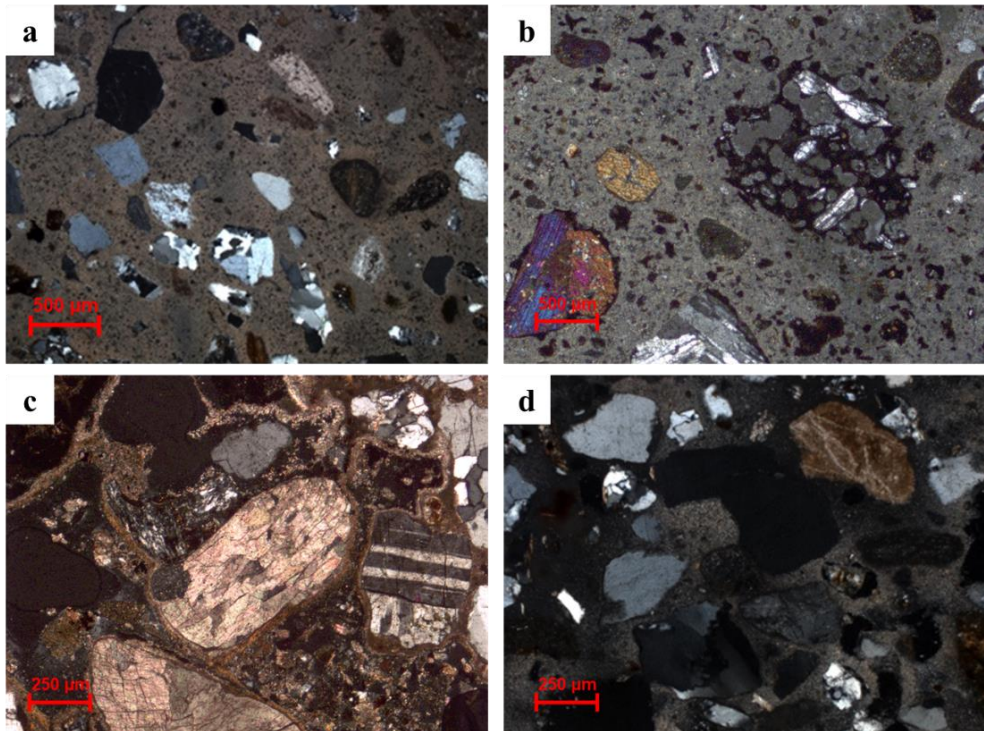


Figure 5.2 – Typical features of binder mortars obtained from petrographic observation: a) natural hydraulic binder: heterogeneous structure, brown colour, micritic texture, small dark impurities; b) aerial binder with addition of materials providing hydraulic characteristics; c) recrystallization of the binder in the form of spathic calcite inside the porosity; d) aerial binder with uneven areas due to a defect of carbonation.

Additional significant insights from petrography involve the identification of diverse lumps and fragment types within the mortar, which manifest whitish/beige/hazelnut hues and exhibit a spectrum of attributes ranging from incoherent, powdery forms to more cohesive and compact structures on a macroscopic scale. The presence of these inclusions suggests the use of traditional lime production methods (as detailed in paragraph 2.2.1). A high amount of these lumps may indicate poor quality production

techniques or the use of specific slaking methods, like hot lime slaking. These characteristics can be encountered in aerial limes, natural hydraulic limes and hydraulic limes.

Using transmitted light optical microscopy (OM), the following types of lumps can be identified:

- residues of stones used for the production of binder: sometimes apparent as under-burned lumps and over-burned lumps, based on furnace conditions and initial stone microstructure (Figure 5.3a,b). Under-burned lumps are distinctly discernible from the binder due to their structure that recall the typical rock features, suggesting low firing temperatures or uneven heat distribution in the kiln. Intermediate forms displaying fragmentary rock characteristics may also emerge due to unsuccessful firing, preserving the original rock structure. Over-burnt lumps represent fragments of overfired stone for lime with slow hydration, displaying higher porosity than under-burnt lumps, indicative of temperature non-uniformity during firing or inadequate attention during lime slaking.
- residues of binder: lime lumps exhibiting porous and eroded features, formed after late hydration and carbonation (Figure 5.3c,d); unmixed lime lumps with similar binder characteristics, resulting from insufficient mixing care during the blending phase.

Among various types of lumps, not all are suitable for identifying the construction structure's age (Van Strydonck et al., 1992; Lindroos et al., 2014). The selection of binder lumps is not unequivocal; whitish colouring and incoherent appearance are common features, also found in different types of binder. However, only binder lumps offer the advantage of not containing the isotopic signature of the aggregate or original limestone.

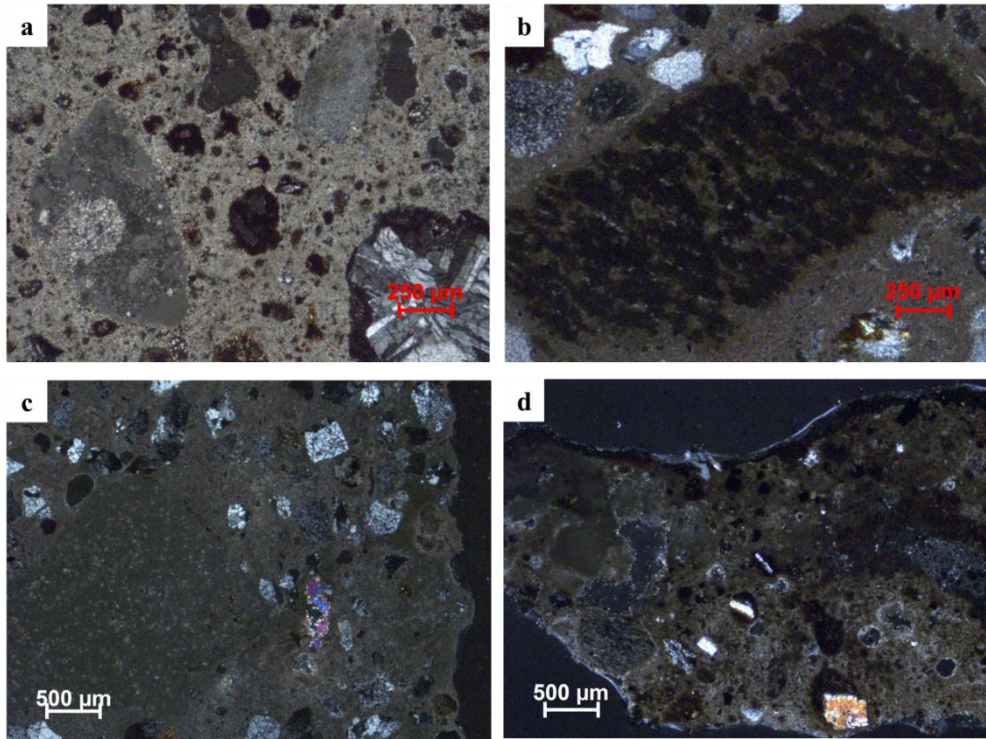


Figure 5.3 – Type of lumps: microphotographs in optical microscopy of the thin sections (xpl): in a, b) residues of original stone for lime: under-burned and over-burned lumps, respectively; in c, d) unmixed lime lumps.

### 5.1.3 Scanning Electron Microscopy with Energy-Dispersive X-ray Spectroscopy

SEM-EDS (Scanning Electron Microscopy with Energy-Dispersive X-ray Spectroscopy) combines microscopy and X-ray spectroscopy to obtain detailed information on the structure and elemental composition of mortar constituents. Observations under the optical microscope can be further enhanced and supplemented by SEM-EDS analysis (Figure 5.4).

Semi-quantitative elemental mapping provides point-by-point chemical composition of the examined area of the thin section. Point analysis is useful for performing:

- residues of stones used for lime production: to estimate the provenance of raw material;

- binder: to understand the composition of the binder and assess the presence of silico-aluminates phases;
- reaction rims: to evaluate changes in elements within these areas;
- lumps: to understand their composition, especially if they have a heterogeneous texture;
- aggregate: to obtain micro-chemical information and suppose their provenance. For instance, SEM-EDS microanalysis of volcanic rocks helps identify the textural composition through the Total Alkali-Silica Diagram (TAS).

In the case of a non-aerial mortar, point analyses conducted on the binder allow for the calculation of the HI value (explained in paragraph 2.2.2).

SEM provides high-resolution images, particularly beneficial for visualizing the structure of the binder or lump. Composition maps are also advantageous for understanding the distribution of Ca and Mg elements in magnesium aerial lime binder and in heterogeneous lumps (Figure 5.4).

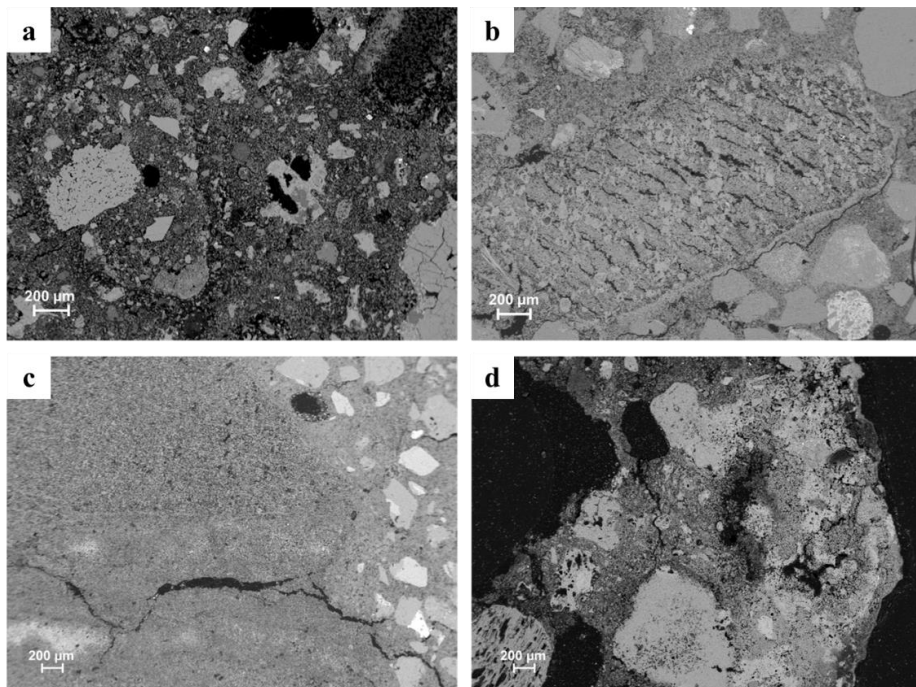


*Figure 5.4 – Type of lumps: backscattered electron images through SEM-EDS analysis of Figure 5.3 areas: in a, b) residues of original limestone: under-burned and over-burned lumps, respectively; in c, d) unmixed lime lumps*

### 5.1.4 X-ray powder diffraction

X-ray powder diffraction (XRPD) conducted on powdered samples allows qualitative or semi-quantitative analysis of polycrystalline components. The result of the XRPD bulk sample analysis includes the composition of the binder and aggregate, which can be compared with the identified phases in thin sections. We can also analyse lumps and binder-enriched mortar to determine the type of binder. This analysis yields crucial information, revealing whether the mortar is non-carbonated (containing portlandite), if the sample contains magnesium lime (brucite, hydromagnesite, magnesite), if the binder exhibits hydraulic properties (tobermorite, hydrogarnet), or if secondary reactions are occurring leading to the formation of new phases (gypsum, hydrotalcite, hydrocalumite). The inclusion of these latter phases in mortar binders has recently been shown to potentially affect the radiocarbon dating of lime mortars because of their high  $(\text{CO}_3)^{2-}$  anion capture capability, as evidenced by their characteristics (Miyata, 1983; Ponce-Antón et al., 2018).

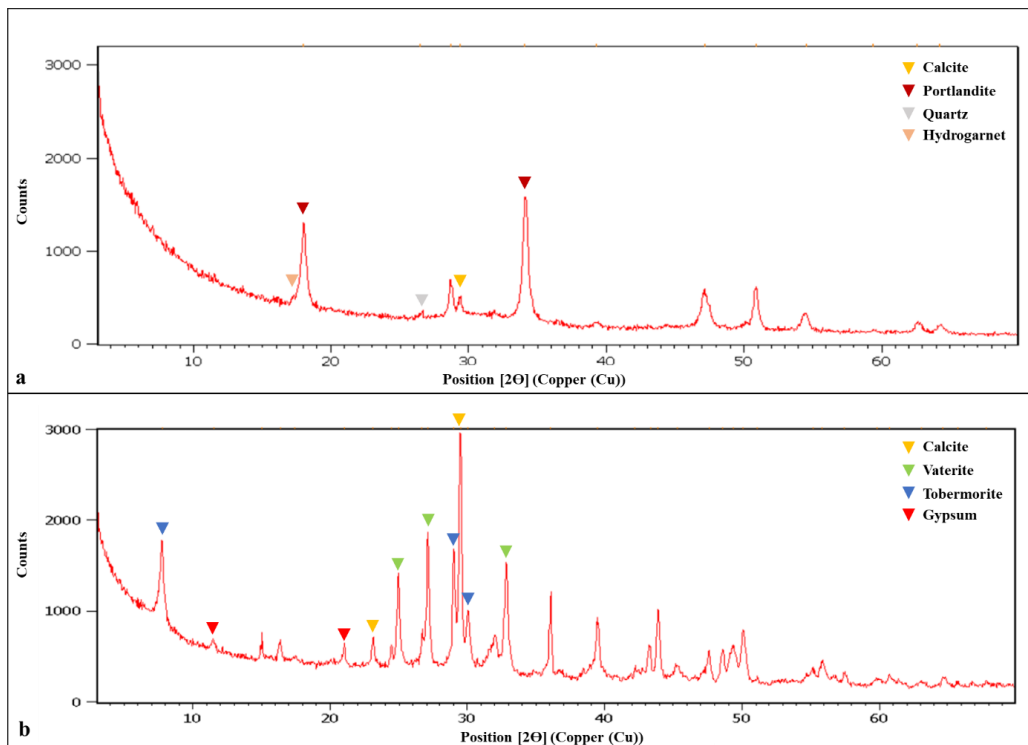




*Figure 5.5 – XRPD patterns of lump samples: in a) lime lump with incomplete carbonation: the main peaks of calcite, portlandite, quartz, hydrogarnet are indicated; in b) hydraulic mortar lump: the most intense peaks for calcite, vaterite, tobermorite and gypsum are indicated (modified by Calandra et al., 2022a).*

### 5.1.5 Thermogravimetric analysis

Thermogravimetric Analysis (TGA) is a technique used in the analysis of historical mortars for various purposes. TGA involves subjecting a sample to controlled temperature changes while measuring its weight change as a function of temperature or time. In the context of historical mortars, TGA serves for characterization of binder materials (aerial binder, hydraulic binder, gypsum, etc.). Different materials decompose or react at distinct temperature ranges, and TGA can reveal the onset, progression, and completion of these processes. A portion of each sample is disaggregated using a porcelain pestle, and a specimen enriched in binder is selected, i.e., the portion that passed through an ISO R 565 Series sieve with 63  $\mu\text{m}$ . The most significant parameters are the weight loss: in the 200–600  $^{\circ}\text{C}$  temperature range identifies the dehydration of the aluminosilicates determining the presence of hydraulic components; and in the 600–900  $^{\circ}\text{C}$  temperature range, a weight loss due to the decomposition of  $\text{CO}_2$  is observed (Bakolas et al., 1995; Moropoulou et al., 1995). The first data refer to hydraulic water (%) and the second the amount of  $\text{CO}_2$  in the sample comes from the calcium hydroxide carbonation process and the contribution of calcium hydrated silica-aluminates (they react slowly with  $\text{CO}_2$  forming  $\text{CaCO}_3$  and separating silica and alumina in the amorphous state). Usually, TGA results are reported in the plot of the percentage of weight loss attributed to  $\text{CO}_2$  (%  $\text{CO}_2$ ), and  $\text{CO}_2/\text{H}_2\text{O}$  ratio (Figure 5.6). Moreover, TGA results can be compared with the calculated HI from point microchemical analyses conducted using SEM-EDS (Riccardi et al., 2007). Combining the results of TGA and SEM allows for a more robust characterization of the hydraulic properties of the mortar.

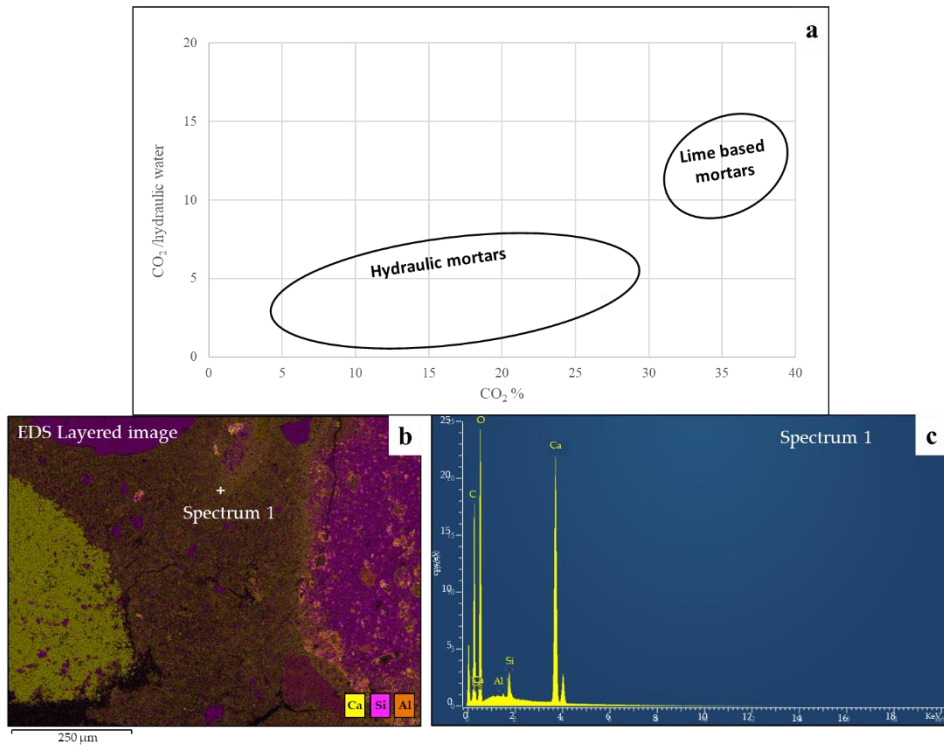


Figure 5.6 – Methods for determining hydraulic behaviour in mortar samples. In a) Plot of CO<sub>2</sub>/Hydraulic water vs CO<sub>2</sub>% to report the results of TGA of mortar samples. In b) and c) Micro-chemical analysis of the binder is conducted using SEM-EDS: a compositional layered image of the binder section (Ca: yellow; Si: pink; Al: orange) (b); EDS spectra results from point-specific analysis (c).

### 5.1.6 Fourier Transform Infrared Spectroscopy

Fourier Transform Infrared Spectroscopy (FTIR) is a technique used for chemical analysis of a bulk sample or a fraction thereof, aiming to understand the nature and structural organization of bonds and the atomic arrangement of mineralogical phases (Farmer, 1974). It requires limited material quantities and is typically employed for qualitative or semi-quantitative analyses. XRPD and FTIR analyses of mortars are complementary techniques: FTIR identifies molecular vibrations associated with various bonds and groups, such as carbonate (CO<sub>3</sub>), sulphate (SO<sub>4</sub>), and silicate (Si-O) groups, confirming components detected in XRPD; and reveals organic materials (hydroxyl (OH), and C-H, C-C, C=C, etc. bonds) and amorphous compounds.

All the information obtained from the spectra is necessary to understand the chemical constituents of the samples selected for dating. In the context of mortar dating, spectroscopy has also been used to distinguish the origins of calcite. These aspects will be further discussed in the next chapter.

### 5.1.7 Cathodoluminescence

Cathodoluminescence is a petrographic technique, an additional way to examine thin sections and other types of geologic samples (Marshall, 1991). The sample is bombarded with a high-energy electron beam and often responds by emitting light of various wavelengths. The emitted radiation is usually observed in the visible spectrum, but UV and IR emissions can also occur. This physical phenomenon is referred to as luminescence. The resulting luminescence can be categorized as intrinsic (self-activated) or impurity-activated. Intrinsic luminescence can be amplified by factors such as nonstoichiometry, structural imperfections, and impurities (non-activators) – either substitutional or interstitial – that lead to lattice distortions.

Different densities and distributions of atomic defects in the calcite crystal structure serve as markers to identify the origin of calcite. The major activators of carbonate minerals are  $\text{Mn}^{2+}$ ,  $\text{Fe}^{2+}$ ,  $\text{Co}^{2+}$  and  $\text{Ni}^{2+}$ . Calcite typically shows bright luminescence (by the combination of yellow, orange, and red colours) when it contains  $\text{Mn}^{2+}$ , while the  $\text{Fe}^{2+}$  ion can serve as a quencher. The ions must be present as substitutional or possibly interstitial impurities. The variation in CL intensity reflects the variation in Mn content. The phenomenon can be observed with petrographic microscopes equipped for CL analysis (OM-CL) because they are relatively inexpensive and easy to use. Scanning electron microscopes can also be equipped with a CL detector (SEM-CL). These instruments allow observation of minerals and sediments in thin sections (30  $\mu\text{m}$ ) or in powdered form by polarized transmitted light.

Geological calcite and anthropogenic calcite may exhibit different luminescence intensities due to distinct formation (Figure 5.7).

Typically, a qualitative analysis was performed, just attributing “hues” to the different observed binder colors (see for example tile red, dull purple, brown, dark brown, grey, dull grey and black). In such a framework, interpretation of data could be influenced by the operator him/herself (Lindroos et al., 2007; Heinemeier et al., 2010; Murakami et al., 2013).

The disadvantage of this technique lies in the resulting hues, especially when multiple emissions from the same crystal result in a composite hue. For example, blue and red emissions can be combined to produce brown or purple hues (e.g., Richter et al., 2003). This issue can be solved by analysing the CL spectra or by combining several analytical techniques to obtain a unique result.

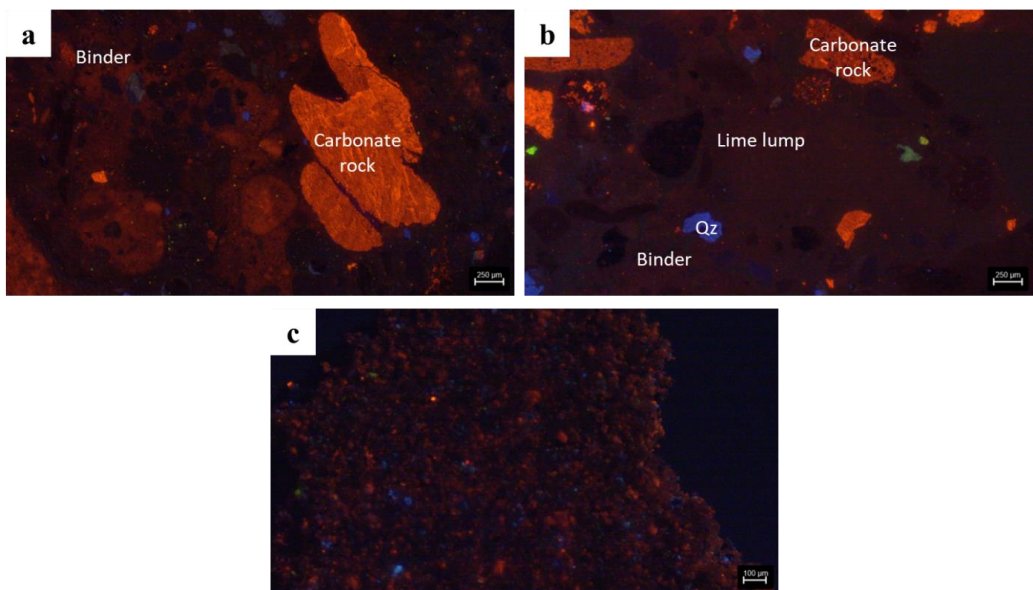


Figure 5.7 – Cathodoluminescence microscopy (OM-CL). In a, b) Microphotographs of mortar thin sections. In c) Sieved mortar sample (<63 μm grain-size fraction). Qz: quartz.

## 5.2 Application of advanced techniques to mortar characterization

The previous techniques are well established analyses conducted on mortars. Here, we present two high-resolution techniques employed, for the first time during the PhD project, to study the heterogeneity of lumps in mortar samples. The spatial distribution of lumps was investigated using the FTIR microscope equipped with a 32x32 element Focal Plane Array detector (FPA-FTIR) and the ID13 beamline at the European Synchrotron Radiation Facility (ESRF) ( $\mu$ XRPD).

Our research focuses on the analysis of the components of lumps in historical Florentine mortars made of natural hydraulic binder, in order to evaluate the carbonate phases in binder and how its presence can alter the radiocarbon concentration. After setting, in natural hydraulic binders, the phases of non-hydrated clinkers, calcite, and calcium-modified silica gel and aluminum oxide stabilize (resulting from the presence of non-hydrated clinkers, hydrated calcium silicates, and calcium aluminates, CSH and CAH) (Cizer et al., 2012). Along with calcite, aragonite and vaterite are commonly found.

The carbonation of  $\text{Ca(OH)}_2$  has as its first step the transformation into amorphous calcium carbonate (ACC), then it is transformed into aragonite (arg), vaterite (vtr) or calcite (cal) (Zhu et al., 2021). This transformation usually proceeds sequentially ACC-arg-vtr-cal without external influences. The ACC is unstable and crystallizes into  $\text{CaCO}_3$  (arg, vtr or cal), with calcite being the most stable form (Rodriguez-Navarro et al., 2015). The fundamental factors influencing the crystallization of  $\text{CaCO}_3$  polymorphs are temperature, pH, concentrations of initial chemical compounds, and the types and concentrations of impurities. There are many hypotheses about their formation. In (Black et al., 2007), it is shown that CSH and CAH phases create imperfect or very fine crystals, favouring the formation of the vaterite and aragonite. However, in other studies (Cantisani et al., 2018), both vaterite and aragonite have been shown to be precursors during the carbonation of portlandite. One possible factor conducive to the crystallization of metastable polymorphs is the mortar maturation conditions in a low  $\text{CO}_2$  environment (Frankeová et al., 2020). According to some authors, the formation of

aragonite and vaterite can be promoted by the addition of an organic compound during mortar mixing (Fiori et al., 2009; Ventola et al., 2011). The presence of  $\text{Ca}(\text{OH})_2$  maintains a  $\text{pH} > 12$  in fresh mortar, providing favourable conditions for carbonate crystallization in the form of calcite. After carbonation, a decrease in the  $\text{pH}$  of the environment is observed, optimal conditions for the formation of vaterite and aragonite (Wang et al., 2020). In Seymour et al., 2023, it is mentioned that vaterite in pozzolanic mortar is created through the modification of calcium-aluminum-silicate-hydrates (CASH). In the post-pozzolanic process, the unreacted ceramic fragments continue to dissolve over time, leading to the formation of CASH and vaterite.

In this framework, the study of the distribution of components in binder lumps and firing remnants of stone could reveal trends and clarify their formation process. Identifying the formation process of  $\text{CaCO}_3$  polymorphs can be useful to understand whether samples with aragonite and vaterite are datable or not (Toffolo et al., 2017).

In the following paragraphs, we present the initial results and potential of the two methods applied to mortar samples. There are no other studies in the literature conducted on ancient mortars using these techniques and materials.

### 5.2.1 FPA-FTIR

Spectroscopic imaging techniques implemented in the last few decades, allow to obtain spatial and spectral information, displaying the chemical distribution of components in bulk samples. This method is applied in different materials of cultural heritage (i.e. multi-layered painted artworks, wood, stone, ceramics and glasses). The advantage of FPA-FTIR is its capability to conduct comprehensive chemical imaging, generating spatially resolved data from numerous points. Mortars are heterogeneous materials; FPA-FTIR can identify the chemical distribution over areas of the samples, such as lumps. In the case of historical Florentine mortars with natural hydraulic binder, the composition of lumps is highly variable, as noted by the analysis using traditional micro-FTIR spectroscopy. The advantage of FPA-FTIR imaging is that one can assess the

distribution of the composition of certain heterogeneous areas and evaluate their potential formation.

The measurement acquisition modes with FPA-FTIR include external reflection, ATR, and transmission. The choice of acquisition mode depends on the type of sample, nature and quantity of available samples, and research questions (Liu and Kazarian, 2022). Mortar samples pose difficulties as their surface is often unsuitable for external reflection mode, even in cross-section, due to porosity and lack of polishability. Additionally, the sample contains an aggregate portion with hardness comparable to that of the instrument crystal, making ATR mode not recommended. We opted to prepare uncovered thin sections, approximately 50 microns thick, directly from the original sample and utilize the reflection mode. Prior to sectioning, a small amount of powder was collected for ATR-FTIR and XRPD analysis (Figure 5.8).

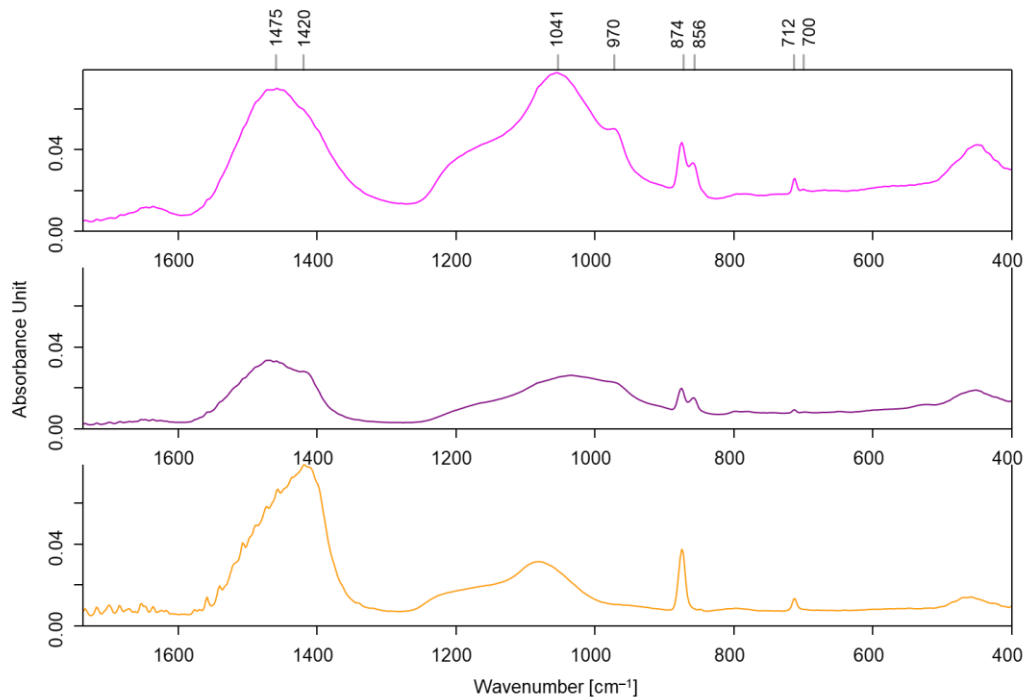


Figure 5.8 – ATR-FTIR evaluation of lumps composition. Calcite, aragonite and silicate present in pink and purple spectrum. Calcite, and silicate present in orange spectra. A guide to the peak positions is depicted in the spectrum above.

The main constituent of the lumps is calcite, but in these cases, the presence of calcite is observed simultaneously with aragonite and/or vaterite, and amorphous silicate. The crystalline phases are confirmed by XRPD analysis.

In the FTIR spectra (Figure 5.8), a strong and broad band is evident around  $1450\text{ cm}^{-1}$  with an extended shape, attributed to the overlap of the main asymmetric  $\nu_3\text{ CO}_3$  vibrations at  $1420\text{ cm}^{-1}$  for calcite, at  $1475\text{ cm}^{-1}$  for aragonite; the band at  $874\text{ cm}^{-1}$  typical of asymmetric  $\nu_2\text{ CO}_3$  vibrations in calcite and vaterite is also visible, as well as the band at  $856\text{ cm}^{-1}$  related to aragonite and vaterite. Finally, the vibration at  $712\text{ cm}^{-1}$  is present, characteristic of both calcite and aragonite, which also exhibits the adjacent peak at  $700\text{ cm}^{-1}$ . Moreover, the presence of silicates is evident from the poorly resolved peak at  $1041\text{ cm}^{-1}$ . The FTIR analysis does not detect the less intense vibrations of vaterite at  $1085\text{ cm}^{-1}$  and  $1070\text{ cm}^{-1}$ , nor the more intense ones at  $970\text{ cm}^{-1}$ . This is due to the presence of silicates from the amorphous phases of hydraulic limes, which have strong and broad peaks, concealing the characteristic peaks of vaterite.

The spatial distribution of carbonate and silicate components in the lump (Figure 5.9a) was highlighted with chemical imaging using FPA-FTIR, exploiting the most characteristic bands mentioned above:  $856\text{ cm}^{-1}$  for aragonite,  $875\text{ cm}^{-1}$  for calcite,  $1000\text{ cm}^{-1}$  for silicate (Figure 5.9b). From the maps, it is observed that the distribution of calcite (Figure 5.9c) can be distinguished from that of aragonite (Figure 5.9d) and silicates (Figure 5.9e).

A key result that emerged is that in areas where there is calcite, there is no aragonite and vice versa; only in transition zones, both compounds are observed. On the contrary, silicates are widely distributed and concentrate in areas where significant amounts of aragonite are present. The use of FPA-FTIR spectroscopy in this topic allows to achieve a high spatial resolution at the sample location. Moreover, ATR-FTIR as well as FPA-FTIR analyses do not detect the presence of organic phases.



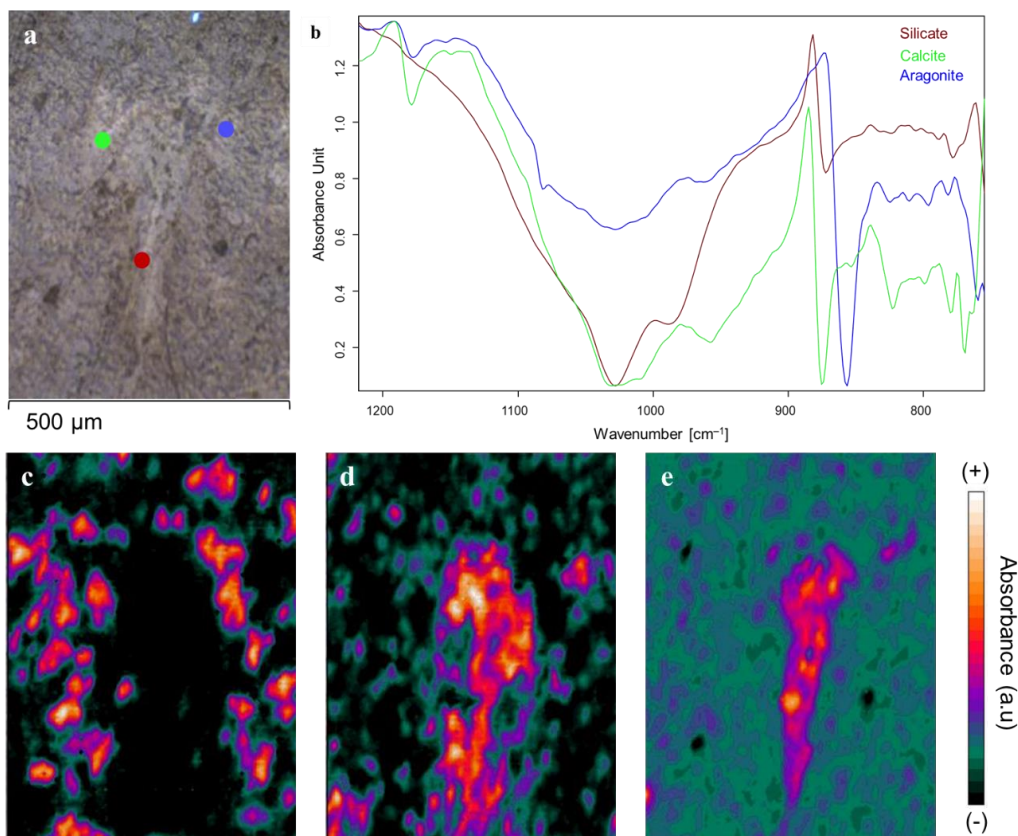


Figure 5.9 – Analysis of Lump components: in a) the investigated area using OM, with point analysis of compound; b) the absorbance spectrum of the silicate, calcite, and aragonite; and in c-e) chemical distribution maps obtained by FPA-FTIR (calcite: c; aragonite: d; silicate: e).

Analysis of lumps with FPA-FTIR shows the spatial distribution of calcite, aragonite and silicate. The results shown by the maps may suggest that silicates are the phases that stabilize aragonite and slow down the kinetics of transformation into calcite.

## 5.2.2 μXRPD

From the FPA-FTIR analysis, it was not possible to distinguish the presence and distribution of vaterite in lumps of ancient mortars with a natural hydraulic binder. The same areas of the samples analysed with FPA-FTIR were studied at the European Synchrotron Radiation Facility (ESRF) using X-ray powder diffraction (XRPD) at the ID13 beamline, enabling 2D high lateral resolution XRPD mapping of bulk analysis. ESRF

recently initiated the "historical materials BAG", a community proposal that provides 10 European institutes the opportunity for guaranteed beamtime (Cotte et al., 2022). We participated in the Experiment session HG-172 "Structural analysis of historical materials" on beamline ID13 from 21/07/2023 at 08:00 to 25/07/2023 at 08:00, doi: 10.15151/ESRF-ES-1171320945.

Below the preliminary results from the same sample discussed in the previous paragraph are reported.

The selected areas consist of small remnants of binder that were not well mixed and residues of inadequately burnt limestone. XRPD analysis of the powders taken from the samples before the preparation of the thin section revealed the presence of vaterite, calcite, aragonite and calcium silicate (Table 5.1).

*Table 5.1 XRPD results of lump extracted from sample analysed by ID13.*

<b>ID sample</b>	<b>Vtr</b>	<b>Cal</b>	<b>Arg</b>	<b>Other</b>
CF1_L1	+++	++	-	CS (++)
CF1_L2	+++	++	++	-
CF1_L3	+++	++	++	-
CF1_L4	+	++	-	-

*Vtr: vaterite; Cal: calcite; Arg: aragonite; CS: calcium silicate. +++: very abundant; ++: abundant; +: present; \*: traces; -: below detection limit.*

The study conducted using ID13 allowed for the evaluation of the distribution of CaCO<sub>3</sub> polymorphs and their formation, which is essential for understanding ancient production technologies and chemical transformations. It was performed on the same areas analysed with FPA-FTIR.

Analyses by  $\mu$ XRPD at ID13 enabled us to discriminate among chemical species based on their distinct diffraction patterns and to create precise maps of crystalline

compounds with high spatial resolution in maps from thin-section, as depicted in Figure 5.10.

The  $\mu$ XRPD maps of the obtained sample are shown in Fig. 5.10c. The main peaks of  $\text{CaCO}_3$  polymorphs were used to create the ROIs of aragonite, calcite, vaterite and calcium silicate (CS).

It is worth noting that the distribution of aragonite and calcite is similar to that found by FPA-FTIR analyses, confirming the complementarity of the two phases. Vaterite is present only to a small extent, the point where it is higher corresponds to a higher amount of calcite. From this it can be deduced that the contribution of vaterite is often associated with calcite, which is confirmed by the transformation sequence ACC-arg-vtr-cal.

The CS phase is more diffuse and traces the distribution of silicate discovered in FPA-FTIR. Its presence could be a factor in keeping the metastable phases of vaterite and aragonite stable.

$\text{CaCO}_3$  polymorphs can coexist in natural hydraulic mortar lumps. The final result of carbonation is calcite; however, aragonite and vaterite may also form and can be detected long after carbonation is complete. The reasons for finding these phases are complex. In this study, it was demonstrated that the presence of silicates can hinder the carbonation process. Calcite, aragonite and vaterite are found in certain areas. Aragonite and calcite do not occur in the same areas, while vaterite and calcite are more correlated and occur together (although vaterite in small amounts).

Another favourable factor for the crystallization of metastable polymorphs is the curing conditions of the mortar. The persistent presence of aragonite and vaterite may be related to the low  $\text{CO}_2$  content, related also to environmental parameters. It is important to evaluate the presence of these carbonates to determine the feasibility of mortar dating.

The presence of amorphous phases (amorphous silicates and calcium silicate) can be well studied with spectroscopy, while vaterite, aragonite can be studied with diffraction. The complementarity of high-resolution imaging techniques such as FPA-FTIR and

$\mu$ SRPD proved necessary to give answers to the controversial aspects of the formation of vaterite and aragonite in various old mortar samples.

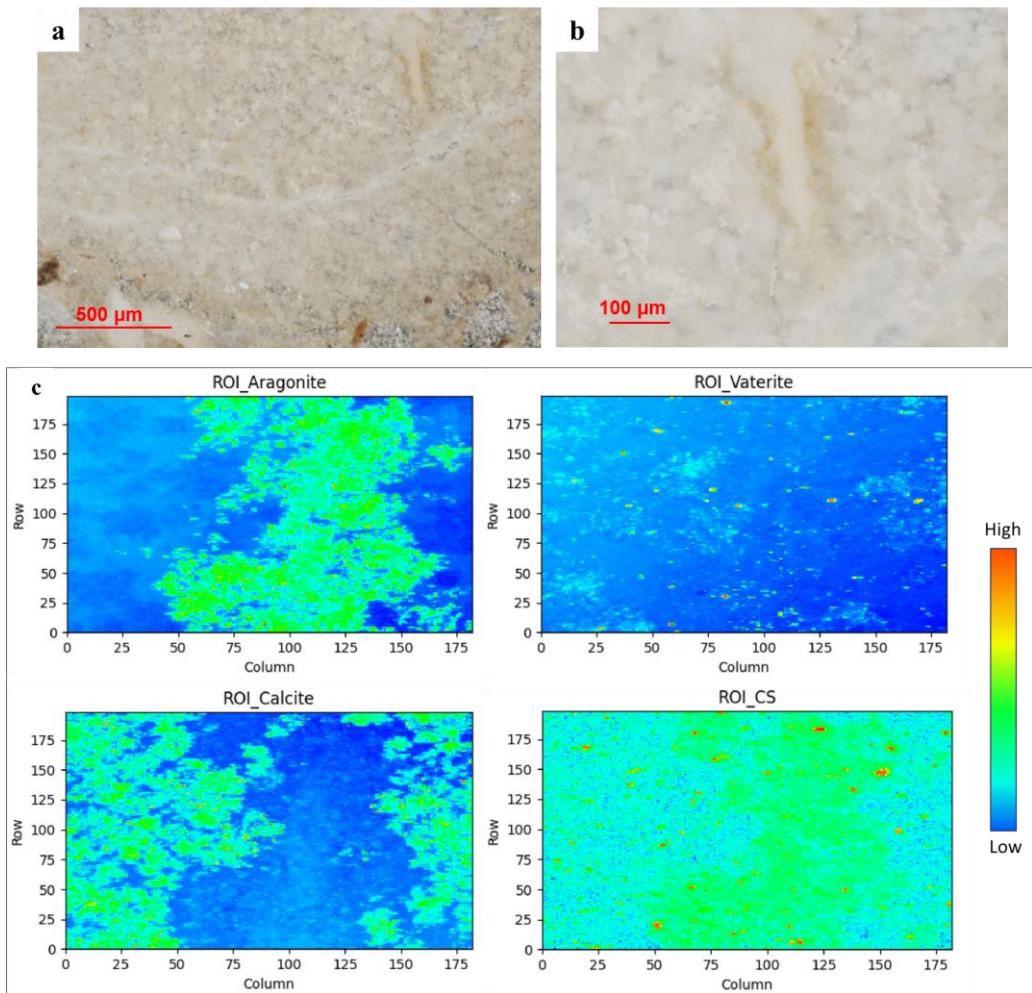


Figure 5.10 – Analysis of the lump of natural hydraulic mortar. a,b) Optical image of the area in thin section; c) The investigated ROI was about  $\sim 500 \times 500 \mu\text{m}^2$  at ID13 ( $\mu$ XRPD).  $\mu$ XRPD distribution maps of aragonite, vaterite, calcite, and calcium silicate (CS) presented in a colourmap spanning from low (blue) to high (red) values of relative intensity.

## 6 Non-destructive characterization on selected portions of sample

The analytical methods in Chapter 5 often require a certain amount of sample material and sample preparation. Often these methods are destructive and do not allow reuse of the samples. In addition, it can be noted that mortars are highly heterogeneous materials, and the characteristics obtained from petrographic, mineralogical, and chemical analyses relate to a small portion of the sample.

The calcite obtained in the carbonation process has the same chemical composition as burned carbonate rocks but different textural, mechanical properties and isotopic signatures. The sample used for dating may exhibit some variation from the observed one. These considerations could lead to the selection of samples with several impurities within the  $\text{CaCO}_3$  binder fraction. The true radiocarbon concentration can be altered by various potential sources of contamination, which can give the mortar the appearance of being either older or younger.

The distinct characteristics of carbonates (geological and anthropogenic) could be detected by the different distortions in the lattice structure within small crystallites. In principle, different kinds of calcite interact with electromagnetic radiation in ways that depend on atomic arrangement. Analytical techniques that examine both long- and short-range atomic order could be used for the monitoring of atomic order. Through Raman spectroscopy and Fourier transform infrared spectroscopy (FTIR), short-range order can be identified at the molecular level. The two techniques are effective, fast and efficient and are used for various research purposes. In this PhD project, these techniques were used to determine the origin of calcite (geologic and anthropogenic). Standard samples of geological and anthropogenic calcite were chosen to determine whether ATR-FTIR can distinguish crystals formed through different mechanisms, using processing methods previously employed with the FTIR technique with KBr pellets (Chu et al., 2008; Regev et al., 2010). Additionally, we assessed, for the first time, whether Micro-Raman spectroscopy shows reliable parameters that enable the identification of

calcite origins. In this case, statistical methods were also employed to validate the method and the influential parameters. Furthermore, cathodoluminescence (CL) analysis, widely used for assessing the origins of calcite, is often not combined with other techniques. CL has been performed to obtain cross-confirmation of the selected sample used for calcite origin studies.

The ATR-FTIR and Raman techniques offer valuable advantages such as non-destructiveness, in the perspective of sample reuse for dating. Therefore, assuming we have small quantities of sample, it is necessary to select a non-destructive spectroscopic technique.

Instrumentation and specific analysis methods (including statistical methods) are detailed in Appendix 1.

## 6.1 Selection of geogenic and anthropogenic/standard samples

### 6.1.1 Preparation of samples

The initial phase of the research involved the selection of standard samples with geological and anthropogenic origins. The chosen samples consist of calcite extracted from the aerial lime binder mortar samples (anthropogenic calcite samples) and calcite from Italian geological materials (geogenic calcite samples). We looked at 13 carbonate rocks from various Italian quarries that are traditionally burned to make quicklime; and 18 carbonate binder from historical mortars, samples made in factories, and produced in laboratory.

The historical anthropogenic samples were treated as in a selection process of true material for dating: therefore, the samples have been characterized (i.e., OM and XRPD), and then selected the suitable portions of the sample. For bulk samples, we initially gently grind using a hammer and then sieve it through a 63  $\mu\text{m}$  mesh. For lumps, under the stereomicroscope, we select the powder to be analysed and then sieve it. All other samples were grinded and sieved, as just described.

Additionally, the compositions and sieving of the samples analysed by Raman were sieved further to obtain granulometric class below 25  $\mu\text{m}$ . Indeed, for this study, it is important that samples have the same grain sizes, minimizing the variables that could result in spectral changes. Prior to the FTIR and Raman analysis, all samples were subjected to preliminary examination via XRPD and SEM-EDS.

### 6.1.2 Characterization of chosen samples

In Table 6.1 the material type, provenance and composition through XRPD and SEM-EDS of geogenic and anthropogenic samples were reported. The SEM-EDS measurements were conducted to evaluate the presence of Mg. Given that Raman spectroscopy is very sensitive to chemical and structural variations in magnesian calcites, carbonate samples containing Mg were excluded from the Raman study. Their presence would lead to wavenumber shifts compared to pure calcite.

For each ancient mortar or plaster, a preliminary mineralogical and petrographic characterization was conducted. This involved examining sample layering, describing the aggregate, lumps, potential additives, and discussing the sampling procedure for Raman and FTIR tests.

The mortar samples from Giotto's Bell Tower in Florence, Italy, consist of a natural hydraulic lime binder extracted from a locally known marly limestone called Alberese limestone (Monte Morello Formation). The aggregate, predominantly silicatic and devoid of organic materials, was collected from the bed of the Arno River (Figure 6.1a). The bulk and lump samples had been selected and designated as: G lump 1, G lump 2, G lump 3, G bulk 1, G bulk 2.

The plaster samples from archaeological sites at Ostia Antica, Italy, were part of a ceiling decoration with three layers: a painted base layer, a layer of lime mixed with travertine and calcite crystals, and a layer of lime mixed with volcanic rock fragments, pyroxene, and some carbonate rocks. Figure 6.1b shows the layer from which the powder was extracted for FTIR analysis (denoted as OS).

The plaster samples from the archaeological site of Utica in Tunisia showed a layered arrangement of lime with sub-rounded quartz grains under the painted layer. Under the stereomicroscope, the powder to be analysed was chosen and sieved (referred to as: UT09, UT10, UT11), as it exclusively consists of anthropogenic calcite (Figure 6.1c).

The analysis of Etruscan plaster from Norchia, Italy, revealed a mixture comprising red pozzolanic rock fragments, lime binder, and surface layer of pure lime (Figure 6.1d). For spectroscopic analysis, two samples were extracted from the superficial layer (referred to as: TCR01-TCR02).

The cathodoluminescence results of the selected carbonate samples confirm the origins of the calcites (Figure 6.2). In the crystal lattice of geogenic calcite, the presence of Mn<sup>2+</sup> substitution sites result in a red-orange luminescence colour (Figure 6.2a,b). Anthropogenic calcite undergoes structural modifications during the production process, resulting in fewer luminescence centres and a brown-red tile luminescence colour (Figure 6.2c,d).

*Table 6.1 Selected samples, specifying their material type and origin, detailing the sample composition, and identifying the type of calcite (geogenic or anthropogenic).*

ID Sample	Material type and provenance	Composition <sup>1</sup>	Calcite type
MAR	Marble, Carrara (Tuscany, Italy)	Cal (+++)	Geogenic
CAMP 1	Marble, Campiglia Marittima (Tuscany, Italy)	Cal (+++)	Geogenic
CAMP 2	Marble, Campiglia Marittima (Tuscany, Italy)	Cal (+++)	Geogenic
CAMP 3	Marble, Campiglia Marittima (Tuscany, Italy)	Cal (+++)	Geogenic
MS	Marble, Montagnola Senese (Tuscany, Italy)	Cal (+++)	Geogenic
LIM	Marble, Carrara (Tuscany, Italy)	Cal (+++), qz (*)	Geogenic
PLEC	Limestone, <i>Pietra di Lecce</i> (Apulia, Italy)	Cal (+++)	Geogenic
ALB L	Limestone, <i>Alberese</i> , Monte Morello (Tuscany, Italy)	Cal (+++), cl min (*), qz (*)	Geogenic
ALB A	Limestone, <i>Alberese</i> , Monte Morello (Tuscany, Italy)	Cal (+++), cl min (*), qz (*)	Geogenic
TRAV	Travertine, Rapolano (Tuscany, Italy)	Cal (+++), qz (*)	Geogenic



PGAL	Limestone, <i>Pietra Gallina</i> (Venetian region, Italy)	Cal (+++)	Geogenic
PMAT	Limestone, <i>Pietra di Matera</i> (Basilicata, Italy)	Cal (+++)	Geogenic
PVIC	Limestone, <i>Pietra di Vicenza</i> (Venetian Region, Italy)	Cal (+++)	Geogenic
G L1-3	Lime lump, Giotto's Bell Tower	Cal (+++), qz (*)	Anthropogenic
G B1, 2	Lime binder, Giotto's Bell Tower	Cal (+++), qz (*); Mg	Anthropogenic
OS	Ancient plaster, Ostia archaeological site	Cal (+++)	Anthropogenic
TCR 01, 02	Ancient plaster, Norchia archaeological site	Cal (+++)	Anthropogenic
UT 09-11	Ancient plaster, Utica archaeological site	Cal (+++); Mg	Anthropogenic
LS01-4	Laboratory mortar	Cal (+++), qz (+), portl	Anthropogenic
Biolime	Factory-made binder	Cal (+++), arag (*), qz (*); Mg	Anthropogenic
WHL	Factory-made binder	Cal (+++), cl min (*), qz (*)	Anthropogenic
HHL	Factory-made binder	Cal (+++), qz (*); Mg	Anthropogenic

Cal: calcite; qz: quartz; cl min: clay minerals; portl: portlandite; Mg: magnesium; arag: aragonite. +++: very abundant; ++: abundant; +: present; \*: traces; -: below detection limit. <sup>1</sup> via XRPD, SEM-EDS and OM, OM-CL. Mg: revealed by SEM-EDS.

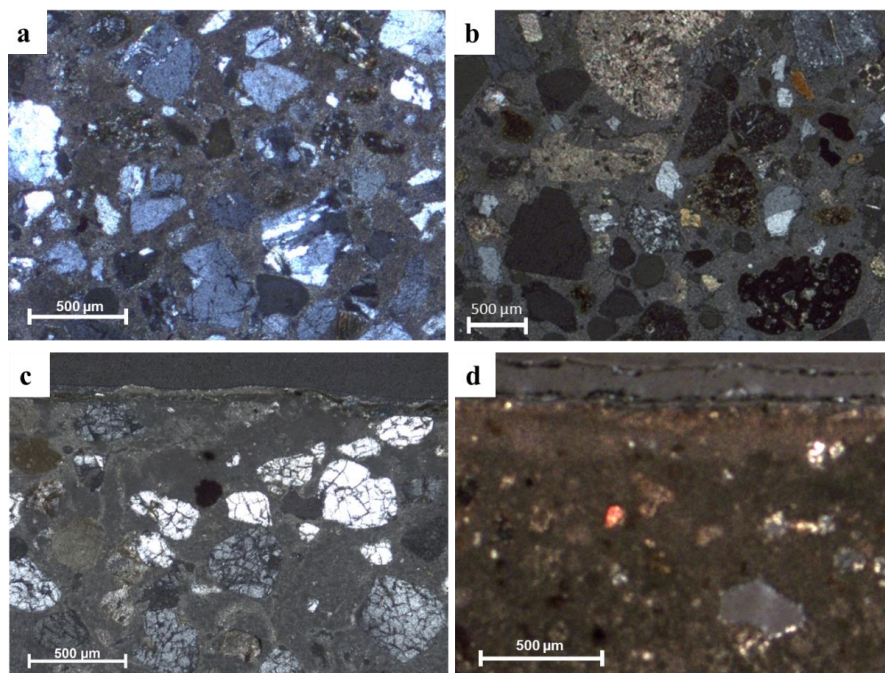


Figure 6.1 – Photomicrograph of thin sections from historical/archaeological anthropogenic samples (crossed polarizers) for ATR FTIR analysis: a) mortar from Giotto's Bell Tower; b) plaster from Ostia Antica; c) plaster from Utica; d) plaster from Norchia.

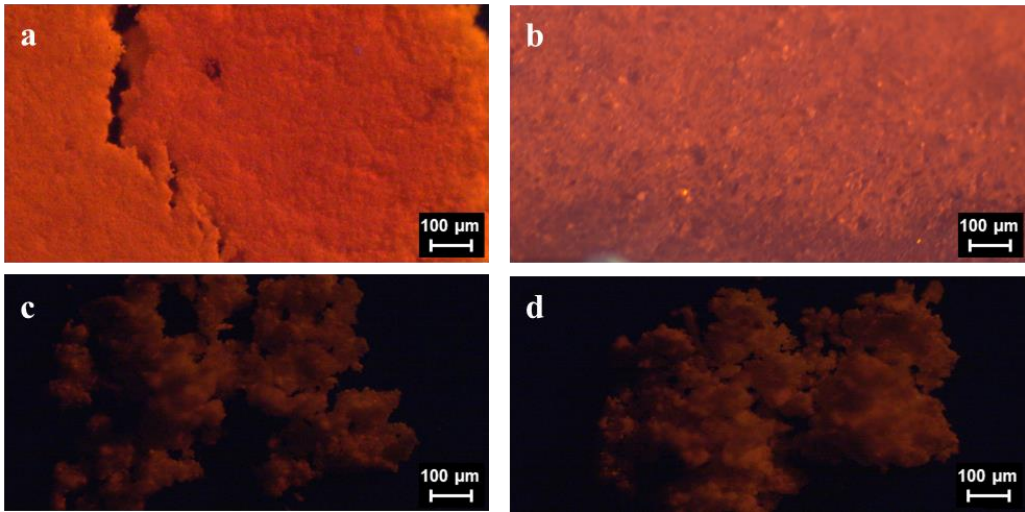


Figure 6.2 – Cathodoluminescence (CL) photomicrographs of carbonate samples: geogenic samples: MAR (a); TRAV (b); anthropogenic samples: OS sample (c), LS01 (d).

## 6.2 Study for the identification of calcites using ATR-FTIR

### 6.2.1 Previous FTIR spectroscopy studies on calcite mortar

As demonstrated in previous studies (Chu et al., 2008; Regev et al., 2010; Toffolo et al., 2020) traditional Fourier transform infrared spectrometry (FTIR) in transmission mode with KBr pellets can be employed for rapid sample analysis in radiocarbon dating of mortars. Chu et al., 2008 used the  $\nu_2/\nu_4$  ratio of calcite, corresponding respectively to the out-of-plane bending ( $874\text{ cm}^{-1}$ ) and to the in-plane bending ( $713\text{ cm}^{-1}$ ) vibrations of the carbonate ions. The ratio results allow to differentiate anthropogenic calcite (where the crystal structure is extremely disordered) from geogenic calcite (which has an ordered structure). The  $\nu_2$  peak remains essentially constant, whereas the  $\nu_4$  peak shape varies, according to the extent of atomic disorder in the calcite crystal.

Regev et al., 2010 observed that the height of the  $\nu_2$  and  $\nu_4$  bands, normalized to the intensity of the  $\nu_3$  band, decreases after repeated grinding of the same KBr pellet. By plotting these ratios, trendlines (or "grinding curves") specific to different types of  $\text{CaCO}_3$  can be drawn. FTIR can distinguish between calcite produced by different

processes using trend lines of anthropogenic and geogenic calcite generated from the intensity of bands. New grinding curves were performed from pyrogenic and biogenic aragonite samples (Toffolo et al., 2019).

Since it has been shown that differences in grinding amount affect peak widths and relative heights of carbonate archaeological materials (Chu et al., 2008; Surovell and Stiner, 2001), we proceeded to analyse samples with same procedures: grinding/selection, sieving (63  $\mu\text{m}$ ), reproducible measurements, and data processing. In order to replicate the typical pre-treatment that might be carried out on unknown samples for dating purposes.

Many papers are present in the literature discussing the use of FTIR with the KBr pellet method, to distinguish the origin of calcite. In this research, the use of ATR-FTIR is evaluated, to understand whether the ATR-FTIR mode could lead to the same results as the FTIR technique with KBr pellet.

### 6.2.2 Infrared measurements

Regarding the FTIR samples, both the KBr pellet method in transmission mode (referred to as KBr) and a diamond ATR system (referred to as ATR) were employed to analyse and detect the calcite origins. For data processing, Spectragryph version 1.2.15 and OPUS 7.2 program were utilized to correct and elaborate the ATR spectra.

A typical FTIR spectrum of calcite is shown in Figure 6.3. The heights of the  $\nu_2$  peak and the  $\nu_4$  peak are used to calculate the values of  $\nu_2$  and  $\nu_4$ , respectively. According to Chu et al., (2008) and Regev et al., (2010), the baselines were established between the closest minima on either side of the recorded peak. These spectra show the same sample that was examined using KBr pellets (spectra a) and an ATR-FTIR mode (spectra b). A few milligrams of each sample were homogenized and ground into powder in an agate mortar and pestle. ATR analysis required about 1 mg, and another 1 mg was combined with 80 mg of KBr and formed into a pellet using a press.

Three pellet samples and three powder samples were used for each sample's analysis in constant aliquots. The reproducibility of the  $\nu_2$  and  $\nu_4$  values was determined by analysing each sample 3 times. According to Regev et al., (2010), the  $\nu_2$  and  $\nu_4$  heights were standardized to a  $\nu_3$  height of 1000, which corresponds to 1.0 absorbance unit. Then, in order to process the data as suggested by Chu et al., (2008), the ratios  $\nu_2/\nu_4$  were determined.

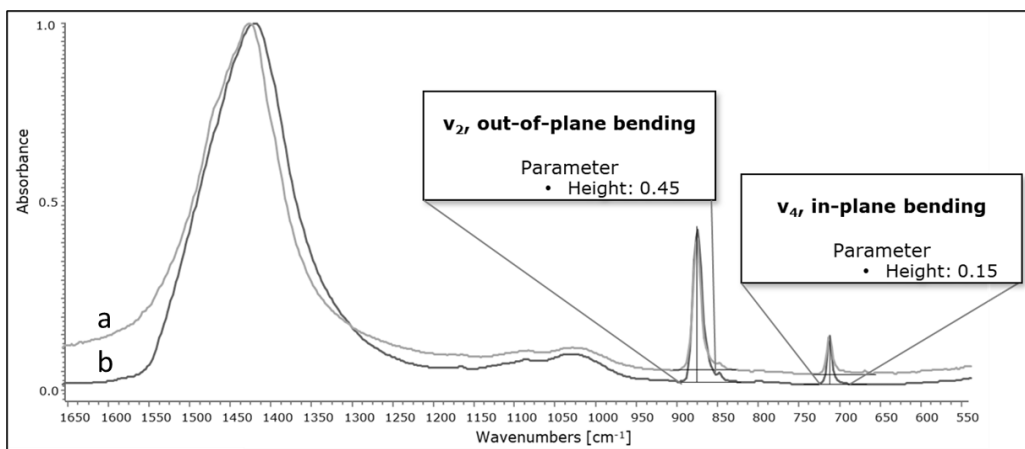


Figure 6.3 – A typical FTIR spectrum of calcite and data collected. Detail of infrared spectra of ALB A: in a) FTIR spectrum in transmission mode, on KBr pellet; and in b) ATR-FTIR spectrum.

A further study was carried out, taking into account the contributions in the literature on the preparation of grinding curves. The used procedure for creating the curve and sample preparation is described in Poduska et al., (2011). Each sample is ground several times, each KBr pellet is analysed and narrower IR peaks with higher intensities and smaller FWHM values are obtained during grinding.

Grinding curve is an analytical method to separate the effects of particle size from other IR spectral features that allow discrimination of the degree of crystalline ordering of the samples.

We applied this procedure to carbonate rocks (MAR, ALB A, TRAV), and for available reason for anthropogenic calcite factory-made binder (WHL).

### 6.2.3 Results and discussion

An FTIR spectrum of calcite typically exhibits characteristic absorption bands in the infrared region (Figure 6.3). Characteristic vibrations for calcite typically include: a strong band at approximately  $1420\text{ cm}^{-1}$  attributed to the symmetric stretching vibration of carbonate ions; sharp peaks at  $875\text{ cm}^{-1}$  ( $\nu_2$ ) and  $712\text{ cm}^{-1}$  ( $\nu_4$ ), attributed to symmetric stretching. The heights of the  $\nu_2$  and  $\nu_4$  peaks are collected to proceed with data processing as conducted by Chu et al., (2008) and Regev et al., (2010).

The standard samples reported in Table 6.1 were analysed.

Table 6.2 displays the average  $\nu_2/\nu_4$  ratio in both ATR and KBr modes for each sample. As documented in the literature, geogenic calcite from limestone samples typically exhibits  $\nu_2/\nu_4$  ratios around 3, falling within the range of 2.14 to 3.42 in KBr mode and 2.79 to 3.63 in ATR mode. Laboratory-produced lime-based plasters (LS01-04) displayed  $\nu_2/\nu_4$  ratios ranging from 5.52 to 8.47 (KBr). The  $\nu_2/\nu_4$  ratios for the standard mortar samples (Bio-lime, WHL, and HHL) ranged from 5.29 to 6.91 in KBr mode and 5.43 to 6.78 in ATR mode. The  $\nu_2/\nu_4$  ratios for the mortars/plasters from the case studies typically fell within the range of 5 to 7. Indeed, the mortar samples were analysed using both methods, with the exception of the samples from Giotto's Bell Tower, revealing  $\nu_2/\nu_4$  ratios ranging from 4.96 to 6.36 (KBr) and from 5.62 to 7.09 (ATR).

Geogenic and anthropogenic calcite obtained using transmission mode (Figure 6.4a) and ATR mode (Figure 6.4b) are plotted in Figure 6.4, showcasing  $\nu_2$  versus  $\nu_4$  peak height trend lines. The distinct trend lines in Figure 6.4 highlight the systematic differences in  $\nu_2$  versus  $\nu_4$  peak heights for calcites formed through various processes. The steeper orange slope corresponds to lime plaster samples, while the shallower blue slope represents samples composed of geogenic calcite, which is known for its high atomic order over macroscopic length scales. The results obtained with our ATR method allow us to obtain distinct patterns, while the transmission mode leads to an excessive dispersion of the data. So, the distribution and size of sample particles in the KBr matrix influences the intensity of IR absorbance peaks, which may involve in a scatter of the samples in Transmission mode. This variability is not present in ATR mode.

This master plot can help determine the origins of unknown samples, offering preliminary insights into their formation. The ability to discern calcite origins through the ATR technique is particularly advantageous in the field of mortar dating, as powdered samples can be collected and reused for dating if they contain anthropogenic calcite.

To differentiate between calcites produced through different processes, ATR-FTIR spectroscopy proves to be an efficient, rapid, and effective tool. The trend ranges were created by using different samples of known composition and origin. This allowed the identification of a representative average trend for geological and anthropogenic samples. The diversity of samples used helps to widen interval associated with the trend line compared to a single sample type approach.

The results of these preliminary findings were presented at the Metroarcho 2021 conference and published in IOP Publishing: Calandra, S., Cantisani, E., Salvadori, B., Barone, S., Liccioli, L., Fedi, M., & Garzonio, C. A. (2022, April). Evaluation of ATR-FTIR spectroscopy for distinguishing anthropogenic and geogenic calcite. In Journal of Physics: Conference Series (Vol. 2204, No. 1, p. 012048). IOP Publishing.

*Table 6.2 Geogenic samples examined in transmission (KBr) and ATR modes were compared to anthropogenic samples in terms of their average  $\nu_2/\nu_4$  ratio.*

Geogenic sample	$\nu_2/\nu_4$ ratio		Anthropogenic sample	$\nu_2/\nu_4$ ratio	
	KBr	ATR		KBr	ATR
MAR	2.14	2.79	LS01	8.04	-
CAMP 1	2.41	2.78	LS02	7.25	-
CAMP 2	2.49	2.97	LS03	8.47	-
CAMP 3	2.40	2.82	LS04	5.52	-
MS	2.21	3.12	Biolime	5.29	5.43
LIM	3.42	3.63	WHL	6.91	6.78
ALB L	2.92	3.55	HHL	6.14	6.42

ALB A	2.75	3.13	G L1	-	6.28
PVIC	3.13	3.43	G L3	-	7.09
PLEC	2.81	3.31	G L3	-	5.99
TRAV	2.43	2.96	G B1	-	6.38
			G B2	-	5.88
			OS	6.36	6.89
			TCR 01	4.96	7.09
			TCR 02	5.93	6.40
			UT 09	4.98	5.62
			UT 10	6.03	5.62
			UT 11	5.06	5.77

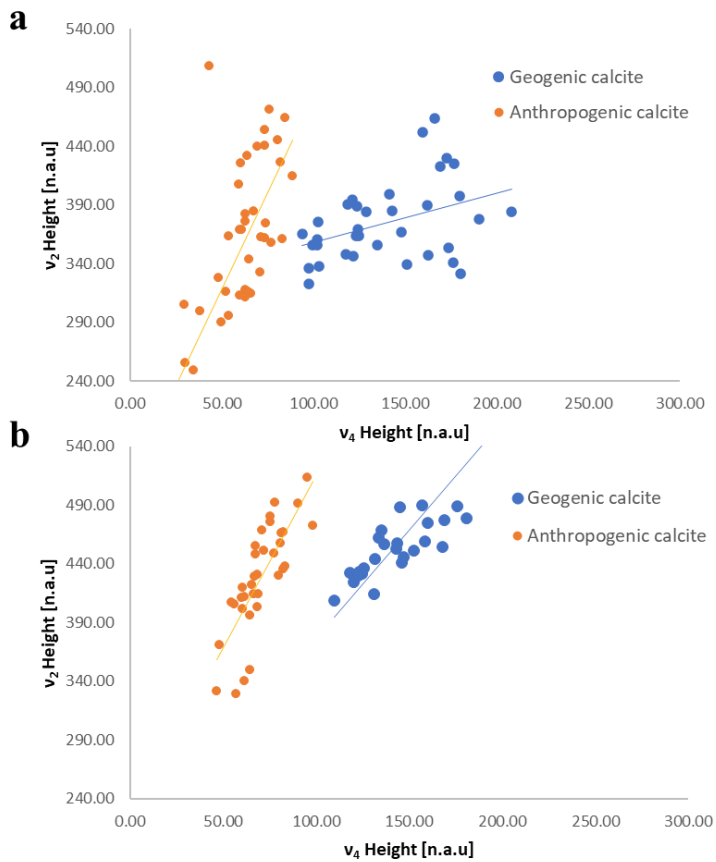


*Figure 6.4 – Graph showing  $v_2$  vs.  $v_4$  peak heights of standard samples normalized to the corresponding  $v_3$  peak height. The blue trend represents the geogenic samples, while the orange trend corresponds to the anthropogenic samples. Plots of  $v_2$  and  $v_4$  are shown in transmission mode using KBr pellets (a) and in ATR mode using the spectrum corrected for ATR (b).*

The origin of calcite was evaluated using the grinding curve method. Grinding curve was carried out on some geogenic samples (MAR, ALB A, TRAV) and one anthropogenic sample (WHL) (Figure 6.5).

The grinding curve method allows us to identify the effects of structural disorder and to explain the significant scattering of the KBr sample data in Figures 6.4a. Each geogenic calcite sample has a characteristic curve, from marble (more crystalline, formed by metamorphic processes) to Alberese limestone (less crystalline, formed by sedimentary processes). In addition, the distinction of the geogenic curves from the anthropogenic curve produced by grinding the factory-made binder sample is observed.

The grinding curve approach is very effective because it does not require a direct measurement of particle size and because our samples can be used in the analysis strategy. However, our goal is to construct a non-destructive procedure for characterising calcite origins. The grinding curve method is not particularly useful because the powder cannot be used for further analysis and dating. In addition, during the grinding procedure, possible contaminants are dispersed in the powder, making it even more difficult to remove geological C.



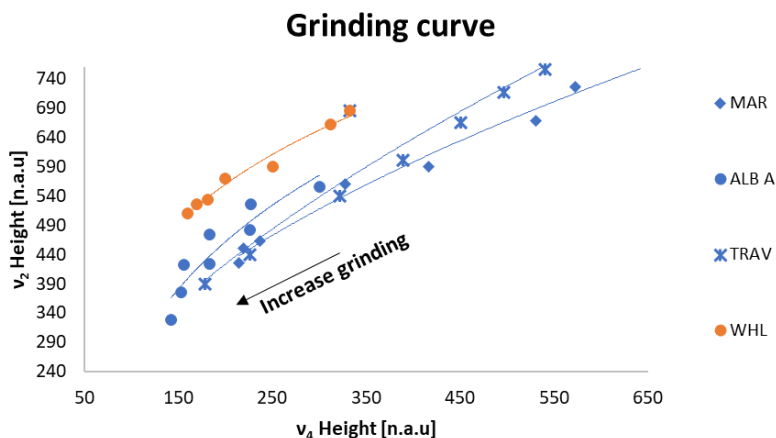


Figure 6.5 – Grinding curves of geogenic calcite (in blue, MAR, TRAV and ALB A) and anthropogenic (in orange, WHL) (n.a.u.: normalized absorbance units). Depending on the calcite, each curve indicates a distinct level of local structural order and particle size. Changes in particle size dictate the shape of each curve, while the degree of local structural order determines the offset.

## 6.3 Study for the identification of calcites using micro-Raman

### 6.3.1 Previous Raman spectroscopy studies on calcite mortar

So far, there are studies that have successfully employed Raman spectroscopy to estimate the content of cations ( $Mg^{2+}$ ,  $Fe^{2+}$ , and  $Mn^{2+}$ ) in carbonates, as the vibrational frequencies of the translational (T) and librational (L) modes of carbonates are significantly related to their cation composition (Bischoff et al., 1985; Borromeo, et al., 2017). Raman spectroscopy has been used to investigate variations in atomic bonds in biogenic calcite crystals and to distinguish the degree of crystallinity of calcium carbonate in biological materials by assessing the frequencies and width of the  $\nu_1$  and  $\nu_4$  bands (Zolotoyabko, et al., 2010). It has never been applied in studies of the origins of calcite. In the Raman analysis of  $CaCO_3$  polymorphs in Wehrmeister et al., (2011), it was noted that the amorphous calcium carbonate displays a broad peak within the lattice modes region (below  $400\text{ cm}^{-1}$ ). Additionally, the most prominent band associated with the carbonate ion at approximately  $1085\text{ cm}^{-1}$  appeared as a broader and notably less intense peak that shifted slightly towards lower wavenumbers.

We evaluate, for the first time, the potential to distinguish between geogenic and anthropogenic calcite using high-resolution micro-Raman spectroscopy.

### 6.3.2 Raman measurements and statistical analysis

#### Raman measurements

For Raman spectroscopy, the investigations were integrated with a machine learning workflow, which is an efficient way to get reliable and representative Raman datasets from which sample origins may be correctly inferred. A typical Raman spectrum of calcite, normalized to the  $\nu_1$  height, was shown in Figure 6.6. We collected 10 Raman spectra for each powder at slightly different positions in the sample area. Spectragryph v 1.2.15 software was used to process the wavenumbers, intensities, and areas of the characteristic vibrations of carbonate groups in calcite ( $L$ , librational mode;  $\nu_4$ , in-plane bending mode; and  $\nu_1$ , symmetric stretching mode). In the preliminary study, the position of the  $L$ ,  $\nu_4$ , and  $\nu_1$  bands and full width at half-maximums (FWHMs) were recorded in order to explore the outcomes of Raman techniques.

For a more in-depth study, the  $L$ ,  $\nu_4$ , and  $\nu_1$  bands of each Raman spectrum were gathered (Figure 6.6): (i) the position of the band, to evaluate the wavenumber shift; (ii) the intensity of band, following the method of Chu et al., (2008), where the intensity value was subtracted from the specific baseline; and (iii) the area subtended by the band without the baseline (Calandra et al., 2023). Several variables were extracted from the spectra. These parameters were then used in a statistical analysis to identify influential parameters for distinguishing geogenic from anthropogenic calcite.

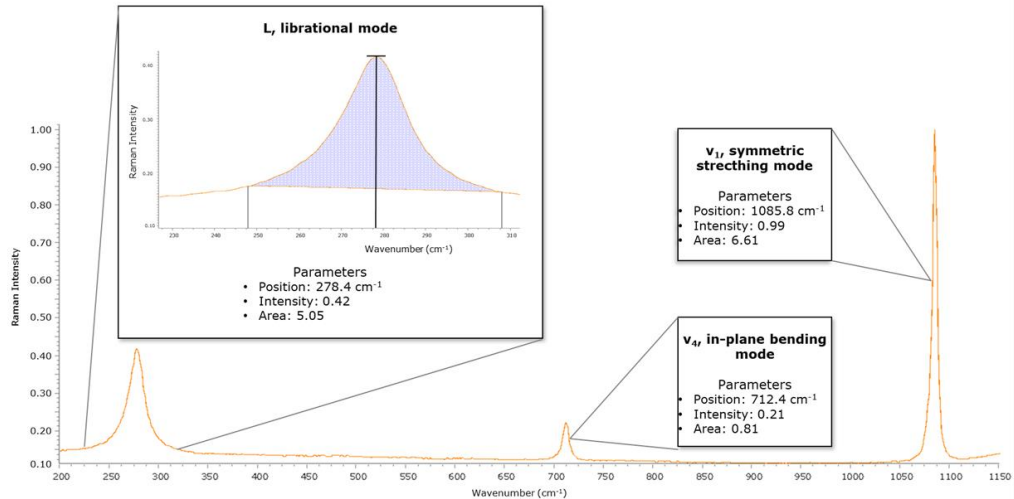


Figure 6.6 - A typical Raman spectrum of calcite and data collected. A selected region and studied bands ( $L$ ,  $v_4$ , and  $v_1$ ) of micro-Raman spectra of the carbonate samples.

### Statistical analysis

The principal steps of the proposed method for data exploration and analysis are as follows: (i) visual inspection of the dataset (using key influence factor (KIF) visual (Sufi 2022); pairplot of the variables and Bubble charts); (ii) segmentation and dimensionality reduction of the dataset (using principal component analysis (PCA) and K-means clustering (Zhu et al., 2019); and (iii) constructing machine learning models that can forecast the value of the target variable (types of calcite) based on the values of the independent variables (using random forest models and logistic regression (Fan et al., 2019; Amjad et al., 2019)).

The statistical analysis was performed using a combination of the data visualization and analysis tool Microsoft Power BI and the Python programming language with the package Scikit-learn (Hao and Ho 2019; Palma-Ruiz et al., 2022).

### 6.3.3 Results and discussion

#### Preliminary investigation

An intense band at  $1086\text{ cm}^{-1}$  ( $\nu_1$ ) and two secondary bands, a weak band at  $712\text{ cm}^{-1}$  ( $\nu_4$ ) and a medium intensity band at  $282\text{ cm}^{-1}$  (L), are the main features of the Raman calcite spectrum (Figure 6.6).

The standard samples reported in Table 6.1 were analysed, except for Mg content samples and samples with low mass.

However, anthropogenic calcite samples exhibit Raman shifts at the L and  $\nu_1$  bands, which diverge from these wavenumbers, characteristic of geogenic calcite samples (Figure 6.7). Table 6.3 reports the wavenumber of the three main bands of the carbonate samples analysed for this study. Geogenic samples exhibit bands within the reported literature range:  $280.9\text{--}282.4\text{ cm}^{-1}$  on average for L,  $712.4\text{--}713.0\text{ cm}^{-1}$  for  $\nu_4$ , and finally  $1086.2\text{--}1086.9\text{ cm}^{-1}$  for  $\nu_1$  bands. On the other hand, anthropogenic samples display an average L that falls between  $276.4$  and  $277.6\text{ cm}^{-1}$ , a relatively constant  $\nu_4$  ranging between  $712.2$  and  $712.3\text{ cm}^{-1}$ , and lastly a  $\nu_1$  that varies between  $1085.6$  and  $1085.8\text{ cm}^{-1}$ . A notable discrepancy is evident in the Figure 6.7a, when comparing the results of the marble (blue spectrum) with the anthropogenic samples, particularly for the L and  $\nu_1$  wavenumbers.

Further insight into the FWHMs (Full Width at Half Maximum) of the L,  $\nu_4$ , and  $\nu_1$  bands was pursued for deeper knowledge, with the mean values displayed in Table 6.3. Well-crystallized carbonate rocks exhibit average FWHM values of  $11.8\text{--}17.4\text{ cm}^{-1}$  for the L band,  $5.1\text{--}6.8\text{ cm}^{-1}$  for the  $\nu_4$  band, and  $4.3\text{--}5.1\text{ cm}^{-1}$  for the  $\nu_1$  band. Conversely, the bands of lime binders with a more disordered structure are characterized by FWHMs of the L band ranging from  $21.9$  to  $25.3\text{ cm}^{-1}$ , and FWHMs of  $\nu_4$  and  $\nu_1$  ranging from  $7.5$  to  $8.8\text{ cm}^{-1}$  and  $5.2$  to  $6.7\text{ cm}^{-1}$ , respectively. It is evident that FWHM values are higher in anthropogenic calcite, indicating a key parameter for distinguishing carbonate species.

The preliminary data acquired, including Raman shifts and FWHM values, indicate a discrepancy between the two calcite groups, prompting us to conduct further investigation.

*Table 6.3 The initial stage of data collection involved recording the wavenumbers and FWHM (Full Width at Half Maximum) values of the carbonate group in geogenic and anthropogenic calcite. The average values of 10 Raman measurements were documented for each sample.*

<b>ID sample</b>	<b>L wavenumber</b>	<b>L FWHM</b>	<b>V<sub>4</sub> wavenumber</b>	<b>V<sub>4</sub> FWHM</b>	<b>V<sub>1</sub> wavenumber</b>	<b>V<sub>1</sub> FWHM</b>
MAR	282.4	12.8	712.9	5.6	1086.8	4.7
CAMP 1	281.9	11.8	712.5	5.3	1086.4	4.5
CAMP 2	280.9	13.4	712.5	5.6	1086.5	4.9
CAMP 3	281.5	11.9	712.4	5.2	1086.4	4.5
MS	282.1	12.6	712.6	5.4	1086.6	4.6
LIM	280.4	15.9	712.7	6.8	1086.4	5.1
PLEC	281.9	16.8	713.0	5.1	1086.9	4.3
ALB L	281.4	13.2	712.8	5.1	1086.7	4.4
ALB A	281.1	17.4	712.5	5.8	1086.5	4.8
TRAV	281.9	13.7	712.8	5.9	1086.7	4.5
PGAL	282.0	13.1	712.7	5.3	1086.7	4.5
PMAT	282.0	13.3	712.5	5.6	1086.6	4.4
PVIC	281.4	12.9	712.4	5.4	1086.2	4.5
OS	276.4	25.3	712.2	8.7	1085.6	6.7
LS01	277.6	22.2	712.3	8.8	1085.8	5.2
WHL	276.4	21.9	712.3	7.5	1085.6	6.3

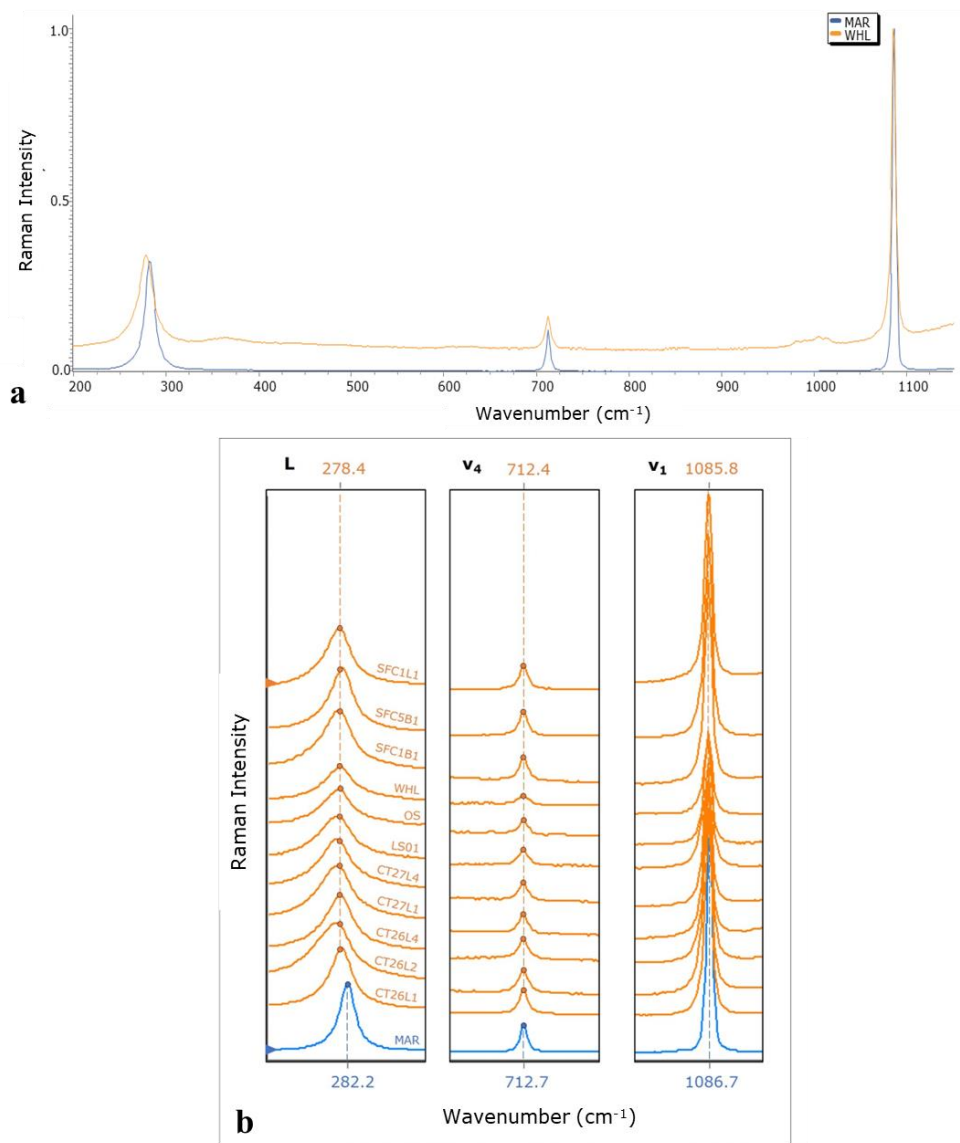


Figure 6.7 – Raman spectral observations of carbonate samples, normalized to the  $\nu_1$  intensity: geogenic calcite (in blue, MAR sample) and anthropogenic calcite (in orange, WHL sample) (a). Details of Raman spectra for the anthropogenic samples (WHL, OS, LS01 in orange) are presented alongside the geogenic sample (b). Bottom, characteristic values of the band position for the MAR sample (blue), and top, characteristic values of the WHL sample (first orange band).

### Comprehensive study

The initial promising observations prompted the implementation of further analysis to gather more confirmation. This was achieved by integrating considerations with

statistical analysis conducted using the Microsoft Power BI data visualization and analysis tool, along with the Python programming language with the package Scikit-learn (Hao and Ho, 2019; Palma-Ruiz et al., 2021). Additionally, other characteristic parameters of the spectra were selected to assess whether they could be useful for our purpose. Apart from the wavenumber and FWHM, parameters like intensity and area of the three main vibrational modes (L,  $\nu_4$ ,  $\nu_1$  bands) were chosen. The average values of these parameters collected for this second phase of the study are reported in Table 6.4.

For this step, a larger number of samples were needed, so we included: CT26L1, CT26L2, CT26L4, CT27L1, CT27L4, SFC1B1, SFC1L1, SFC5B1, belonging to Florentine Historical Buildings (the results are reported in Chapter 8). Their compositions were studied using XRPD, SEM-EDS, and analysed with ATR-FTIR to assess the origins of the calcite (shown in Figure 6.8). Samples CT26L2, CT26L4, SFC1B1, SFC1L1, SFC5B1 consist mainly of calcite with traces of quartz, while in CT26L1, quartz is more present. On the other hand, samples CT27L1 and CT27L4 are exclusively composed of calcite. Mg is below the detection limit of SEM-EDS in all the samples.

As observed from the parameter values reported in the Table 6.3, the additional samples also exhibit systematic wavenumber shifts in the L and  $\nu_1$  bands.

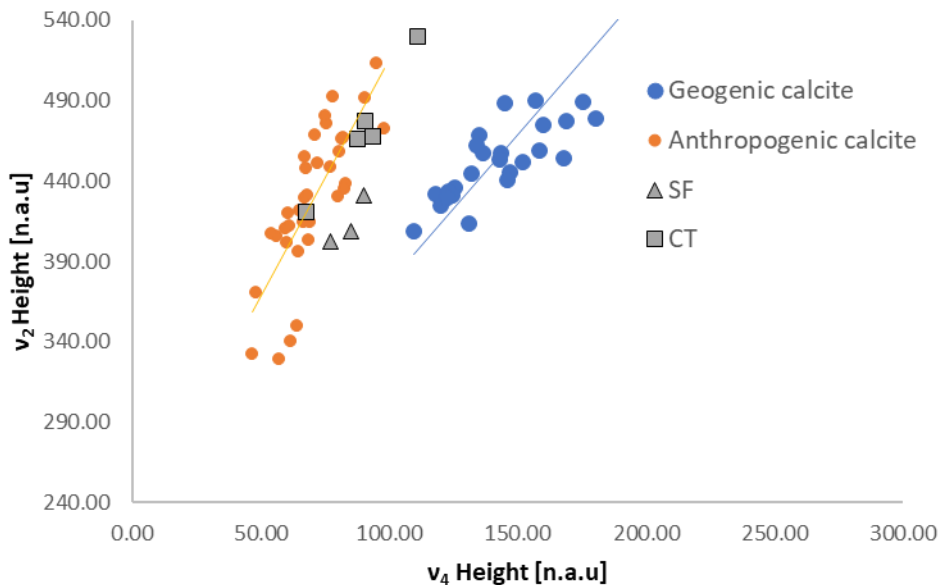


Figure 6.8 – ATR-FTIR analyses of anthropogenic samples added in-depth study of Raman analyses. Plot of the  $v_2$  vs.  $v_4$  peak heights of anthropogenic samples, starting from a database produced by a previous study. CT and SF samples are historical mortar binder.

Table 6.4 The wavenumbers, intensities, and areas of L,  $v_1$ , and  $v_4$  bands. The collected variables were reported on average.

ID sample	L			$v_4$			$v_1$		
	Wave number	Intensity	Area	Wave number	Intensity	Area	Wave number	Intensity	Area
MAR	282.4	0.29	4.07	712.9	0.10	0.68	1086.8	0.94	4.81
CAMP 1	281.9	0.29	4.38	712.5	0.09	0.54	1086.4	0.86	4.24
CAMP 2	280.9	0.27	4.44	712.5	0.10	0.62	1086.5	0.91	5.01
CAMP 3	281.5	0.23	3.48	712.4	0.08	0.49	1086.4	0.75	3.73
MS	282.1	0.28	4.26	712.6	0.11	0.67	1086.6	0.61	4.88
LIM	280.4	0.28	5.56	712.7	0.11	0.84	1086.4	0.96	6.71
PLEC	281.9	0.06	1.51	713.0	0.01	0.08	1086.9	0.14	0.68
ALB L	281.4	0.05	1.53	712.8	0.01	0.09	1086.7	0.11	0.57
ALB A	281.1	0.06	1.72	712.5	0.01	0.08	1086.5	0.19	0.78
TRAV	281.9	0.19	3.20	712.8	0.07	0.43	1086.7	0.60	3.44



PGAL	282.0	0.09	1.73	712.7	0.02	0.14	1086.7	0.24	1.24
PMAT	282.0	0.09	1.80	712.5	0.03	0.18	1086.6	0.28	1.47
PVIC	281.4	0.13	2.28	712.4	0.05	0.27	1086.2	0.41	2.08
OS	276.4	0.08	2.41	712.2	0.02	0.19	1085.6	0.20	1.59
LS01	277.6	0.09	2.11	712.3	0.03	0.30	1085.8	0.36	2.37
WHL	276.4	0.18	5.14	712.3	0.06	0.52	1085.6	0.66	5.15
CT26L1	275.0	0.14	4.02	712.1	0.05	0.42	1085.4	0.46	3.36
CT26L2	277.4	0.21	5.34	712.4	0.08	0.58	1085.8	0.68	4.14
CT26L4	277.2	0.21	5.08	712.4	0.08	0.55	1085.8	0.77	5.04
CT27L4	273.8	0.20	6.46	712.2	0.07	0.62	1085.4	0.62	5.11
CT27L1	277.8	0.25	5.99	712.5	0.09	0.70	1086.0	0.87	5.76
SFC1B1	277.5	0.18	4.67	712.5	0.06	0.53	1085.9	0.62	4.89
SFC1L1	277.7	0.23	5.65	712.4	0.08	0.66	1085.8	0.77	5.92
SFC5B1	278.3	0.24	5.42	712.5	0.09	0.69	1085.9	0.78	5.73

---

The first step in the data analysis workflow involves the utilization of key influence factors (KIF) (Sufi et al., 2022), bubble charts, and pairplot visuals to visually assess the dataset. To determine which among the numerous collected parameters allows for the distinction between geogenic and anthropogenic calcite, the KIF is employed, identifying the L wavenumber and  $\nu_1$  wavenumber as the most significant influencers (Figure 6.9). The scatterplot in Figure 6.9 demonstrates that geogenic calcite exhibit L wavenumber values consistently above approximately  $280.0 \text{ cm}^{-1}$ , along with  $\nu_1$  wavenumber values greater than  $1086.2 \text{ cm}^{-1}$ .

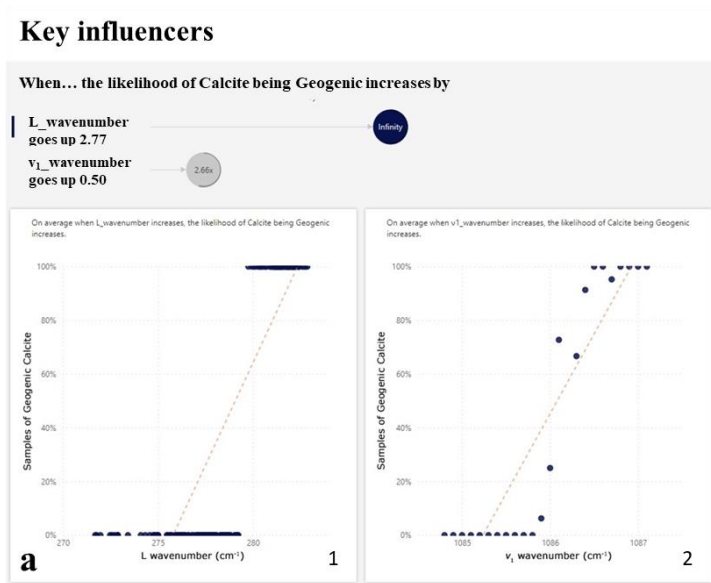
The parameters added for the more in-depth analysis of the bands do not appear to be particularly influential; only the  $\nu_4$  intensity seems to have some impact on the internal distinction of geological calcites (differentiation between geological formations, a consideration that requires further investigation elsewhere). A pairplot is constructed

to illustrate pairwise relationships between the variables and conclude the visual inspection process in the dataframe (Figure 6.9). Since several variables have a strong correlation with one or more other variables, Figure 6.9 demonstrates the original dataframe's high level of multicollinearity. The L and  $v_1$  wavenumbers, when associated with all other characteristics, enable us to discriminate between the various calcites more clearly, which is consistent with the results of the KIF analysis (Figure 10a). The  $v_4$  wavenumber is subject to the same analysis, however a precise discriminating factor cannot be considered.



Figure 6.9 – Pairplot of the variables of the whole dataset. The pairplot is in matrix format where the row name represents the x axis, and the column name represents the y axis; the main-diagonal subplots are the univariate distributions for each attribute.

From the preliminary data analysis, the L,  $\nu_1$ , and  $\nu_4$  wavenumber correlations are assessed. To find a correlation or comparable pattern between at least three variables, bubble charts are employed. The L and  $\nu_4$  wavenumbers are plotted on the x and y axes, respectively, and  $\nu_1$  wavenumber value reported in bubble diameter in the bubble chart visualization in Power BI (Figure 6.10b). These variables appear to be the most significant variables for distinguishing between geogenic and anthropogenic calcite. A different distribution of the samples can be identified, as presented in the KIF analysis. Geogenic samples cluster in an area with wavenumbers above  $280.0 \text{ cm}^{-1}$  (L) and  $1086.2 \text{ cm}^{-1}$  ( $\nu_1$ ), while anthropogenic samples are characterized by values below  $280.0 \text{ cm}^{-1}$  (L) and  $1086.2 \text{ cm}^{-1}$  ( $\nu_1$ ). The  $\nu_4$ /L plot (Figure 6.10b) also clearly distinguishes the two groupings, indicating that even a shift in one of the bands would satisfy to allow the distinction of calcite origins.



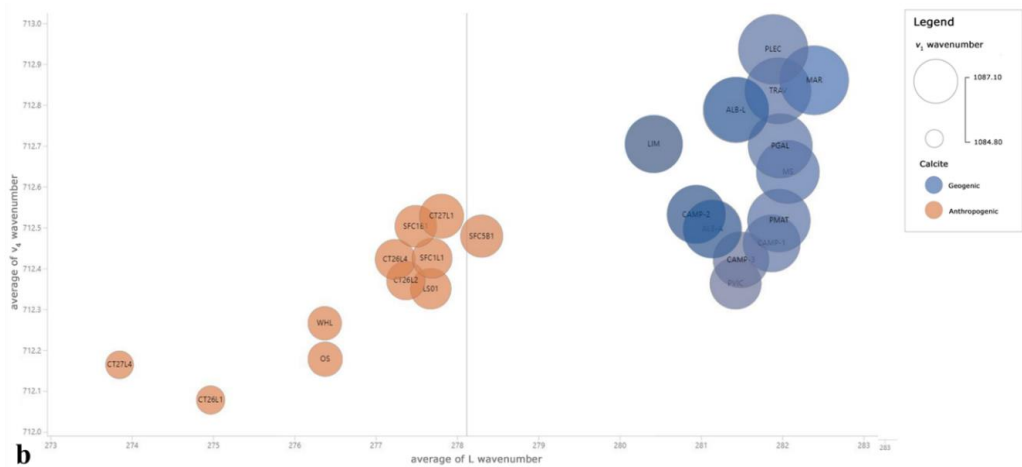


Figure 6.10 – Visual inspection of the dataset. In a) KIF results: 1) all the geogenic calcite samples exhibit an L wavenumber value over about 280.0  $\text{cm}^{-1}$ ; while in 2) shows that 85% of samples with a  $v_1$  wavenumber value higher than 1086.2  $\text{cm}^{-1}$  consist of geogenic calcites. In b) bubble chart.

To eliminate multicollinearity, reduce the dimensionality of the dataframe, and enhance the performance of the machine-learning algorithm, PCA is applied in the second phase of data analysis (Zhu et al., 2019). PC1 and PC2 explain 90.2% of the total variance (56.7% and 33.5% respectively). Consequently, a secondary PCA is conducted using only the first two principal components. A heatmap of the modified dataset reveals that there are no significant associations between variables.

The biplot of the two principal components is then visualized using Power BI after implementing the Python code (Figure 6.11a). The PCA biplot showcases both the loadings of the variables (vectors) and the PC scores of the samples (dots). Apart from a few samples, the PC1 vs. PC2 scores distinctly separate geogenic from anthropogenic calcites (Figure 6.11a). The most influential factors for distinguishing calcite types are the L,  $v_1$ , and  $v_4$  wavenumbers.

When two vectors are close to each other and form a small angle, the variables they represent (such as L wavenumber,  $v_1$  wavenumber, and  $v_4$  wavenumber) are positively correlated; conversely, if they are nearly perpendicular, they are unlikely to be correlated. This is another observation regarding loadings. K-means clustering is

conducted using the Power BI visual with the PCA-transformed dataframe (Figure 6.11b). Based on the new data representation created by PCA, K-means is applied to identify groups of related features. Utilizing unsupervised machine learning algorithms like PCA and K-means clustering enables us to reduce and categorize the data.

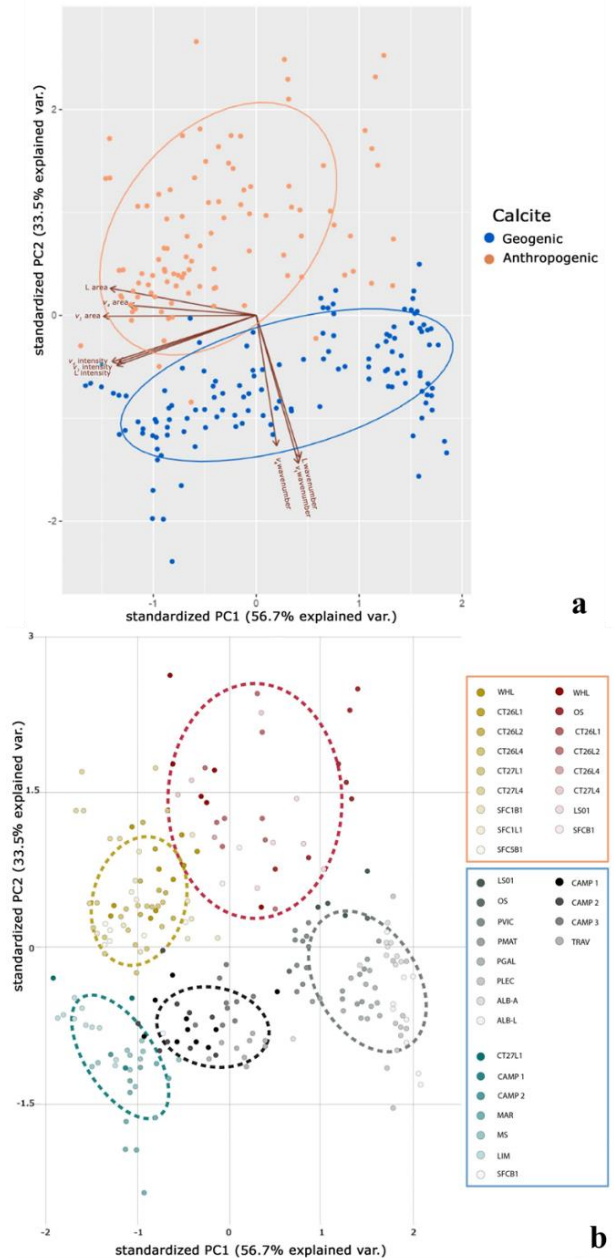


Figure 6.11 – Segmentation and dimensionality reduction of the dataset: PCA (a); K-means clustering (b).

A comparison of supervised machine learning techniques was conducted in the third step of data analysis, involving the development of a model to elucidate the relationship between the target variable (calcite types) and the newly generated variables through PCA. For further investigation of prediction accuracy, the classification methods of random forest and logistic regression were employed (Amjad et al., 2018; Zhu et al., 2019; Fan et al., 2019). When there are multiple hypotheses about the link between parameters and the target class, comparing various classification or regression models is important.

The test set comprises 67 instances, and the logistic regression algorithm accurately predicts 64 of them with a 96% accuracy rate, while the random forest approach correctly predicts 62 of them with a 93% accuracy rate (Table 6.5). The two models exhibit comparable accuracies, as indicated in Table 6.5. However, logistic regression demonstrates higher precision, recall, and F1-score values, suggesting it as the more effective model for depicting the association between the target variable and the predictor variables, and for predicting binary outcomes. On the other hand, the performance of the random forest model is relatively robust to parameter variations and less prone to overfitting compared to other machine learning methods like logistic regression (Couronné et al., 2018).

*Table 6.5 Performance classification results for the random forest and logistic regression models.*

<b>Validation methods</b>	<b>Calcite</b>	<b>Precision</b>	<b>Recall</b>	<b>F1-score</b>	<b>Support</b>
Logistic Regression	Anthropogenic	0.95	0.97	0.96	38
	Geogenic	0.96	0.93	0.95	29
Accuracy				0.96	67
Macro avg		0.96	0.95	0.95	67
Weighted avg		0.96	0.96	0.96	67
Random Forest	Anthropogenic	0.90	0.97	0.94	38
	Geogenic	0.96	0.86	0.91	29

Accuracy			0.93	67
Macro avg	0.93	0.92	0.92	67
Weighted avg	0.93	0.93	0.92	67

In conclusion, the variables with the most influence in distinguishing calcite domains are the L and  $\nu_1$  wavenumbers, with the  $\nu_4$  wavenumber also contributing significantly. The L band, referred to as the lattice modes, is generated by vibrations involving the entire cell; conversely, the  $\nu_1$  and  $\nu_4$  bands result from internal modes of the molecular carbonate ion. Structural disorder within calcite crystals or the presence of minor crystalline order is reflected in relatively broad FWHM values, the wider the spectral bandwidth, the lower the crystallinity within the mineral. This disorder leads, probably, to more Raman active phonon modes, expanding the array of spectral features. Consequently, the selection criteria for Raman active modes are altered (Wang et al., 1995). As a result, the bands shift depending on the slope of the phonon dispersion curves of the vibrational modes; a negative slope induces a shift towards lower wavenumbers (Wehrmeister et al., 2011; Xu et al., 2014; Perrin et al., 2016). Multiple factors can impact crystallinity, with the primary ones being an increase in crystal defects or the presence of amorphous or nanocrystalline phases in the sample. Calcite's degree of structural order can be disordered during both the calcination and carbonation processes due to various variables (e.g., kiln temperature, setting time, and ambient conditions). The findings of this study, which have also been corroborated by previous publications (Artioli et al., 2019; Alvarez et al., 2021; Seymour et al., 2023; Toffolo et al., 2023), demonstrate that the carbonation process leads to the formation of structurally disordered calcite crystals.

These results were presented at the TECHNART 2023 conference and published in Analyst journal: Calandra, S., Conti, C., Centauro, I., & Cantisani, E. (2023). Non-destructive distinction between geogenic and anthropogenic calcite by Raman spectroscopy combined with machine learning workflow. Analyst.

## 6.4 Final remarks

FTIR has been implemented in ATR-FTIR mode and allows the distinction of geogenic and anthropogenic calcite. This study has enabled the construction of a distinctive trend for amorphous calcites or those with low crystallinity (considering ancient and laboratory samples), and a characteristic trend of calcites with crystalline structure (considering various carbonate rocks). The collected data and constructed calcite trend lines are utilized to preliminarily assess the origin of calcite (applied in various contexts for dating purposes in Chapter 8 and 9).

The creation of different grinding curves of various carbonate rocks allows for specific reference trends of each geogenic calcite. Depending on the carbonate rock used for lime production (information obtained from characterization), the correct geogenic trend line can be selected.

High-resolution micro-Raman spectroscopy was employed in a non-destructive approach to differentiate between geogenic and anthropogenic calcite, using machine learning methods. The influencer parameters (including band position, band intensity, area covered by the bands, and FWHM values of  $L$ ,  $\nu_4$ , and  $\nu_1$ ) for distinguishing the origins of calcite have been successfully identified. These parameters can be utilized to ascertain the calcite origin in unknown samples intended for dating.

The two techniques result are a useful tool to choose the datable fraction from the binder or lumps in ancient mortars, avoiding contamination with geogenic calcite (due to presence of carbonate aggregates or remnants of underburned stone fragments for lime).

ATR-FTIR and micro-Raman, along with CL and XRPD, are non-destructive methods that allow the characterization and the reuse of samples for radiocarbon dating.



## 7 Mortar dating at LABEC

### 7.1 Micro-sample preparation for the measurement

The previous chapter discussed the use of non-destructive methods to preserve the sample mass so that the same sample can be subjected to multiple analytical procedures prior to dating. Sampling is necessary for mortar characterization, but the numerous steps of sample preparation for  $^{14}\text{C}$  measurement may result in a loss of mass compared to the originally collected sample.

When dealing with mortars, the superintendence or the conservation authority responsible for protecting Cultural Heritage rarely allows large-scale sampling. Sampling may compromise the aesthetic or archaeological aspects of the manufacture. Also, as explained in Section 3.3.1, we need to follow good sampling strategies, which often leads to a reduction in the number of samples that can be taken (e.g. removal of surface layers).

Given these factors, there is a strong incentive in the context of mortar dating to optimize methods to achieve results even with limited sample sizes. Similarly, this applies to all applications where a highly selective pre-treatment process results in small residual masses.

For this reason, at the LABEC laboratory in Florence, one of the laboratories of CHNet, the INFN network for Cultural Heritage, a facility, the so-called Lilliput graphitization line, has been set up created to reduce the carbon sample mass needed for the AMS measurement down for dating to 50  $\mu\text{g}$ , well below compared to the "traditional" larger samples of about 700  $\mu\text{g}$  (Fedi et al., 2007; Fedi et al., 2020). This approach allows the exploration of new applications for radiocarbon dating, such as the analysis of individual lumps of binder in mortar samples.

The first step in mortar sample preparation is represented by mechanical separation. The procedure varies depending on the sample selected. Lump and bulk samples are selected under a stereomicroscope. For bulk samples, a portion enriched with binder is

separated and slightly crushed after both the enriched binder sample is sieved to 63  $\mu\text{m}$ . The lump samples are also sieved to 63  $\mu\text{m}$ .

## 7.2 The acidification line

For the extraction of C in the form of  $\text{CO}_2$  from the selected inorganic fraction of the mortar, a new optimized line for the acid digestion of carbonate samples was developed and integrated into the graphitization line at LABEC in Florence. The carbonate sample, mechanically separated and previously characterized with non-destructive techniques, is treated in the acidification line using  $\text{H}_3\text{PO}_4$ .

The acidification line is schematized in Figure 7.1. The residual pressure conditions before starting the acidification process are approximately  $10^{-4}$  mbar. The sample is inserted in the so-called “dissolution” vial (B in Figure 7.1), a quartz tube.  $\text{H}_3\text{PO}_4$  acid is injected into the acidification line through a PTFE/silicon septum (indicated as A in Figure 7.1) using a syringe. PTFE/silicon has been chosen because it is acid-resistant, capable of withstanding temperatures ranging from  $-40$  °C to  $200$  °C and exhibits excellent resistance to multiple punctures while maintaining high vacuum levels (around  $10^{-4}$  mbar).

The reaction between the carbonate and the acid is quick and produces water, which is trapped in the trap (D in Figure 7.1). A valve (E in Figure 7.1) separates the acidification line from the rest of the graphitization line, allowing one or more  $\text{CO}_2$  fractions produced during the acidification to be selected as the reaction progresses. Thereafter, the  $\text{CO}_2$  fractions are cryogenically moved to one of the graphitization reactors, then purified, and finally converted to graphite (process explained in section 7.3).

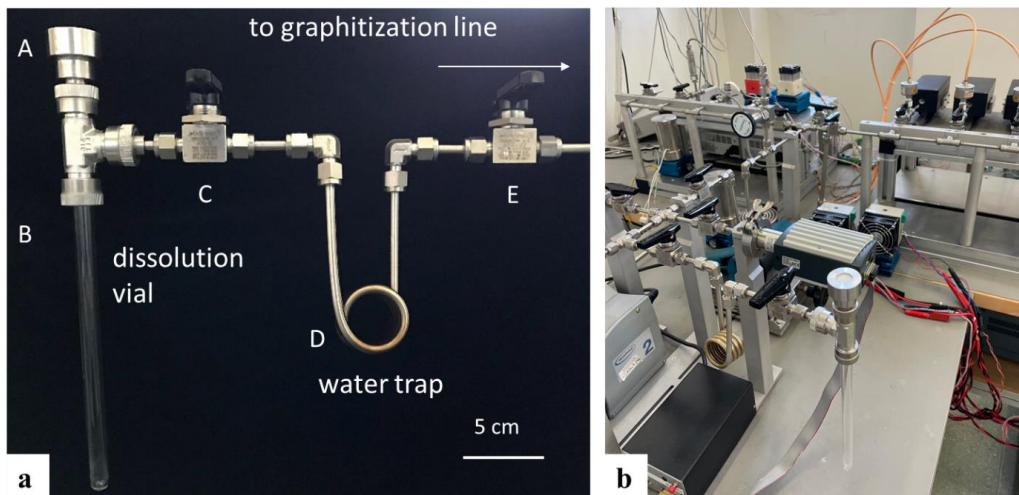


*Figure 7.1 – Extraction of CO<sub>2</sub> from the carbonate samples. In a) Schematic representation of the acidification line. In b) Image of the acidification line coupled with the graphitization line designed at LABEC laboratory (INFN, Florence).*

After integrating the new acidification line into the graphitization line, various tests were performed with mortars of known origin and composition to evaluate the reproducibility of the acidification process and to understand the correlation between CO<sub>2</sub> yield, sample mass and composition.

Typical processed masses for mortar samples are:

- approx. 2.5 mg in the case of lump
- approx. 5 mg in the case of bulk.

When bulk samples are involved, 2 evolving CO<sub>2</sub> fractions are usually collected per sample: the first collected in a few seconds (0-10/30 seconds) and the second following (10/30-60 seconds). The reduced reaction times chosen should avoid the risk of geological contamination, at least in the first fraction, since contaminants may still be present despite mechanical separation.

For lump samples, a fraction is collected from the first seconds of the reaction, without the risk of contaminants reacting with the acid.

The described set-up was used to collect CO<sub>2</sub> from mortar samples from Florentine historical buildings and the public building in Pompeii.

### 7.3 Graphitization line

In Figure 7.2 is shown the combustion/acidification and graphitization line installed at LABEC (Fedi et al., 2007). Combustion is used to extract carbon from organic samples as CO<sub>2</sub>, employing the Thermo Flash EA 1112 elemental analyser (EA). The elemental analyser basically is composed of three different blocks: a combustion column filled with reagents for sample oxidation and reduction, a gas chromatograph and a gas detector. The sample is weighed, sealed in a tin capsule, and combusted at 950°C with an excess of oxygen. While passing through the gas chromatographic column, the different gases composing the mixture evolved after combustion are separated. Their evolution with time is shown in a so-called chromatogram. The outlet of the elemental analyser is connected to the graphitization line through a three-way valve, so that only CO<sub>2</sub> is collected. The CO<sub>2</sub> extracted from the acidification line or combustion process is then transferred to the graphitization chamber. The CO<sub>2</sub> produced during the reaction is cryogenically transferred to the graphitization chamber using liquid nitrogen.

Each micro-size sample graphitization chamber consists of a small quartz tube and a silver bar (as shown in Figure 7.2). This material and its form (very thin channel and hollow inside) is used for its excellent thermal conductivity. The graphitization reaction occurs in the quartz tube, while the silver segment acts as a cold finger to prevent water from entering the reaction chamber during the graphitization process (Figure 7.2a). The internal volume of the reactor is approximately 1.5 cm<sup>3</sup>. The graphitization reaction is triggered at 600°C in the presence of Fe (pressed into copper inserts placed into the reactor) as a catalyst and an excess of H<sub>2</sub>. The quartz tube is placed in a furnace to reach the optimal reaction temperature, while the cold finger is attached to a Peltier device for collecting the reaction water (Figure 7.2b).

The collected amount of CO<sub>2</sub> is monitored through pressure measurements (in mbar). Typically, about 100 mbar of CO<sub>2</sub> is collected for each sample to obtain comparable graphite samples, which corresponds to about 50 µg of graphite at the end of the reaction. After the graphitization process, the copper inserts with graphite deposited

on are mounted into specially modified aluminium holders to fit into a multi-sample carousel, inserted into the ion source of the accelerator for measurement of the radiocarbon concentration.

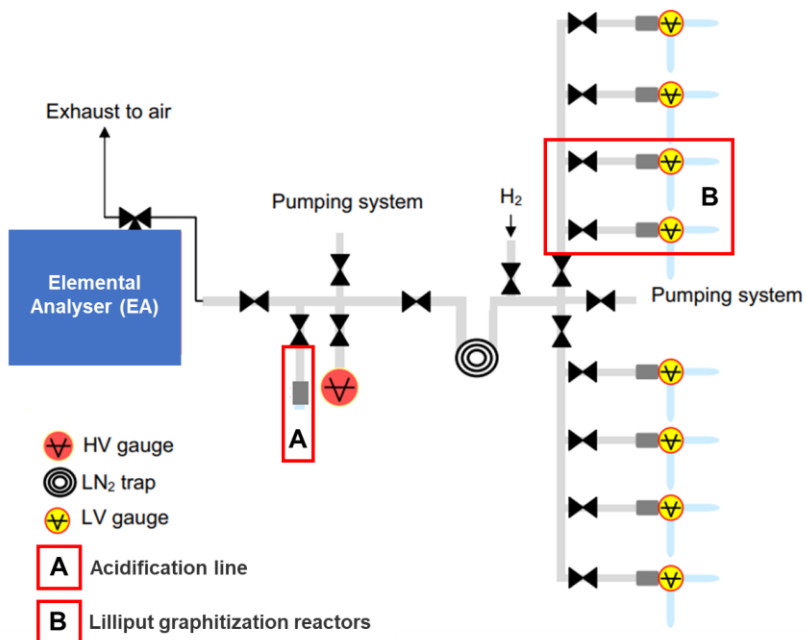


Figure 7.2 – Graphitization line set-up diagram at LABEC in Florence coupled with combustion and acidification lines. Modified by (Fedi et al., 2007).

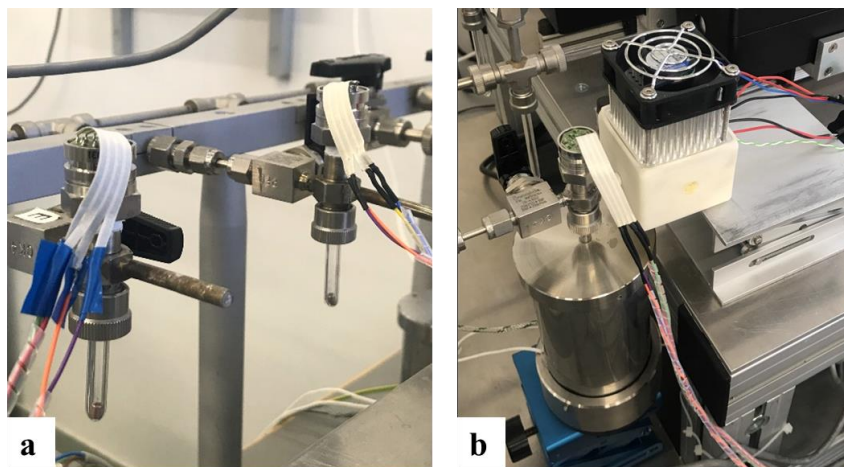


Figure 7.3 – Lilliput graphitization reactors: in a) graphitization chamber consisting of a quartz tube with a copper support and a silver cold finger; in b) operating conditions for graphitization.

## 7.4 Accelerator Mass Spectrometry

Accelerator Mass Spectrometry (AMS) is an experimental technique that allows for the measurement of the abundance of rare isotopes by considering their mass, energy, and charge state (Kutschera, 2013). One of its most common applications is the determination of radiocarbon content. In contrast to decay-based methods, AMS employs a particle accelerator to accelerate ions to medium-high energies, achieving remarkable sensitivity (down to approximately  $10^{-15}$ ) (Tuniz, 2001). This technique enables the analysis of significantly smaller sample masses.

A simple mass spectrometer is not adequate for the determination of  $^{14}\text{C}$  concentration due to isobaric interference and its extremely low concentration. Tandem accelerators, which integrate a beam transmission system and a highly sensitive mass spectrometer, are commonly used. These instruments effectively eliminate interferences caused by molecular and elemental isobars like  $^{14}\text{N}$ ,  $^{13}\text{CH}$ , and  $^{12}\text{CH}_2$ , which have the same mass as  $^{14}\text{C}$ . Extraction of a negative ion beam suppresses  $^{14}\text{N}$  interference due to its instability as a negative ion, while stripping at the high voltage terminal suppresses molecular isobars such as  $^{13}\text{CH}$  and  $^{12}\text{CH}_2$ . The AMS system installed at INFN-LABEC in Florence is based on a Tandem electrostatic accelerator with a maximum terminal voltage of 3 MV (Fedi et al., 2007). The Tandem accelerator consists of a low energy section (from the ion source to the accelerator tube), the accelerator tube itself, and a high-energy section extending from the accelerator exit to the detector, as shown in Figure 7.4.

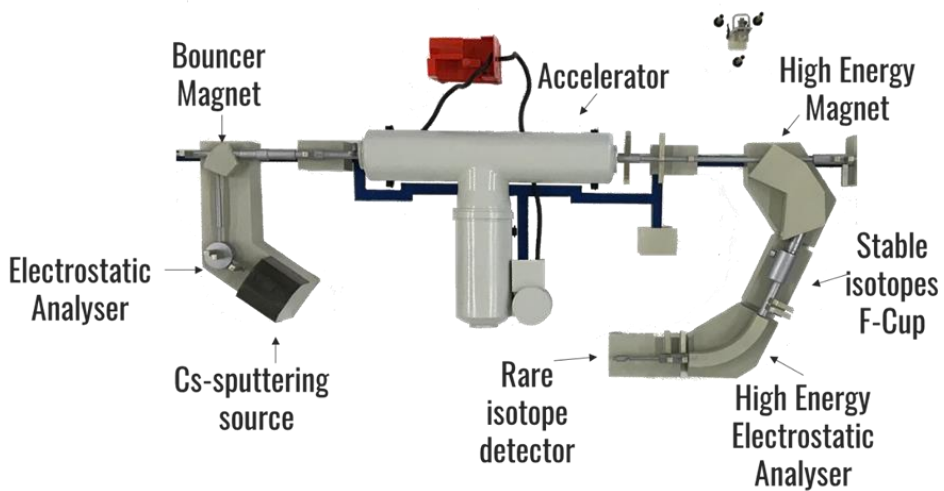


Figure 7.4 – Configuration scheme of the AMS beam line installed at the 3MV Tandem accelerator installed at INFN-LABEC laboratory (Florence).

In AMS analyses, as already mentioned, samples are inserted into the source, which is located in the low-energy section, as graphite pellets. The samples undergo bombardment with Cs<sup>+</sup> ions, resulting in the production of a beam of negative ions (Fedi, 2009).

A total voltage of 35 kV is used to extract the negative ions from the source. The <sup>12</sup>C, <sup>13</sup>C, and <sup>14</sup>C ions that are present in the sample are those that are accelerated along the tandem channel. Since <sup>14</sup>N does not produce stable negative ions, its contribution to the source is directly inhibited.

In order to analyse and isolate the desired ion, electrostatic and magnetic "filters" are employed on the beam line. The first element is an electrostatic analyser (ESA), which selects ions based on their energy-to-charge ratio ( $E/q$ ) by applying an electric field along a fixed circular trajectory with radius  $R$ . The Bouncer Magnet, which is located downstream of the ESA, uses the Lorentz force to transmit the ions according to their masses, once the  $E/q^2$  ratio is fixed. This magnet is also equipped with a system to alternatively inject mass 14, mass 13 and mass 12 at a very high repetition rate.

The beam of negative ions passes through the first section, which is characterized by a high vacuum, and is then accelerated to the high-voltage terminal, which is maintained at 2.5 MV. In the terminal, the stripping process takes place, during which the accelerated ions collide with the argon gas particles present in this section, changing their charge state. Under the typical measurement conditions at LABEC (ion type and their energy), the most probable charge state is 3+. Consequently, the final energy of the ions leaving the tube is about 10 MeV.

Another magnet on the high-energy side selects ions according to their mass. For example, when measuring radiocarbon, we select only the ions with charge state +3 and mass 14 ( $^{14}\text{C} + 3$ ). Following the magnet, the ion beam is further analysed by another ESA, which only transmits ions with an E/q ratio of 10 MeV/3e, thereby removing any additional potential interference.

Molecular isobars such as  $^{12}\text{CH}_2$  and  $^{13}\text{CH}$  are filtered during the stripping process due to the loss of C-H bonding stability.

Finally, the abundances of stable isotopes  $^{12}\text{C}$  and  $^{13}\text{C}$  are measured by two Faraday Cups that detect their respective current intensities. Lastly, the beam reaches a solid-state silicon detector, which provides a spectrum that allows for ion discrimination based on their energy and enables the counting of  $^{14}\text{C}$  ions.



## 8 <sup>14</sup>C dating of natural hydraulic mortar in Florentine building

### 8.1 Literature background of Florentine mortar

Radiocarbon dating of mortar is affected by the raw materials used for the production of mortars, especially the rock used to make lime.

Several studies (Pecchioni et al., 2005; Lezzerini et al., 2017; Aquino et al., 2019; Cantisani et al., 2021; Calandra et al., 2022a; Calandra et al., 2022b) highlight that the Alberese limestone was widely used for lime production in the Florentine area. The Alberese limestone belongs to the Monte Morello Formation (Eocene age) of the Morello Tectonic Unit within the Calvana Supergroup (Abbate and Sagri, 1970) or the Morello Tectonic Unit (Principi et al., 2008). It is characterized by a grey-brown colour on fresh surfaces, conchoidal fractures, and frequent calcite veins. This lithotype is widespread in the area of Florence: it can be found in the Monte Morello area (northwest of Florence), along the Calvana ridge (north of Prato), and on the surrounding hills of Pistoia. Small outcrops can also be identified south of Florence, near places such as Grassina and Galluzzo, and to the west, in areas such as Soffiano, Scandicci and Lastra a Signa. In Tuscany, there are also important outcrops in the Chianti Hills, in the Casentino area, in Val Tiberina, and outside Tuscany in Val Marecchia (Montefeltro-Marche) and in the Monti della Tolfa in northern Lazio (Carmignani et al., 2004). The Monte Morello Formation consists of marly limestones with minor marly-limestone intercalations. Bedding thickness varies from cm to m, often with grey or black flint. Fossil content ranges from 6% to 20%, with occasional grey biocalcarenite beds at the base and rare grey marly limestone sandstones.

The lithotypes used for lime production are compact marly limestones that are white or very light yellowish-brown and have a fairly fine grain size. The calcium carbonate content varies between 85% and 93% (Sartori, 2007). Depending on the clay mineral content in the starting limestone, different types of lime are obtained to produce bedding mortars, plaster, and finishes, defined respectively as *calcina forte* and *calcina*

*dolce*, resulting in distinct physical and mechanical properties. The presence of clay minerals in the limestone provides the obtained natural hydraulic binder with specific durability and hydraulic characteristics. The setting reaction is explained in paragraph 2.2.2, it is not entirely aerial, and this introduces challenges for dating. Another characteristic and critical aspect of this type of mortar is the presence of unburned limestone. Traditional calcination techniques and the high percentage of clay minerals in the rock present challenges during calcination.

### 8.1.1 Case studies of historical Florentine buildings

Lime mortars and plasters belonging to historical Florentine buildings have been studied to assess their feasibility to be dated using the radiocarbon method. This question is directly related to the mortar technologies, the raw materials used and the state of conservation, but is also influenced by the sampling strategies.

In the Florentine area, various buildings with different functions were selected, ranging from civil structures to places of worship, built in different historical periods. The sites investigated and the number of samples collected for a comprehensive characterization of each study site are listed in Table 8.1. Customized approaches were employed at different sites, considering the sampling possibilities granted by the authorities. Consequently, the sampling methodologies for each building are described in detail below. Architects, officials, and historical researchers have guided the sampling of mortars for in-depth studies.

In the next sections, for each historic building in Florence: 1) the collection of mortar samples, 2) the results of minero-petrographic and chemical characterization of the mortar samples (analytical methods described in Section 5.1), 3) the criteria for the selection and non-destructive characterization of lump/bulk samples (methods exposed in 6.1), 4) the procedure of acid dissolution of selected powders (procedure described in 7.2), 5) the AMS measurements are reported.

Table 8.1 List of the collected mortar samples in the different historical buildings, their localization on the monument.

Florentine historical building	Samples Number	Type of sample	Position	Sampling notes
Castle of Trebbio CT	27	Fragments of plasters and bedding mortars	External wall of tower	The top centimeters were discarded, and the underlying mortar was collected. Cores were extracted from the mortar joints.
S. Felicita Church SF	8	Fragments of bedding mortars	Internal wall of dome in Capponi Chapel	Small fragments from the joints were gathered.
Medici Riccardi Palace PMR	6	Core samples of mortar core wall (up to 2 m)	Internal wall of two different construction phases	Deep core samples were extracted using dry coring.
S. Giovanni Baptistery BG	17	Core samples of bedding mortar (up to 0.4 m)	Internal wall of Attic, matroneum and foundations	Cores were extracted from the bedding mortars.

## 8.2 Castle of Trebbio

### 8.2.1 Sampling

The samples were taken from the walls of the tower of the Castle of Trebbio, a building that represents one of the most important and significant examples of aristocratic villas owned by the Medici in the surroundings of Florence (Mugello) and currently well preserved architecturally. The construction activities of the castle are documented from the late 13th century to the first decades of the 17th century.

In 2022, an archaeological analysis of the architectural features of the complex was conducted. The analysis included the reconstruction of the transformation phases through a stratigraphic study of the individual constructive and destructive acts that characterized the structure over time (following the methods and interpretation in Brogiolo and Cagnana, 2012). The findings obtained from this analysis were then related

to the historical documentation and chrono-typological atlas of the masonry of Mugello (Arrighetti, 2016) described previously.

The findings of this investigation allowed the determination of the main construction phases of Trebbio Castle:

- Phase 1: The site initially featured a single tower, remnants of which are visible in the lower portion of the masonry of the current tower located on the southern side of the architectural complex. Consistent with the information from written sources, this phase could be attributed to a period preceding the 13th century.
- Phase 2: This phase witnessed the elevation of the pre-existing tower, constructed with a more precise masonry technique than the previous one. The towered building is crowned with merlons, as the newly walls of containment. Based on the archaeological reading, this phase can be attributed to interventions carried out in the mid-14th century.
- Phase 3: The third phase sees the elevation of the tower and a complete renovation of the upper part of the structure, featuring corbels and wider walkways, along with new roofing structures. This phase could be correlated with Michelozzo's interventions carried out between 1420 and 1428.
- Phase 4: This phase is associated with specific restorations and reconstructions conducted in the modern and contemporary eras. Interventions of mortar sealing and reconstructing almost all of the openings in the complex, addressing specific structural issues or restoring the complex to a late-medieval appearance.

The archaeological reading of the masonry and the resulting hypotheses about the construction phases formed the basis for the selection of sampling sites for the mortar samples. A total of 27 bedding mortar and plaster samples were collected using a hammer and chisel, removing the outer portion of the masonry and selecting material at a depth of approximately 5 cm (Figure 8.1). Figure 8.1b shows one of the perspective drawings of the tower, the north side where the collected samples are marked, and

Figure 8.1c shows an example of a collected mortar fragment. Table 8.2 contains the codes of the samples, their positions, the sampling points and the sampling depth.

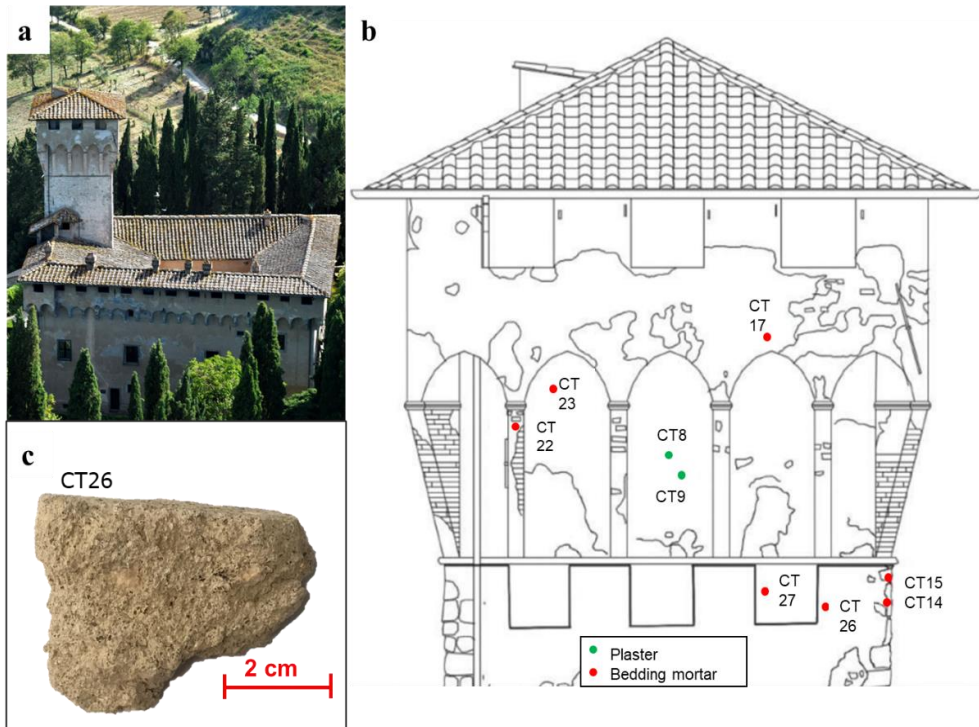


Figure 8.1 – Castle of Trebbio: building (a); sampling point on North side perspective drawing (b), and an example of a macro sample extracted (c).

Table 8.2 List of plaster and bedding mortar samples taken from the tower of Castle of Trebbio, and reconstruction phase based on archaeological analysis.

ID sample	Sampling point	Sampling depth	Construction phase
CT1	Plaster, South side	0-1 cm, surface layer	Phase 3/4
CT2	Plaster, South side	5 cm, same point as CT1	Phase 3
CT3	Plaster, South side	0-1 cm, surface layer	Phase 3/4
CT4	Plaster, East side	0-1 cm, surface layer	Phase 3/4
CT5	Plaster of the corbel, East side	0-1 cm, surface layer	Phase 3/4

CT6	Plaster of the corbel, East side	0-1 cm, surface layer	Phase 3/4
CT7	Plaster of the corbel, East side	3 cm, same point as CT5	Phase 3
CT8	Plaster, North side	0-1 cm, surface layer	Phase 3/4
CT9	North side	4 cm, same point as CT8	Phase 3
CT10	Plaster, West side	0-1 cm, surface layer	Phase 3/4
CT11	Plaster, West side	4 cm, same point as CT10	Phase 3
CT12	Bedding mortar, North-West side	4 cm	Phase 3
CT13	Bedding mortar, South side	4 cm	Phase 3
CT14	Bedding mortar, North-West side	2 cm	Phase 2
CT15	Bedding mortar, North-West side	2 cm	Phase 2
CT16	Bedding mortar of the corbel, East side	4 cm	Phase 3
CT17	Bedding mortar, North side	0-1 cm, surface layer	Phase 3
CT18	Bedding mortar, West side	4 cm	Phase 3
CT19	Bedding mortar, South side	4 cm	Phase 3
CT20	Bedding mortar of merlon, East side	0-1 cm, surface layer	Phase 3
CT21	Bedding mortar, East side	0-1 cm, surface layer	Phase 3
CT22	Bedding mortar of the corbel, North side	3 cm	Phase 3
CT23	Bedding mortar, North side	3 cm	Phase 3
CT24	Bedding mortar, West side	4 cm	Phase 3
CT25	Bedding mortar of the corbel, South side	0-1 cm, surface layer	Phase 3
CT26	Bedding mortar of merlon, North side	5 cm	Phase 2
CT27	Bedding mortar between two merlon, North side	4 cm	Phase 3

## 8.2.2 Characterization of mortars to select the most suitable samples for in radiocarbon dating

Mineralogical composition analysis of bulk mortars by XRPD revealed (Table 8.3): calcite, quartz, feldspars (K feldspar and plagioclase), lizardite, micas, and gypsum. While calcite can be referred to binder, lime lumps or fragments of aggregate, gypsum is a probable alteration phase. Quartz, feldspars, lizardite and micas can be related to aggregate.

*Table 8.3 Mineralogical composition (semiquantitative data) of CT mortar samples.*

ID sample	Quartz	Calcite	Plagioclase	K feldspar	Other
CT1	++	+++	+	-	Lizardite (*), mica (*)
CT2	+	+++	*	-	Lizardite (*), mica (*)
CT3	++	+++	+	-	Lizardite (*), mica (*)
CT4	+++	++	+	-	Lizardite (*), mica (*)
CT5	+++	++	*	+	Lizardite (*)
CT6	++	+++	+	-	Lizardite (*), mica (*)
CT7	++	+++	+	*	Lizardite (*), mica (*)
CT8	+	+++	+	-	Lizardite (*), mica (*)
CT9	+++	++	+	-	Chlorite (*), lizardite (*), mica (*)
CT10	+	+++	*	-	Lizardite (*), mica (*)
CT11	+	+++	*	-	Lizardite (*)
CT12	++	+++	+	-	Chlorite (*), lizardite (*), mica (*)
CT13	++	+++	+	*	Chlorite (*), lizardite (*), mica (*)
CT14	++	+++	+	-	Mica (*)
CT15	+	+++	+	-	Lizardite (*), mica (*)
CT16	+++	+++	++	-	Chlorite (*), lizardite (*)
CT17	+	+++	+	-	Chlorite (*), lizardite (*), mica (*)
CT18	+++	+++	+	-	Lizardite (*), mica (*)
CT19	++	+++	+	-	Lizardite (*), mica (*), gypsum (*)
CT20	++	+++	+	-	Lizardite (*), mica (*)
CT21	+	+++	*	-	Lizardite (*)
CT22	++	+++	+	-	Lizardite (*), mica (*)
CT23	+++	+++	+	-	Chlorite (*), lizardite (*), mica (*)

CT24	+++	+++	*	-	Chlorite (*), lizardite (*), mica (*), gypsum (*)
CT25	+	+++	+	-	Lizardite (*)
CT26	+++	+++	+	-	Chlorite (*), lizardite (*), mica (*)
CT27	++	+++	+	-	Lizardite (*), mica (*)

+++: very abundant; ++: abundant; +: present; \*: traces; -: below detection limit. Calcite ( $\text{CaCO}_3$ ), quartz ( $\text{SiO}_2$ ), plagioclase ( $\text{NaAlSi}_3\text{O}_8$ - $\text{CaAl}_2\text{Si}_2\text{O}_8$ , albite-anorthite series), k feldspar ( $\text{KAlSi}_3\text{O}_8$ ), lizardite ( $\text{Mg}_3\text{Si}_2\text{O}_5(\text{OH})_4$ ), mica (e. g. muscovite  $\text{KAl}_2(\text{Si}_3\text{Al})\text{O}_{10}(\text{OH},\text{F})_2$ ), chlorite ( $\text{MgFeAl})_8(\text{SiAl})_8\text{O}_{20}(\text{OH})_{16}$ ), gypsum ( $\text{CaSO}_4 \cdot 2 \text{H}_2\text{O}$ )

The main mineralogical and petrographical characteristics of the samples studied are given in Table 1, Appendix 2. From the summarized petrographic observations, some differences between the plasters and mortars can be noticed. For the plasters: the samples (CT1-CT2, CT3, and CT4) have relatively lower binder content mixes with bimodal aggregate size distribution, while other samples (CT6, CT7; CT8, CT9; and CT10, CT11) display higher binder content in a mix with fine, unimodal aggregate size distribution. These differences seem to be due to different manufacturing techniques. In the case of the bedding mortars, samples CT12, CT15, CT17, CT19, CT20, CT22, CT23, CT24, CT25 have binder-rich mixes with a unimodal grain size distribution of aggregate, while samples CT13, CT14, CT27 have binder-rich mixes with a somewhat coarser, bimodal aggregate size distribution. Samples CT16, CT18, CT21 and CT26 exhibit a lower binder content.

It should be noted that the binder in the plaster samples appears to have undergone some recrystallization due to the dissolution and slow recrystallization of calcite by the circulating moisture in the masonry. This prevented us from selecting these samples for dating.

As for the bedding mortars, the observed differences are minor and can be attributed to different working days within the same construction phase rather than to different technologies and supplies. Nonetheless, care in the preparation of the mixes is evident, involving careful selection of aggregate and consistently high binder content, indicating abundant economic resources.



From the mineralogical-petrographic characterization of samples from Trebbio Castle, it is identified the raw materials used, of local source. The binder was produced by firing marly limestone (Alberese limestone, Monte Morello Formation). The aggregate exhibits a heterogeneous composition, utilizing sandy sediments from local watercourses. Finer sands (<400  $\mu\text{m}$ ) predominantly consist of single crystals of quartz, feldspars, spathic calcite, while coarser fractions contain fragments of arenaceous rocks, serpentinites, and Alberese limestone. Rare fragments of cocchiopesto were also found.

We focused on two bedding mortar samples that could provide crucial insights into the historical attribution of construction phases and with mineralogical-petrographic characteristics more suitable for dating. These samples are from the crenelated masonry, CT26 (Phase 2), and the infill masonry, CT27 (Phase 3). The samples show a complete carbonation through phenolphthalein test.

Upon preliminary macroscopic examination, the CT26 sample appears to have compact mortar with few fractures and a hazel coloration. Millimetre-sized lumps of varying tones, from white to yellowish, are noticeable. The thin-section examination of CT26 mortar reveals a weakly hydraulic lime binder with a micritic appearance. It contains numerous lumps attributed to unmixed binder remnants and unburned limestone remnants (Figure 8.2). Dark inclusions are observed within the binder, these could be product of the calcination reaction between the calcium oxide derived from the dissociation of calcite and amorphous silicate compounds resulting from the breakdown of clay minerals in marly limestone. The aggregate consists of sub-angular granules with a bimodal grain size distribution (predominantly 200-300  $\mu\text{m}$ , secondary 700-800  $\mu\text{m}$ ). It comprises fragments of arenaceous rocks, micritic limestones, single crystals of quartz and plagioclase, with less abundant spathic calcite and rare serpentinite fragments. The macroporosity mainly consists of shrinkage cracks, with no observed recrystallized calcite. The Binder/Aggregate ratio (B/A) is 1/3.

The CT27 mortar sample is compact and hazel in colour. Millimetre-sized lumps from yellowish to white hues are also observed. The CT27 mortar sample is realized by a

weakly hydraulic lime binder, with a micritic appearance and small dark inclusions (similar to CT26). The aggregate consists of sub-angular granules with a bimodal grain size distribution (predominantly 200-300  $\mu\text{m}$ , secondary 700  $\mu\text{m}$ -1 mm). The aggregate has the same silico-carbonate composition as CT26. Numerous lumps of lime putty and less abundant unburned limestone are present (more than CT26), as shown in Figure 8.2. The macroporosity mainly consists of shrinkage cracks, with no observed recrystallized calcite. The binder content is relatively abundant, with a B/A of 1/2. Analysis of the XRPD bulk composition is consistent with the crystalline phases observed in the petrographic study.

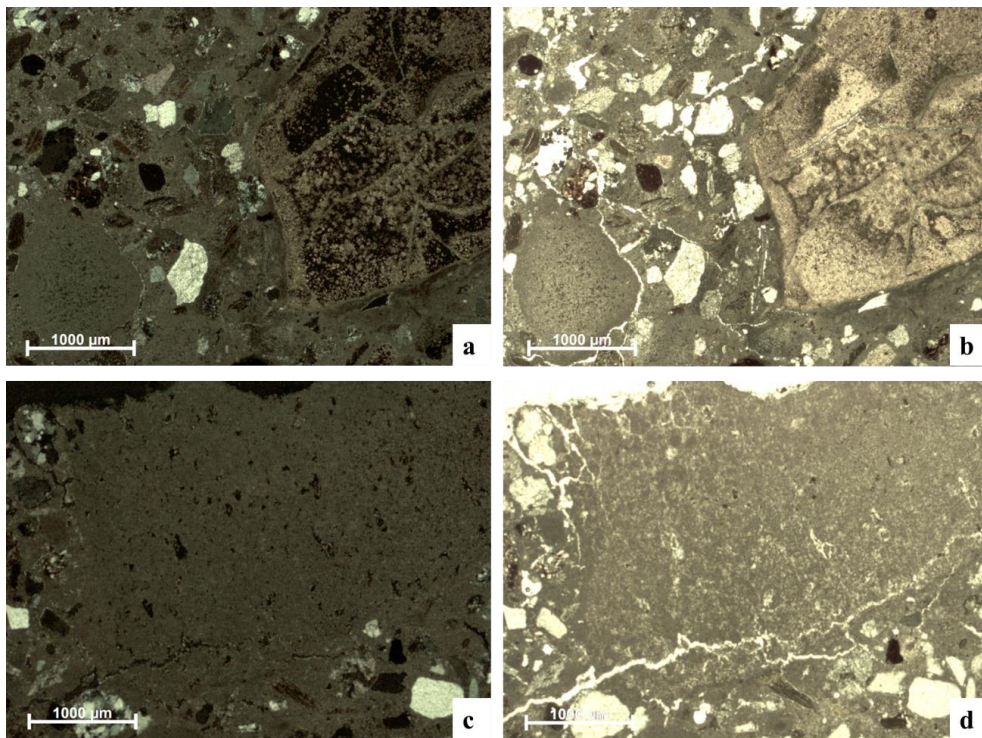


Figure 8.2 – Microphotographs of mortar samples: CT26 (in (a) image under PLM, xpl, in (b) Image under PLM, ppl); and CT27 (in (c) image under PLM, xpl, in (d) Image under PLM, ppl).

XRPD analysis on binder lump samples revealed that the primary component is calcite. However, further analysis of these lumps using ATR-FTIR identified the additional

presence of amorphous silicates (Figure 8.3), likely originating from the calcination of stone rich in silicate components (e.g., clay minerals). This presence was detected as a broad band centred at  $1080\text{ cm}^{-1}$ . The spectrum of FTIR highlights the absorption bands at  $1413$ ,  $873$ , and  $712\text{ cm}^{-1}$ , which are due to calcite.

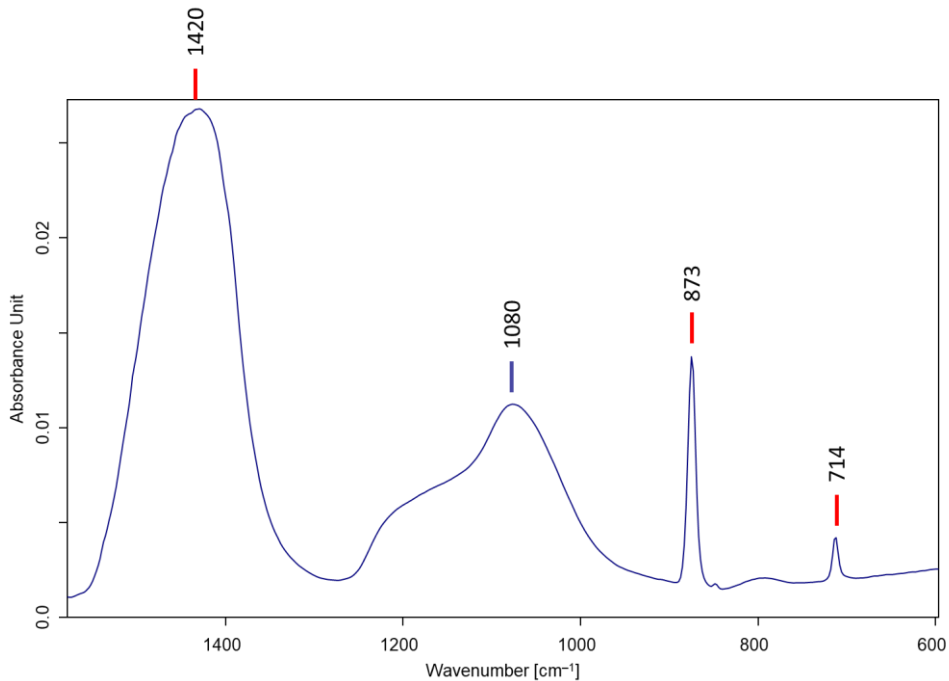


Figure 8.3 – Detail of the FTIR spectrum of CT26 lump (range of interest  $1500\text{--}600\text{ cm}^{-1}$ ): the absorption bands of calcite (in red), and amorphous silicate (in blue).

SEM-EDS analyses on the binder showed significant variability in the content of  $\text{SiO}_2$  and  $\text{CaO}$ , along with the presence of different types of lumps.

The composition and morphology results obtained by SEM-EDS analyses, confirm the use of Alberese limestone (characterized by their typical spongy morphology and calcite vein remains). A comprehensive study of lumps, combining OM, OM-CL, and SEM-EDS analyses in the same area, revealed that also the texture of lump of unmixed binder is heterogeneous (Figure 8.4). They exhibit a similar texture to the binder in OM, appearing brick-red in cathodoluminescence, and SEM analysis indicates a  $\text{CaO}$  and  $\text{SiO}_2 + \text{Al}_2\text{O}_3 + \text{Fe}_2\text{O}_3$  composition comparable to that of the binder.

To gain further insight into the binder composition, SEM-EDS microanalyses were conducted on polished thin sections of both binder and lime lumps (Figure 8.4). The micro-chemical composition of lime lumps and binder is reported in Table 8.4. In addition, the HI was calculated using Boynton's formula (see Section 2.2.2). The measure HI is an average of 5 and 7 individual point measurements from CT26 and CT27, respectively.

CT26 exhibits an average HI of  $0.19 \pm 0.08$ , CT27 shows an HI of  $0.18 \pm 0.09$ , classifying as moderately hydraulic.

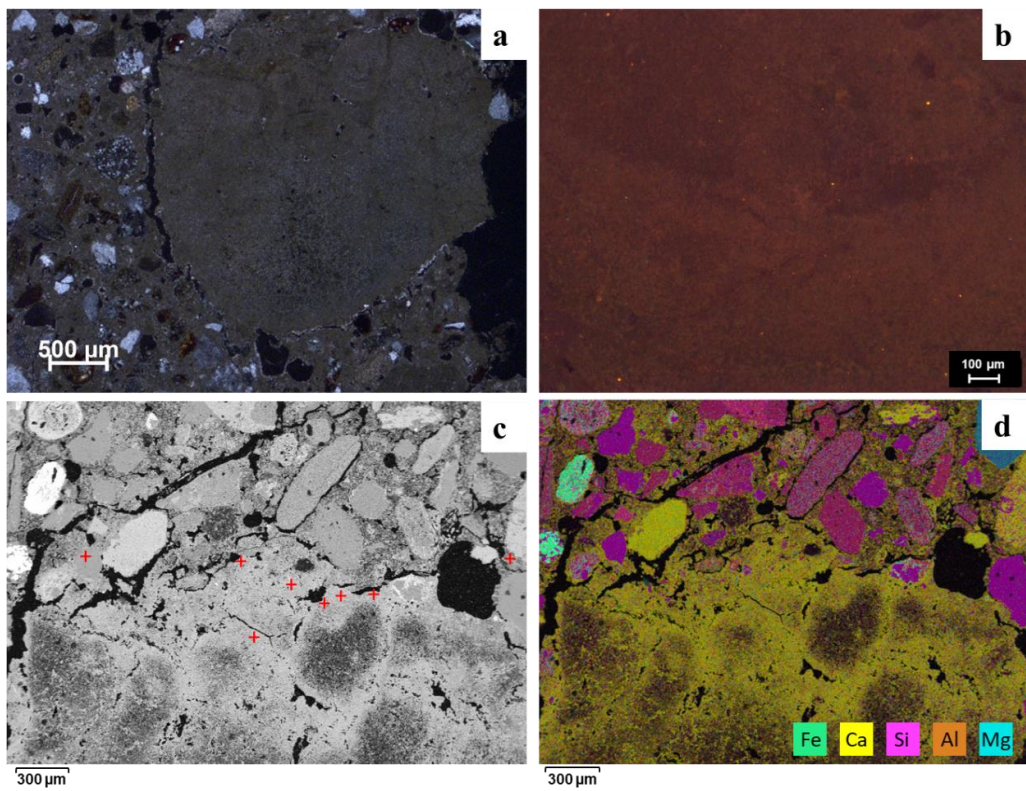


Figure 8.4 – OM (a), OM-CL (b), SEM-EDS (c,d) analyses on lime lump. In c), BS image of a detail of the lump, in which red crosses indicate the performed punctual analysis. In d), SEM-EDS map layered on the previous area.

Table 8.4 Semi-quantitative SEM-EDS micro-chemical analyses of binder and lumps (unburned and lime types).

<b>CT26</b>	<b>MgO</b>	<b>Al<sub>2</sub>O<sub>3</sub></b>	<b>SiO<sub>2</sub></b>	<b>CaO</b>	<b>Fe<sub>2</sub>O<sub>3</sub></b>	<b>Total</b>
Unburned lump	1.4	1.6	12.3	84.7	-	100.0
Lime lump	-	0.7	9.3	90.1	-	100.0
Lime lump	0.4	0.8	10.3	88.6	-	100.0
Lime lump	0.4	0.5	15.9	82.1	1.1	100.0
Binder	0.3	1.2	16.4	82.1	-	100.0
Binder	0.6	0.8	11.8	86.8	-	100.0
<b>CT27</b>	<b>MgO</b>	<b>Al<sub>2</sub>O<sub>3</sub></b>	<b>SiO<sub>2</sub></b>	<b>CaO</b>	<b>Fe<sub>2</sub>O<sub>3</sub></b>	<b>Total</b>
Lime lump	0.3	1.2	16.4	82.1	-	100.0
Lime lump	0.4	2.3	9.6	87.7	-	100.0
Binder	0.5	2.0	19.9	77.7	-	100.0
Binder	1.8	4.4	11.2	78.7	3.9	100.0
Binder	-	1.6	9.2	89.3	-	100.0
Binder	1.2	5.7	15.8	76.1	1.3	100.0
Binder	-	0.9	7.9	91.3	-	100.0

HI results are compared with TGA analyses performed on 3 portions of binder-rich mortar per sample (CT26, CT27), (Figure 8.5). Crucial parameters for distinguishing the type of mortar binder include temperature range and weight loss. The decrease in mass between 200–600°C indicates aluminosilicate dehydration, indicative of hydraulic elements. Hydraulic water (%) varies from 7.02% to 8.89%. A reduction in mass between 600–900°C results from CO<sub>2</sub> decomposition due to calcium hydroxide carbonation and hydrated silico-aluminates, providing insights into the type of lime. Mortars with over 30% CO<sub>2</sub> reduction suggest the presence of aerial lime binder, while those with under 30% indicate hydraulic lime. The examined samples display a modest CO<sub>2</sub> content

(ranging from 27.0% to 31.9%), indicating slight hydraulic characteristics. SEM-EDS and TGA results are consistent, indicating that the mortars have hydraulic behaviour.

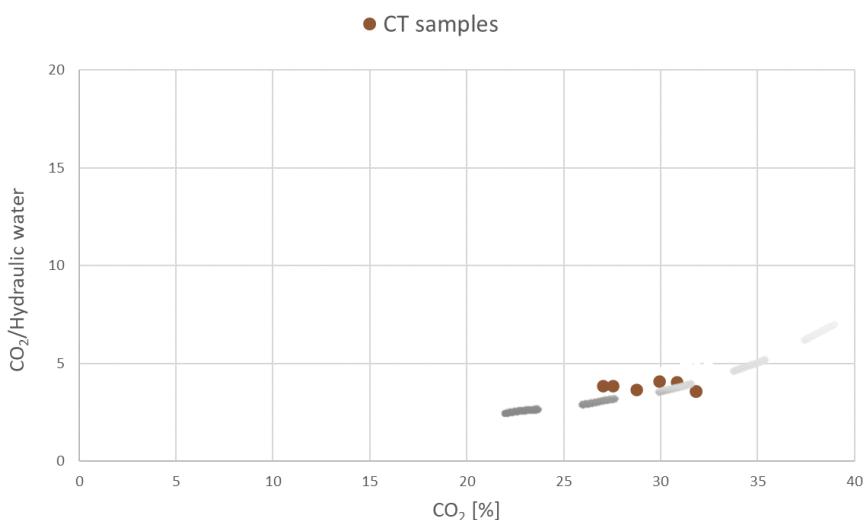


Figure 8.5 – TGA results of CT sample. Diagram of CO<sub>2</sub> vs CO<sub>2</sub>/hydraulic water with the theoretical curve of binders obtained burning Alberese limestone is reported (modified from (Lezzerini et al., 2017)).

### 8.2.3 Selection and characterization of calcite mortar powders

CT26 and CT27 are the samples chosen from the Trebbio Castle characterization. Due to the high presence of carbonate in the aggregate we select only the lumps for <sup>14</sup>C dating. 4 lumps were selected for CT26 samples (labelled as CT26L1, L2, L3, and L4), and 3 for samples CT27 (labelled as CT27L1, L2, L3, and L4).

XRPD analyses are conducted on the powdered lump samples after sieving to determine mineralogical composition, OM-CL, ATR-FTIR (Table 8.5) and micro-Raman analyses are performed to assess the origin of the calcite (Table 8.6).

CT26L1, CT26L2, CT26L4, and CT27L1, CT27L4 exhibit red-brown luminescence, consistent with their position on the anthropogenic calcite trend in ATR-FTIR, classifying them as pyrogenic carbonate. However, CT26L3, CT27L2, and CT27L3 exhibit orange CL and geogenic trends in ATR-FTIR, confirming that these lumps consist of geogenic calcite.

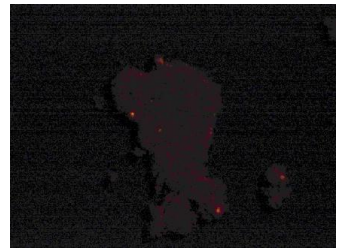
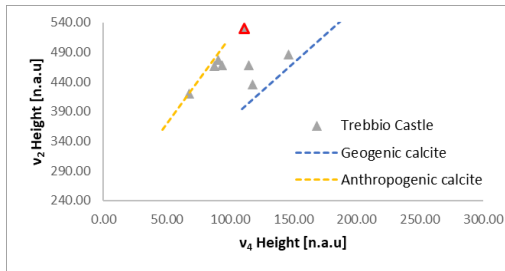
Micro-Raman analyses, conducted only on anthropogenic samples, show Raman shifts at bands L and  $\nu_1$  wavenumber, along with higher FWHM values, which is also observed for the  $\nu_4$  band. The micro-Raman results further confirm the data collected by other techniques. The observed values are typical of anthropogenic calcite. SEM-EDS analysis (Table 8.4) of the thin sections indicate that only small amounts of Mg are present (less than 1.8%). Furthermore, no Mg was detected in the SEM-EDS analyses of powders used for the Raman study in Chapter 6.2.

Table 8.5 Summary of XRPD, ATR-FTIR, and OM-CL analyses on the lumps from Trebbio Castle samples. In the ATR-FTIR plot, the analysed sample is highlighted in red.

ID sample	XRPD	ATR-FTIR	OM-CL
CT26L1	Cal (+++) qz (+)		
CT26L2	Cal (+++), qz (*)		
CT26L3	Cal (+++) qz (+)		

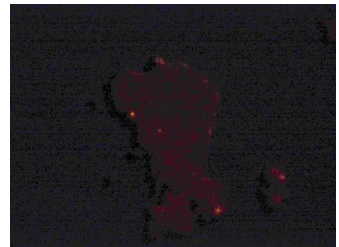
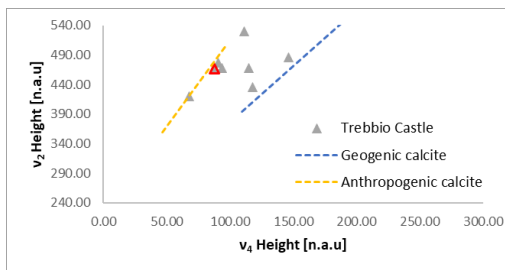
CT26L4

Cal  
(+++)  
qz  
(+)



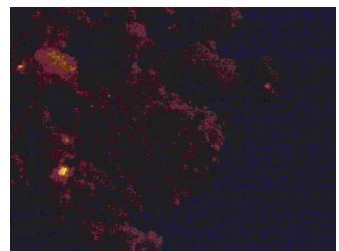
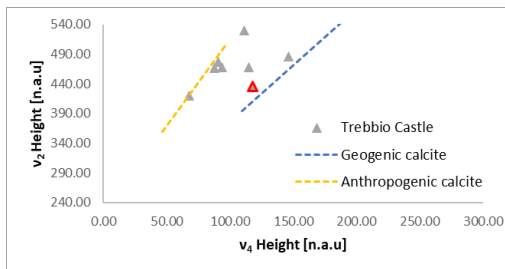
CT27L1

Cal  
(+++)



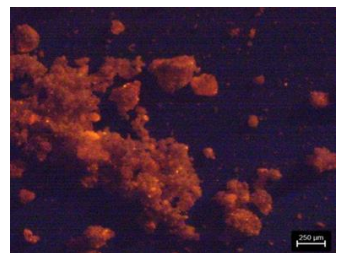
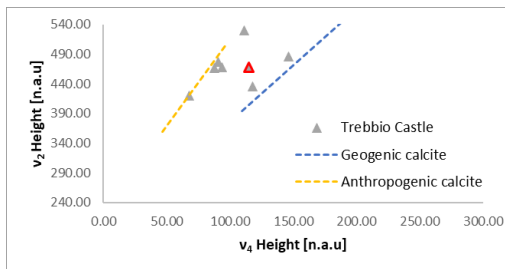
CT27L2

Cal  
(+++)  
qz  
(\*)



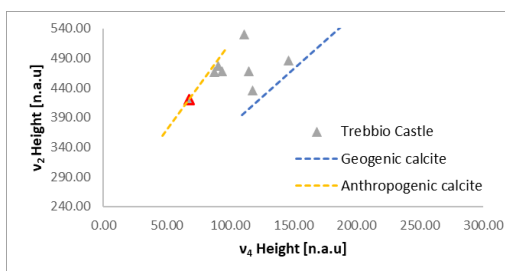
CT27L3

Cal  
(+++)





CT27L4 Cal  
(+++)



+++ : very abundant; ++ : abundant; + : present; \* : traces; - : below detection limit. Cal : calcite; qz : quartz.

Table 8.6 Raman results of calcite mortar powders: the average of the wavenumbers, FWHMs of  $L$ ,  $v_1$ ,  $v_4$  from 10 Raman measures performed for each sample.

ID sample	L wavenumber	L FWHM	$v_4$ wavenumber	$v_4$ FWHM	$v_1$ wavenumber	$v_1$ FWHM
CT26L1	275.0	24.3	712.1	7.2	1085.4	5.9
CT26L2	277.4	20.2	712.4	6.5	1085.8	5.3
CT26L4	277.2	19.3	712.4	6.6	1085.8	5.4
CT27L4	273.8	26.6	712.2	7.5	1085.4	6.4
CT27L1	277.8	18.1	712.5	6.3	1086.0	5.2

#### 8.2.4 Pre-treatment and acid dissolution of selected mortar powders

The lumps CT26L1, CT26L2, CT26L4, CT27L1, and CT27L4 are suitable for dating, since they do not exhibit contamination. The reaction times, along with the masses of the graphitized samples, are listed in Table 8.7. The reaction time of 30 seconds was chosen, since the risk of contaminants reacting with the acid and the sample mass were low.

Table 8.7 Mass, typology and reaction time chosen for the acid dissolution of Florentine historical mortars.

ID samples	Type of sample	Mass (mg)	Reaction time (s)
CT26L1	Lime lump	4.08	0-30
CT26L2	Lime lump	2.62	0-30
CT26L4	Lime lump	2.34	0-30
CT27L1	Lime lump	2.10	0-30
CT27L4	Lime lump	4.12	0-30

## 8.2.5 AMS measurements

In Table 8.8, the radiocarbon concentrations (expressed in pMC) and conventional radiocarbon dates (expressed in years BP) of the samples are reported.

*Table 8.8 Measured radiocarbon concentrations and conventional radiocarbon ages of CT samples.*

ID samples	<sup>14</sup> C concentration (pMC)	T <sub>rc</sub> (yrs BP)	Calibrated age (68% probability)	Calibrated age (95% probability)
CT26L1	93.8 ± 1.7			
CT26L2	93.4 ± 1.1	530 ± 66	1323-1356, 1392-1442	1296-1472
CT26L4	93.9 ± 1.4			
CT27L1	98.4 ± 1.0	130 ± 80	1683-1736, 1803-1936	1657-...
CT27L4	-	-	-	-

Looking at the results, one might be surprised by the experimental uncertainties in some of the samples, which are larger than one would expect from a radiocarbon measurement on this type of material. This is mainly due to the fact that we are measuring samples with very low sample masses. The low currents extracted during the measurements contribute to the increase in experimental error.

When samples belonging to the same fragment or construction phase have consistent radiocarbon concentration each other, a weighted average is performed to obtain an accurate measurement and reduce the error range.

The lumps CT26L1, CT26L2, and CT26L4 from the same mortar portion exhibit consistent radiocarbon concentrations. The results of the weighted average of the three radiocarbon concentrations and the corresponding conventional radiocarbon age are reported in Table 8.8. From the measured conventional radiocarbon age, the calibrated age for the CT26L1+CT26L2+CT26L4 samples is obtained (Figure 8.6a). The calibrated age of the lump samples from CT26, taken from the masonry of the battlements, is compatible and consistent with the archaeological interpretation of the masonry and

the written documentation, so that they can be chronologically placed in the second phase of construction around the middle of the 14th century.

The dating results for sample CT27L1 are reported in Table 8.8, but not for CT27L4, which experienced technical problems during measurement, causing damage to the sample during analysis. Given the measured conventional radiocarbon age (Figure 8.6b), sample CT27L1 is considered modern. In contrast to the previous case, a discrepancy is observed between the assumed archaeological dating and the radiocarbon concentration measurement. Based on historical-archaeological readings, it is assumed that the masonry dates back to the middle of the 15th century (phase 3). This result could indicate that part of the building was built later during the restoration season after the seismic events that characterized the Mugello area between the mid-15th and the early 16th century. After this intense and destructive period of earthquakes, intensive restoration and reconstruction activities were undertaken in all Medici properties in the area (e.g., Cafaggiolo, the Fortezza di San Martino, the town of Scarperia), involving numerous portions of the damaged buildings. Sample CT27 may have intercepted one of these activities, possibly characterized by the new joint stylization of the outer walls of the high portion of the tower, consequently post-dating that section of the building. The results obtained from the comparison of the mortars with the historical-archaeological analysis have provided interesting insights into the construction history of the building.

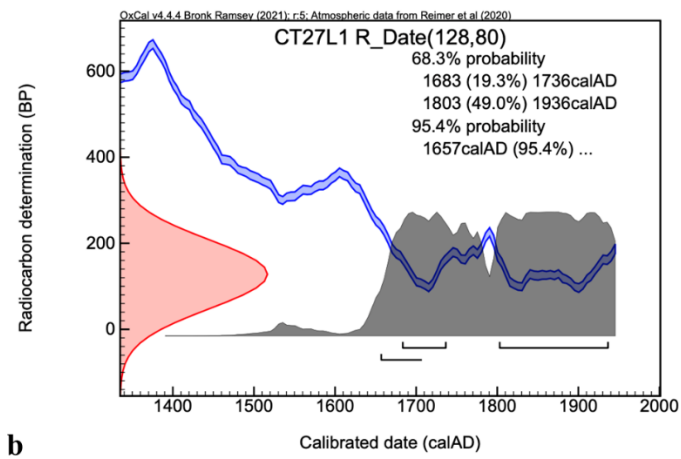
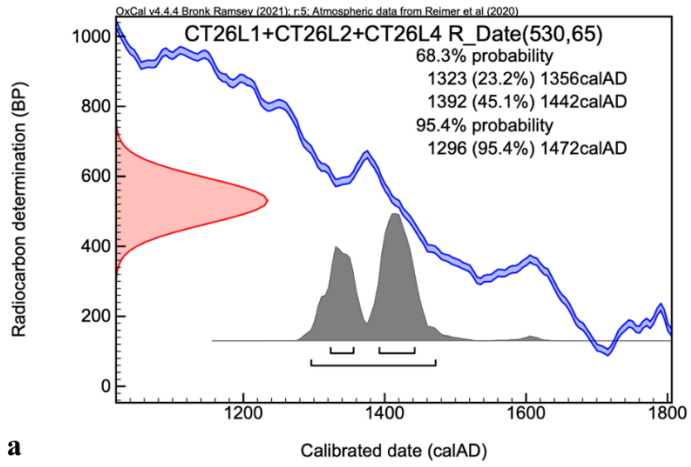


Figure 8.6 – Calibrated age for the CT samples.

## 8.3 S. Felicita Church

### 8.3.1 Sampling

The mortar samples were taken from the domes of the Church of S. Felicita in the historic centre of Florence. The construction of the church of S. Felicita is a remarkable testimony of the architectural development and historical importance of Florence.

The results of the historical documentation show different phases of construction, reflecting the changing aesthetic canon over time. The church was originally a Romanesque chapel and was rebuilt during the Renaissance. The Medici family added the Medici Chapel and the Vasari Corridor, while later Mannerist alterations enriched the interior. The Barbadori Chapel, now known as the Capponi Chapel, is located on the right side of the church and is the object of our research.

This Chapel is characterized by a double-domed structure consisting of a larger (outer) dome attributed to Filippo Brunelleschi and his grandson Filippo di Lorenzo around 1420, and a smaller (inner) dome added later in the 1700s that blends into the larger dome.

It is a significant architectural work as it is hypothesized that part of the original dome was built with the same model structure as the dome of the Florentine Cathedral. According to this suggestion, before building the dome of Santa Maria del Fiore, the architect designed the Barbadori Chapel, implementing the characteristic herringbone pattern of the bricks.

The architectural investigation identified the two different phases of roofing. Therefore, 8 mortar samples were taken with chisel and hammer from two domes. Sampling was conducted on interior masonry that had limited exposure to weathering. The outermost mortar layers were carefully removed, and samples were selected at a depth of 1-2 cm below the wall surface. Table 8.9 provides the sample IDs, sampling points, and depths. Given the structural function of the element under investigation, centimetre-sized fragments could be extracted only at certain sampling points (Figure 8.7).

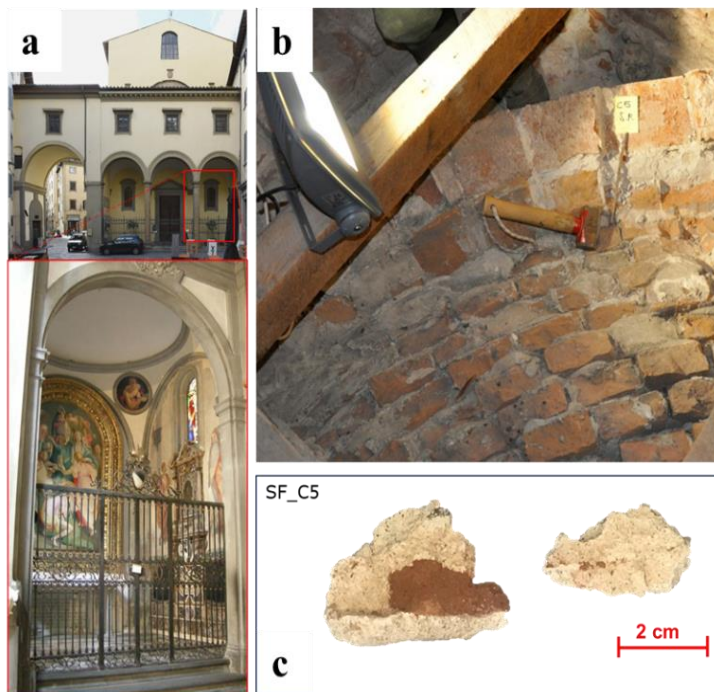


Figure 8.7 – S. Felicità Church. In a) Capponi Chapel, the mortar sampling area; b) Brick structure of the large dome; c) Fragment of collected mortar.

Table 8.9 List of the bedding mortar samples extracted from the domes of S. Felicità Church.

ID sample	Sampling point	Sampling depth
SFC1	Bedding mortar, larger dome	2 cm
SFC2	Bedding mortar, between the small dome and the larger one	0-1 cm, surface layer
SFC3	Bedding mortar, smaller dome	0-1 cm, surface layer
SFC4	Bedding mortar, larger dome	0-1 cm, surface layer
SFC5	Bedding mortar, larger dome	1-2 cm
SFC8	Bedding mortar, between the small dome and the larger one	0-1 cm, surface layer
SFC9	Bedding mortar, between the small dome and the larger one	2-3 cm
SFC10	Bedding mortar, between the small dome and the larger one	0-1 cm, surface layer

### 8.3.2 Characterization of mortars to select the most suitable samples for in radiocarbon dating

Analysis of the mineralogical composition of the bulk mortars by XRPD revealed (Table 8.10): calcite, quartz, k feldspar, plagioclase, mica, and gypsum. While, calcite could be binder, lime lumps or fragments of aggregates, gypsum is a probable alteration phase of the binder. Quartz, k feldspar, plagioclase, and mica may be associated with aggregates.

Petrographic observations have revealed some differences. The main mineralogical and petrographical characteristics of the samples studied are given in Table 2, Appendix 2.

In summary, three types of mortars are distinguished:

- SF1, SF5, SF8, and SF10 are mortars made of binder with a texture from micritic to microsparitic, with lumps. The mixture has higher binder content. The aggregate is generally fine and with a well selected grain size. The aggregate is composed of mono and polycrystalline quartz, feldspars, micas and rock fragments. Low macroporosity is observed.
- SF2, SF4 are mortars made of binder with a texture from micritic to microsparitic, and heterogeneous aspect. The mixture has higher aggregate content. The aggregate is generally fine and well selected grain size. The aggregate is composed of mono and polycrystalline quartz, feldspars, micas and rock fragments. Medium macroporosity is observed, due to subspherical pores.
- SF3, and SF9 are mortars made of a heterogeneous binder with pozzolan fragments (as material providing hydraulic characteristics). The mixture has higher aggregate content and recrystallization calcite binder. The aggregate has heterogeneous composition and not well selected grain size. Medium macroporosity is observed, due to subspherical pores.

Samples SF1, SF5, SF8 and SF10 exhibit very similar compositional and technological characteristics among themselves. They were produced with a traditional technique but differ from sample SF5 by a higher percentage of aggregates. These samples exhibit a

weak hydraulic lime binder and numerous binder lumps, indicating a traditional lime preparation technology but not optimal mixing conditions. For these samples, it can be assumed that marly limestones were used in the kiln, which, together with the addition of river sands (e.g., from the Arno River), imparted some hydraulics to the mortar. SF8 and SF10 exhibit a low recrystallization of the binder.

Samples SFC2 and SFC4 stand out from the previous samples. Samples SF3 and SF9 show a different composition and manufacturing technology. They contain fragments of pozzolan that do not align with the historical production tradition of Florentine mortars; they could be more recent interventions.

Table 8.10 Mineralogical composition (semiquantitative data) of SF mortar samples.

ID sample	Quartz	Calcite	Plagioclase	K feldspar	Other
SFC1	+++	+++	-	+	Mica (*), chlorite (*)
SFC2	+++	+++	-	*	Gypsum (*)
SFC3	++	+	++	*	Mica (+)
SFC4	+++	++	-	-	Gypsum (*)
SFC5	++	+++	*	+	Chlorite (*)
SFC8	+++	++	+	+	Chlorite (*)
SFC9	++	+	++	*	Mica (+)
SFC10	+++	++	+	+	Chlorite (*)

+++ : very abundant; ++ : abundant; + : present; \* : traces; - : below detection limit.

Calcite ( $\text{CaCO}_3$ ), quartz ( $\text{SiO}_2$ ), plagioclase ( $\text{NaAlSi}_3\text{O}_8$ - $\text{CaAl}_2\text{Si}_2\text{O}_8$ , albite-anorthite series), k feldspar ( $\text{KAlSi}_3\text{O}_8$ ), mica (e. g. muscovite  $\text{KAl}_2(\text{Si}_3\text{Al})\text{O}_{10}(\text{OH},\text{F})_2$ ), chlorite ( $\text{MgFeAl})_8(\text{SiAl})_8\text{O}_{20}(\text{OH})_{16}$ ), gypsum ( $\text{CaSO}_4 \cdot 2 \text{H}_2\text{O}$ )

Of the eight samples from the church of S. Felicita, two were selected for dating, SF1 and SF5. SFC1 and SFC5 belong to the group of mortars with typical technology and raw materials found in historical Florentine mortars. They do not show recrystallization, unlike the other samples SFC8 and SFC10. Since samples SFC2 and SFC4 are similar, have



poor production technology, and sample 2 has a surface layer, both could be a restoration mortar.

Samples SFC1 and SFC5 probably date from Brunelleschi's construction phase, and it would be historically important to confirm this.

SFC1 mortar sample appears, at a macroscopic level, as having a compact, hazel-coloured appearance. It exhibits the presence of compact millimetric-sized lumps, predominantly white in colour. In SFC5, a light hazel mortar with a compact structure is observed, and no visible lumps are discernible to the naked eye. The samples are fully carbonated in the phenolphthalein test.

OM analysis reveals that the mortar in SFC1 is composed of weakly hydraulic lime binder with a heterogeneous aspect, and a texture from micritic to microsparitic (Figure 8.7). It is characterized by the presence of numerous lime lumps attributable to unmixed binder (Figure 8.8a). Dark inclusions, also found in the CT samples, are observed within the binder (Figure 8.8b). The aggregate is moderately fine, consists of rock fragments (mainly sandstone), mono and polycrystalline quartz, k feldspar, mica, and fragments of carbonate rocks, siltites, and a few cocchiopesto fragments (without reaction rims with binder, not added as a hydraulic agent). The aggregate has homogeneous distribution, the grain size ranging from 200 to 400  $\mu\text{m}$ . Macroporosity is low and due to irregularly shaped pores. B/A ratio is 1/2.

Sample SFC5 is a mortar made with a weakly hydraulic lime binder, featuring a micritic to microsparitic texture. It contains various types of lumps, ranging from binder remnants to firing residues (Figure 8.8c) and is characterized by dark inclusions (Figure 8.8d). The aggregate is mainly fine, well selected grain size, and with homogeneous distribution. It is composed of mono and poly-crystalline quartz, feldspars, a few rock fragments, and rare cocchiopesto fragments (reaction rims are not observed). The average grain size is 300  $\mu\text{m}$ . Macroporosity is low and consists of irregularly shaped pores. B/A ratio is 1/1, indicating a binder-rich mortar, but one without shrinkage cracks (Figure 8.8d).

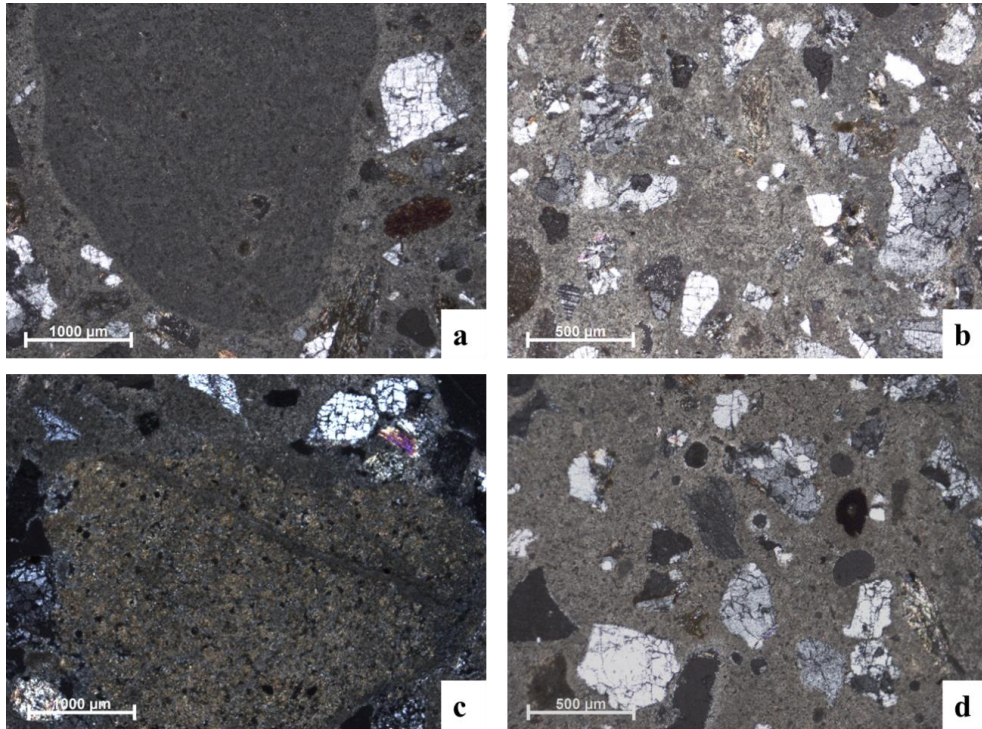


Figure 8.8 - Microphotographs of SFC1 (in a,b): image under PLM, xpl, at different magnification) and SFC5 (in c,d): image under PLM, xpl, at different magnification) mortar samples.

The bulk composition of XRPD analysis agrees with the crystalline phases found in the petrographic analysis.

XRPD analysis of the lumps highlights a predominant composition of calcite and traces of quartz (due to the selection of part of the aggregate). Similar to the CT samples, ATR-FTIR analysis reveals an intense silicate band, likely attributed to the contribution of quartz and amorphous silicates (reported in Figure 1, Appendix 2).

The characteristics of the binder and lumps were thoroughly studied using combined microscopic techniques (i.e., OM, OM-CL), as shown in Figure 8.9.

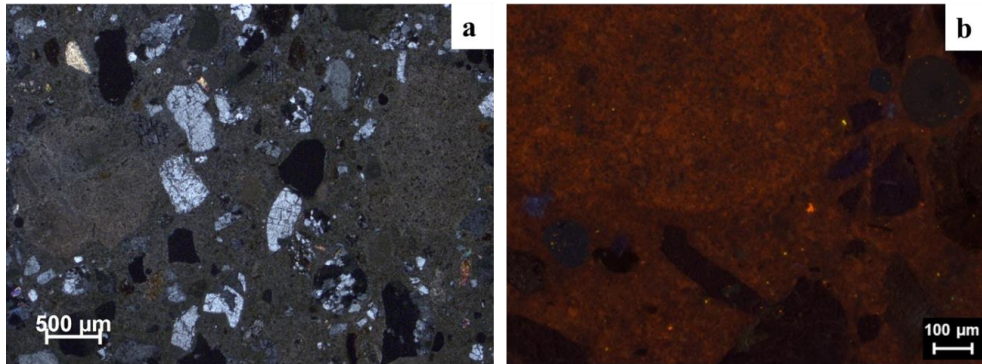


Figure 8.9 – OM (a), OM-CL (b), analyses on lump. In a) The lump analysed is on the right side of OM.

Although the lumps observed in OM are primarily attributed to unmixed binder residues, some of them exhibit a highly complex texture. Indeed, cathodoluminescence analysis reveals crystalline remnants of the original limestone. The SEM-EDS image shows the typical rounded structures attributed to the shells of planktonic foraminifera characteristic of the Alberese limestone. Figure 8.10 also shows certain fossil remains present in both the rock and the unburned lumps. In these areas, a strong heterogeneity in the composition of Ca and Si is observed. Figures 8.10c and 8.10d show a detail of the fossil content: Areas composed entirely of Ca are framed, and those composed of Si are also framed. Table 8.11 shows the microchemical SEM-EDS analysis.

Microforaminifera (e.g., Globorotalia and Globigerina) and calcareous nanofossils typical of the beds of marly limestone from the Upper Cretaceous and Lower Eocene can be found. Macroforaminifera (e.g., Nummulites, Alveolina, and Discocyclina) are also present in the calcarenitic beds (Bortolotti et al., 1962). The remains of the structure could be these fossils; however, it is not possible to identify the species from these images.

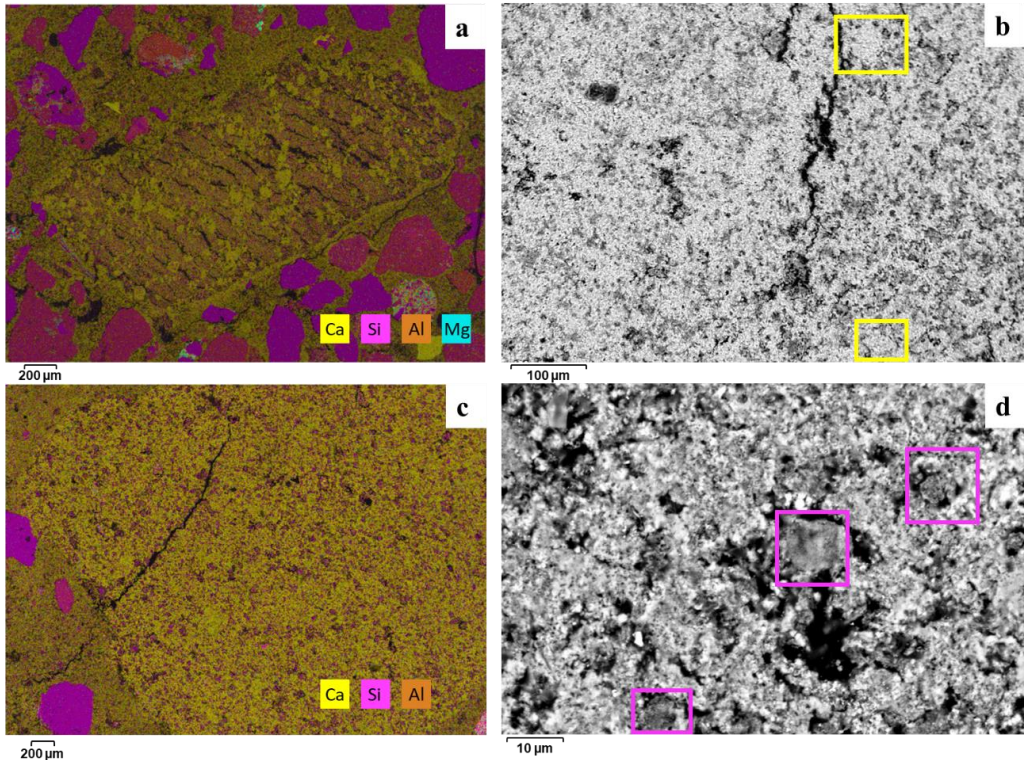


Figure 8.10 – The fossil content in unburned lumps: SFC1 in a) SEM-EDS map layered, and b) BS image of a detail of the lump, in which yellow squares indicate the carbonate fossils remains. SFC5 in c) SEM-EDS map layered, and d) BS image of a detail of the lump, in which pink squares indicate the silico-carbonate fossil remains.

From the SEM-EDS analysis of samples SFC1 and SFC5, similarities in binder composition are observed. The composition found in the binder points is the same as that found in the unmixed binder lumps (Table 8.11).

At least 12 measurement points were performed on the binder for each sample. SFC1 has an average HI of  $0.18 \pm 0.07$  and is thus classified as moderately hydraulic, while SFC5 has an HI of  $0.19 \pm 0.08$ , also falling within the same category.

Table 8.11 Semi-quantitative SEM-EDS micro-chemical analyses of lumps (unburned and lime types) and binder.

SFC1	MgO	Al <sub>2</sub> O <sub>3</sub>	SiO <sub>2</sub>	CaO	Fe <sub>2</sub> O <sub>3</sub>	Total
Unburned lump	0.5	-	4.1	95.4	-	100.0
Unburned lump	0.4	1.1	7.8	90.7	-	100.0

Unburned lump	1.6	4.8	56.5	35.9	1.2	100.0
Unburned lump	1.3	4.7	35.5	56.9	1.7	100.0
Lime lump	0.6	-	8.9	90.6	-	100.0
Lime lump	-	-	8.9	91.1	-	100.0
Binder	0.6	-	5.4	94.0	-	100.0
Binder	1.2	1.9	14.0	82.9	-	100.0
Binder	0.9	4.1	13.0	82.1	-	100.0
Binder	0.5	2.2	9.6	87.7	-	100.0
Binder	1.3	1.8	10.2	86.8	-	100.0
Binder	0.7	1.2	12.5	85.7	-	100.0
Binder	1.1	5.0	15.0	78.9	-	100.0
Binder	1.1	2.2	20.0	76.8	-	100.0
Binder	0.8	1.6	18.8	78.8	-	100.0
Binder	0.7	1.3	16.9	81.0	-	100.0
Binder	1.4	2.1	17.9	78.6	-	
<b>SFC5</b>	<b>MgO</b>	<b>Al<sub>2</sub>O<sub>3</sub></b>	<b>SiO<sub>2</sub></b>	<b>CaO</b>	<b>Fe<sub>2</sub>O<sub>3</sub></b>	
Unburned lump	-	1.2	61.5	37.3	-	100.0
Unburned lump	-	1.0	54.1	44.8	-	100.0
Unburned lump	0.7	1.5	43.6	54.2	-	100.0
Lime lump	1.1	0.6	4.4	94.0	-	100.0
Lime lump	-	1.6	5.6	92.8	-	100.0
Lime lump	1.6	3.9	11.2	82.2	1.2	100.0
Binder	0.9	1.4	13.9	83.7	-	100.0
Binder	1.0	1.1	15.1	82.9	-	100.0
Binder	0.8	1.0	13.0	85.2	-	100.0
Binder	0.7	1.1	12.3	85.8	-	100.0

Binder	1.2	1.3	13.1	84.3	-	100.0
Binder	1.3	1.9	10.0	86.8	-	100.0
Binder	1.3	4.0	18.0	75.2	1.6	100.0
Binder	0.7	1.0	22.7	75.6	-	100.0
Binder	1.0	1.2	16.0	81.9	-	100.0
Binder	1.2	1.6	17.1	79.0	1.0	100.0
Binder	1.2	1.6	12.7	84.6	-	100.0
Binder	1.5	4.0	12.9	81.7	-	100.0

TGA analysis of 3 portions of the binder-rich mortar per sample (SFC1 and SFC5) shows that the hydraulic water (%) ranges from 4.18% to 5.83% and the CO<sub>2</sub> content ranges from 30.28% to 32.44%, indicating hydraulic lime. The samples show similar thermal behaviour (Figure 8.11). The samples are exactly close to the Alberese curve, confirming that the hydraulic properties of the mortar are obtained by burning this marly limestone.

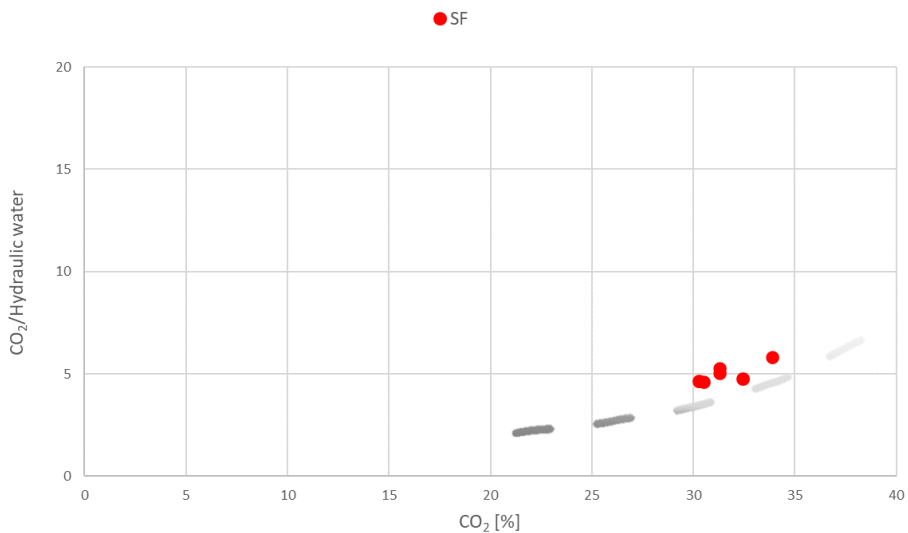


Figure 8.11 – TGA results of SF samples. Diagram of CO<sub>2</sub> vs CO<sub>2</sub>/hydraulic water with the theoretical curve of binders obtained burning Alberese limestone is reported (modified from (Lezzerini et al., 2017)).

### 8.3.3 Selection and characterization of calcite mortar powders

SFC1 and SFC5 are the samples selected for the characterization of S. Felicita Church. Lump and bulk (binder-enriched mortar) samples were selected, since the mortars are characterized by rare carbonate aggregates.

From sample SFC1, 2 lumps and 1 bulk sample (labelled SFC1L1 and L2, SFC1B1) were selected; and from sample SFC5, 1 bulk sample (labelled SFC5B1) was selected. In sample SFC5, it was not possible to extract lumps, which were only visible at the microscopic level (Table 8.12).

After the selection, we estimated the mineralogical phases present with XRPD and evaluated the origin of the calcite with ATR-FTIR, OM-CL and micro-Raman (Table 8.12, Table 8.13). The results of the analyses in ATR-FTIR, OM-CL and XRPD are shown in Table 8.12. Samples SFC1L1, SFC1B1, and SFC5B1 are within the anthropogenic trend in ATR-FTIR and show brown colours in CL.

However, SFC1L2 shows orange CL and geogenic trends in ATR-FTIR, confirming that these lumps are composed of geogenic calcite.

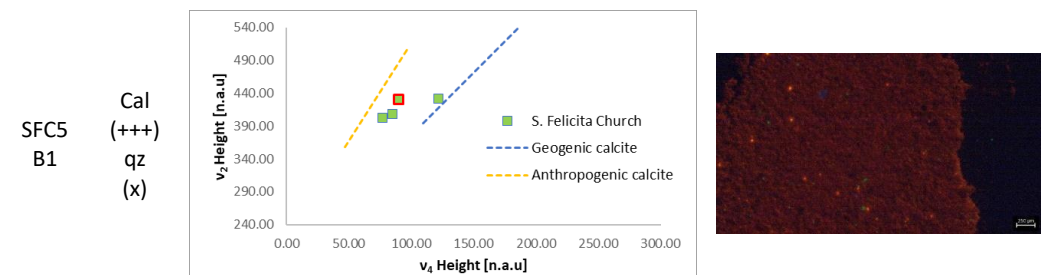
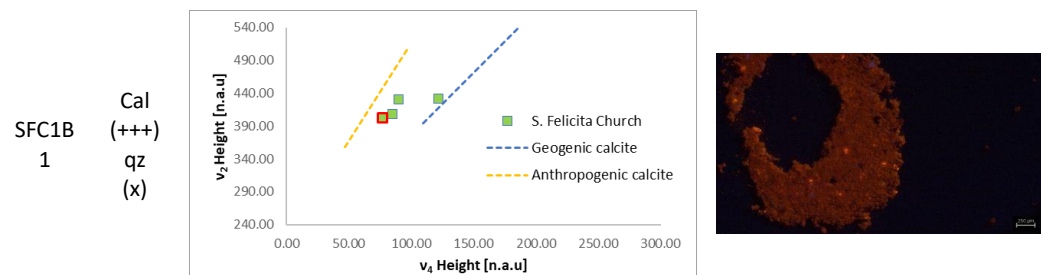
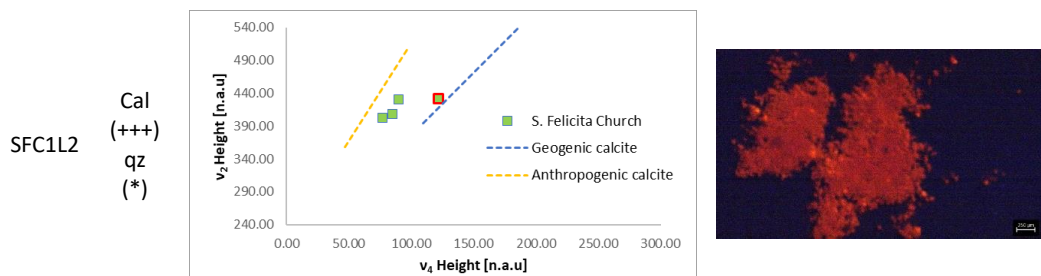
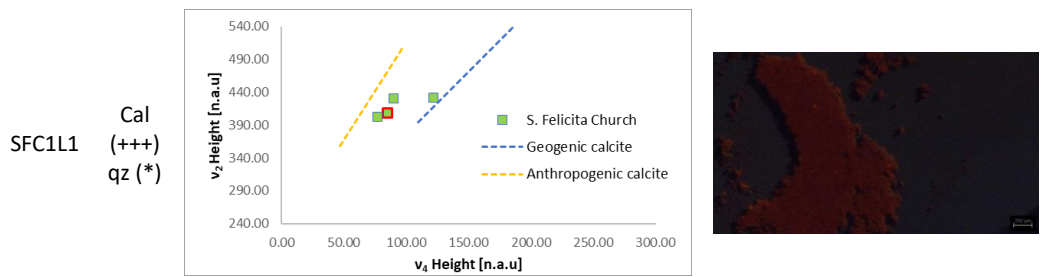
These samples were analysed by micro-Raman analysis. The results are shown in Table 8.13. The samples show broadening of the L,  $\nu_1$ , and  $\nu_4$  bands (FWHM values) and a simultaneous shift of wavenumbers towards lower values. Micro-Raman confirms the calcite origin of samples discovered by other techniques, which are composed of anthropogenic calcite. Low amounts of Mg (less than 1.6%) have been detected in thin sections based on SEM-EDS analysis (Table 8.11). In addition, no Mg was found in powders analysed by SEM-EDS for examination by the Raman method in Section 6.2.

*Table 8.12 Summary of XRPD, ATR-FTIR, and OM-CL analyses on the lump and bulk mortar samples from S. Felicita Church. In the ATR-FTIR plot, the analysed sample is highlighted in red.*

---

ID sample	XRPD	ATR-FTIR	OM-CL
-----------	------	----------	-------

---



+++; very abundant; ++; abundant; +; present; \*; traces; -; below detection limit. Cal: calcite; qz: quartz.



Table 8.13 Raman results of calcite mortar powders: the average of the wavenumbers, FWHMs of L,  $\nu_1$ ,  $\nu_4$  from 10 Raman measures performed for each sample.

ID sample	L wavenumber	L FWHM	$\nu_4$ wavenumber	$\nu_4$ FWHM	$\nu_1$ wavenumber	$\nu_1$ FWHM
SFC1B1	277.5	21.4	712.5	7.6	1085.9	6.0
SFC1L1	277.7	20.6	712.4	7.6	1085.8	6.2
SFC5B1	278.3	18.5	712.5	7.0	1085.9	5.5

#### 8.3.4 Pre-treatment and acid dissolution of selected mortar powders

Samples SFC1L1, SFC1B1, and SFC5B5 are suitable for dating because they have negligible contamination. The reaction times are listed in Table 8.14 along with the masses of the graphitized samples. A reaction time of 30 seconds was chosen for the lump sample since contaminants and the sample mass were unlikely.

From a bulk sample, we collected the first CO<sub>2</sub> fraction formed in the first 20 seconds and the second fraction produced between 20 and 60 seconds. Despite complete characterization of the powders, small grains of geologic calcite may still be present. To avoid any risk of geological contamination, short reaction times were chosen.

Table 8.14 Mass, typology and reaction time chosen for the acid dissolution of Florentine historical mortars.

ID samples	Type of sample	Mass (mg)	Reaction time (s)
SFC1L1	Lime lump	4.45	0-30
SFC1B1(1)	Bulk mortar	12.10	0-30
SFC1B1(2)			30-60
SFC5B1(1)	Bulk mortar	11.00	0-30
SFC5B1(2)			30-60

### 8.3.5 AMS measurements

Table 8.15 shows the results of the AMS measurements.

*Table 8.15 Measured radiocarbon concentrations and conventional radiocarbon ages of SF mortars.*

ID samples	<sup>14</sup> C concentration (pMC)	T <sub>rc</sub> (yrs BP)	Calibrated age (68% probability)	Calibrated age (95% probability)
SFC1L1	96.1 ± 1.5	320 ± 120	1443-1670, 1780-1798	1409-1708, 1719-1819, 1832-...
SFC1B1(1)	-	-	-	-
SFC1B1(2)	94.5 ± 1.8	450 ± 150	1325-1353, 1393-1636	1264-1695, 1725-1812, 1839-1843, 1863-1867, 1872-1877, 1916-...
SFC5B1(1)	98.1 ± 1.6	220 ± 75	1527-1554, 1633-1695, 1725-1812,	1505-1596,
SFC5B1(2)	96.9 ± 1.1		1839-1877, 1916-...	1617-...

The samples from S. Felicita Church, SFC1 and SFC5, probably belong to the same construction phase, namely the Brunelleschi phase. The measured samples were selected considering the results of the characterization campaign, which indicated that they had no significant contamination. In fact, the data obtained exclude the possibility that the samples are contaminated at least by geogenic calcite.

Sample SFC1B1(1) experienced technical problems during the measurement. The sample was damaged during analysis, preventing an evaluation of discrepancies/similarities with the second fraction SFC1B1(2). However, it is possible to observe a coherence between the results of the latter and the lump from the same mortar sample. Therefore, conventional radiocarbon ages were estimated for SFC1B1(2), SFC1L1, and SFC5B1(1)+SFC5B1(2) (Table 8.15). Calibrated ages were determined from these, and are shown in Figure 8.12a,b,c.

However, the experimental uncertainties do not allow us to assign a constructive phase to samples SFC1 and SFC5. Based on the measurement of the radiocarbon concentration

of the mortar, it cannot be excluded that the samples belong to the phase of Brunelleschi or to the later interventions carried out around 1700.

The broad calibrated age range of samples also includes the 1700-1950 one (the so-called 'Stradivarius gap'), the modern age where accurate radiocarbon dating is not possible.

Nevertheless, the production techniques of the measured samples are traditional, as testified by the use of historical raw materials that allow to exclude interventions with industrial methods.

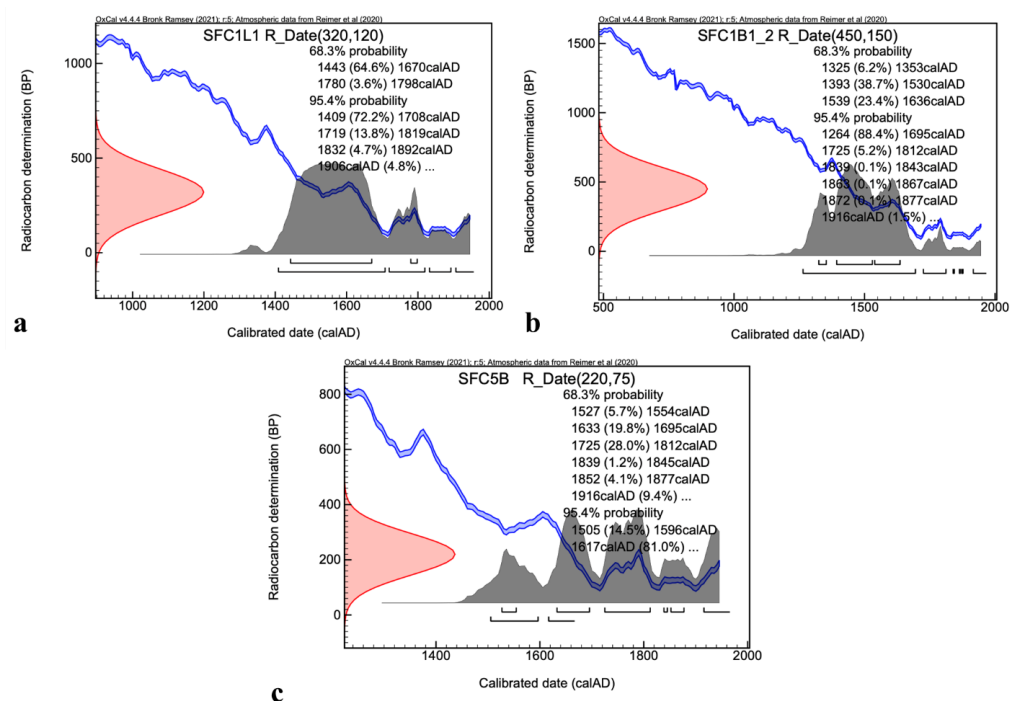


Figure 8.12 – Calibrated age for the SF samples.

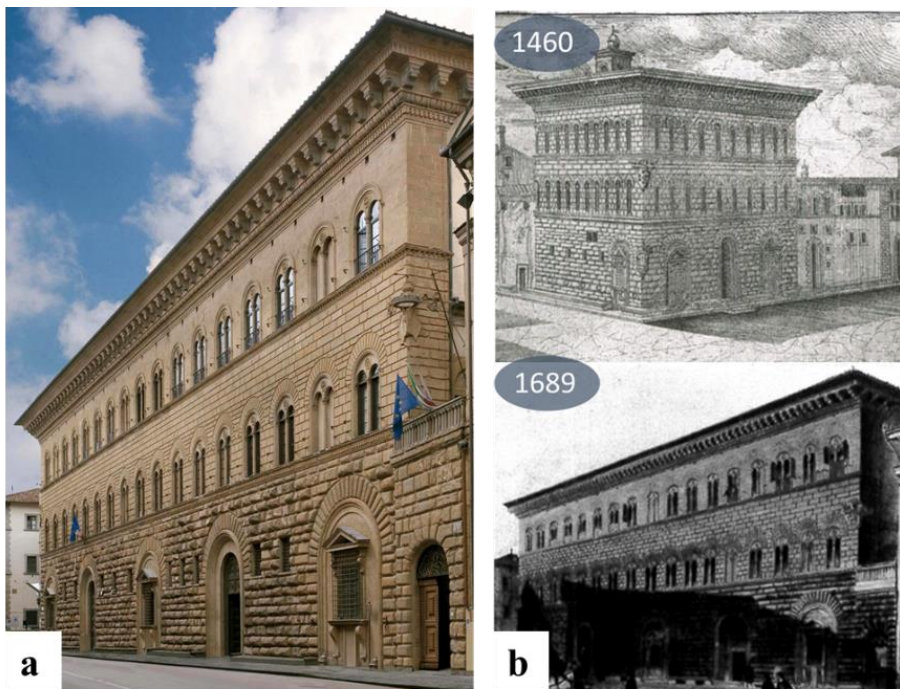
## 8.4 Medici Riccardi Palace

### 8.4.1 Sampling

For the restoration project of the Medici Riccardi Palace, an important palace in the historic center of Florence (Figure 8.13a), a work protocol and monitoring plans were developed that included historical analysis, architectural surveys, and a comprehensive characterization of the rough-hewn stone blocks (Centauro et al., 2022). In this context, the mortars were extracted from the interior walls in order to carry out an archaeometric study of the palace. The history of Palace's construction and subsequent transformations is primarily linked to the events of the Medici dynasty and the subsequent owners, the Riccardi family. The palace was designed by Michelozzo in 1444 and in the following decade the first part of the building was completed. The structure remained unchanged until the palace was acquired by Francesco Riccardi in 1659. In the following decades, the Riccardi family extended the building by including some adjacent properties of the Ughi family on the north side, designed by Pier Maria Baldi and later by Giovanbattista Foggini between 1679 and 1695. In addition to the enlargement and renovation of the interior spaces, the works also led to an extension of the façade facing Via Larga, maintaining the architectural style of Michelozzo's original design, as can be seen in Figure 8.13a. The connection between the old and new parts is so imperceptible that the present building was perceived as a coherent whole from the beginning. Historic views of the palace show an existing structure (Figure 8.13b) built up to the second level of rusticated masonry in the area affected by the expansion. The possibility of dating mortar samples using radiocarbon is of particular interest in determining whether the second phase of construction was built with new masonry or with existing surfaces. Based on the documentation, it is certain that the last level did not previously exist.

In this building, mortar samples were taken from the interior masonry by continuous coring using the dry method (without water) and a suction system to obtain mortar core samples with a diameter of 5 cm. The coring was carried out in the masonry of the first

construction phase, designated as cores C1, C5 and C7, and in the subsequent extension phase of the palace, core samples C3, C4 and C6 were taken. The sampling locations are shown in Figure 8.13c. The removal of mortar cores from the masonry allowed the characterization of the masonry structure. Based on the macroscopic description of the extracted part and the videoendoscopic examinations of the borehole, the stratigraphic reconstruction of the masonry structure was carried out (an example of such reconstruction is shown in Figure 8.13d). For each drill core, two mortar samples were taken, one from the first wall section and one from the subsequent section, in order to also evaluate variations within the same wall section (ID, description and sampling depth can be found in Table 8.16).



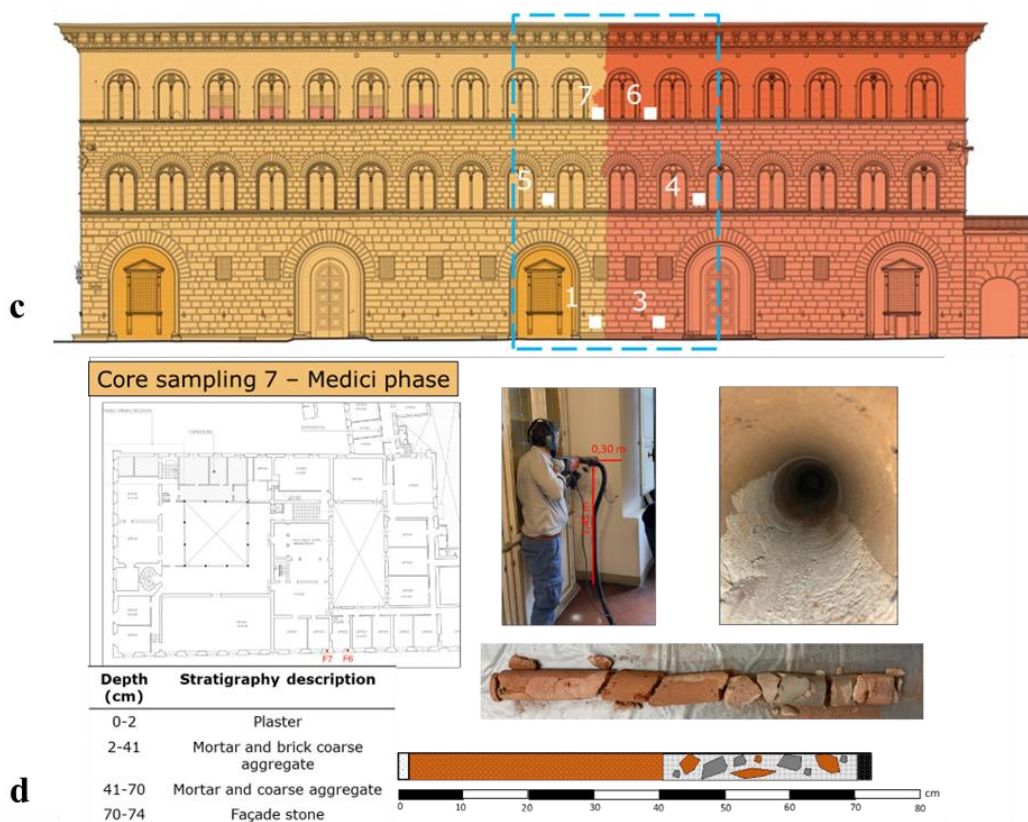


Figure 8.13 – Medici Riccardi Palace. In a) Current view of Medici Riccardi Palace In b) View of the Palace after the initial construction and subsequent expansion. In c) Mortar sampling of Medici Riccardi Palace: 1<sup>st</sup> phase of the Medici family (orange), 2<sup>nd</sup> phase of the Riccardi family (pink-red). In d) Sampling sheet of mortar core sample and reconstruction of the wall's stratigraphy.

Table 8.16 List of mortar samples selected from core samples for the characterization of the masonry of Medici Riccardi Palace.

ID core sample	Sampling point	Total Depth of Core Length (m)	Selected depth (cm)	ID sample
C1	Mortar core sample of Medici phase, 1 <sup>st</sup> level of façade	0.70	13-15	PMRC1(13-15)cm
			58-63	PMRC1(58-63)cm
C3	Mortar core sample of Riccardi phase, 1 <sup>st</sup> level of façade	0.65	40-41	PMRC3(40-41)cm
			55-56	PMRC3(55-56)cm

C4	Mortar core sample of Riccardi phase, 2 <sup>nd</sup> level of façade	0.70	20-21	PMRC4(20-21)cm
			53-54	PMRC4(53-54)cm
C5	Mortar core sample of Medici phase, 2 <sup>nd</sup> level of façade	0.65	17-20	PMRC5(17-20)cm
			45-47	PMRC5(45-47)cm
C6	Mortar core sample of Riccardi phase, 3 <sup>rd</sup> level of façade	0.40	16-17	PMRC6(16-17)cm
			31-32	PMRC6(31-32)cm
C7	Mortar core sample of Medici phase, 3 <sup>rd</sup> level of façade	0.75	17-18	PMRC7(17-18)cm
			49-51	PMRC7(49-51)cm

#### 8.4.2 Characterization of mortars to select the most suitable samples for in radiocarbon dating

The mortar samples from two construction phases of the Medici Riccardi Palace (Medici and Riccardi) allowed the determination of mortar quality, the highlighting of commonalities/differences in the raw materials used and the assessment of the feasibility of dating. The study of the cores taken allows the reconstruction of the stratigraphy of the masonry core. The results are shown in Figure 8.14. Characterization was performed for each core at two different depths to evaluate possible variations in the mortar and to assess the degree of carbonation. Cores C1, C5 and C7 (Medici side), taken at different levels of the palace, showed less drilling difficulty and the masonry appeared to be less tough. In fact, the material taken consisted of loosely cohesive mortar and coarse aggregate. Nevertheless, the mortar remained compact. Cores C3, C4 and C6 (Riccardi side) showed greater resistance to drilling, with a very consistent, compact mortar that adhered firmly to the coarse aggregates. The palace exhibits rubble masonry composed of coarse aggregate and mortar. The coarse aggregate consists mainly of bricks on the 2<sup>nd</sup> and 3<sup>rd</sup> levels (C4, C5, C6 and C7) and of sandstone

(such as Pietra Serena and Pietraforte) on the 1<sup>st</sup> level (C1 and C3) with only a small percentage of bricks.

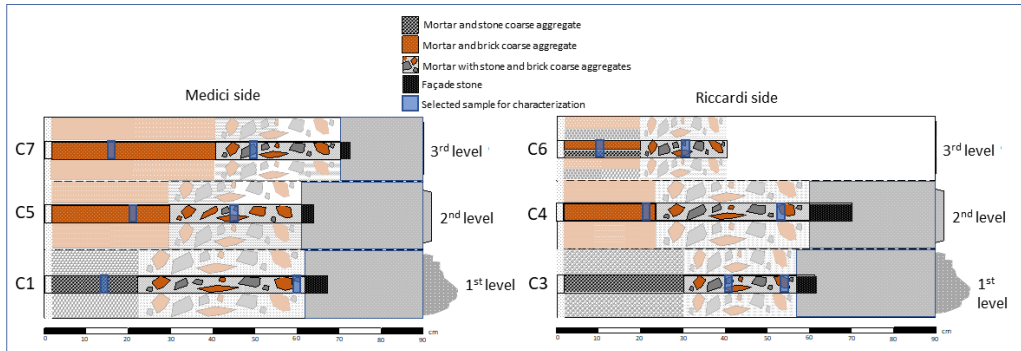


Figure 8.14 – Reconstruction of the wall stratigraphy at the core drilling locations and indication of the analysed samples (in blue).

Petrographic analysis, X-ray diffraction of bulk samples, and phenolphthalein tests were performed.

Mineralogical composition analysis of bulk mortars by XRPD revealed (Table 8.17): calcite, quartz, plagioclase, k feldspar, mica, chlorite, gypsum, portlandite and hydrocalumite. Calcite can be referred to binder, lime lumps or fragments of aggregate, gypsum is a probable alteration phase, while the other phases can indicate the aggregate composition.

Gypsum was detected only in cores C3 and C4, in the innermost parts of the masonry. Portlandite and hydrocalumite, minerals indicative of incomplete carbonation of the binder, were detected in the innermost cores C1, C3, and C4, suggesting delayed carbonation in certain sections. In general, portlandite transforms into stable forms such as calcium carbonate, which is the binder. However, in the presence of aluminium ions ( $\text{Al}(\text{OH})_4$ ) derived from the decomposition of clay minerals present as impurities in the raw material, portlandite is transformed into hydrocalumite (Ponce-Antón et al., 2018; Ricci et al., 2020).



Table 8.17 Mineralogical composition (semiquantitative data) of PMR mortar samples.

ID sample	Quartz	Calcite	Plagioclase	K feldspar	Other
PMRC1(13-23)cm	+++	++	+	*	Mica (*)
PMRC1(58-63)cm	+++	+	+	+	Mica (*), portlandite (+), hydrocalumite (*), chlorite (*)
PMRC3(40-41)cm	+++	+	+	+	Mica (*), portlandite (*), hydrocalumite (*), chlorite (*)
PMRC3(55-57)cm	+++	+	++	+	Mica (*), portlandite (*), gesso (*), chlorite (*)
PMRC4(20-21)cm	+++	+	+	+	Mica (*), chlorite (*)
PMRC4(53-54)cm	+++	+	+	+	Mica (*), portlandite (+), gypsum (*), chlorite (*)
PMRC5(17-20)cm	+++	++	+	+	Chlorite (*)
PMRC5 (45-47)cm	++	+++	+	+	Chlorite (*)
PMRC6(16-17)cm	+++	++	+	+	Mica (*), chlorite (*)
PMRC6(31-32)cm	+++	++	-	+	Mica (*), chlorite (*)
PMRC7(17-18)cm	+++	+++	+	+	-
PMRC7(49-51)cm	+++	++	++	-	Mica (*), chlorite (*)

+++ : very abundant; ++ : abundant; + : present; \* : traces; - : below detection limit. Calcite ( $\text{CaCO}_3$ ), quartz ( $\text{SiO}_2$ ), plagioclase ( $\text{NaAlSi}_3\text{O}_8$ - $\text{CaAl}_2\text{Si}_2\text{O}_8$ , albite-anorthite series), k feldspar ( $\text{KAlSi}_3\text{O}_8$ ), mica (e. g. muscovite  $\text{KAl}_2(\text{Si}_3\text{Al})\text{O}_{10}(\text{OH},\text{F})_2$ ), clay minerals (e. g. chlorite  $(\text{MgFeAl})_8(\text{SiAl})_8\text{O}_{20}(\text{OH})_{16}$ ), gypsum ( $\text{CaSO}_4 \cdot 2\text{H}_2\text{O}$ ), portlandite ( $\text{Ca}(\text{OH})_2$ ) and hydrocalumite ( $\text{Ca}_4\text{Al}_2(\text{Cl},\text{CO}_3,\text{OH})_2(\text{OH})_{12} \cdot 4\text{H}_2\text{O}$ )

The main mineralogical and petrographical characteristics of the samples studied are given in Table 3, Appendix 2. In summary, the microscopic examination of the masonry mortar samples could be divided into the following groups:

- Cores C1, C5, and C7 share common characteristics: a relatively binder-rich mortar, well-selected aggregate grain size, a predominantly siliceous composition, and low macroporosity, indicating careful mixing. The binder is derived from Alberese limestone.

- Cores C3 and C4, different from the previous group, show similarities with each other. They show a heterogeneous composition and granulometry of the aggregates, higher aggregate content mortar, and a binder with dark heterogeneity, indicating the presence of portlandite. Alberese limestone was used for the lime, as evidenced by numerous lumps.
- Core C6 has similarities with both groups. It has a binder similar to the first group (characterised by a micritic texture with small dark inclusions, complete carbonation without defects) and an aggregate more similar to the second group (more heterogeneous composition and granulometry).

For dating, sections of cores with portlandite and hydrocalumite and deeper samples were excluded because carbonation was incomplete in most cases (e.g., PMRC1(13-15)cm, PMRC1(58-63)cm, PMRC3(40-41)cm, PMRC3(55-57)cm, PMRC4(53-54)cm). In such cases, the unusually slow carbonation process could be due to low porosity of the mortar or the use of nonporous bark stone that prevents evaporation of hygroscopic water. Among the mortar samples suitable for dating from Medici Riccardi Palace include PMRC4(20-21)cm, PMRC5(15-17)cm, PMRC6(16-17)cm, and PMRC7(17-18)cm. These samples exhibited complete carbonation without carbonation defects or recrystallized calcite.

Macroscopically, PMRC4(20-21)cm mortar displays a light beige colour, compactness, and numerous millimetric-sized whitish lumps. Microscopically, the PMRC4(20-21)cm sample consists of a weakly hydraulic lime binder with a micritic texture typical of Alberese limestone (Figure 8.15a). It contains lumps attributed to both unburned remnants and unmixed binder in the mixture. The binder shows heterogeneity with small dark inclusions. The aggregate is subangular, heterogeneously distributed, and poorly sorted, primarily consisting of fine particles with multiple grain size classes ranging from 300 to 500  $\mu\text{m}$ , occasionally including 1 mm rock fragments. Quartz (both mono and polycrystalline), mica, numerous fragments of spathic calcite, fragments of sandstone rocks, pelitic materials, various carbonate rocks (such as calcarenite, Alberese, and fossiliferous limestone), and occasional fragments of cocchiopesto and iron

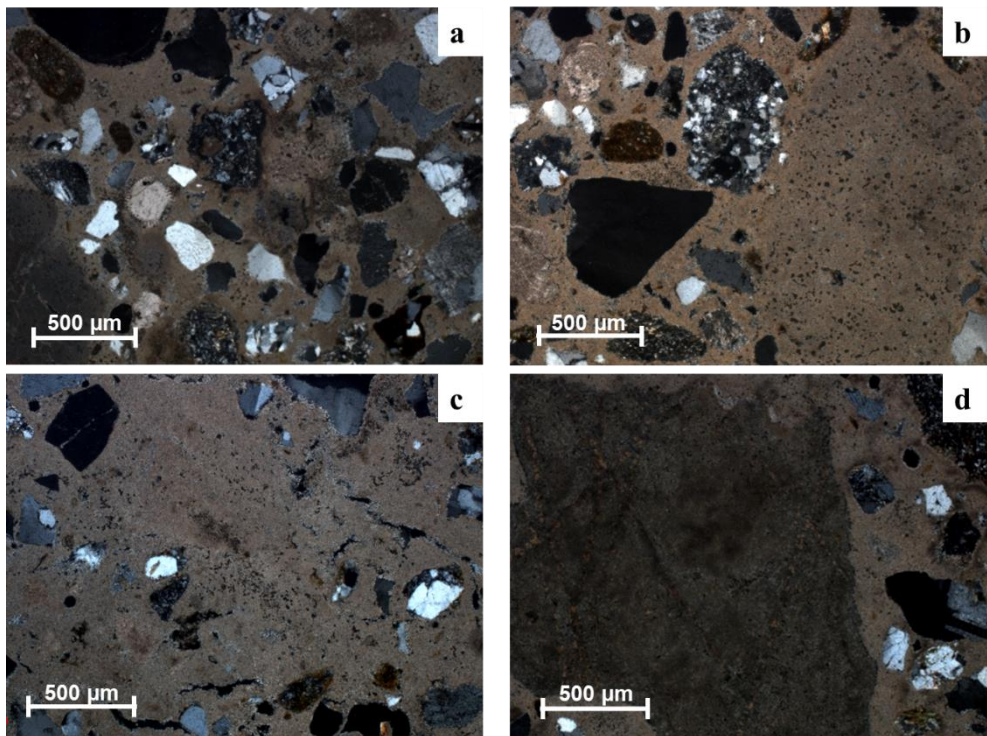
oxides are identifiable components (Figure 8.15b). The B/A ratio is approximately 1/3-1/4. Macroporosity is medium to low and characterized by rounded pores.

PMRC5(17-20)cm mortar exhibits a light beige colour, moderate compactness, millimetric-sized lumps, and fine aggregate. Microscopically, the PMRC5(17-20)cm sample consists of a weakly hydraulic lime binder with a micritic texture (Figure 8.15c). The binder exhibits notable heterogeneity, featuring lumps attributed to both firing remnants and unmixed binder within the mixture. The textural characteristics of the rock used to produce the lime are recognizable (Figure 8.15d). In some areas, the binder contains small dark inclusions and heterogeneous regions. The aggregate is subangular, homogeneously distributed, and well selected. It displays a bimodal size distribution, with a major class ranging around 600-650  $\mu\text{m}$  and a finer class at 250-300  $\mu\text{m}$ . The composition is predominantly silicatic (Figure 8.15c), comprising quartz (both mono and polycrystalline), plagioclase, mica, with occasional fragments of spathic calcite, sandstone rocks, pelitic materials, and iron oxides. Macroporosity is low, characterized by rounded pores. The B/A ratio ranges from 1/2 to 1/3.

PMRC6(16-17)cm mortar presents a light greyish beige colour, high compactness, and a relatively homogeneous binder, with a few visible lumps and fine aggregate. Microscopically, PMRC6(16-17)cm consists of a weakly hydraulic lime binder with a micritic texture (Figure 8.15e). Numerous lumps, predominantly firing remnants, and rare unmixed binder are present (Figure 8.15f). The aggregate is subangular, evenly distributed, and poorly sorted. It is seriate, ranging from 200 to 500  $\mu\text{m}$ , up to some rock fragments measuring 1 mm. Quartz (mono- and poly-crystalline), plagioclase, mica, numerous fragments of spathic calcite, fragments of sandstone rocks, pelitic materials, and carbonates (calcarenites, Alberese limestone, fossiliferous fragments) are identifiable, with a higher quantity compared to sample C5, along with cocchiopesto fragments and iron oxides. The B/A ratio is 1/3, and macroporosity is low, featuring irregularly shaped pores and some shrinkage cracks.

PMRC7(17-18)cm mortar features a light beige colour, moderate compactness, millimetric-sized lumps, and fine aggregate. At the microscopic level, sample PMRC7(17-

18)cm consists of a weakly hydraulic lime binder, with micritic texture. Various types of lumps are present, including unburned and unmixed binder remnants (also present in millimetric dimensions), Figure 8.15g, h. The binder has a heterogeneous structure with dark inclusions. The aggregate is subangular, homogeneously distributed, and well selected grain size. The size distribution is bimodal, with a major size class of approximately 600-700  $\mu\text{m}$  and a finer one ranging from 200-300  $\mu\text{m}$ . The composition is predominantly silicatic, with identifiable components including quartz (mono- and poly-crystalline), plagioclase, feldspars, along with occasional fragments of spathic calcite, fragments of sandstone rocks, pelitic materials, and iron oxides. The B/A ratio is 1/2, and the macroporosity is low, due to rounded pores. Analysis of the XRPD bulk composition is consistent with the crystalline phases observed in the petrographic study.



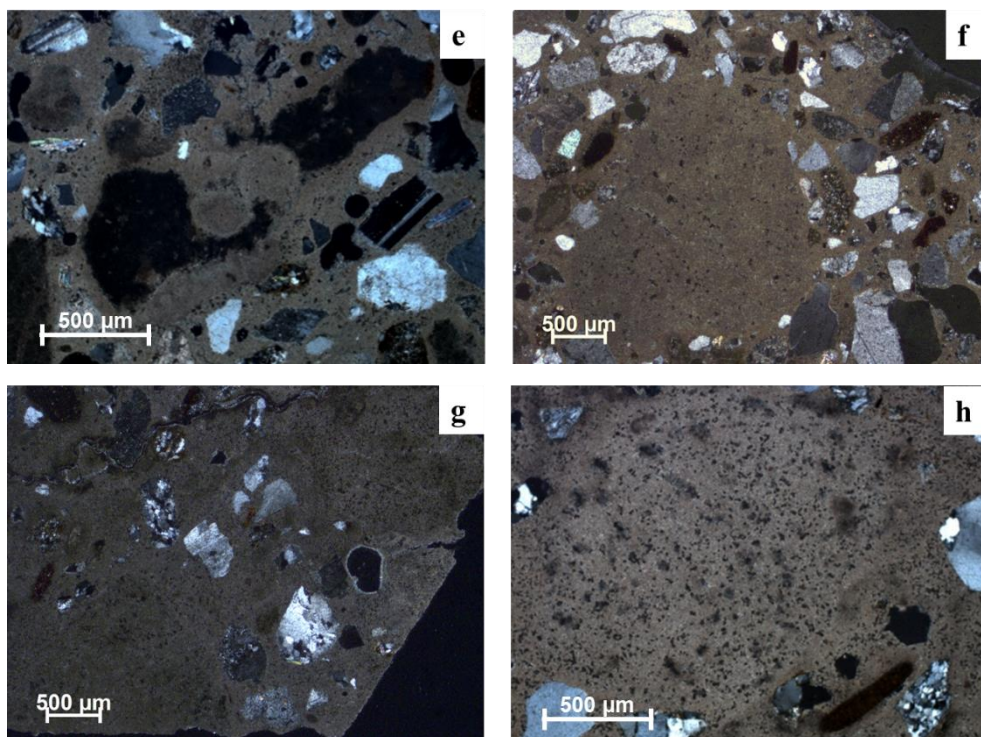


Figure 8.15 – Microphotograph of Medici Riccardi Palace mortar sample: in a, b) PMRC4(20-21)cm; c, d) PMRC5(17-20)cm; e, f) PMRC6(16-17)cm; g, h) PMRC7(17-18)cm.

Calcite predominates in the lump composition, with traces of aggregates (i.e., quartz) in the XRPD pattern; while ATR-FTIR spectra, such as the CT, SF samples, show a strong silicate band in addition to calcite (reported in Figure 1, Appendix 2).

A thorough analysis of the binder and lumps was performed using combined microscopic techniques (OM-CL, SEM-EDS), examining various microtextural features of the Alberese limestone (Figure 8.16). As in the samples of S. Felicita Church, some fossil remains in rock fragments and unburned lumps are observed. Their presence in the lumps produces a strong compositional heterogeneity with mixtures of Ca and Si.

From the SEM-EDS analysis of the samples, typical structures of the weakly hydraulic binder obtained from the firing of Alberese limestone, similar to the previous samples, are observed (Figure 8.16). The round shapes consisting of Ca are probably remains of

foraminifera. The composition of the binder and lime and unburned lumps and Alberese aggregate is shown in Table 8.18.

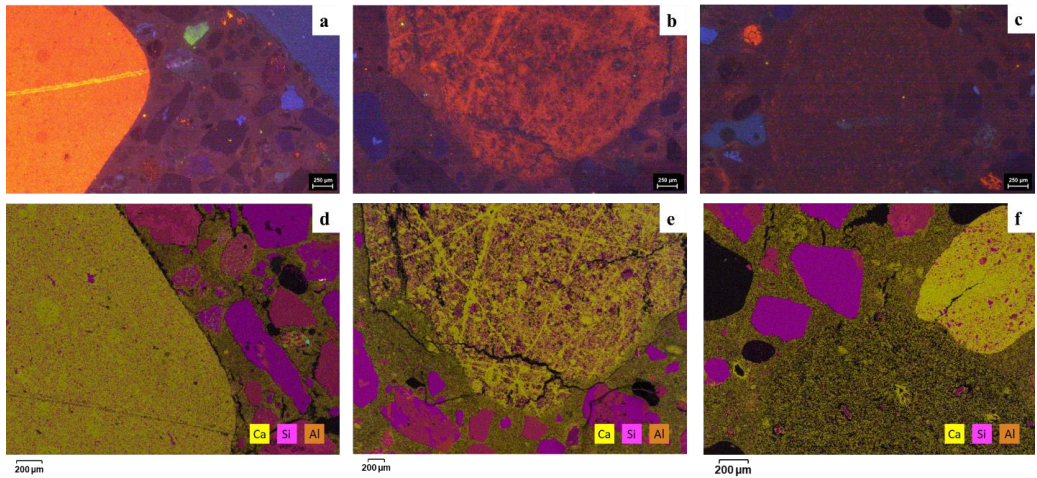


Figure 8.16 – Comparison between OM-CL (a,b and c) and SEM-EDS images (d,e and f) with lumps and Alberese limestone as aggregate. Microtextural features of Alberese rock fragments: in a) OM-CL analysis and d) SEM-EDS map layered. Two different microtextural unburned lumps obtained by firing Alberese limestone: in b,c) OM-CL analysis and e,f) SEM-EDS map layered.

Table 8.18 Semi-quantitative SEM-EDS micro-chemical analyses of binder and lumps (underburned, overburned and lime).

PMRF4	MgO	Al <sub>2</sub> O <sub>3</sub>	SiO <sub>2</sub>	CaO	Fe <sub>2</sub> O <sub>3</sub>	Total
Unburned lime	0.7	1.0	4.8	92.7	0.8	100.0
Unburned lime	0.9	-	-	98.2	1.0	100.0
Unburned lime	0.5	0.4	11.4	87.7	-	100.0
Unburned lime	1.1	1.0	11.5	85.0	1.5	100.0
Unburned lime	0.8	3.7	92.6	1.8	1.1	100.0
Unburned lime	1.2	5.3	86.8	4.6	2.1	100.0
Unburned lime	-	-	69.7	30.3	-	100.0
Unburned lime	-	-	71.4	28.6	-	100.0
Unburned lime	-	0.7	6.6	92.7	-	100.0

Unburned lime	0.5	0.6	7.7	91.2	-	100.0
Unburned lime	0.7	0.8	11.1	87.3	-	100.0
Unburned lime	1.7	1.9	12.8	83.6	-	100.0
Unburned lime	0.9	0.9	13.8	84.4	-	100.0
Unburned lime	-	-	91.8	8.2	-	100.0
Unburned lime	-	-	81.3	18.7	-	100.0
<hr/>						
Lime lump	-	1.0	14.0	85.0	-	100.0
Lime lump	0.7	1.4	14.0	83.9	-	100.0
Binder	0.7	1.4	23.2	74.7	-	100.0
Binder	-	1.7	14.3	84.0	-	100.0
Binder	1.0	1.4	13.7	83.9	-	100.0
Binder	1.0	1.9	19.4	77.7	-	100.0
Binder	0.6	2.4	22.1	73.6	1.3	100.0
Binder	1.3	3.4	18.8	76.4	-	100.0
Binder	0.7	1.3	13.8	84.3	-	100.0
Binder	1.0	-	10.4	88.6	-	100.0
Binder	1.2	1.1	9.0	87.9	0.8	100.0
<hr/>						
<b>PMRF6</b>	<b>MgO</b>	<b>Al<sub>2</sub>O<sub>3</sub></b>	<b>SiO<sub>2</sub></b>	<b>CaO</b>	<b>Fe<sub>2</sub>O<sub>3</sub></b>	<b>Total</b>
<hr/>						
Unburned lime	0.6	7.5	44.7	47.2	-	100.0
Unburned lime	0.7	7.8	45.7	45.0	0.8	100.0
Unburned lime	1.0	7.5	58.4	31.9	1.2	100.0
Unburned lime	2.5	3.9	14.4	77.5	1.7	100.0
Overburned lime	0.9	-	26.9	72.2	-	100.0
Overburned lime	1.7	-	45.8	52.5	-	100.0
Overburned lime	2.4	0.7	37.1	59.0	0.7	100.0
Lime lump	1.1	-	10.5	88.4	-	100.0

Lime lump	0.8	0.6	11.7	87.0	-	100.0
Binder	-	-	8.3	91.7	-	100.0
Binder	1.0	1.4	15.8	81.8	-	100.0
Binder	0.9	1.8	17.5	79.8	-	100.0
Binder	0.5	1.4	11.3	86.8	-	100.0
Binder	0.6	1.5	18.0	80.0	-	100.0
Binder	0.8	1.3	18.3	79.5	-	100.0
Binder	-	-	8.2	91.8	-	100.0
<b>PMRF7</b>	<b>MgO</b>	<b>Al<sub>2</sub>O<sub>3</sub></b>	<b>SiO<sub>2</sub></b>	<b>CaO</b>	<b>Fe<sub>2</sub>O<sub>3</sub></b>	<b>Total</b>
Alberese aggregate	-	2.2	92.0	5.2	0.7	100.0
Alberese aggregate	-	-	4.8	95.2	-	100.0
Alberese aggregate	-	-	5.0	95.0	-	100.0
Alberese aggregate	1.4	1.0	13.2	84.4	-	100.0
Alberese aggregate	0.9	-	10.5	88.6	-	100.0
Unburned lime	0.5	1.1	83.1	15.3	-	100.0
Unburned lime	1.2	-	94.3	4.6	-	100.0
Unburned lime	0.7	0.7	10.4	87.4	0.8	100.0
Unburned lime	0.6	-	3.2	96.3	-	100.0
Unburned lime	3.3	3.9	44.3	44.3	4.1	100.0
Unburned lime	1.0	0.9	14.7	83.3	-	100.0
Lime lump	0.7	1.1	10.0	88.2	-	100.0
Lime lump	0.5	2.2	16.7	78.5	2.0	100.0
Binder	1.9	0.7	1.8	95.7	-	100.0
Binder	1.1	2.4	6.9	86.1	3.6	100.0
Binder	1.0	2.3	5.2	89.6	1.9	100.0
Binder	0.9	1.2	14.2	83.8	-	100.0



Binder	0.7	1.6	10.3	87.4	-	100.0
Binder	0.8	1.8	11.7	85.7	-	100.0

Based on least 6 measurements taken on the binder for each sample, PMRC4(20-21)cm and PMRC6(16-17)cm have the similar average HI of  $0.22 \pm 0.09$  and  $0.18 \pm 0.07$ , respectively; while PMRC7(17-18)cm have an HI of  $0.12 \pm 0.06$ . PMRC4(20-21)cm and PMRC6(16-17)cm fall into the class of moderately hydraulic binders, while PMRC7(17-18)cm are weakly hydraulic.

From the TGA analysis of the binder-enriched mortar samples of PMRC5(15-17)cm, PMRC6(16-17)cm, PMRC7(17-18)cm (average of 3 analyses for each sample in Figure 8.17), Hydraulic water (%) varies from 4.20% to 5.80%, and CO<sub>2</sub>% ranges from 30.3% to 32.4%, suggesting the presence of hydraulic lime.

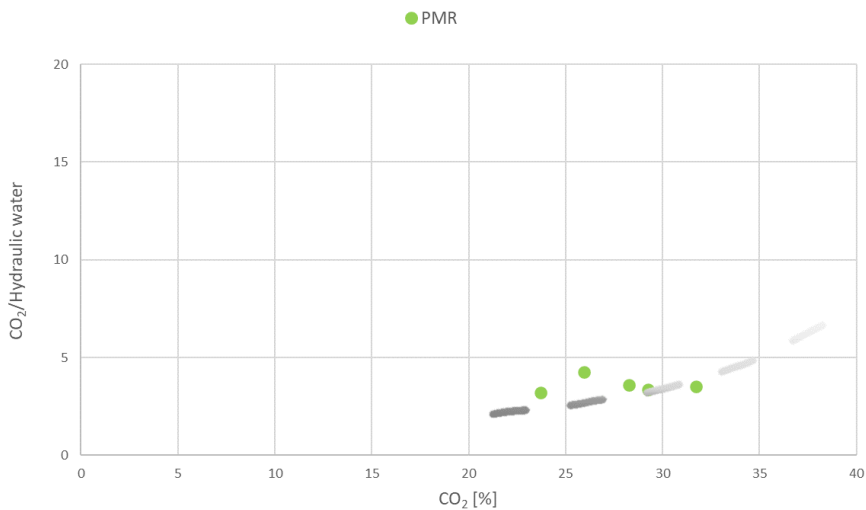


Figure 8.17 – TGA results of PMR samples. Diagram of CO<sub>2</sub> vs CO<sub>2</sub>/hydraulic water with the theoretical curve of binders obtained burning Alberese limestone is reported (modified from (Lezzerini et al., 2017)).

### 8.4.3 Selection and characterization of calcite mortar powders

PMRC4(20-21)cm, PMRC5(15-17)cm, PMRC6(16-17)cm, and PMRC7(17-18)cm are the samples selected from Palazzo Medici Riccardi. Lumps and bulk (binder-enriched mortar) powders are indicated without depth information, using the notations Ln and Bn, respectively.

Sample PMRC4(20-21)cm contains lumps of different origins, as well as a considerable amount of carbonate aggregates. Lump and the enriched binder powder were prepared (designated PMRC4L1, PMRC4B1).

Sample PMRC5(15-17)cm exhibits mortar composed mainly of siliceous aggregate, with lumps of various types. Therefore, lumps (labelled as PMRC5L1, L2, L3, L4) and bulk fraction (labelled as PMRC5B1) was also selected.

In PMRC6(16-17)cm, various types of lumps and carbonate aggregates were observed. 1 lump (labelled as PMRC6L1) and 1 bulk sample (labelled as PMRC6B1) were selected from PMRC6(16-17)cm. Finally, 1 lump PMRC7L1 and 1 bulk sample PMRC7B1 were selected from the PMRC7(17-18)cm sample.

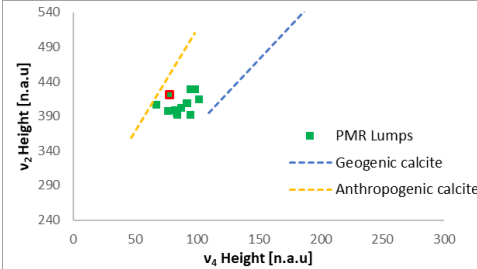
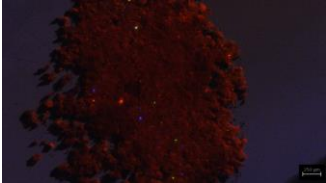
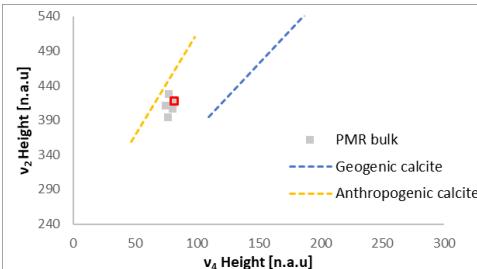
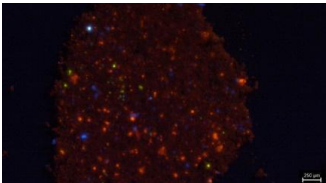
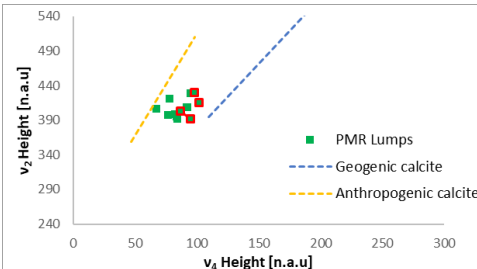
Both lump and bulk samples were characterized by XRPD, OM-CL and ATR-FTIR. The analytical results are shown in Table 8.19.

PMR samples that fall within the trend of anthropogenic calcite (in ATR-FTIR) and exhibit brown colour in CL include PMRC4L1, PMRC4B1, PMRC5B1, PMRC6L1, PMRC6B1, PMRC7L1, PMRC7B1. Some small orange grains in CL are observed in PMRC4B1, PMRC5B1.

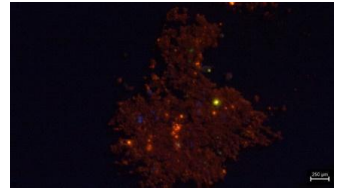
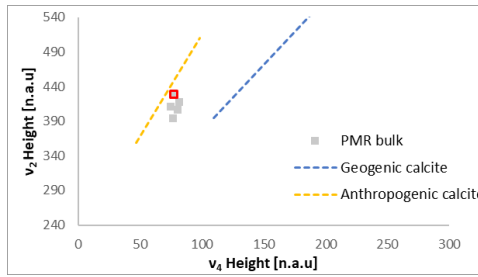
These samples were analysed by micro-Raman and the results for FWHM, L,  $\nu_1$  and  $\nu_4$  wavenumbers are shown in Table 8.20. A broadening and shift in wavenumber to lower values is observed in all samples compared to geologic calcite, especially in  $\nu_1$ , which is consistent with anthropogenic calcites. This trend is also observed in the  $\nu_4$  band. Micro-Raman confirms calcite origin of samples discovered by other techniques that consist of anthropogenic calcite.

Low amounts of Mg (less than 2.0%) have been detected in thin sections based on SEM-EDS analysis (Table 8.18). According to Borrromeo et al., (2017) and previous results to CT, SF samples, there are no peak position variations in these compositional conditions.

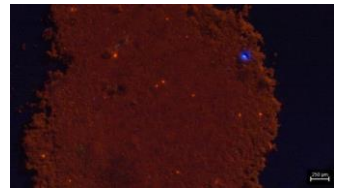
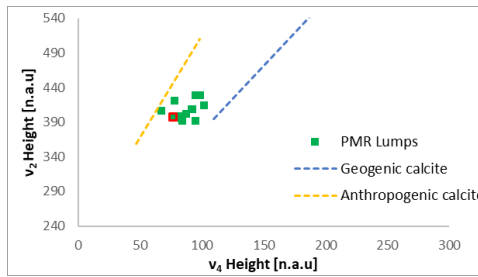
Table 8.19 Summary of XRPD, ATR-FTIR, and OM-CL analyses lump and bulk mortar samples from Medici Riccardi Palace. In the ATR-FTIR plot, the analysed sample is highlighted in red.

ID sample	XRPD	ATR-FTIR	OM-CL
PMRC4 L1	Cal (+++) qz (*)		
PMRC4 B1	Cal (+++) qz (+) plg (*)		
PMRC5 L	Cal (+++) qz (*) vat (*)		<p>From the ATR-FTIR analyses, the selected samples appear to be mainly composed of geogenic calcite.</p>

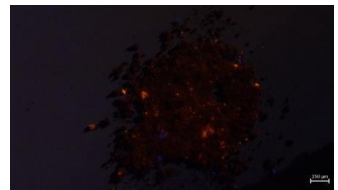
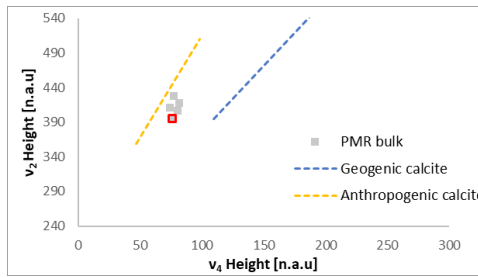
PMRC5  
B1  
Cal  
(+++)  
qz (+)  
plg (\*)



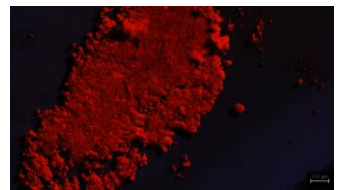
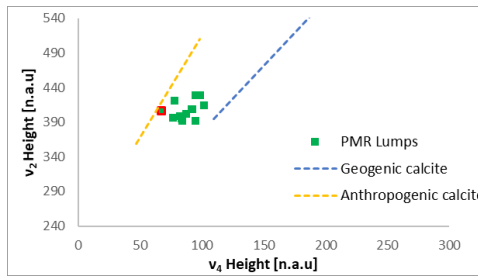
PMRC6  
L1  
Cal  
(+++)  
qz (\*)



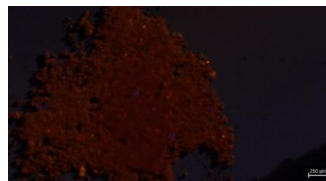
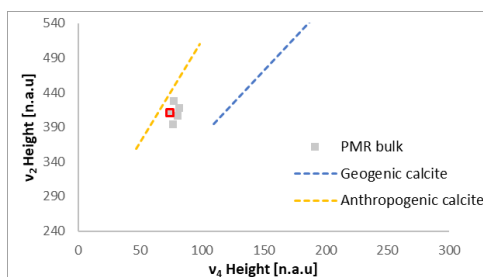
PMRC6  
B1  
Cal  
(+++)  
qz (++)  
k feld  
(\*)



PMRC7  
L1  
Cal  
(+++)  
qz (\*)



PMRC7  
B1  
Cal  
(+++)  
qz (+)

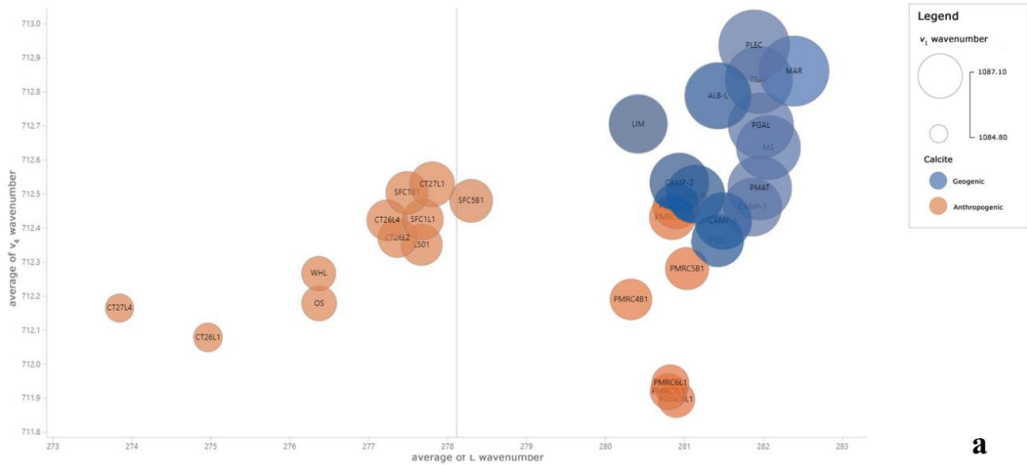


+++; very abundant; ++; abundant; +; present; \*: traces; -; below detection limit. Cal: calcite; qz: quartz; k feld: k feldspar; plg: plagioclase.

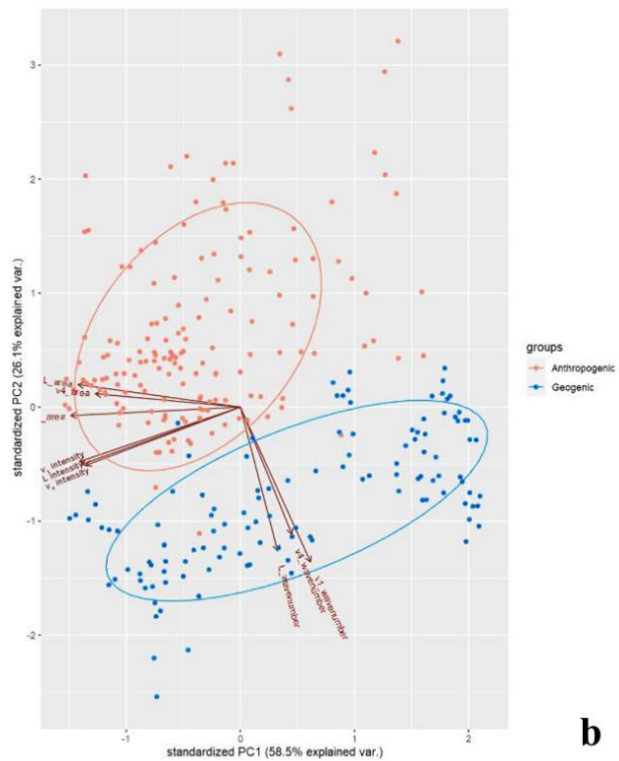
Table 8.20 Raman results of calcite mortar powders: the average of the wavenumbers, FWHMs of L,  $v_1$ ,  $v_4$  from 10 Raman measures performed for each sample.

ID sample	L wavenumber	L FWHM	$v_4$ wavenumber	$v_4$ FWHM	$v_1$ wavenumber	$v_1$ FWHM
PMRC4L1	280.9	14.0	711.9	6.4	1085.7	4.9
PMRC4B1	280.3	15.3	712.2	5.9	1085.8	4.7
PMRC5B1	281.0	14.4	712.2	5.9	1085.9	4.6
PMRC6L1	280.8	15.1	711.9	6.7	1085.7	5.0
PMRC6B1	280.8	14.8	712.4	6.2	1086.0	6.0
PMRC7L1	280.8	18.6	711.9	6.0	1085.7	4.9
PMRC7B1	280.9	15.7	712.5	6.4	1086.0	5.1

For the statistical analysis described in section 6.3, these data were included to investigate their behaviour in the machine learning model. Visual inspection of the dataset was performed to identify new trends or tendencies. For this purpose, the pairplot and bubble plot were used along with PCA (Figure 8.18).



**a**



**b**

Figure 8.18 – Visual inspection and PCA on new dataset of calcite samples. In a) Bubble chart: average values of  $v_4$  wavenumber vs.  $L$  wavenumber, with  $v_1$  wavenumber as the bubble size of both calcites. In b) Biplot from the PCA analysis.

Figure 8.18a shows that the PMR samples have  $v_4$  and  $v_1$  wavenumber values that allow them to be distinguished from geological samples:  $v_1$  values are consistent with

anthropogenic calcites, L values are more similar to geological samples, while  $\nu_4$  values consistently show a shift to lower wavenumbers and a broadening of the FWHM (a factor partially observed in the previously analysed samples). Based on the bubble diagram and the collected wavenumbers (Figure 8.18b), it can be seen that the sieved mortar samples (bulk mortar) tend to have values closer to geological calcite. It cannot be excluded that the micro-Raman analyses were performed on grains of geological calcite, which may be finely distributed in the sample. The PCA in Figure 8.18c confirms the ability to distinguish the origin of the calcite, as the two clusters (geogenic, anthropogenic) remain clearly separated. PC1 and PC2 describe 84.6% of the variance (58.5% and 26.1%, respectively). Therefore, PCA is performed using only the first 2 PCs (Figure 8.18 shows the PCA biplot). The L,  $\nu_1$ , and  $\nu_4$  wavenumbers are the most influential variables for discriminating calcite origin and strongly influence PC2, making it a valid method for distinguishing calcite origin.

#### 8.4.4 Pre-treatment and acid dissolution of selected mortar powders

The lump samples PMRC4L1, PMRC6L1, and PMRC7L1, and bulk samples PMRC4B1, PMRC5B1, PMRC6B1, PMRC7B1 are suitable for dating, since they exhibit negligible contamination. The reaction times, along with the masses of the graphitized samples, are listed in Table 8.21.

Lump samples were reacted for 10 seconds in acid; bulk samples PMRC4B1, PMRC5B1, PMRC6B1, PMRC7B1, two CO<sub>2</sub> fractions were extracted, one at 10 seconds and the other from 20 to 30 seconds (resulting in the following samples: PMRC4B1(1), PMRC4B1(2); PMRC5B1(1), PMRC5B1(2); PMRC6B1(1), PMRC6B1(2); PMRC7B1(1), PMRC7B1(2)) (Table 8.21). To avoid possible geological contamination, the extraction process was optimized to minimize CO<sub>2</sub> collection time and ensure sufficient gas for graphitization.

*Table 8.21 Mass, typology and reaction time chosen for the acid dissolution of Florentine historical mortars.*

ID samples	Type of sample	Mass (mg)	Reaction time (s)
PMRC4L1	Lime lump	6.10	0-10
PMRC4B1(1)	Bulk mortar	10.0	0-10
PMRC4B1(2)			20-30
PMRC5B1(1)	Bulk mortar	10.6	0-20
PMRC5B1(2)			20-30
PMRC6L1	Lime lump	3.14	0-10
PMRC6B1(1)	Bulk mortar	13.5	0-20
PMRC6B1(2)			20-30
PMRC7L1	Lime lump	4.13	0-10
PMRC7B1(1)	Bulk mortar	10.3	0-20
PMRC7B1(2)			20-30

#### 8.4.5 AMS measurements

Table 8.22 shows the results of the AMS measurements.

*Table 8.22 Measured radiocarbon concentrations and conventional radiocarbon ages of Medici Riccardi Palace mortars.*

ID sample	<sup>14</sup> C concentration (pMC)	T <sub>rc</sub> (yrs BP)	Calibrated age (68% probability)	Calibrated age (95% probability)
PMRC4L1	100.5 ± 0.8		1695-1725, 1810-1835, 1880-1910, 1950-...	1685-1730, 1805-1925, 1950-...
PMRC4B1(1)	99.4 ± 1.5	-20 ± 50		
PMRC4B1(2)	94.9 ± 1.4	420 ± 40	-	-
PMRC5B1(1)	95.2 ± 1.8	400 ± 155	1325-1340, 1395-1665, 1785-1795	1285-1700, 1720-1815, 1830-...
PMRC5B1(2)	92.6 ± 1.6	610 ± 140	-	-
PMRC6L1	100.0 ± 1.7		1680-1735, 1755-1760, 1800-1930, 1950-...	1655-1955
PMRC6B1(1)	98.3 ± 2.0	60 ± 150		
PMRC6B1(2)	96.1 ± 1.1	60 ± 105	-	-
PMRC7L1	96.7 ± 1.6		1515-1590, 1620-1680, 1740-1800, 1940-...	1470-1700, 1720-1815, 1835-1880, 1915-...
PMRC7B1(1)	96.9 ± 0.8	255 ± 60		
PMRC7B1(2)	95.7 ± 1.0	250 ± 70	-	-



With the exception of the PMRC5 sample, we have at least two concentrations of radiocarbon that can be evaluated as conceptions corresponding to the CO<sub>2</sub> of the binder. When samples from the same fragment have matching radiocarbon values, a weighted average is used to obtain an accurate value and reduce the margin of error. Table 8.22 shows the results of the weighted average of the four conventional radiocarbon ages of the sample that have matching radiocarbon values.

The Palazzo Medici Riccardi samples are consistent with the expected ages for the Palazzo Medici Riccardi construction phases.

From the measured conventional radiocarbon age, the calibrated age for PMRC4L1+ PMRC4B1(1), PMRC5B1, PMRC6L1+ PMRC6B1(1), and PMRC7L1+ PMRC7B1(1) are obtained (Figure 8.19).

The <sup>14</sup>C concentrations of samples PMRC5 and PMRC7 are consistent and compatible with the Medici phase, while samples PMRC4 and PMRC6 are consistent with the Riccardi phase, as shown by the calibrated data. The calibrated age of samples PMRC6, from the innermost floor of the palazzo, is compatible and consistent with the dates of the written documentation, placing them chronologically in the second phase of construction. PMRC4 also dates from this phase, ruling out the possibility that pre-existing walls documented in the 1460 historical view were used (Figure 8.13b).

The results are satisfying, since:

- the measured samples do not show any geological contamination, which confirms the potential of complete procedures (OM-CL, ATR-FTIR and micro-Raman techniques and the pre-treatment procedure);
- the <sup>14</sup>C concentrations of the lump samples are consistent with the first fraction of the bulk, as observed for PMRC4L1, PMRC4B1(1), PMRC6L1, PMRC6B1(1), PMRC7L1, PMRC7B1(1). Weighted averages of pairs of conventional radiocarbon age values can be calculated to obtain a Calibrated age (Figure 8.18);

- the radiocarbon concentrations of the second fractions are older than the first fraction, indicating that the pre-treatment allowed for the removal of geological carbon. This is evident in PMRC4B1 (as the sample contains a carbonate aggregate) and to a lesser extent in PMRC5B1 and PMRC6B1.

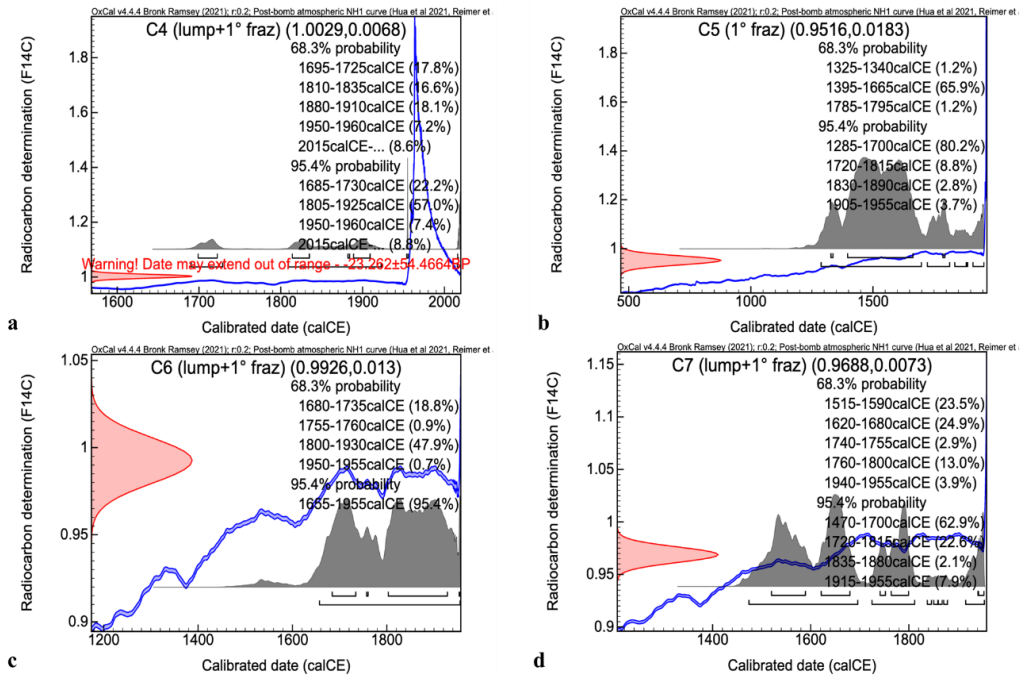


Figure 8.19 – Calibrated age for the PMR samples.

## 8.5 The S. Giovanni Baptistery

### 8.5.1 Sampling

During the recent restoration campaign of the Baptistery of San Giovanni in Florence, Italy, a comprehensive characterization of the natural and artificial stone materials, including the mortar, and an assessment of the state of preservation of the exterior surfaces were carried out (Calandra et al., 2022b). Mortar samples in the Baptistery of San Giovanni were taken from the attic, matroneum, and foundations. The Baptistery of S. Giovanni is one of the oldest and most important monuments of Florence. Located in front of the Cathedral of Santa Maria del Fiore (Figure 8.20a), it has an octagonal plan (Figure 8.20b) and is decorated with marble and bronze decorations, including Ghiberti's famous "Gates of Paradise" Although it is one of the most important buildings in the city, its exact date of construction remains uncertain. Different hypotheses assume eight centuries for its foundation.

Over time, numerous theories have emerged. Recent studies suggest a 5th century construction that took its present form in the 11th century and was completed around the 13th century. Since there is no definitive date for the Baptistery, this case study presents a situation where mortar dating can be a means of confirming one of the various dating hypotheses. Seventeen mortar core samples were collected from various depths corresponding to the different phases of construction (Figure 8.20c). Using an aspirator and the dry method, continuous coring was used to gather mortar samples (diameter of 3 cm) from the internal masonry. Table 12 lists the sample IDs, descriptions, sampling locations, and selected sample depths for characterization.

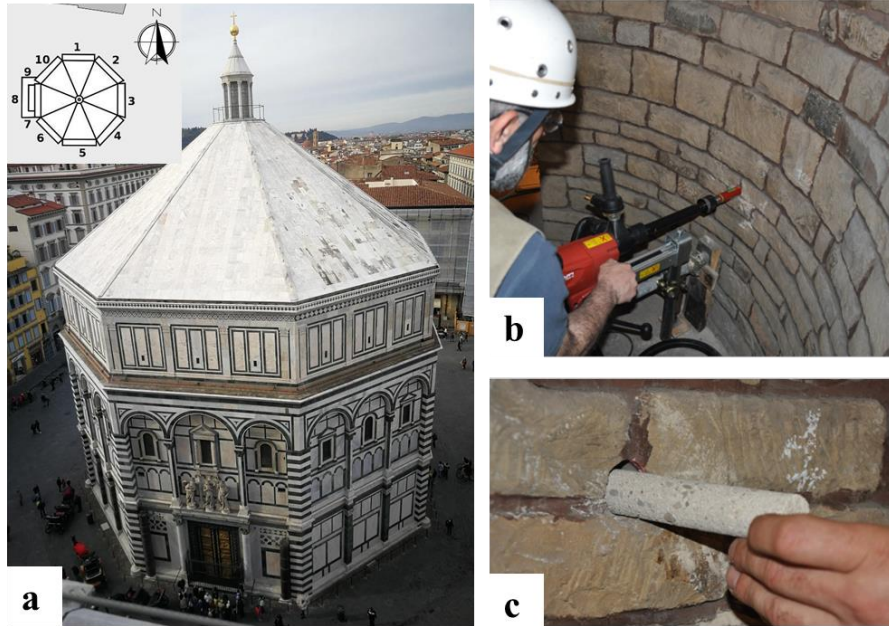


Figure 8.20 – Baptistery of San Giovanni. In (a) architectural plan with numbered labels for sampling side identification; b) mortar core sampling c) mortar sample extracted from the masonry.

Table 12 List of mortar samples selected for the characterization of the masonry of S. Giovanni Baptistery from core samples.

ID core sample	Sampling point	Total Depth of Core Length (m)	Selected depth	ID sample
S1	Mortar core sample of attic, side 10	0.15	10–15 cm	BG1(10–15)cm
S2	Mortar core sample of attic, side 10	0.15	9–14 cm	BG2(9–14)cm
S3	Mortar core sample of attic, side 4–5	0.30	9–25 cm	BG3(9–25)cm
			25–30 cm	BG3(25–30)cm
S4	Mortar core sample of attic, side 4	0.35	4–20 cm	BG4(4–20)cm
			20–35 cm	BG4(20–35)cm
S5	Mortar core sample of matroneum, side 1	0.45	7–12 cm	BG5(7–12)cm
			12–26 cm	BG5(12–26)cm
			26–38 cm	BG5(26–38)cm

S6	Mortar core sample of foundations, side 9–10	0.35	0–10 cm	BG6(0–10)cm
			10–32 cm	BG6(10–32)cm
S7	Mortar core sample of foundations, side 9–10	0.35	0–11 cm	BG7(0–11)cm
			11–32 cm	BG7(11–32)cm
S8	Mortar core sample of foundations, side 8	0.40	0–12 cm	BG8(0–12)cm
			12–38 cm	BG8(12–38)cm
S9	Mortar core sample of foundations, side 9	0.40	0–11 cm	BG9(0–11)cm
			11–21 cm	BG9(11–21)cm
			21–38 cm	BG9(21–38)cm
S10	Mortar core sample of foundations, side 9–10	0.40	0–15 cm	BG10(0–15)cm
			15–38 cm	BG10(15–38)cm
S11	Mortar core sample of foundations, side 9	0.20	0–5 cm	BG11(0–5)cm
S12	Mortar core sample of foundations, central part	0.15	0–4 cm	BG12(0–4)cm
S13	Mortar core sample of foundations, central part	0.15	0–5 cm	BG13(0–5)cm
S14	Mortar core sample of foundations, central part	0.15	0–4 cm	BG14(0–4)cm
S15	Mortar core sample of foundations, central part	0.15	0–2 cm	BG15(0–2)cm
S16	Mortar core sample of foundations, side 7	0.15	4–12 cm	BG16(4–12)cm
S17	Mortar core sample of foundations, side 6	0.15	0–2 cm	BG17(0–2)cm

### 8.5.2 Characterization of mortars to select the most suitable samples for in radiocarbon dating

The analysed mortar samples from the Baptistery of San Giovanni belong to the attic: BG1, BG2, BG3, and BG4; the matroneum: BG5, and different foundation walls, from

BG6 to BG17. The main mineralogical and petrographical characteristics of the samples studied are given in Table 4, Appendix 2. In Table 16, the mineralogical analyses conducted with XRPD are reported. Calcite, quartz, feldspars are the main identified minerals. Mica, chlorite, gypsum, portlandite and vaterite are present in minor quantities. Vaterite has typically been found in Florentine mortars, associated with the production of natural hydraulic binders obtained from the calcination of marly limestone. Amorphous silica (as indicated by ATR-FTIR analyses, reported below) may slow down the transformation of calcite, resulting in a phase within the mortar that is typically not stable under temperature and pressure conditions. The presence of portlandite ( $\text{Ca}(\text{OH})_2$ ) was noted in the deepest sample of BG4, linked to incomplete carbonation of the binder. Gypsum was recorded in BG13, located in the basement, likely caused by sulfation phenomena of the binder.

*Table 16 Mineralogical composition (semiquantitative data) of BG mortar samples.*

Mortar samples	Quartz	Calcite	Plagioclase	K feldspar	Other
BG1(10–15)cm	+++	+	+	-	Mica (*), chlorite (*)
BG2(9–14)cm	+++	++	+	+	Mica (+), chlorite (*)
BG3(9–25)cm	+++	+	+	+	Mica (*), chlorite (*)
BG3(25–30)cm	+++	+	+	+	Mica (*), chlorite (*)
BG4(4–20)cm	+++	+	+	-	Mica (*), chlorite (*)
BG4(20–35)cm	+++	++	++	*	Mica (*), chlorite (*), portlandite (*)
BG5(7–12)cm	+++	++	+	+	Mica (+), chlorite (*)
BG5(12–26)cm	+++	++	+	+	Mica (*), chlorite (*)
BG5(26–38)cm	+++	++	++	+	Mica (*), chlorite (*)
BG6(0–10)cm	++	+++	+	-	Mica (*)
BG6(10–32)cm	+++	++	*	-	Mica (*)
BG7(0–11)cm	+++	++	*	*	Mica (*), chlorite (*), vaterite (*)
BG7(11–32)cm	+++	+	+	-	Mica (*), chlorite (*), gypsum (*)
BG8(0–12)cm	+++	++	++	+	Mica (+), chlorite (*)
BG8(12–38)cm	+++	+	+	*	Mica (*), chlorite (*)
BG9(0–11)cm	+++	+	*	-	Mica (*)
BG9(11–21)cm	+++	+	+	+	Mica (*), chlorite (*)
BG9(21–38)cm	+++	++	+	-	Mica (*), chlorite (*)
BG10(0–15)cm	+++	++	*	-	Mica (*)
	+++	++	*	*	Mica (*)

BG10(15–38)cm					
BG11(0–5)cm	+++	++	+	+	Mica (*)
BG12(0–4)cm	+++	++	+	+	Mica (*), vaterite (+)
BG13(0–5)cm	+++	+	+	-	Mica (*), chlorite (*), gypsum (*), vaterite (+)
BG14(0–4)cm	+++	++	+	*	Mica (*), chlorite (*)
BG15(0–2)cm	+++	++	+	*	Mica (*), chlorite (*)
BG16(4–12)cm	+++	+	*	-	Mica (*)
BG17(0–2)cm	+++	+	+	+	Mica (*), chlorite (*)

+++: very abundant; ++: abundant; +: present; \*: traces; -: below detection limit. Calcite and vaterite ( $\text{CaCO}_3$ ), quartz ( $\text{SiO}_2$ ), plagioclase ( $\text{NaAlSi}_3\text{O}_8$ - $\text{CaAl}_2\text{Si}_2\text{O}_8$ , albite-anorthite series), k feldspar ( $\text{KAlSi}_3\text{O}_8$ ), mica (e. g. muscovite  $\text{KAl}_2(\text{Si}_3\text{Al})\text{O}_{10}(\text{OH},\text{F})_2$ ), chlorite ( $\text{MgFeAl}_8(\text{SiAl})_8\text{O}_{20}(\text{OH})_{16}$ ), gypsum ( $\text{CaSO}_4 \cdot 2 \text{H}_2\text{O}$ ), portlandite ( $\text{Ca}(\text{OH})_2$ )

Despite all the core samples being obtained from quite similar raw materials, various technological characteristics were examined: B/A ratio, mean grain size, distribution of aggregates, and porosity.

Petrographic observation of the Baptistery mortar samples mainly reveals a binder with heterogeneous structure and a micritic/microsparitic texture, along with the presence of lumps, both as residues of poorly mixed binder and as residues of unburned limestone fragments (Figure 8.21a). The aggregate is, on average, abundant, composed of quartz, feldspars, micas, calcite, and fragments of carbonate rocks. An exception is represented by sample BG12, from the basement, collected from the mosaic masonry, composed of hydraulic lime with crushed ceramics (Figure 8.21b). Hydraulic lime with crushed ceramics was observed due to the development of reaction rims, a heterogeneous structure, a micritic/microsparitic texture, and the absence of lumps. In general, the binder is recrystallized in the attic samples (Figure 8.21c), in the matroneum (except for intermediate sample BG5), and in the foundations (except for interior samples BG7 and BG8). High amounts of carbonate rock (Figure 8.21d) in the aggregates of the samples from the matroneum and the foundations (in BG6, S10, BG11, BG12 and BG14) are observed under OM.

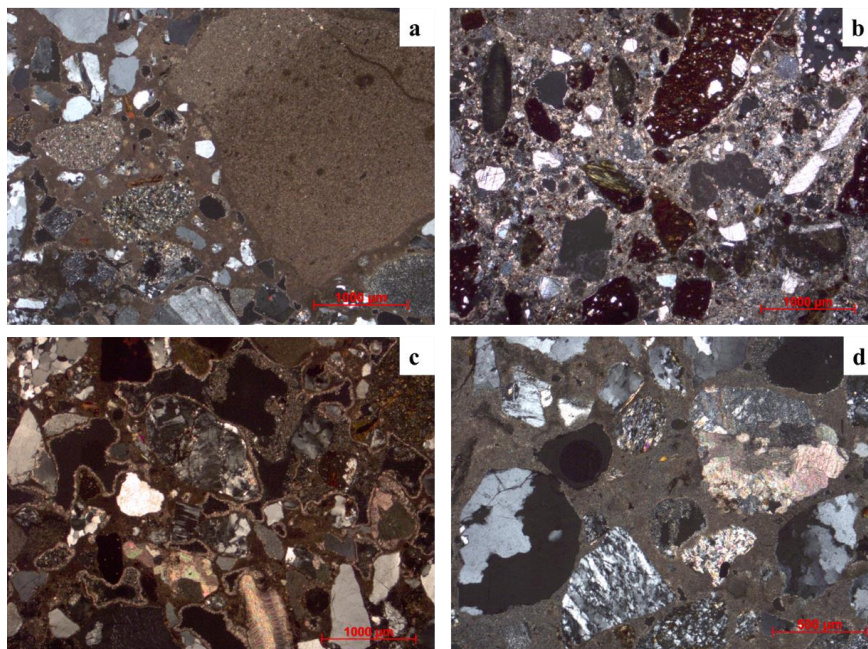


*Figure 8.21 – Microphotographs of Baptistery of S. Giovanni mortar samples.*

Due to the abundance of carbonate aggregates and unburned lumps, as well as the limited presence of binder and recrystallization phenomena, the samples are not ideally suited for dating.

In the samples that do not show recrystallization, such as the innermost samples of BG7 and BG8, taken from foundations is not suitable for dating. Foundation samples were excluded because the binder may have been contaminated by groundwater (e.g., flooding in 1966). In fact, a heterogeneous binder is observed in the petrographic analysis.

Sample BG5, although consisting of carbonate aggregate and lumps of unburned residue, was analysed further because it was unique with a homogeneous structure binder.

The BG5(12–26)cm mortar exhibits a light beige colour and a relatively homogeneous binder, with several visible lumps and predominantly fine and few coarse subrounded aggregate. The sample shows complete carbonation by the phenolphthalein test. Microscopically, the mortar consists of a weakly hydraulic lime binder with a micritic



texture. Numerous lumps, predominantly unburned remnants, and rarely unmixed binder are present (Figure 8.22a). The aggregate is subangular-subrounded, uniformly distributed and fine-grained. It is seriate, ranging from 100 to 600  $\mu\text{m}$ . Quartz (mono- and poly-crystalline), feldspars, mica, spathic calcite, fragments of carbonate and sandstone rocks are recognisable (Figure 8.22b). The B/A ratio is 1/2-1/3 and the macroporosity is medium, which is due to irregularly shaped and subspherical pores. Analysis of OM-CL shows that the thin section of BG5(12-26)cm has intense orange lumps and a texture with heterogeneous coloration (Figure 8.22c,d).

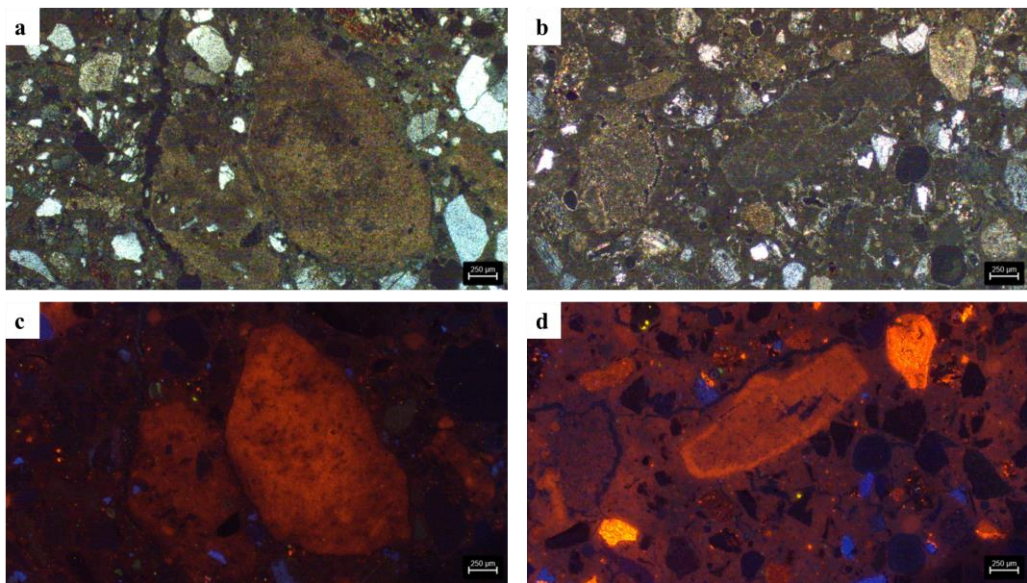


Figure 8.22 – OM and OM-CL analysis of BG5(12-26)cm, combined microphotograph of: a,c) unburned lump; b,d) textural binder and carbonate and silicate aggregates.

ATR-FTIR analysis of the lump taken from BG5(12–26)cm shows an intense band at 1100  $\text{cm}^{-1}$  attributed to amorphous silicates (reported in Figure 1, Appendix 2), since no traces of quartz are observed in the XRPD.

TGA was performed on representative samples. The presence of hydraulic components is detected by the weight loss in the temperature range 200–600  $^{\circ}\text{C}$  with values ranging from 3.82% to 8.11%. The percentage  $\text{CO}_2$  loss in the temperature range of 600–900  $^{\circ}\text{C}$

varies between 18.8% and 26.5%, indicating a material with hydraulic behaviour. The TGA results show that the samples from the attic, the matroneum and the foundations of the Baptistery fall into the typical group of hydraulic mortars and are characterised by relatively homogeneous hydraulics. The TGA result confirms the hydraulic behaviour attributed to the burning of the Alberese limestone, as suggested by the presence of underburned lump of the Alberese limestone in the petrographic observations (Figure 8.23). The comparison of data of the TGA of Florentine mortar samples are in Figure 2, in Appendix 2.

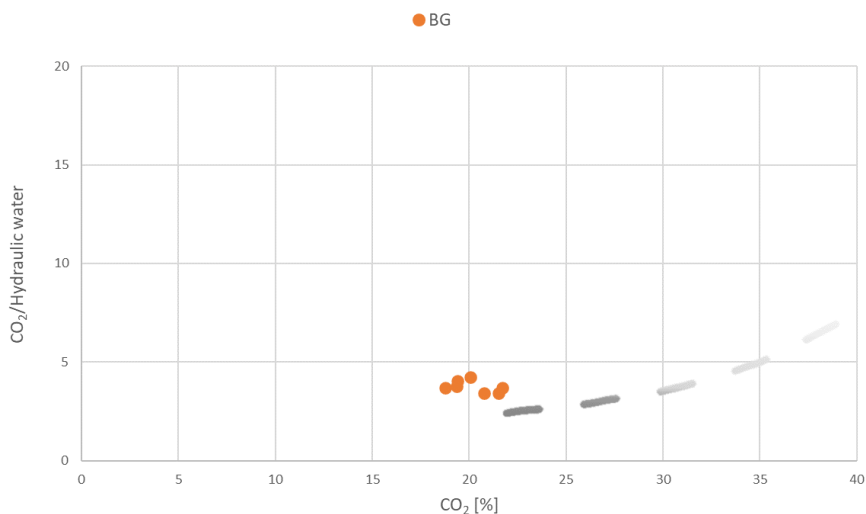


Figure 8.23 – TGA results of BG samples. Diagram of CO<sub>2</sub> vs CO<sub>2</sub>/hydraulic water with the theoretical curve of binders obtained burning Alberese limestone is reported (modified from (Lezzerini et al., 2017)).

### 8.5.3 Characterization of calcite mortar powders

Samples from the Baptistery of S. Giovanni were excluded due to abundant carbonate aggregate and recrystallization of binder and mainly presence of unburned lumps. A lump was selected from the sample BG5(12-26)cm, indicated as BG5L1. The lump sample was sieved and characterized using XRPD, OM-CL, ATR-FTIR. The analysis results are reported in Table 8.23.

From the ATR-FTIR and OM-CL analysis of the selected lump, it appears that the calcite in the lumps could originate from either geogenic or anthropogenic sources, as the sample falls between the two trends observed in the graph. The observed colour in CL may corroborate this observation, particularly due to the presence of grains exhibiting a bright orange hue. Consequently, samples from the Baptistery of S. Giovanni were excluded from radiocarbon dating.

Table 8.23 Summary of XRPD, ATR-FTIR, and OM-CL analyses on the lump from BG sample.

ID sample	XRPD	ATR-FTIR	OM-CL
BG5L1	Cal (+++) qz (*)		

+++ : very abundant; ++ : abundant; + : present; \* : traces; - : below detection limit. Cal: calcite; qz: quartz.

## 8.6 Final remarks

A weak hydraulic binder of burned Alberese limestone, a micritic limestone with minor clay impurities, is observed in most of the samples studied. This is often indicated by residues in thin sections of underburned rock fragments. In general, the presence of multiple types of lumps is a complication for radiocarbon dating because it is necessary to classify the lumps and accurately select the lime lump to avoid geogenic carbonate contamination. This important information is obtained by petrographic analysis of the thin section, but this sample cannot be used for dating. For this reason, it is essential to perform characterization using non-destructive techniques on the selected carbonate powder.

The binder lumps derived from Alberese are composed of calcite and amorphous silicate, as shown at ATR-FTIR. Their presence must be taken into account, since part of the powder mass can be attributed to the contribution of the amorphous silicates present.

The procedure used (gentle crushing to select the binder and extraction of the lumps, then sieving + characterization of the powdered sample (with OM-CL, ATR-FTIR and micro-Raman + collection of CO<sub>2</sub> from the first seconds of the reaction) can be considered a good strategy to isolate anthropogenic calcite and remove contaminants from natural hydraulic mortars.

The results obtained in dating mortar samples from historic buildings in Florence are satisfactory, considering that the sample was not quite ideal, as the binder was not entirely aerial. The application of the procedure to many samples allowed us to see the limitations and potential of this methodology.

## 9 Feasibility study of bedding mortar dating in Pompeii

### 9.1 Literature background

To assess the feasibility of  $^{14}\text{C}$  dating of Pompeian pozzolanic mortars, an in-depth study was conducted to understand the raw materials and ancient technologies used in mortar preparation. In the literature, many studies discuss the materials commonly used in ancient mortars in the Roman Age, namely pozzolanic mortars (Izzo et al., 2018; Rispoli et al., 2019), while fewer provide specific information on Pompeian buildings (Miriello et al., 2010; Joosten, 1999; Morra et al., 2013; Miriello et al., 2018; De Luca et al., 2015; Demauro, 2020; Dilaria et al., 2022). Research on pozzolanic mortars also focuses on evaluating their construction properties (resistance, durability, and performance as building materials), understanding the chemical reactions and their hydraulic properties, and on the characterization of aggregates in order to support the identification of constructive phases. Little attention is given to the analysis of binder, which is crucial for radiocarbon dating.

Radiocarbon measurements on pozzolanic mortars have been performed since the 1960s, yielding results of difficult interpretation. This was because their hydraulic behaviour and complexity were not considered, and preliminary characterization was not performed. In particular, in the literature there is only one application of  $^{14}\text{C}$  dating to pozzolanic mortar from Pompeii, carried out by one of the pioneering laboratories in this field of research (AMS  $^{14}\text{C}$  Dating Centre, Department of Physics and Astronomy, Aarhus University, Denmark). The results obtained are biased and illustrate the complexity of dating this type of mortar due to a number of critical aspects (Lindroos et al., 2011). The same difficulties were obtained in other studies on the dating of pozzolanic mortars (Nonni et al., 2018; Michalska et al., 2020), providing inconsistent results and application limitations of the dating method.

Now, numerous characterizations have been made on pozzolanic mortars, and it is known how complex they are (Sabbioni et al., 2001; Veiga et al., 2009; Rispoli et al., 2018). They are impermeable to atmospheric  $\text{CO}_2$ , contain less datable carbonate, and

are constantly chemically active, producing new carbonates (Seymour et al., 2023). All these processes indicate that radiocarbon dating of these materials may not be possible. Nothing has yet been published in the literature that relates the findings from characterization to the reasons why radiocarbon dates may not be reliable.

In this doctoral project, several analytical techniques were employed, such as optical microscopy, digital image analysis, SEM coupled with EDS analysis and XRPD, to characterize the mortar samples. Following the comprehensive characterization of the mortars, the selection of the most suitable samples for dating was performed. From each selected sample of mortars, powders from binder or lumps were analysed using the well-established approach proposed in this thesis: XRPD, OM-CL, ATR-FTIR, micro-Raman, SEM-EDS). In this chapter, we report the results and discussion from in-situ sampling to sample pre-treatment and  $^{14}\text{C}$  measurement using AMS.

## 9.2 The mortars of the public building in Pompeii

As part of a broader study of the chronology of the public monuments at the Forum of Pompeii, aimed at analysing the ancient restoration work on these buildings, it was possible to examine the bedding mortar. The study focuses on a systematic analysis of the Forum of Pompeii, in particular of the masonry of the original phase and of the subsequent phases until the eruption of 79 CE (PhD thesis by Giacomo Casa, Università di Bari). The analysis of the archival sources and the architectural and technological analysis of the buildings allows to identify the main developments of the Forum of Pompeii:

- Archaic age (6th century BCE): it was a place with a temple dedicated to Apollo.
- 4th-2nd century BCE: it became a commercial center with tabernae along the sides.
- 2nd century BCE (Samnite phase): significant renovations were carried out, including the pavement and construction of the Temple of Jupiter, the

Macellum, the Comitium and other buildings, including the reconstruction of the Temple of Apollo.

- Between the 1st century BCE and the 1st century CE (Augustan phase): new construction of the square and cultic buildings such as the Temple of Genius Augusti and the Eumachia.
- The earthquake of 62 CE destroyed parts of the buildings such as the Temple of Genius Augusti and the Eumachia, as well as the Temple of Apollo, which were restored with more or less extensive interventions.
- The eruption of 79 CE, the last phase of construction of the Forum and all of Pompeii.

The present form is the result of changes made by ancient restorations after the earthquake of 62-63 CE. In addition, there are modern restorations after the discovery of the site in 1748, which lasted until 1860 (under the command of the Bourbons), but also by more recent interventions (Demauro, 2020). The complexity of the site of Pompeii is also due to its territorial location. The eruptions of the Campanian Ignimbrite (39,000 years ago), as well as those of Pompeii in 79 CE, 472 CE, and 1631 CE, had a profound impact on the geological and geomorphological landscape, significantly affecting human activities.

The archaeologists determined the construction phases on the basis of the building techniques and the stone materials used. Sampling was carried out based on these considerations.

A total of 53 samples of bedding mortar were collected using a chisel and hammer, with the first few centimetres of surface mortar removed. The buildings and sampling locations of the collected mortars are shown in Figure 9.1a. Inconsistent and powdery white lumps were observed during sampling. The collected mortar fragments are very small (Figure 9.1d), and it was not always possible to take deeper samples. Table 9.1 lists the IDs of the samples, their location, the type of masonry, the depth of collection, and the constructive phase.

Table 9.1 List of bedding mortar samples taken from public buildings in Pompeii.

<b>ID sample</b>	<b>Building</b>	<b>Phase</b>	<b>Construction technique</b>	<b>Sampling depth</b>
C01A	Eumachia	after 62 CE	<i>opus vittatum</i>	4 cm
C01C	Eumachia	after 62 CE	<i>opus vittatum</i>	0-1 cm, surface layer
C01D	Eumachia	Augustan phase	<i>opus latericium</i>	0-2 cm, surface layer
C01E	Eumachia	after 62 CE*	<i>opus incertum</i> with mixed rocks	2 cm
C02A	Eumachia	Augustan phase	<i>opus incertum</i> with carbonate rocks	4 cm
C02C	Eumachia	Augustan phase	<i>opus incertum</i> with carbonate rocks	0-2 cm, surface layer
C03A	Eumachia	Augustan phase	<i>opus incertum</i> with carbonate rocks	4 cm, near the foundations
C03C	Eumachia	after 62 CE	<i>opus latericium</i>	2 cm
C04A	Eumachia	after 62 CE	<i>opus latericium</i>	2 cm
C04C	Eumachia	Modern phase	<i>opus incertum</i>	2 cm
C05	Eumachia	Augustan phase	<i>opus vittatum</i>	2 cm
C06A	T. Genius Augusti	after 62 CE	<i>opus latericium</i>	2-3 cm
C07A	T. Genius Augusti	after 62 CE	<i>opus latericium</i>	3-4 cm
C09	Sanct. of the P. Lares	Augustan phase	<i>opus latericium</i>	0-2 cm, surface layer
C10A	Sanct. of the P. Lares	Augustan phase*	<i>opus latericium</i>	1-3 cm, surface layer
C10C	Sanct. of the P. Lares	Augustan phase	<i>opus latericium</i>	5 cm
C11A	Sanct. of the P. Lares	Augustan phase	<i>opus reticulatum</i>	0-2 cm, surface layer



---

C11C	Sanct. of the P. Lares	Augustan phase	<i>opus latericium</i>	0-3 cm, surface layer
C11D	Sanct. of the P. Lares	Augustan phase	<i>opus reticulatum</i>	0-2 cm, surface layer
C12A	Macellum	Augustan phase	<i>opus latericium</i>	3-4 cm
C12C	Macellum	Augustan phase	<i>opus latericium</i>	0-2 cm, surface layer
C13A	Macellum	after 62 CE	<i>opus reticulatum</i>	0-2 cm, surface layer
C13B	Macellum	after 62 CE*	<i>opus incertum</i> with lava rocks	3-4 cm
C13C	Macellum	after 62 CE	<i>opus incertum</i> with carbonate rocks	7 cm
C13D	Macellum	after 62 CE	<i>opus latericium</i>	0-2 cm, surface layer
C14A	Macellum	after 62 CE*	<i>opus incertum</i> with lava rocks	3 cm
C14B	Macellum	after 62 CE*	<i>opus incertum</i> with lava rocks	3 cm
C14C	Macellum	after 62 CE*	<i>opus incertum</i> with lava rocks	3 cm
C14F	Macellum	after 62 CE	<i>opus incertum</i> with lava rocks	0-1 cm, surface layer
C15A	Temple of Jupiter	2nd cent. BCE	<i>opus incertum</i> with lava rocks	0-2 cm, surface layer
C15C	Temple of Jupiter	2nd cent. BCE	<i>opus incertum</i> with lava rocks	0-2 cm, surface layer
C16A	Arch of Germanicus	2nd cent. BCE*	<i>opus latericium</i>	0-1 cm, surface layer
C16B	Arch of Germanicus	Augustan phase – after 62 CE	<i>opus latericium</i>	0-1 cm, surface layer
C17A	Temple of Apollo	after 62 CE	<i>opus incertum</i> with mixed rocks	3-4 cm

---

C18A	Temple of Apollo	Augustan phase	<i>opus incertum</i> with carbonate rocks	2-3 cm, near the foundations
C18B	Temple of Apollo	2nd cent. BCE*	<i>opus incertum</i>	0-2 cm, surface layer
C19C	Temple of Apollo	2nd cent. BCE*	<i>opus incertum</i> with mixed rocks	3-4 cm
C20	Basilica	2nd cent. BCE	<i>opus incertum</i> with lava rocks	0-2 cm, surface layer
C21A	Duoviri Building	after 62 CE*	<i>opus latericium</i>	0-2 cm, surface layer
C21B	Duoviri Building	Augustan phase	<i>opus incertum</i> with lava rocks	4-5 cm
C22A	Tabularium	after 62 CE	<i>opus latericium</i>	2-3 cm
C23A	Curia	after 62 CE	<i>opus latericium</i>	2-3 cm
C23B	Curia	after 62 CE	<i>opus incertum</i>	2-3 cm
C25A	T. Fortuna Augusta	after 62 CE	<i>opus vittatum</i>	3-4 cm
C25B**	T. Fortuna Augusta	after 62 CE*	<i>opus incertum</i>	1-2 cm, surface layer
C25C	T. Fortuna Augusta	Augustan phase	<i>opus incertum</i>	2-3 cm
C25E	T. Fortuna Augusta	Augustan phase	<i>opus latericium</i>	2-3 cm
C26A	Odeion	2nd cent. BCE – Augustan phase	<i>opus latericium</i>	8-9 cm
C27A	Theater	after 62 CE	<i>opus latericium</i>	1-2 cm, surface layer
C27B	Theater	after 62 CE	<i>opus latericium</i>	1-2 cm, surface layer
C28A	Triangular Forum	after 62 CE	<i>opus incertum</i>	1-2 cm, surface layer

C29A	Temple of Isis	after 62 CE	<i>opus incertum</i> with mixed rocks	1-2 cm, surface layer
------	----------------	-------------	---------------------------------------	-----------------------

\* Doubtful construction phase. T. Genius Augusti: Temple of Genius Augusti; Sanctuary of the Public Lares: Sanct. of the P. Lares; T. Fortuna Augusta: Temple of Fortuna Augusta.

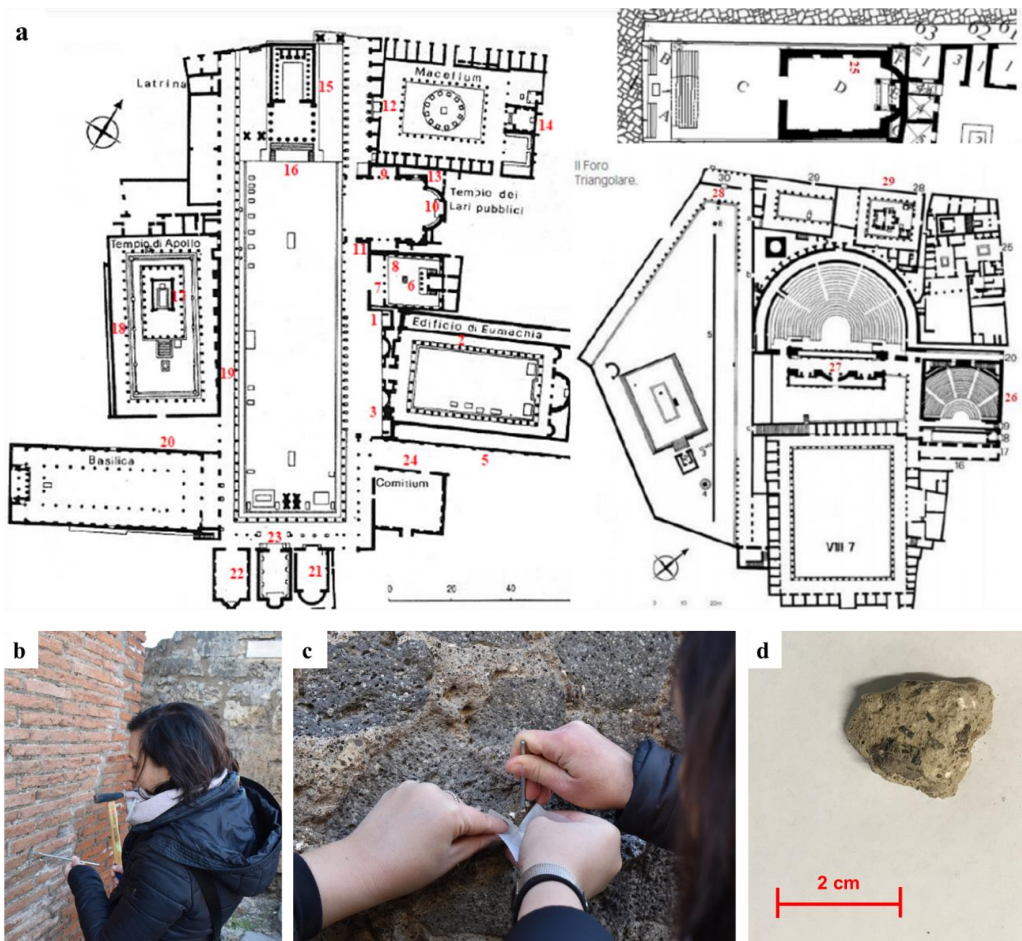


Figure 9.1 – Pompeii: a) plan with sampling points; b, c) sampling of mortar fragments and lumps; and d) an example of a macro sample taken.

### 9.3 Characterization of mortars for sample selection in radiocarbon dating

All samples were subjected to mineralogical, petrographic and chemical characterization (OM, XRPD, TGA, SEM-EDS). The main mineralogical and petrographic

characteristics of the samples studied are given in Table 5, Appendix 2. In this section, an overview of the samples is given, with emphasis on describing those most suitable for dating.

Table 9.2 presents semi-quantitative analyses of the mineral phases in the mortar samples. Mineralogical analysis identified phases related to the composition of the mortar: calcite in the binder fraction and, in some samples, CASH and CAS in the aggregate fraction due to the presence of carbonate rock fragments (micritic limestone, marly limestone, and individual calcite crystals). K feldspar, plagioclase, quartz, clinopyroxene, leucite, analcime, and mica were associated with the aggregate composition, which is fully compatible with Vesuvius pyroclastic deposits. Gypsum was detected only in some sections, probably originating from newly formed material due to weathering.

*Table 9.2 Mineralogical composition (semiquantitative data) of Pompeii mortar samples.*

ID sample	Cal	Qz	Plg	K feld	Cpx	Feldspathoid		CASH, CAS
						Lct	Anl	
1A	+++	-	+	+	+	-	+	-
1C	++	-	+	+++	+	+	+	-
1D	++	++	++	+++	+	-	-	-
1E	+++	-	++	+	+	+	+	-
2A	+++	-	+	-	+	+	+	-
2C	+++	-	++	-	+	+	++	+
3A	+++	-	+	++	+	+	+	*
3C	+++	-	+	+	+	-	+	*
4A	++	-	-	++	++	+	+	-
4C	+++	-	+	+	+	-	+	-
5	+++	-	++	+	+	-	+	-
6A	++	-	+++	-	+	-	+	+
7A	+++	-	+	++	+	-	+	-
9	+++	-	++	-	-	-	+	-
10A	+++	+	+	+	+	-	*	-
10C	+++	+	+	+	+	-	+	*

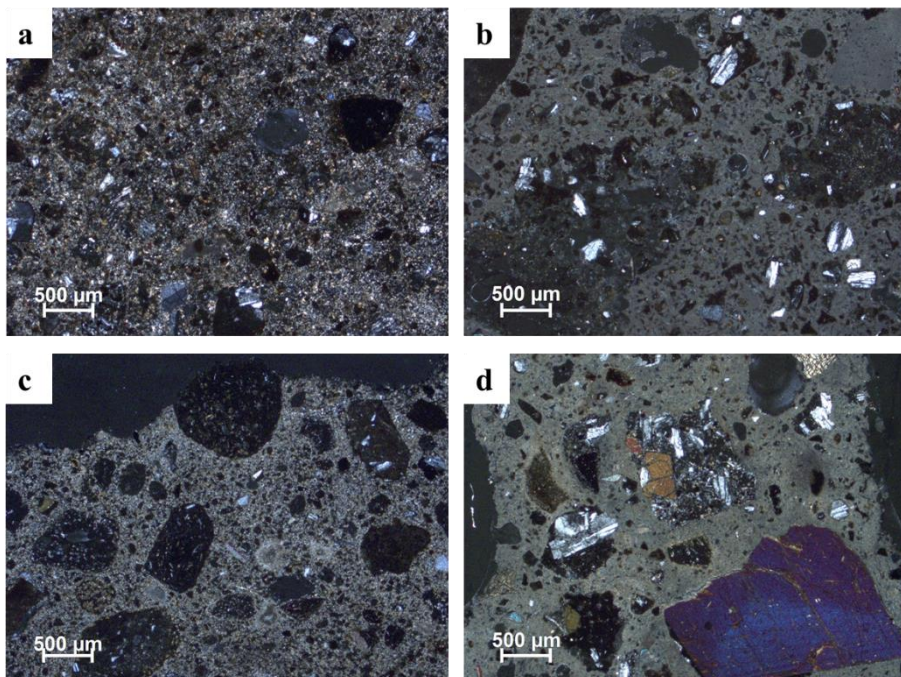
---

11A	+++	-	++	++	++	-	+	-
11C	+++	-	++	++	+	-	+	-
11D	+++	-	+	+	+	-	+	*
12A	+++	-	+	+	+	-	+	-
12C	+++	+	-	-	-	-	-	+
13A	+++	-	+	+	+	-	+	-
13B	+++	-	+	-	-	-	+	-
13C	+++	-	+	+	+	-	+	-
13D	+++	-	+	++	++	-	+	-
14A	+++	-	+	+	+	-	+	-
14C	+++	-	++	++	+	-	+	-
14D	+++	-	+	+	+	-	+	-
14F	++	-	+++	+	+	-	+	-
15A	++	-	++	++	+	-	++	-
15C	+++	-	+	+	+	-	+	-
16A	+++	-	++	++	+	-	+	-
16B	+++	-	-	+	*	-	-	-
17A	+++	-	+	-	+	-	*	-
18A	+++	-	+	+	+	-	+	-
18B	+	-	++	+	+	-	+	+
19A	++	-	+++	-	+	-	+	+
19C	+	-	-	+	+	-	+	+++
20	+++	-	++	++	+	-	+	-
21A	+++	-	+	+	-	-	+	+
21B	++	-	-	+	+	-	*	-
22A	++	-	++	++	+	-	+	+++
23A	+++	-	++	-	+	-	+	-
23B	+++	-	+	-	+	+	-	-
24A	+++	-	++	+	+	-	*	-
25A	+++	-	+	+	+	+	-	-
25B	+++	+	-	*	-	-	-	-
25C	+++	+	+	+	+	-	*	-
25E	+++	-	-	+	+	*	-	-
26A	+++	+	+	-	+	-	*	-
27A	+++	-	-	+	+	*	-	-
27B	+++	-	+	+	+	-	+	-
28A	+++	+	-	+	+	*	+	-
29A	++	-	-	++	+++	*	-	-

---

+++: very abundant; ++: abundant; +: present; \*: traces; -: below detection limit. Cal: calcite ( $\text{CaCO}_3$ ), qz: quartz ( $\text{SiO}_2$ ), plg: plagioclase ( $\text{NaAlSi}_3\text{O}_8$ - $\text{CaAl}_2\text{Si}_2\text{O}_8$ , albite-anorthite series), K feld: K feldspar ( $\text{KAISi}_3\text{O}_8$ ), Cpx: clinopyroxene ( $\text{Ca}(\text{Mg,Fe})\text{Si}_2\text{O}_6$ ), lct: leucite ( $\text{KAISi}_2\text{O}_6$ ), anl: analcime ( $\text{NaAlSi}_2\text{O}_6 \cdot (\text{H}_2\text{O})$ ), CASH, CAS: amorphous phase, gy: gypsum ( $\text{CaSO}_4 \cdot 2 \text{H}_2\text{O}$ ), ms: mica, e.g. muscovite ( $\text{KAISi}_3\text{AlO}_{10}(\text{OH,F})_2$ )

Supported by OM analysis, samples were grouped by construction phases and petrographic features. The texture of the binder (Figure 9.2a,b), the B/A ratio, the shape of the aggregate (Figure 9.2c,d), and the grain size distribution (Figure 9.2e,f) are the main distinguishing features between the phases. Unburned limestone and lime lumps are present in most samples (Figure 9.3a,b); their presence indicates the use of traditional technologies and allows the identification of certain properties of the lime. The specimens are realized by hydraulic binder, obtained by aerial lime-based mortars blended with a pozzolanic additive that forms reaction rims with the binder (Figure 9.3c). The hydraulic behaviour is generated by pozzolanic additives, with the exception of sample 21a, which also contains fragments of cocchiopesto with reaction rims (Figure 9.3d).



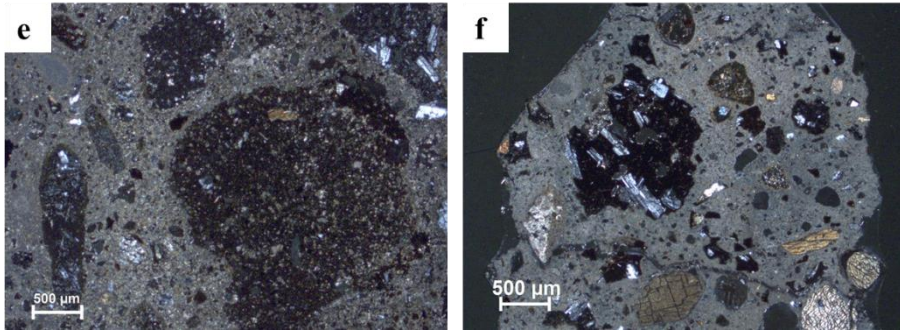


Figure 9.2 – Characteristics used for groupings: texture of the binder: a) microsparitic, b) micritic; aggregate shape: c) sub-rounded, d) sub-angular; grain size distribution: e) multiple size classes, f) bimodal. (under OM, xpl at different magnifications).

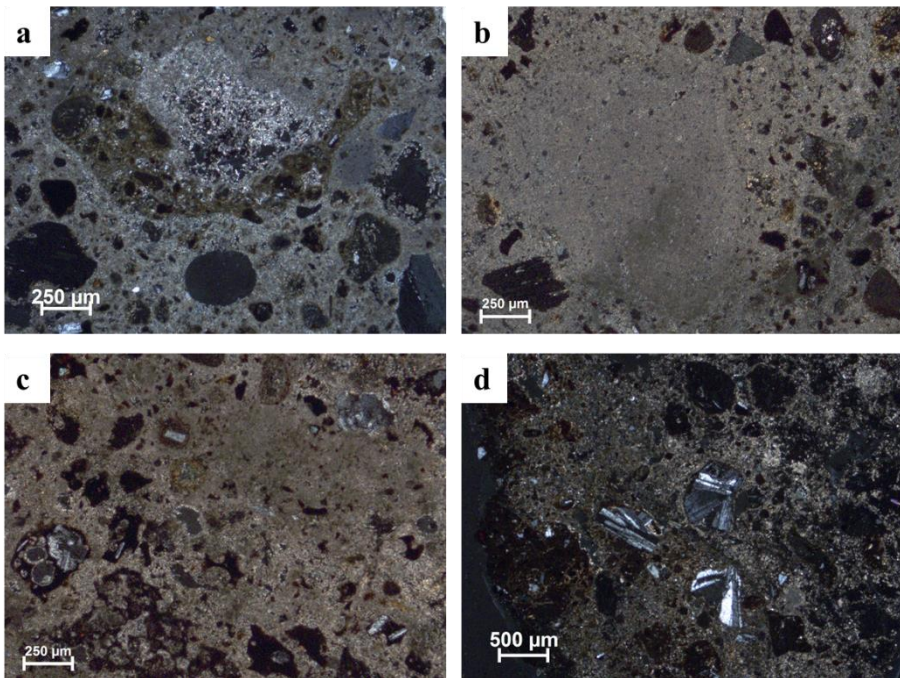


Figure 9.3 – Characteristics of lump and binder: a) heterogeneous area in binder and unburned lump; b) lime lump; c) reaction rims around pozzolans; d) reaction rims around pozzolans and cocchiopesto. (At OM, xpl at different magnifications).

The mortars from different buildings belonging to the same construction phase (either the Samnite period, the Augustan phase or the after 62 CE) exhibit some common characteristics:

- mortars dated to the late Samnite period (2nd century BCE) exhibit a micritic binder, with a variable amount of lumps (unmixed binder and underburned fragments), heterogeneous-shaped aggregates, rare pluri-millimetric clasts, and a binder to aggregate B/A ratio of 1/1-1/2.
- mortars dated to the Augustan period tend to have a micritic binder, with rare lumps, prevalently unmixed binder, sub-rounded and well-selected aggregate, and a unimodal grain size distribution with rare millimetric aggregates. Almost the totality of these samples has a B/A ratio of 1/2.
- mortars from after 62 CE walls typically have a micritic to microsparitic binder, with abundant lumps (prevalently underburned fragments), angular aggregate, and a seriated grain size distribution with widespread millimetric clasts (maximum size about 1 cm). These samples have a B/A ratio tending towards 1/3. All of these samples contain a coarser aggregate, with a greater textural variability and compositional, coupled with occasional reuse of mortar.

The mineralogical and petrographical analysis has allowed us to confirm that the samples are ancient and made of local raw materials. The samples are characterized by a hydraulic lime binder with pozzolan and predominantly magmatic aggregates. The aggregate composition is very complex due to the different volcanic products (lava rocks, pyroclastic products, crystals of magmatic origin such as clinopyroxenes, feldspars, leucites/analcimes). In a geologically and environmentally highly dynamic area, it is necessary to take into account the eruptive history of the Somma-Vesuvius and Campi Flegrei igneous complexes to assess the accessibility and supply of rock material in the deposits. However, it can be noted that the composition of magma progressively changes during eruption depending on environmental conditions and, after deposition, is subject to post-depositional geochemical processes that further alter its composition over time. Therefore, multiple analyses need to be performed to obtain robust and representative data (e.g., geochemical analyses, trace elements), which are beyond the scope of this PhD thesis.



Samples for  $^{14}\text{C}$  dating were selected considering the previously described results (e.g., samples with degraded binder, microsparitic texture, and recrystallized calcite were excluded, as were those with insufficient mass and samples taken too superficially) and construction phase (at least one for each phase).

From the Eumachia building, sample 2A was selected, showing characteristics consistent with the second grouping above (Augustan phase). Macroscopically, it appears light brown, with predominantly fine rock of varying colour (from white to black) and numerous millimetre-sized white lumps. Phenolphthalein test indicates complete carbonation.

Microscopically, it is a mortar with aerial lime binder with the addition of pozzolanic hydraulic material (Figure 9.4a), with a micritic texture and reaction rims. It is characterized by the presence of millimetric lumps attributed to firing remains with signs of residual crystallinity from the stone and remnants of unmixed binder (Figure 9.4b). The predominantly angular magmatic aggregate consists of clinopyroxenes, some with glass rims, scoriae, pumice, and lavas, along with occasional feldspars. Fine volcanic glass shards are present in the fine fraction, probably obtained from grinding pumice and scoriae for aggregate production. The grain size is unimodal, with a prevalence of fine particles of 70-250, up to 600  $\mu\text{m}$  and rare 800  $\mu\text{m}$ -1 mm. Porosity is low, with subspherically shaped pores. The binder is not recrystallized. The B/A ratio is approximately 1/2.

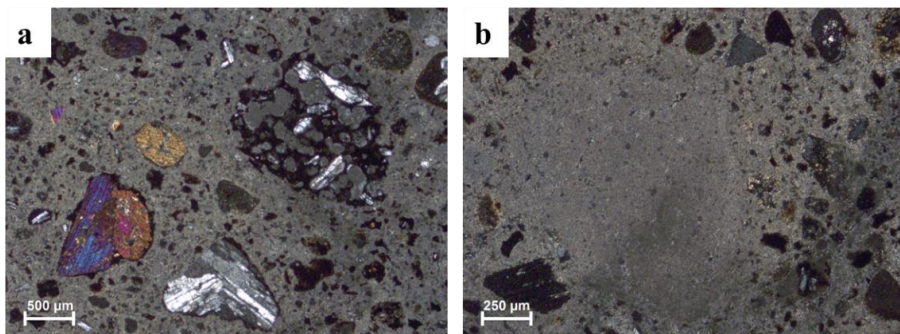


Figure 9.4 – Microphotographs of mortar samples: 2A. (image under OM, xpl, at different magnification).

Specimen 7A from the Temple of Genius Augusti, which has features consistent with the third grouping, was also selected and attributed to the restoration phase after 62 CE. Macroscopically, the sample is light pinkish-brown, with predominantly fine aggregate and some medium-sized aggregates in dark colour. Numerous white lumps of millimetric to centimetric size were observed, and the phenolphthalein test indicates that the binder was fully carbonated.

Microscopically, the sample consists of aerial lime binder with pozzolan (hydraulic binder) and exhibits a micritic to microsparitic structure (Figure 9.5a). It is characterized by the presence of millimetric lumps attributed to firing remains and remnants of unmixed binder (Figure 9.5b). The aggregate, mostly sub-rounded, consists of pumice, lavas, crystals (fine fraction). The grain size is bimodal, with a prevalence of particles ranging from <500 µm to multi-mm rock fragments. Porosity is medium to high, with fractures and some pores showing binder recrystallization. The B/A ratio is not identifiable. Along with the samples from the third group, it presents a sub-rounded aggregate, with no aggregate selection or grinding.

Sample 22A from the Tabularium is attributed to the after 62 CE restoration phase and has features consistent with the third grouping. The mortar fragment is hazel, with fine aggregates of different colours (from white to black) and millimetre-sized white lumps, with complete carbonation of binder (from phenolphthalein test).

The analysis of the thin section showed that the mortar was made with hydraulic binder: aerial lime binder with added pozzolan, showing a micritic texture (Figure 9.5c) and a heterogeneous appearance with numerous rims and lumps (unmixed binder and unburned limestone) (Figure 9.5d). The aggregate, mostly sub-angular and of magmatic nature, consists of lavas, scoriae, pumice, and fragments of clinopyroxene, plagioclase, and sanidine crystals (ranging from fine to coarse). Rare fictile fragments. Grain size is seriate, with particle sizes ranging from 200 µm to pluri-mm. Porosity is medium to high, characterized by subspherical shaped pores. The B/A ratio is approximately 1/2-1/3.

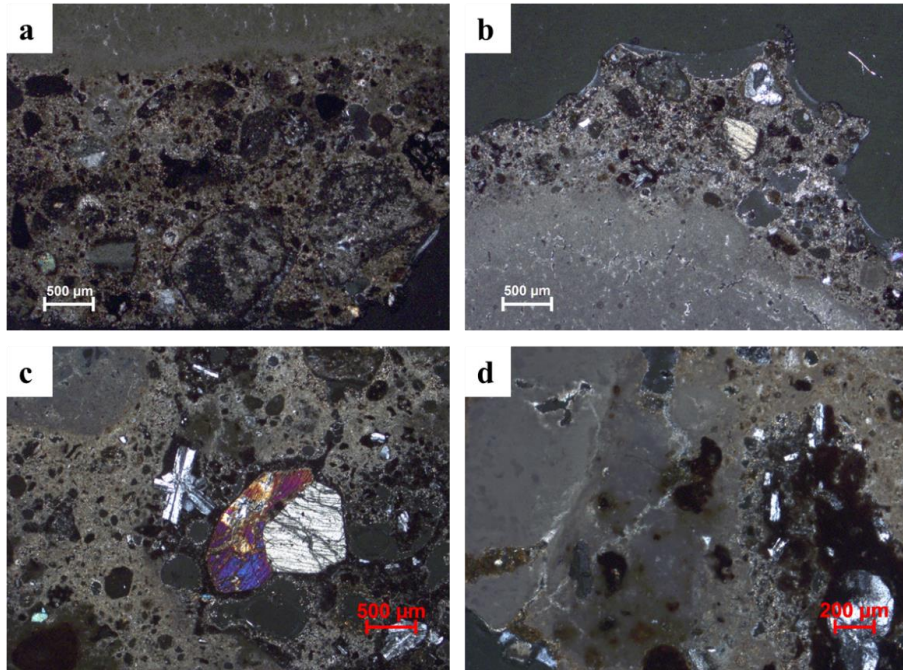


Figure 9.5 – Microphotographs of mortar samples: 7A: a, b) image under PLM, xpl, in different magnification; 22A: c, d) image under OM, xpl, in different magnification.

Two samples from different construction phases were selected from the Temple of Apollo, namely samples 17A and 19C, which date from the period after 62 CE and from the 2nd century BCE, respectively.

Sample 17A was macroscopically hazel with fine-grained aggregate and some millimetre-sized white lumps. The phenolphthalein test indicated carbonation. Microscopically, the mortar is made of hydraulic binder, aerial lime with pozzolan and has a micritic texture and some rims (Figure 9.6a). It contains some lumps of binder and reused mortar fragments (Figure 9.6b,c). This is the only sample in which reused mortar was found. Historical surveys indicate the presence of an adjacent lime production furnace near the masonry. The characteristics of this sample are not completely similar to those of the samples from the after 62 CE phase. The aggregate, which is mainly of magmatic nature and sub-angular, consists of scoriae, lava fragments, pumice, crystals of clinopyroxene, plagioclase and sanidine (in the fine fraction). Rare fictile fragments. Grain size is seriate, with prevalence of particles ranging from 100 µm to a size class of

pluri-mm rock fragments. Angular volcanic glass shards are present in the fine part, likely obtained from grinding pumice and scoriae for aggregate production. The porosity is low, characterized by round-shaped pores. The B/A ratio is approximately 1/2.

Sample 19C is a fragment of light hazel mortar, inconsistent, with fine aggregates of variable colour (from white to black). It is carbonated according to the phenolphthalein test. Microscopically, the mortar is made of hydraulic binder, aerial lime binder with pozzolana, exhibiting a heterogeneous appearance with a micritic texture, numerous rims, and zones of unmixed binder (Figure 9.6d,e). The aggregate, mainly sub-rounded and of magmatic nature, consists of scoriae (some centimetric), lavas, pumice, and fragments of clinopyroxene, plagioclase, and sanidine (in the fine part). The grain size is seriate, with a prevalence of particles ranging from 100  $\mu\text{m}$  to 600  $\mu\text{m}$ , rare pluri-mm rock fragments. Porosity is high, characterized by subspherical shaped pores and fractures. The B/A ratio is 1/2.

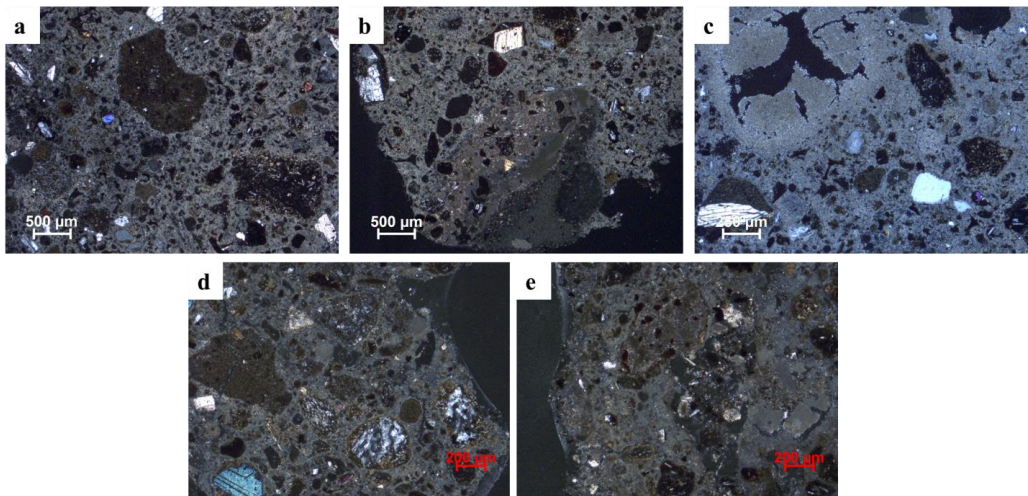


Figure 9.6 – Microphotographs of Temple of Apollo mortar samples: 17A: a, b, c) image under PLM, xpl, in different magnification; 19C: d, e) image under PLM, xpl, in different magnification.

The binder analysis performed by SEM-EDS and TGA confirms the hydraulic behaviour of the samples (Table 9.3, Figure 9.7a,b). The analysis was performed for both the lump

and the binder to evaluate the behaviour and composition and to assess the nature of the binder.

The hydraulic index (HI) calculated from SEM analysis is relatively low for lime lumps, ranging from 0.02 to 0.05 for samples 2A, 7A, 17A, 19C, and 22A. These values classify the lump as an aerial lime binder. This classification is confirmed by the thermogravimetric analysis of the lump from sample 2A (2A\_L), which falls into the aerial mortar group. The HI values calculated by SEM for the binder points and reaction rims show higher values between 0.11 and 0.34 (Figure 9.7a). These values, together with the TGA results that place the samples in the hydraulic mortar group, classify them as weakly to moderately hydraulic lime (Figure 9.7b). These HI values, together with the petrographic observations, confirm that hydraulicity is closely related to the presence of finely dispersed pozzolanic material. The Si, Al, and Ca(OH)<sub>2</sub> components react to form calcium and aluminium hydrated silicates (CASH gel), phases that confer durability to the mortars, as observed in the XRPD analysis.

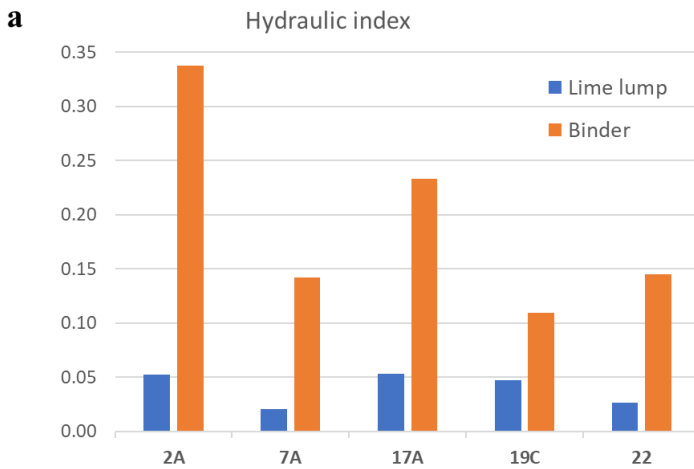
*Table 9.3 Semi-quantitative SEM-EDS micro-chemical analyses of binder and lumps (unburned and lime types).*

2A	MgO	Al <sub>2</sub> O <sub>3</sub>	SiO <sub>2</sub>	CaO	Fe <sub>2</sub> O <sub>3</sub>	Total
Area 1 - Unburned lime	1	-	-	99.1	-	100.0
Area 1 - Unburned lime	9.4	7.2	32.5	45.7	5.2	100.0
Area 2 - Unburned lime	-	1.6	1.8	96.6	-	100.0
Area 2 - Unburned lime	-	-	-	100	-	100.0
Area 2 - Unburned lime	0.7	2.6	1	95.7	-	100.0
Area 3 - Unburned lime	1.1	1	-	97.9	-	100.0
Area 3 - Unburned lime	1.7	-	-	98.3	-	100.0
Area 3 - Unburned lime	1.3	3.8	10.8	84.1	-	100.0
Area 3 - Mg-rich nodule in unburned lime	5.8	13.1	25.2	53.9	2.0	100.0
Lime lump	2.1	1.7	3.3	92.9	-	100.0

Lime lump	1.1	1.3	3.7	93.9	-	100.0
Binder	3.9	6.7	18.8	69.5	1.1	100.0
Binder	1.7	8.2	24.6	65.5	-	100.0
Binder	1.6	21.8	6.6	70.0	-	100.0
Binder	1.2	15.7	7.7	75.4	-	100.0
Binder	0.9	5	14.7	79.4	-	100.0
Binder	0.9	4.7	10.6	82.7	1.1	100.0
Binder	1.4	5.5	15.4	77.7	-	100.0
Binder	1.6	8	22.6	67.8	-	100.0
<b>7A</b>	<b>MgO</b>	<b>Al<sub>2</sub>O<sub>3</sub></b>	<b>SiO<sub>2</sub></b>	<b>CaO</b>	<b>Fe<sub>2</sub>O<sub>3</sub></b>	<b>Total</b>
Lime lump	1.1	0.6	1.8	96.5	-	100.0
Lime lump	1.8	1.7	5.2	91.3	-	100.0
Lime lump	1.8	0.6	1.4	96.2	-	100.0
Lime lump	1.3	-	0.7	96.9	1.1	100.0
Lime lump	0.6	1.1	2.8	95.5	-	100.0
Lime lump	1	-	-	99	-	100.0
Lime lump	1.1	-	0.6	98.3	-	100.0
Lime lump	1.1	-	0.5	98.4	-	100.0
Lime lump	0.9	-	0.8	98.3	-	100.0
Lime lump	1.7	-	1.1	97.2	-	100.0
Binder	1.9	1.5	3.7	92.9	-	100.0
Binder	4.1	6.4	13	74.1	2.4	100.0
Binder	1.7	2.5	9.8	86	-	100.0
Binder	1.4	2.1	7.5	89	-	100.0
Binder	1.2	2.6	8.8	87.4	-	100.0
<b>17A</b>	<b>MgO</b>	<b>Al<sub>2</sub>O<sub>3</sub></b>	<b>SiO<sub>2</sub></b>	<b>CaO</b>	<b>Fe<sub>2</sub>O<sub>3</sub></b>	<b>Total</b>
Reuse mortar	0.9	0.5	-	98.6	-	100.0

Reuse mortar	1.2	0.7	1.2	96.9	-	100.0
Reuse mortar	0.7	0.7	0.7	97.9	-	100.0
Reuse mortar	-	-	0.5	99.5	-	100.0
Reuse mortar	0.5	0.9	1.3	97.3	-	100.0
Reuse mortar	1.4	1.3	3.4	93.9	-	100.0
Reuse mortar	-	3.7	6.4	89.9	-	100.0
Mg-rich nodule	11.0	1.1	3.0	84.9	-	100.0
Mg-rich nodule	17.6	1.1	4.0	77.3	-	100.0
Mg-rich nodule	16.4	4.6	4.0	75.0	-	100.0
Lime lump	1.8	0.8	2.2	95.2	-	100.0
Lime lump	2.3	1.2	3.2	93.3	-	100.0
Lime lump	2.1	1.8	5.8	90.3	-	100.0
Binder	1.9	4.9	15.4	77.8	-	100.0
Binder	2.4	6.5	18.1	73	-	100.0
Binder	1.7	6.3	16.0	74.2	1.8	100.0
Binder	0.5	1.2	2	96.3	-	100.0
<b>19C</b>	<b>MgO</b>	<b>Al<sub>2</sub>O<sub>3</sub></b>	<b>SiO<sub>2</sub></b>	<b>CaO</b>	<b>Fe<sub>2</sub>O<sub>3</sub></b>	<b>Total</b>
Unburned lime	1.9	-	-	98.1	-	100.0
Unburned lime	1.5	-	-	98.5	-	100.0
Mg-rich nodule	15.3	9.2	32.9	41	1.6	100.0
Lime lump	2.9	1.3	4.1	91.7	-	100.0
Lime lump	2.1	1.5	2.2	94.2	-	100.0
Binder	4.2	4	8.3	83.5	-	100.0
Binder	2.1	2.3	6.7	88.9	-	100.0
Binder	4.7	2.4	9.4	83.5	-	100.0
Binder	4.2	2.6	3.7	89.5	-	100.0
Binder	5.8	2.3	7.3	84.6	-	100.0

22A	MgO	Al <sub>2</sub> O <sub>3</sub>	SiO <sub>2</sub>	CaO	Fe <sub>2</sub> O <sub>3</sub>	Total
Mg-rich nodule	31.7	23.7	41.5	1.7	1.4	100.0
Mg-rich nodule	29.7	24.8	42.6	1	1.9	100.0
Lime lump	3	-	-	97	-	100.0
Lime lump	3.1	-	-	96.9	-	100.0
Lime lump	3.4	0.4	0.7	95.5	-	100.0
Lime lump	2.5	2.2	1.0	94.3	-	100.0
Lime lump	4.5	1.1	0.9	93.5	-	100.0
Lime lump	4.3	1.8	2.3	91.6	-	100.0
Lime lump	5.5	2.8	4.5	87.2	-	100.0
Binder	1.7	3.5	9.5	85.3	-	100.0
Binder	1.5	2	10.5	86	-	100.0
Binder	1.2	3.2	9.2	86.4	-	100.0





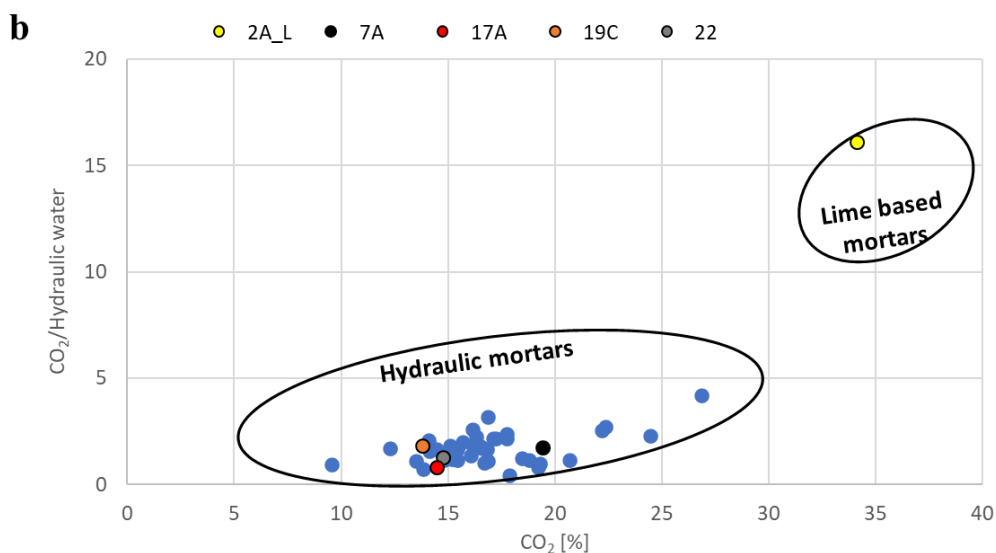


Figure 9.7 – Comparison between hydraulic behaviour analysis: in a) HI values for binder and lime lumps of mortar samples; in b) TGA results: diagram of CO<sub>2</sub> vs CO<sub>2</sub>/hydraulic of mortar samples and a lump sample.

In addition, the analysis of the lumps of unburned residue allowed us to hypothesise the origin of the rock used for lime production. Based on the SEM-EDS analysis, the use of a limestone with Mg impurities and a heterogeneous composition was demonstrated. As evidence, the lumps of pure CaCO<sub>3</sub> and lumps with 20% Mg were analysed (Figure 9.8a, Table 9.3). This is due to the poor selection of the limestone, which consists of Mg-rich and completely carbonate layers, typical of the Monti Lattari. In the same unburned lump are found (Figure 9.8a): areas of higher Mg content (formed by the decomposition of CaMg(CO<sub>3</sub>)<sub>2</sub> into MgO), where the former texture of the rock is not observed, and areas composed exclusively of CaCO<sub>3</sub> with residual crystallinity. During calcination, the dissociation reaction of carbonates with high Mg content starts at about 300°C, while for pure carbonates it occurs at about 850°C, which means that the furnace temperature was uneven and did not always reach 850°C in the chamber.

In addition, a variable Mg content of 1 to 4% is observed in the binder, with subspherical dark nodules richer in Mg (> 10%) (Figure 9.8b, Table 9.3) and areas without Mg. This heterogeneity of the limestone is also observed in the lumps of the same sample, some

of which have the typical appearance of unmixed binder residue and others of burning residue with Mg-rich nodules (Figure 9.8c). In the thin sections of the samples from the Sanctuary of the Public Lares, the Theatre, Eumachia, the Temple of Apollo, and the Tabularium (i.e., 2A, 10A, 11C, 22A, 27A, 27B), terrigenous zones are observed around the lumps, suggesting that the limestone originated from deposition (Figure 9.8d). That is, it can be assumed that the material used as stone for lime was not extracted from dedicated quarries but collected as available pebbles in detrital areas or as stockpiles. Bioclast residues are also found in the unburned lumps (Figure 9.8a), compatible with the Monti Lattari lithologies. In addition, small carbonate fragments are observed in the 2A analysis, possibly originating from the cavities and fissures of the volcanic rocks present as aggregates.

The general geologic map of the Bay of Naples and the location of the Pompeii archaeological site are shown in Figure 9.9. The excavation site is located between Somma-Vesuvius and the carbonate relief of Monte Lattari in the alluvial plain of the Sarno River. The materials used for the aggregate and the production of the binder are fully compatible with those found in the area.

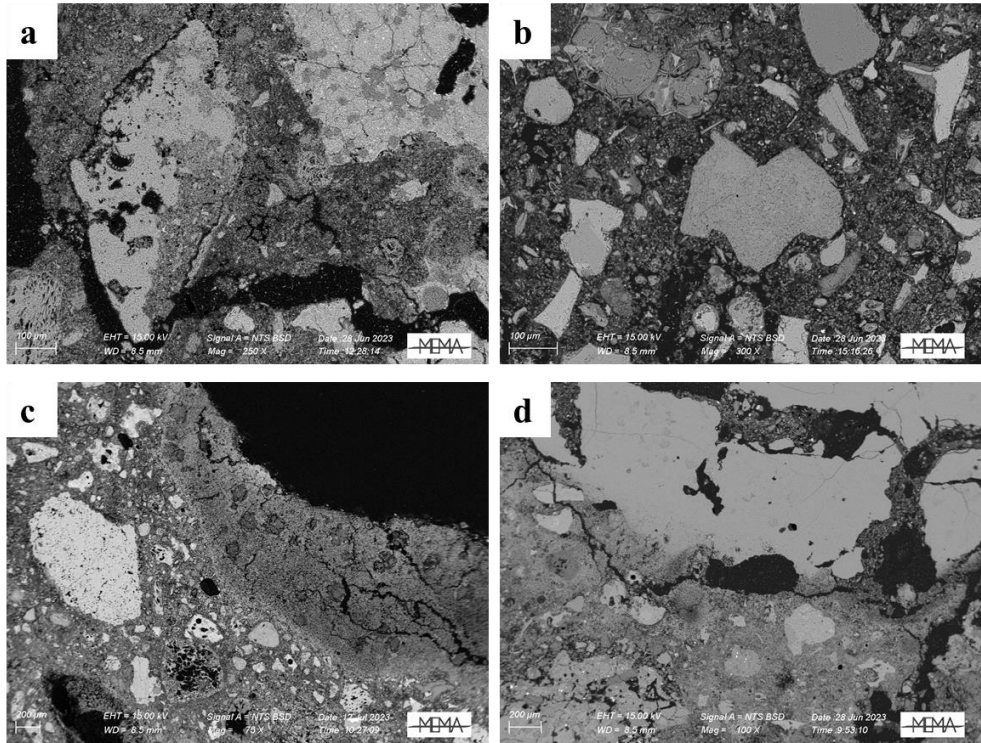


Figure 9.8 – Binder characteristics: a) Unburned limestone of sample 2A, in Table 9.3, microchemical analysis of area 1 refers to this zone; b) Mg-rich nodule of sample 17A, in Table 9.3; c) unburned lump with Mg-rich nodules of sample 2A; d) terrigenous area around lump of sample 22A.

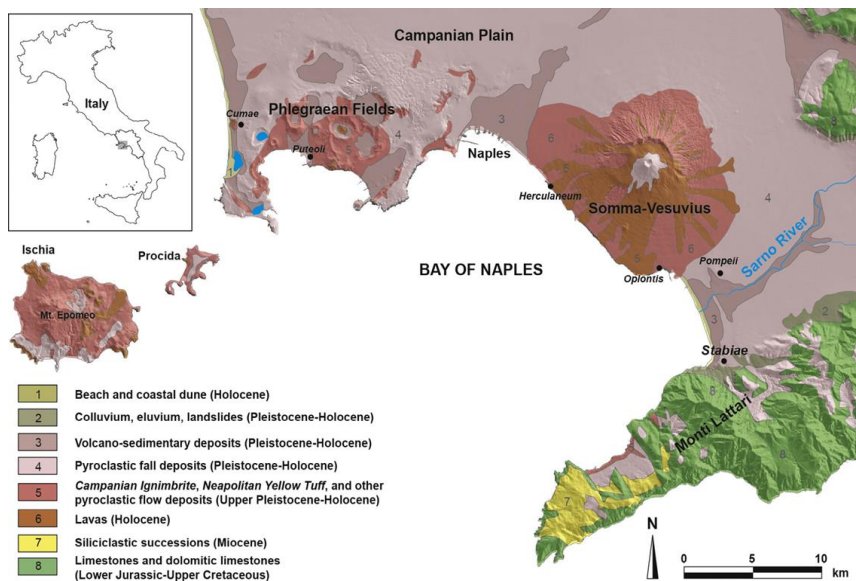


Figure 9.9 – Geological map of the Gulf of Naples (De Bonis et al., 2016), with location of the site of Pompeii.

## 9.4 Non-destructive characterization, pre-treatment and acid dissolution of selected samples

The mechanical selection process, powder characterization, pre-treatment, and CO<sub>2</sub> extraction in the graphitization line are performed. Two powders are selected for each sample (1 lump and one bulk or two of the same type). The selected sample consists of particles with size less than 63 μm. After sieving, each sample is analysed using non-destructive techniques such as XRPD, OM-CL, ATR-FTIR and micro-Raman, and SEM-EDS. Sections 6.2 and 6.3 describe the procedure, spectrum acquisition, and data processing for ATR-FTIR and micro-Raman, respectively. Section 7.2 shows the CO<sub>2</sub> extraction and graphitization procedures.

### 9.4.1 Selection and characterization of calcite mortar powders

Samples from Pompeii 2A, 7A, 17A, 19C, 22A were selected to evaluate the reliability of their dating. Samples with significant hydraulic binder and lumps with aerial binder were taken (Table 9.4). Samples labelled L and B, respectively, were selected as lump and bulk samples.

*Table 9.4 Selected samples from Pompeii*

<b>ID sample</b>	<b>Selected sample</b>
2A	2AL1, 2AB1
7A	7AL1, 7AB1
17A	17AL1, 17AL2
19C	19CL1, 19CB1
22A	22AL1, 22AB1

All powder samples were characterized by XRPD, OM-CL, and ATR-FTIR, and the analytical results are shown in Table 9.5. From the XRPD results, it is evident that all samples are predominantly calcite. The presence of mineral phases associated with hydraulic limes, referred to as calcium silicate (CS), with traces of plagioclase from the

aggregate, is highlighted. In 22AB1, the presence of hydrated phases of calcium silicate (CSH) is evident. ATR-FTIR results show that samples 2AL1, 17AL1, and 17AL2 are consistent with the trend of anthropogenic calcite. However, they have higher  $\nu_2$  values than the typical values for anthropogenic calcite. Sample 7AL1 lies between the two trends. This result and the bright orange tones observed in OM-CL indicate the geologic origin of the lump samples. Samples 2AB1, 7AB1, 19CL1, 19CB1, and 22AL1 are within the trend of anthropogenic calcite in ATR-FTIR, and the colours in OM-CL are predominantly red-tile brown, with small grains brighter (orange) and aggregate remnants (blue).

Additionally, the samples were analysed with micro-Raman and SEM-EDS. The samples were analysed using micro-Raman to assess the origin of calcite, and SEM-EDS analysis was conducted on the powders. Table 9.6 shows the L,  $\nu_4$ , and  $\nu_1$  wavenumbers and their respective FWHM values. The 10 Raman spectra collected for each sample are quite heterogeneous; SEM-EDS reveals the presence of Mg in lump samples. In this case, Raman results can be distorted. We found that by measuring the FWHM of the bands and their shifts, Raman analysis can distinguish whether calcite is geological or anthropogenic. Anthropogenic calcite exhibits peaks shifted to lower wavenumbers and broadening of the bands. However, if there is magnesian calcite, as the magnesium content increases in the crystalline structure, the Raman peaks shift to higher  $\text{cm}^{-1}$  (e.g., L shifts from  $281 \text{ cm}^{-1}$  in carbonates without Mg to  $286 \text{ cm}^{-1}$  with 15% Mg), due to the decrease in interatomic distances following the substitution of  $\text{Ca}^{2+}$  with the smaller  $\text{Mg}^{2+}$  ion. The positions of the Raman bands are directly related to the amount of magnesium present in the calcite structure (Bischoff et al., 1985; Borromeo et al., 2017), exhibiting the opposite phenomenon to that observed for anthropogenic calcites. In principle, FWHM values are more reliable for distinguishing anthropogenic calcite in this case. Lump samples consistently show L wavenumbers above  $281 \text{ cm}^{-1}$ , indicating the possible presence of magnesian calcite, supported by  $\nu_4$  and  $\nu_1$  wavenumbers tending to be higher, often associated with FWHM values typical of geological carbonates. Bulk

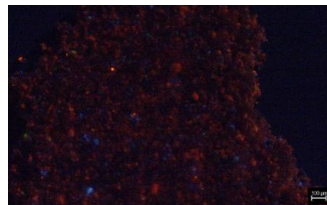
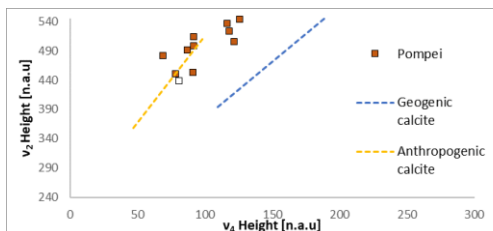
samples, on the other hand, exhibit L wavenumbers below  $281\text{ cm}^{-1}$  and varying  $\nu_4$  and  $\nu_1$  values, with FWHM typical of anthropogenic calcites.

Table 9.5 Summary of XRPD, ATR-FTIR, and OM-CL analyses on the lump and bulk samples from Pompeii. In the ATR-FTIR graph, the analysed sample is not highlighted.

ID sample	XRPD	ATR-FTIR	OM-CL
2AL1	Cal (+++), CS (+)		
2AB1	Cal (+++), CS (+), plg (tr)		
7AL1	Cal (+++), CS (+)		

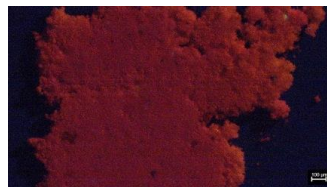
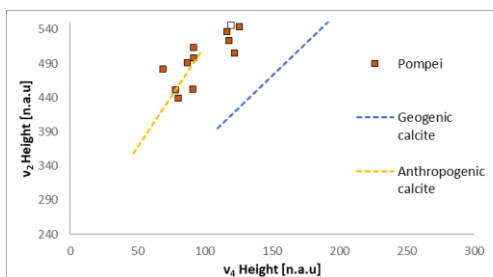
7AB1

Cal  
(+++),  
CS  
(+),  
plg  
(tr)



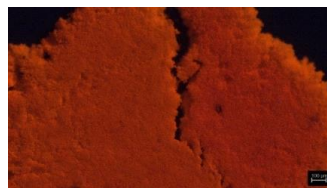
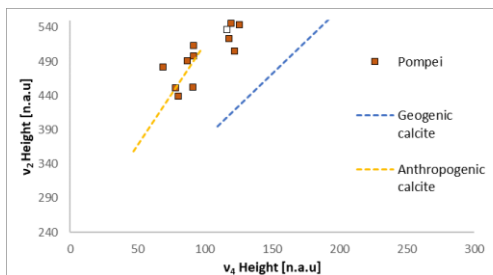
17AL1

Cal  
(+++),  
CS (+)



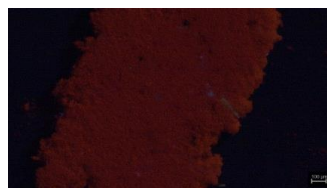
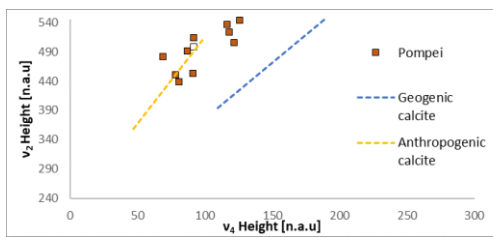
17AL2

Cal  
(+++),  
CS (+)



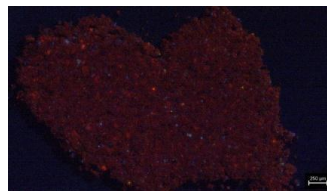
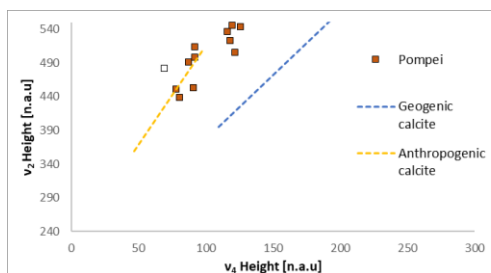
19CL1

Cal  
(+++),  
CS (+)



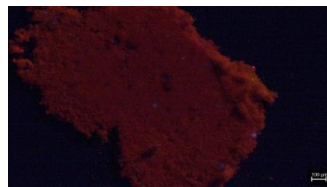
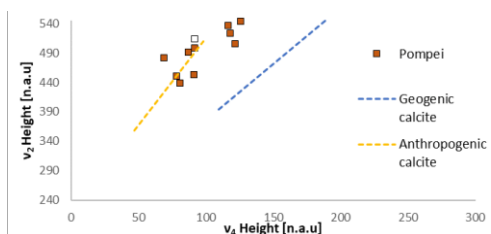
19CB1

Cal  
(+++),  
CS  
(+),  
plg  
(tr)



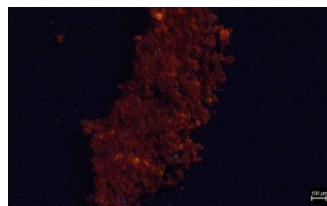
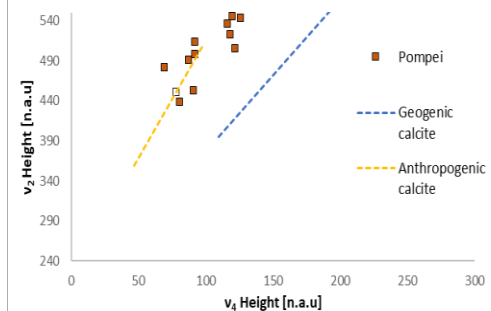
22AL1

Cal  
(+++),  
CS (+)



22AB1

Cal  
(++),  
CS  
(++),  
CSH  
(+), k-  
feld  
(tr)



+++ : very abundant; ++ : abundant; + : present; tr : traces; - : below detection limit. Cal : calcite; CS : Calcium silicate; CSH : calcium silicate hydrate; qz : quartz; k-feld : k-feldspar; plg : plagioclase.

Table 9.6 Raman results of calcite lumps and bulk of Pompeii: the average of the wavenumbers, FWHMs of L,  $v_1$ ,  $v_4$  from 10 Raman measures performed for each sample.

ID sample	L wavenumber	L FWHM	$v_4$ wavenumber	$v_4$ FWHM	$v_1$ wavenumber	$v_1$ FWHM
2AL1	282.4	13.7	713.0	5.8	1086.9	4.5
2AB1	279.0	19.7	712.6	7.0	1086.4	5.5
7AL1	282.5	13.4	713.1	5.9	1086.9	4.6
7AB1	279.8	24.8	712.1	7.3	1085.9	5.6



17AL1	282.3	12.9	712.7	5.6	1086.7	4.5
17AL2	282.4	12.5	712.7	5.2	1086.7	4.2
19CL1	280.9	16.2	712.5	7.1	1086.1	5.5
19CB1	280.8	19.8	713.1	8.0	1086.8	6.1
22AL1	280.9	18.5	712.7	7.4	1086.4	6.0

#### 9.4.2 Pre-treatment and acid dissolution of selected mortar powders

The mechanically separated powders (lump extraction/mass selection + sieving) were chosen for dating, except for sample 22AB1, which exhibits a hydrated phase (CSH). The reaction times and the masses of the graphitized samples are listed in Table 9.7. The lump samples were treated with H<sub>3</sub>PO<sub>4</sub> acid for 10 seconds. For sample 22AL1, 20 seconds were required to reach the pressure of 100 mbar (which is required for graphitization of microsamples). For bulk mortar samples, the first fraction of CO<sub>2</sub> produced within the first 10 seconds was collected (indicated by sample name and (1)), and the second fraction of CO<sub>2</sub> produced between 20 and 30 seconds of the reaction was collected (indicated by sample name and (2)).

*Table 9.7 Mass, typology and reaction time chosen for the acid dissolution of Pompeii mortars.*

<b>ID sample</b>	<b>Type of sample</b>	<b>Mass (mg)</b>	<b>Reaction time (s)</b>
<b>2AL1</b>	Lime lump	4.46	10
<b>2AB1(1)</b>	Bulk mortar	6.74	10
<b>2AB1(2)</b>			20-30
<b>7AL1</b>	Lime lump	3.62	10
<b>7AB1(1)</b>	Bulk mortar	5.45	10
<b>7AB1(2)</b>			20-30
<b>17AL1</b>	Lime lump	3.74	10
<b>17AL2</b>	Lime lump	3.42	10
<b>19CL1</b>	Lime lump	4.00	10
<b>19CB1(1)</b>	Bulk mortar	10.20	10

<b>19CB1(2)</b>			20-30
<b>22AL1</b>	Lime lump	3.50	20

## 9.5 AMS measurements

Table 9.8 shows the results of the AMS measurements.

*Table 9.8 Measured radiocarbon concentrations and conventional radiocarbon ages of Pompeii samples.*

ID samples	<sup>14</sup> C concentration (pMC)	t <sub>rc</sub> (yrs BP)	Calibrated age (68% level of probability)	Calibrated age (68% level of probability)
<b>2AL1</b>	73.3 ± 4.2	2590 ± 90	890-880 BCE, 835-730 BCE, 700-545 BCE	915-415 BCE
<b>2AB1(1)</b>	76.0 ± 4.4	2200 ± 120	395-100 BCE	545 BCE-80 CE
<b>2AB1(2)</b>	73.2 ± 3.3	2510 ± 100	-	-
<b>7AL1</b>	33.0 ± 5.5	8700 ± 280	8215-7535 BCE	8550-7135 BCE, 7105-7080 BCE
<b>7AB1(1)</b>	59.8 ± 5.5	4100 ± 200	2910-2400 BCE, 2385-2345 BCE	3335-3215 BCE, 3190-3150 BCE, 3135-2130 BCE, 2080-2060 BCE
<b>7AB1(2)</b>	50.7 ± 5.4	5300 ± 190	-	-
<b>17AL1</b>	69.1 ± 3.5	2950 ± 80	1270-1015 BCE	1400-930 BCE
<b>17AL2</b>	69.3 ± 3.5			
<b>19CL1</b>	77.5 ± 4.1	2180 ± 70	365-155 BCE	390-50 BCE
<b>19CB1(1)</b>	75.1 ± 5.8			
<b>19CB1(2)</b>	71.7 ± 6.6	2830 ± 140	-	-
<b>22AL1</b>	73.6 ± 9.1	2460 ± 270	900-345 BCE, 320-200 BCE	1265 BCE-110 CE

The extremely small sample masses introduced into the ion source and the low currents extracted during measurements increase the experimental error. For each sample, at least two powders were obtained (lump and bulk or 2 lumps), except for sample 22A. The results do not allow for a clear interpretation and in some cases are quite to be expected considering the typology of the processed materials.

Sample 2A: the lump has a  $^{14}\text{C}$  concentration consistent with 2AB(2). Indeed, both are contaminated with geological C, as seen from the cathodoluminescence analysis and the presence of Mg from SEM analysis. The best estimate for this sample dating can be thus associated to the first collected fraction 2AB(1). Figure 9.10a shows the calibration of the measured radiocarbon age for the first fraction 2AB(1). Considering the experimental uncertainties, the sample is compatible with archaeological attribution.

Sample 7A: the lump does not appear as reliable; indeed, a low  $\text{CO}_2$  yield was collected from the dissolution process, and consequently lower currents during the AMS measurement were extracted. Furthermore, characterization of the powder indicates that 7AL1 is contaminated with geologic carbon, which may also be indicated by the significant contribution of Mg.

As far as the two bulk fractions are concerned, both appear as contaminated, as one can expect from the composition analyses. For instance, from thin section characterization, porosity with recrystallized calcite was observed; in addition, cathodoluminescence analysis of the section showed zones with brighter colours. These data suggest that the first fraction 7AB1(1), slightly younger than the other 7AB1(2), can be partly contaminated by some young carbon due to recrystallization, while in general they both are too old with respect to what expected.

In sample 17A, the two lumps have consistent  $^{14}\text{C}$  concentrations. However, OM-CL and micro-Raman data suggested a presence of geological carbon: in fact, they appear to be older than expected.

In sample 19C, the first bulk fraction (19CB1(1)) and the lump (19CL1) are consistent according to statistics, as expected in good mortar samples for dating. We can thus evaluate the best estimation of the date of this sample by calculating their weighted average. Figure 9.10b shows the calibration graph of the measured radiocarbon age: the obtained age is compatible with the construction phase.

Finally, the lump sample 22AL1 does not appear reliable; as in the case of the already discussed 7AL1, a low  $\text{CO}_2$  yield was collected from the dissolution reaction and low currents were extracted from the ion source during the AMS measurement.

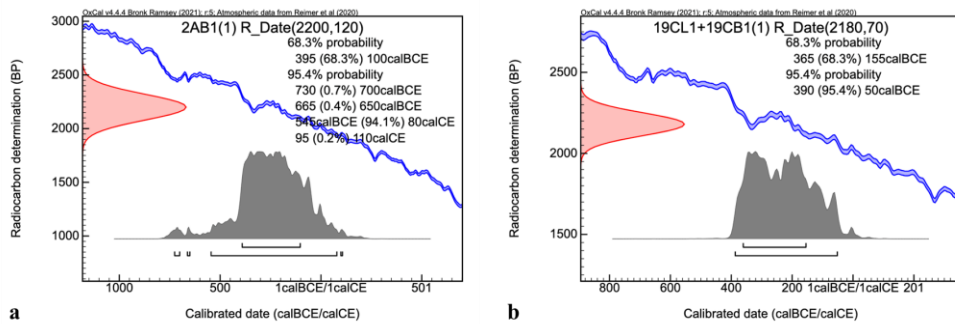


Figure 9.10 - Calibrated age for the Pompeii samples: a) 2AB1(1); b) 19CL1 + 19CB1(1).

## 9.6 Final remarks

The studied mortars from Pompeii made of binders with addition of pozzolan providing hydraulic characteristics and volcanic aggregate with some small recrystallized binder components. The addition of pozzolan complicates the setting and carbonation conditions of the mortar and therefore has a significant impact on the possible application of radiocarbon dating. Regardless of the approach used, the literature predominantly reports unsuccessful cases in this context.

In addition, the mortars in Pompeii were completely buried under a layer of volcanic ash and became part of geological cycles and diagenetic processes. These processes include various chemical, physical, and biological transformations that sediments undergo after their original deposition. The most important process that can affect radiocarbon dating is the formation of a carbonate matrix in the cavities of the depositional products and the recurrent precipitation of groundwater containing interfering carbon.

In addition, CO<sub>2</sub> emissions from the active Somma-Vesuvio volcano and the Campi Flegrei volcanic system in the Bay of Naples result in an atmosphere contaminated with excess CO<sub>2</sub>. It is impossible to estimate to what extent the <sup>14</sup>C age is affected by the concentration of radiocarbon coming from the volcanoes.

The readily available rock material is volcanic rock derived from the volcanic conduit with a Mesozoic limestone basement. Ascending magmas interact with the limestone foundation before reaching the surface, and volcanic eruptions release CO<sub>2</sub> and sulfur dioxide, which can alter volcanic deposits and even produce carbonate minerals in volcanic rocks and travertine deposits. When dating Roman mortars, the risk of carbonate contamination from pozzolanic fillers is high. However, these contaminants may dissolve more slowly in acid than most binding carbonates. Indeed, CO<sub>2</sub> extracted at an early stage of the dissolution process is consistent with the expected age.

After excavation, the ruins are exposed to the weather, so the binder may be subjected to recrystallization phenomena. There are studies that have shown that Roman pozzolanic mortars have the ability to self-heal when in contact with water. These intrinsic chemical reactions occurring within the material over the centuries complicate the application with <sup>14</sup>C. However, if geologic carbonates are also present, accurate age determination from a <sup>14</sup>C profile can be difficult because interference between young carbonates and geologic carbonates can occur, which can confound dating results.

Characterization of the powder indicates difficulties in dating. The lime used for mortar production is not entirely suitable. Analyses of the lime lumps using different analytical techniques show the presence of geological carbonates in the structure. The very heterogeneous textures of the lumps observed in thin section with OM and SEM-EDS are further evidence. Cathodoluminescence, SEM-EDS, and micro-Raman analyses confirm the partial presence of limestone unburned residues.

It should be emphasized that the knowledge gained by characterizing the mortar fragments and selected powders with our procedure provides a clear understanding of the nature of the material, especially the origin of the calcite, which affects the dating results.

In general, we use characterization measurements to select materials that we believe best reflect the requirements for radiocarbon application. However, in the case of Pompeii, given the methodological purpose of the project, we chose to submit a selection of samples for <sup>14</sup>C measurement. These results were consistent with what we

expected and analysed from the characterization. From the measurements, we can infer that our characterization procedure is effective in identifying anthropogenic powder intended for dating. Moreover, in similar cases in the future, attempts to date such samples will likely be avoided.

## 10 Radiocarbon dating of organic fragments in the mortar mixture

As discussed in the previous chapters, a full characterization of mortars and plasters supports us in the identification of the most suitable components for absolute dating. In certain contexts, however, the performed analyses can reveal the presence of various sources of contamination, stemming from geological and geochemical settings, as well as the raw materials used, thus hindering  $^{14}\text{C}$  binder dating. In this case, the possibility of relying on organic residues such as the additives can be a successful approach, as demonstrated for the mortars/plaster of St. Philip Church in Hierapolis (Turkey).

### 10.1 The plasters of the St. Philip Church in Hierapolis (Turkey)

The St. Philip Church is located in the archaeological site of Hierapolis of Phrygia, Denizli, Turkey (Figure 10.1).

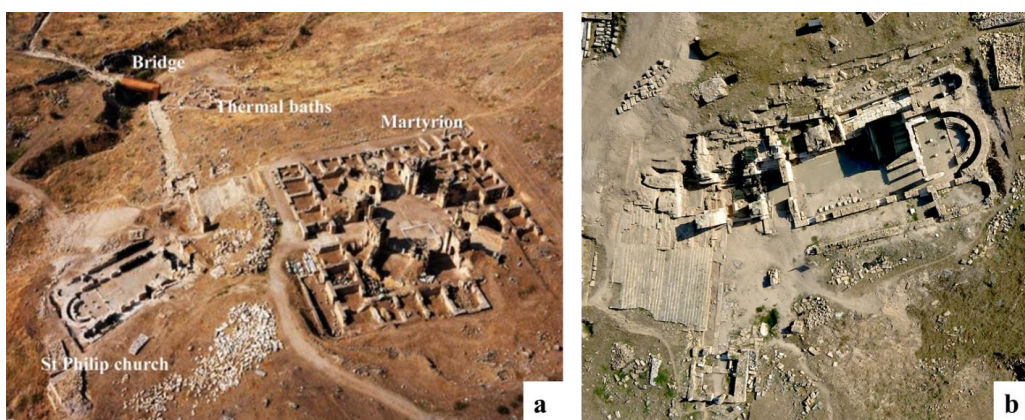


Figure 10.1 – The archaeological site of Hierapolis of Phrygia, Denizli, in Turkey: in a) aerial photo of the whole site; and in b) a detail of St. Philip Church.

Hierapolis, located in southwest Turkey, stands as an exceptional ancient city from the Hellenistic, Roman and Byzantine periods, gaining UNESCO protection in 1988. In spite of the fact that the area around Denizli has always been characterized by dangerous

earthquakes and hydrothermal fluid circulation, which can clearly affect the preservation of monuments, the site has survived for millennia.

The main historical phases of the building of the Church of St. Philip can be summarized as follows (Caggia, 2016; Caggia, 2022):

- in 3rd century BCE was built;
- in the second half of the 6th century CE, a three-nave church was built on the eastern hill of Hierapolis;
- during the 9th century CE, the building underwent significant transformations;
- in the 10th century CE, a catastrophic earthquake seriously damaged the church;
- until the 14th century was used for residential purposes by the Seljuks.

Reconstructing the chronology of the site is challenging due to various factors. The presence of an active fault system, which has caused numerous collapses of walls and architectural elements over centuries, makes the possibility to discriminate between the different archaeological construction phases difficult. Dating the mortars and plasters used in the construction would be essential in such a scenario. However, from the published literature, the materials collected from the church does not appear to be suitable for radiocarbon dating; in fact:

- Travertine and marble from nearby quarries were used as raw materials for mortar production, they were employed for the production of lime binder and as aggregates (Cantisani et al., 2016; Caggia, 2018; De Giorgi, 2018) (Figure 10.2).
- Thermal waters flow through the site, and their high concentration of CO<sub>2</sub> is responsible for corrosion processes (Vettori et al., 2019) and the precipitation of various carbonate phases. This might have led to contamination of the mortar mixture with geogenic carbon, appearing to have affected the age of the mortar (Ricci et al., 2020) (Figure 10.2).



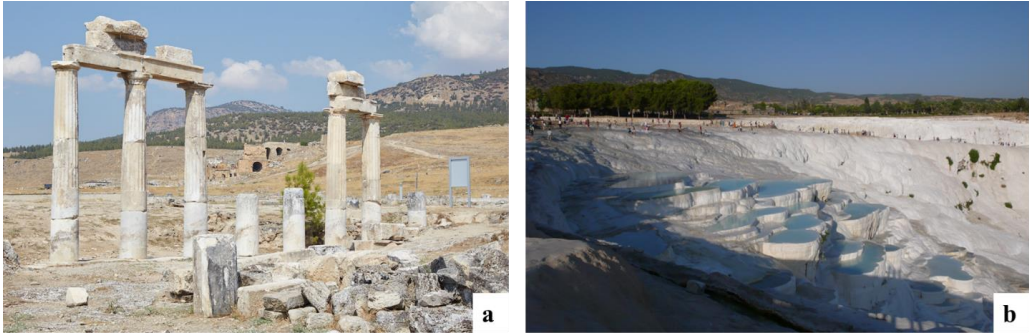


*Figure 10.2 – Critical Aspects of Plaster Radiocarbon Dating at Hierapolis: a) Collapse of architectural elements constructed using carbonate rocks; b) Percolation of hydrothermal water throughout the site.*

For the current research seven samples of plaster were selected from St. Philip Church, encompassing all the materials studied at the site (Cantisani et al., 2016). The selected samples of several mortar/plaster fragments contain minute straw fragments within the matrix, which are listed below (the location in the plant is shown in Figure 10.3):

- MSF04 and MSF15 were collected from pillars in the northern nave;
- MSF06 from west wall of northern nave;
- MSF33 from west wall of the southern nave;
- US543, US546 and US547 from the west wall of the narthex.

Even though we are unsure whether the plaster revetments are a part of the original phase, MSF-labelled samples are connected to buildings constructed in the early Byzantine period (second half of the 6th century). The narthex can be dated to the middle Byzantine period, which began in the 9th century CE.

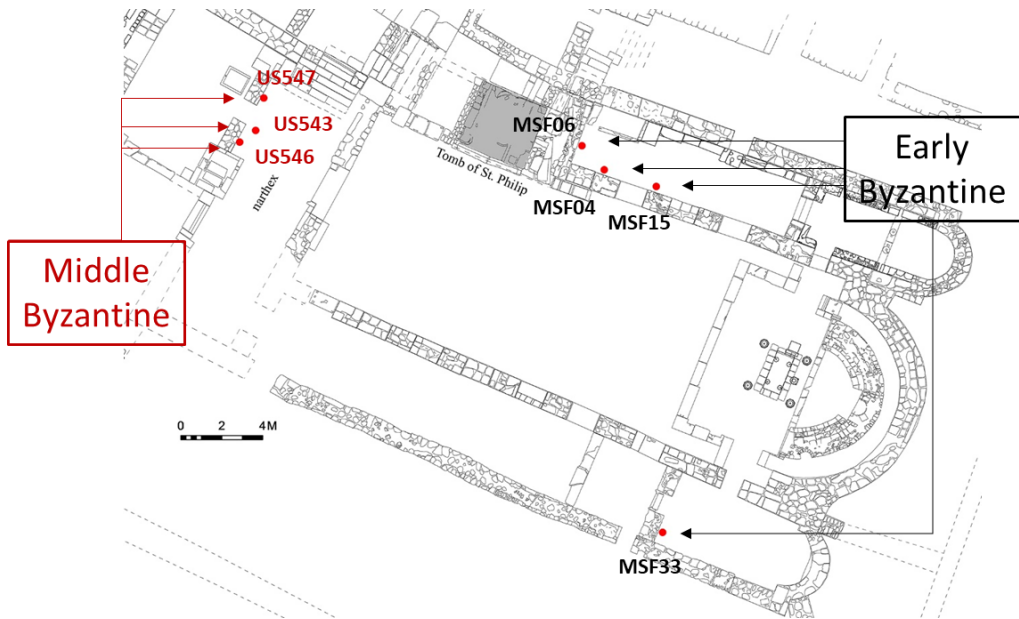


Figure 10.3 – Plan of the church, with sampling point of the plaster studied.

## 10.2 Characterization results of the plaster from the St. Philip Church

As previously indicated, Cantisani et al., 2016 presented the full characterization of the mortar and plaster samples from the St. Philip Church. In summarizing the results of a broader research involving over 40 samples, three distinct categories of mortars/plasters have been identified in the St. Philip Church:

- mortars/plasters obtained by mixing air hardening calcic lime with a very abundant amount of aggregates, which consist of local rocks fragments (e.g., schists, quartzites, travertines and marbles), not well sorted and with heterogeneous grain size distribution (type 1, Figure 10.4a);
- mortars/plasters obtained by mixing air hardening calcic lime with fragments of crushed ceramic materials (cocciopesto) to produce a hydraulic mortar, which hardens also in contact with water or in presence of high humidity; a few sands made of silicatic and carbonatic rock fragments are present as aggregates (type 2, Figure 10.4b);
- plasters produced by mixing air hardening calcic lime with straw and very low amount of aggregates (consisting of either carbonate or earthy materials); in most of the

analysed samples, the binder is not homogeneous and numerous lumps are present due to prevalently to underburned stone fragments (type 3, Figure 10.4c).

The petrographic analysis highlighted the predominant presence of different sources of contaminants. The abundance of carbonaceous aggregates of different sizes, until a few micrometres in size, the presence of hydraulic binder and secondary calcite in the mortars does not offer the possibility of radiocarbon dating of binder and lime lumps. Thus, we focused on the straw fragments observed in the plasters.

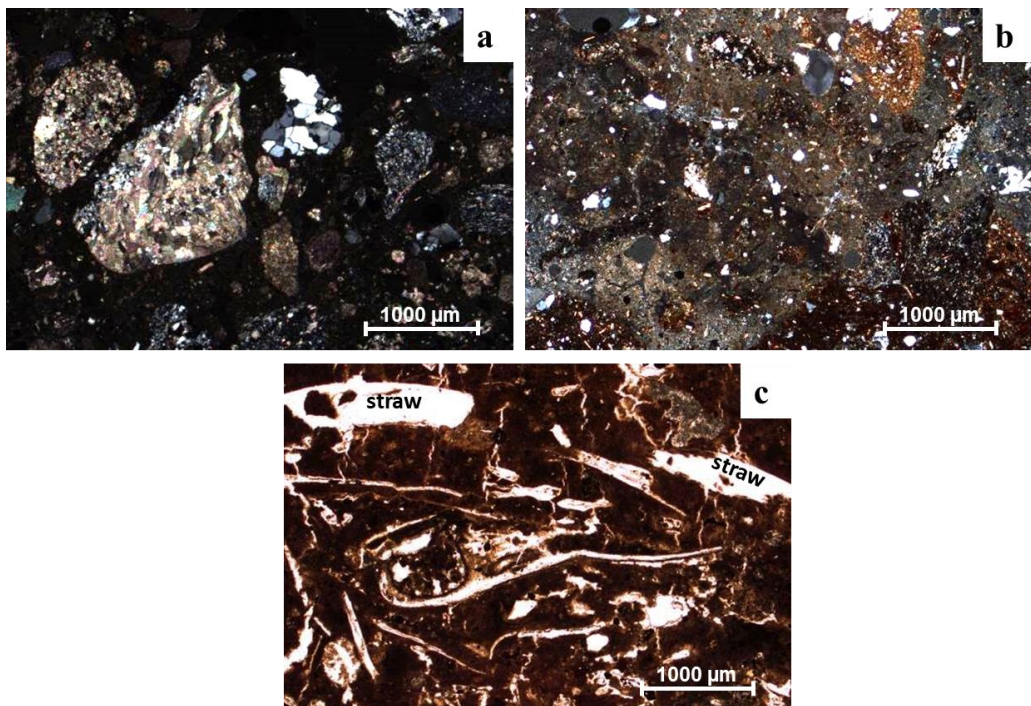


Figure 10.4 – Microphotographs of thin sections of representative types of mortar and plaster in the St. Philip Church: in a) Type 1 mortar; in b) Type 2 mortar; and c) Type 3 plaster. (OM: (a), (b) crossed nicols, (c) parallel nicols).

Table 10.1 lists the analytical information for the plaster samples from this latter category that were chosen for this context because they contained enough straw elements. Samples MSF06, MSF33, US546, and US547 exhibit medium to high porosity and have a binder/aggregate ratio of 3/1 to 4/1, with a very low aggregate content, mainly composed of rock fragments such as schists, quartzite, travertines, and marbles.

On the other hand, samples MSF04, MSF15, and US543 were made without aggregates, displaying very high porosity with shrinkage microcracks and elongated pores due to straw loss. The binder is typically heterogeneous, with noticeable lumps, except for US543, which exhibits a homogeneous binder and no lumps. The marble unburned lumps implies that it was employed for lime production, consistent with traditional manufacturing methods. Concerning radiocarbon dating, geogenic carbonate aggregates and unburned marble fragments present a significant challenge. The medium to high binder porosity indicates the presence of secondary calcite, likely resulting from dissolution and recrystallization processes. The mineralogical analysis in XRPD (Table 10.1) highlights calcite (referred to the binder and aggregate composition), and quartz and plagioclase, and minor amounts of phyllosilicates (mica-like minerals and chlorites) (referred to the aggregate composition). Aragonite was usually found in mortars, associated with travertine, present as aggregate. The presence of gypsum is due to alteration phenomena caused by the sulphation of carbonate binder. The obtained data demonstrate that these plasters are unsuitable for radiocarbon dating using binder and lime lumps. Dating the residues of straw is the most promising approach, even if some difficulties must be addressed in the collection of adequate amounts of these fragments from the mortar/plaster samples and in pre-treatment procedure.

*Table 10.1 The analytical information of the Type 3 plaster samples: location, XRPD data, and petrographic characteristics.*

<b>ID sample</b>	<b>Type</b>	<b>Location</b>	<b>XRPD composition</b>	<b>OM observation</b>
MSF04	ext. layer	Third pillar in the northern nave	Cal, gp, traces of qz	Air lime binder heterogeneous with lumps, addition of straw, only binder, porosity: very high
MSF15	ext. layer	Second pillar in the northern nave	Cal	Air lime binder heterogeneous with lumps, addition of straw, only binder, porosity: very high

MSF06	ext. layer	Wall	Cal, arg, traces of qz and gp	Air lime binder heterogeneous with lumps, addition of straw, B/A: 3/1 - 4/1, porosity: medium/high
MSF33	ext. layer	Wall of southern nave	Cal, qz, traces of ms and chl	Air lime binder heterogeneous with lumps, addition of straw, B/A: 3/1 - 4/1, porosity: very high
US543	inr. layer of painted plasters	Narthex	Cal, traces of qz	Air lime binder homogeneous, addition of straw, only binder, porosity: very high
US546	inr. layer of painted plasters	Narthex	Cal, qz, traces arg	Air lime binder heterogeneous with lumps, addition of straw, B/A: 3/1 - 4/1, porosity: very high
US547	inr. layer of painted plasters	Narthex	Cal, qz, traces pl	Air lime binder heterogeneous with lumps, addition of straw, B/A: 3/1 - 4/1, porosity: very high

*Cal= calcite; gp= gypsum; qz= quartz; arg= aragonite; ms= muscovite; chl= chlorite; pl= plagioclase. Ext.= external; inr. = inner.*

### 10.3 Mechanical selection and sample preparation of straw fragments

The straw fragments identified as aggregates in the plaster matrices in OM (thin and cross sections), were selected examining bulk samples under stereomicroscope (Figure 10.5). The mechanical separation of these fragments posed significant challenges. The bulk samples, from which the straw was derived, were approximately 2-3 cm in size, and the straw structures were mostly visible only under the microscope (Figure 10.5). The gathered materials consisted of extremely thin stems, measuring between 1-2 mm in length. The presence of some mortar grains in the separated sample made it difficult to accurately determine the amount of straw obtained by the mechanical separation process.

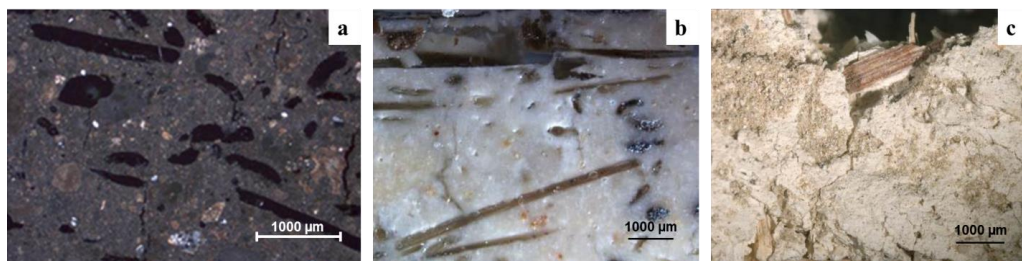


*Figure 10.5 – Straw Fragments in US543: a) Microphotograph of a thin section of plaster with straw fragments (crossed nicols); b) Microphotograph of a cross-section of plaster under a stereomicroscope; and c) Bulk sample view under a stereomicroscope.*

The initial phase of sample preparation primarily focused on pre-treatment to eliminate potential contaminants, such as carbonates from mortars. A modified ABA (acid-base-acid) pre-treatment was employed to eliminate any impurities from the straw fragments, carefully considering temperature and duration for each step to make a balance between effective cleaning and sample preservation. The pre-treatment followed for straw samples is summarized below:

- 1 hour bath in 1M HCl at room temperature (instead of at 80°C as in our typical procedure), to remove all the possible carbonate residues from the fragments;
- a quick bath in 0.1M NaOH at room temperature, for up to few minutes, i.e. until the complete “whitening” of the fragments; in fact, when this condition is achieved, we expect to have removed the possible organic contaminations;
- 1 hour bath in 1M HCl at room temperature (instead of, again, at 80°C as in our typical procedure).

After the described pre-treatment procedure, the masses of the straw fragments were reduced to a few hundred micrograms, thus we decided to use the Lilliput graphitization reactors as well. The carbon dioxide to be converted to graphite was obtained by combustion in the elemental analyser.

Some of the collected samples were anyway too small, even for the Lilliput line, thus we decided to merge some of the recovered straw samples considering archaeological factors including chronological and functional criteria. Table 10.2 lists the samples' total masses, how they were combined, and the CO<sub>2</sub> that was collected.

*Table 10.2 Information regarding the treated samples: The combined straw fragments, their overall masses, and the collected CO<sub>2</sub> pressures.*

Sample ID	Mass (mg)	CO <sub>2</sub> pressure (mbar)
MSF04 + MSF15	0.40 ± 0.05	50 ± 5

MSF06 + MSF33	0.40 ± 0.05	90 ± 5
US543 + US546 + US547	0.35 ± 0.05	80 ± 5

## 10.4 AMS measurements

The results of the AMS measurements of the straw samples are displayed in Table 10.3. The calibrated ages were obtained from conventional  $^{14}\text{C}$  ages and reported in Figure 10.6.

*Table 10.3 Measured  $^{14}\text{C}$  concentrations, associated conventional radiocarbon ages and calibrated age time intervals of straw samples.*

Sample ID	$^{14}\text{C}$ concentration (pMC)	$t_{\text{rc}}$ (yrs BP)	Calibrated age (68% level of probability)	Calibrated age (95% level of probability)
MSF04 + MSF15	75.30 ± 1.4	2278 ± 144	715 – 120 BCE	775 BCE – 5 CE
MSF06 + MSF33	87.20 ± 1.1	1100 ± 105	770 – 1035 CE	675 – 1160 CE
US543 + US546 + US547	88.50 ± 1.0	979 ± 88	990 – 1170 CE	885 – 1260 CE

The calibrated age of sample MSF04 + MSF15 does not agree with the archaeological findings, and the sample looks to be older (Figure 10.6a). This suggests that the sample may still be contaminated by old  $\text{CaCO}_3$  from the plaster, together with the low yield of  $\text{CO}_2$  collected after combustion. During the pre-treatment, some marble residues likely weren't eliminated. Additionally, it is difficult to completely burn marble using an elemental analyser, therefore the potential existence of  $\text{CaCO}_3$  residues may be the cause of the poor carbon dioxide yield. Archaeologists' predicted ages are compatible with the samples MSF06 + MSF33 and US543 + US546 + US547 (see also Figure 10.6b,c). The sample MSF06 + MSF33 seems to be slightly older than the other dated sample. In fact, given that the church was constructed and altered as a result of numerous earthquakes, at least two distinct building phases may be anticipated based on the time

period in which the church was used. We are unable to statistically distinguish between them, however, due to experimental errors in the measured radiocarbon concentrations.

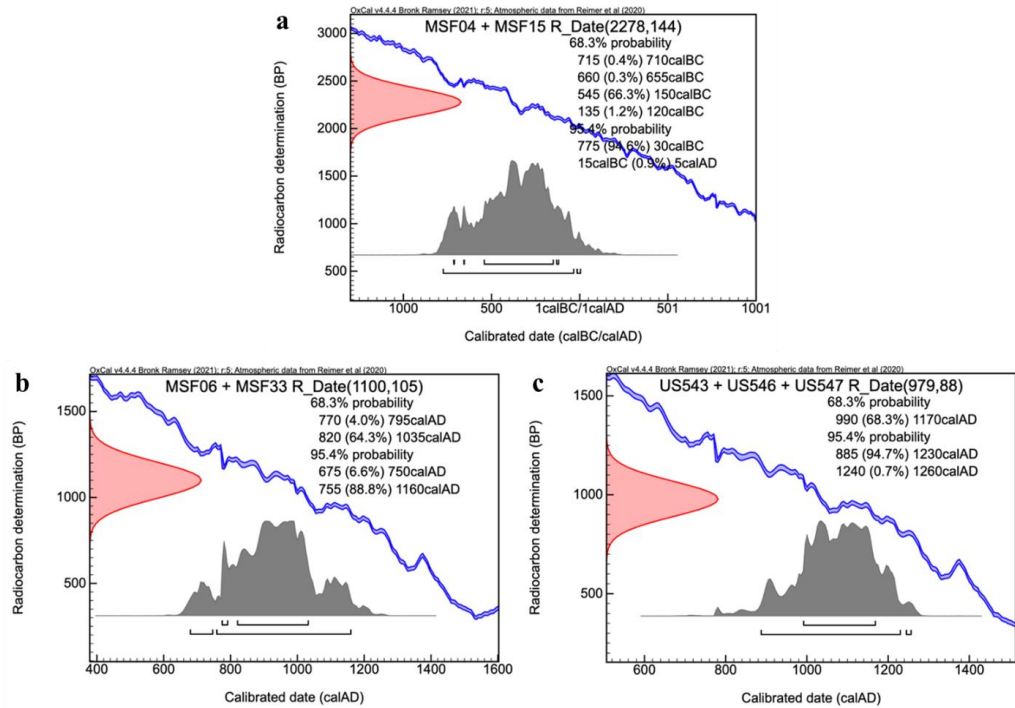


Figure 10.6 – Calibration graphs of samples MSF04 + MSF15 (a), MSF06 + MSF33 (b), and US543 + US546 + US547 (c).

The MSF06 + MSF33 and US543 + US546 + US547 results are satisfactory because they largely agree with the anticipated archaeological dates (Table 10.4).

Table 10.4 Comparison of attribute dating from archaeological readings and radiocarbon dating.

Sample ID	Archaeological date	<sup>14</sup> C findings
MSF04 + MSF15	Early Byzantine period	Not agree
MSF06 + MSF33	Early Byzantine period	Agree
US543 + US546 + US547	Middle Byzantine period	Agree



The presence of carbonate aggregates, secondary calcite, and hydraulic binder, radiocarbon dating of the binder is not feasible. In such cases, the potential radiocarbon dating of straw fragments, which act as organic inclusions, emerges as a well-founded option. This is because the radiocarbon concentration in these fragments can be directly associated with the time when the mortar was set.

However, our data also highlight a potential drawback of employing this type of material: a milder pre-treatment, such as the one we choose to conserve as much mass as possible, could not be enough to remove clear of all potential contamination sources. The method is not appropriate in routine operations due to the challenging steps of the sample preparation procedure and the significant attention that must be paid when preparing samples with extremely low masses.

The results of this research were published in Calandra, S., Barone, S., Cantisani, E., Caggia, M. P., Liccioli, L., Vettori, S., Fedi, M. (2023). Radiocarbon Dating of Straw Fragments in the Plasters of ST. Philip Church in Archaeological Site Hierapolis of Phrygia (denizli, Turkey). *Radiocarbon*, 65(2), 323-334.

## 11 Conclusion

In this thesis, I have presented the research conducted during the three years of Ph.D., working at the DST-UNIFI, ISPC-CNR, and INFN-LABEC laboratory in Florence.

During these years, we implemented a procedure to analyse and possibly select mortar samples to be dated by  $^{14}\text{C}$ -AMS.

We evaluated which techniques, among those that are typically employed for mineralogical, petrographic and chemical analyses, are the most useful to identify the mortar raw material, i.e. the nature and composition of the binder, the aggregates and the possible presence of additives. Carbonation test, optical and electron microscopies (OM, SEM-EDS), X-ray diffraction on powders (XRPD), thermogravimetric analysis (TGA) and infrared spectroscopy (FTIR) have been proven to permit the selection of the most suitable mortar to be dated. Moreover, we combined for the first time during the PhD project two high resolution techniques to study the heterogeneity of lumps in mortar samples. FTIR microscope Focal Plane Array detector (FPA-FTIR), and  $\mu\text{XRPD}$  at the ID13 beamline in the European Synchrotron Radiation Facility were used to study the distribution of  $\text{CaCO}_3$  polymorphs commonly found in ancient mortars.

Upon assessing that the sample exhibits datable characteristics, as a consequence of all the analyses performed in the characterization step, the following process involves the selection and further characterization of the carbonate fraction. Specific mortar portions, such as binder-enriched samples or lump samples, were selected. The aim of this step is to design a powder characterization, using non-destructive techniques, to reduce contamination sources in small samples and preserve for subsequent analyses and dating.

The application of new techniques is integrated with methods just used in literature to select sample powder for the AMS measurement of only anthropogenic calcite, thereby reducing the time and cost.

Standard samples of geogenic and anthropogenic calcite were selected to investigate whether ATR-FTIR and micro-Raman can distinguish crystals formed by different

mechanisms. Using ATR-FTIR, by plotting the  $\nu_2$  line versus the  $\nu_4$  line, samples characterized by different types of  $\text{CaCO}_3$  group in two distinct regions.

The distinction between anthropogenic calcite and geogenic calcite by micro-Raman analysis is based on systematic observations of Raman shifts in the L,  $\nu_4$ , and  $\nu_1$  bands. The anthropogenic calcite shows a shift towards lower wavenumbers and wider FWHM values in the L,  $\nu_4$ , and  $\nu_1$ . These findings enabled the use of infrared spectroscopy (ATR-FTIR), and micro-Raman spectroscopy to characterize the datable fraction in non-standard samples.

As already commented in the text (see paragraph 7.1), from the beginning of the overall process, we focused our attention on small samples. In addition, the final mechanical separation to obtain mortar samples enriched in binder forces us to work with very small masses, so that particular efforts were employed in the optimization of the  $\text{CO}_2$  extraction procedure. As an order of magnitude, the typical processed masses are 2.5 mg for lumps, in order to allow us to also manage the single lump, and 5 mg for bulk samples. The new acidification line to extract carbon dioxide was coupled to the so-called Lilliput's graphitization line.

We decided to use sequential dissolution to extract the  $\text{CO}_2$  from the carbonate sample. In doing so, we selected only the first  $\text{CO}_2$  fraction for lump samples and collected the evolving  $\text{CO}_2$  fractions for bulk samples (2 per sample).

Our procedures were applied to mortar samples from Florentine historical buildings and public buildings in Pompeii (Figures 11.1, 11.2). The study cases were selected because these areas typically produced ancient mortars with not completely aerial binders. The innovative aspect of the project lies in the evaluation and possible extension of the procedure for the selection and  $^{14}\text{C}$  dating of the binder of these historic mortars.

- Florentine historical buildings

From the characterization of numerous samples (through OM, SEM-EDS, XRPD, TGA, FTIR), we selected the most representative and interesting samples for the reconstruction of the construction phases of each of the studied buildings. All

the samples have a natural hydraulic binder given by the firing of Alberese limestone (Monte Morello Formation). A complete characterization of the samples permitted the selection of the most suitable portions to be dated by  $^{14}\text{C}$  method: lump samples for Trebbio Castle, bulk and lump samples for S. Felicita Church and Medici Riccardi Palace were selected. On the contrary, the characteristics of the mortar samples from the Baptistery of S. Giovanni have not allowed the selection of datable material for the presence of possible sources of contamination. XRPD, ATR-FTIR, OM-CL and micro-Raman analyses were performed to select the sample consisting mainly of anthropogenic calcite. The results of the AMS measurements are consistent with the expected age, indicating that the overall analysis was essential to select a material that could be assumed to be free of the contaminations. In fact, the dating results confirm that ATR-FTIR, OM-CL and micro-Raman analyses allow the selection of powder without geologic contaminations. The use of non-destructive methods is mandatory for multi-analytical studies of unique and small samples.

Our procedure, applied to Florentine mortar samples, allowed us to select samples suitable for dating a natural hydraulic binder, a type of mortar that is not completely aerial and which would otherwise have been excluded (Figure 11.1). The graph shows the calibrated data obtained from the conventional ages of those samples that have been identified as anthropogenic calcite and are therefore considered as "favorable". This assessment is based on the results of the characterization and the success of the dating preparation. Favorable conditions exist when  $^{14}\text{C}$  concentrations are consistent between: different lumps belonging to the same sample (CT26L1 + CT26L2 + CT26L4); lime lump and the first fraction of the bulk (PMRC4L1 + PMRC4B1(1), PMRC6L1 + PMRC6B1(1), PMRC7L1 + PMRC7B1(1)); or two fractions of the bulk (SFC5B1(1) + SFC5B1(2)) when no carbonate aggregate is present. Second fractions are not reported if they are contaminated with geogenic carbon.

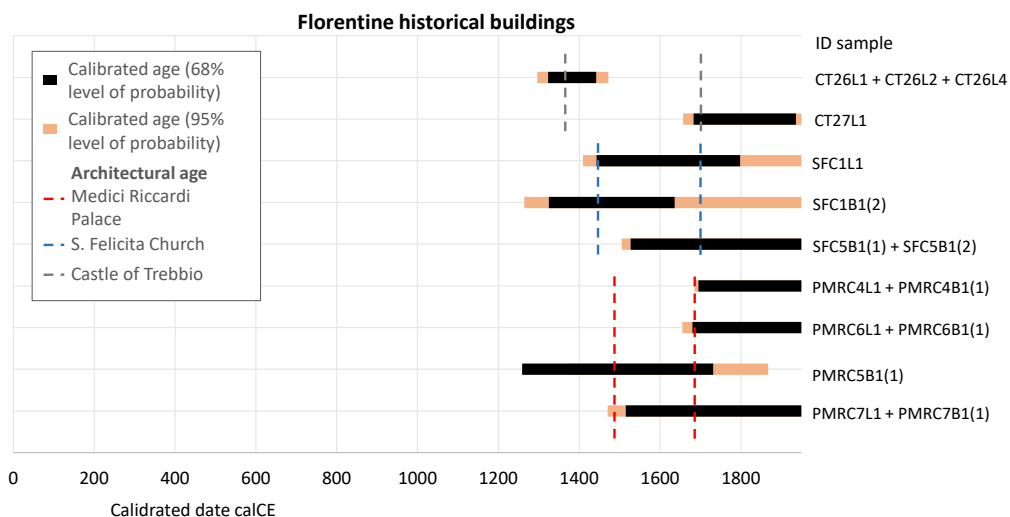


Figure 11.1 – Summary of calibration graphs of dating of mortar samples from Florentine historical buildings.

- Public buildings in Pompeii

Based on a complete documentation of the written sources and the archaeological reading of the walls, the mortars of the walls of different construction phases of the public buildings of Pompeii were sampled. Based on the preliminary characterization, the raw materials used were identified. The samples are characterized by hydraulic lime binder with pozzolana and predominantly magmatic aggregate. The composition of the aggregate is very complex due to the various volcanic products found in the area (lava rocks, pyroclastic products, crystals of magmatic origin such as clinopyroxenes, feldspars, leucites/analclimes). Some criteria (texture of the binder, shape of the aggregate, grain size distribution and B/A ratio) have allowed us to identify groupings compatible with the assigned construction phases. For each construction phase, some samples from the Eumachia building, Temple of Genius Augusti, Tabularium and Temple of Apollo were selected to apply radiocarbon. However, the measurements performed to characterize the composition of both lump and bulk samples pointed to a critical situation. The

lime used for mortar production is not entirely suitable; in addition, geological carbonates and Mg were found in the lump samples. Cathodoluminescence, SEM-EDS and micro-Raman analyses confirm the partial presence of limestone burning residues with magnesium.

As the characterization procedure itself suggested, AMS measurements resulted in samples apparently older than expected, except for two samples (together with another sample, which exhibits a large error) whose age is compatible with the archaeological phase (Figure 11.2). The radiocarbon results are consistent with the characterization results. The graph shows the calibrated data of the dated samples, without the second bulk fractions.

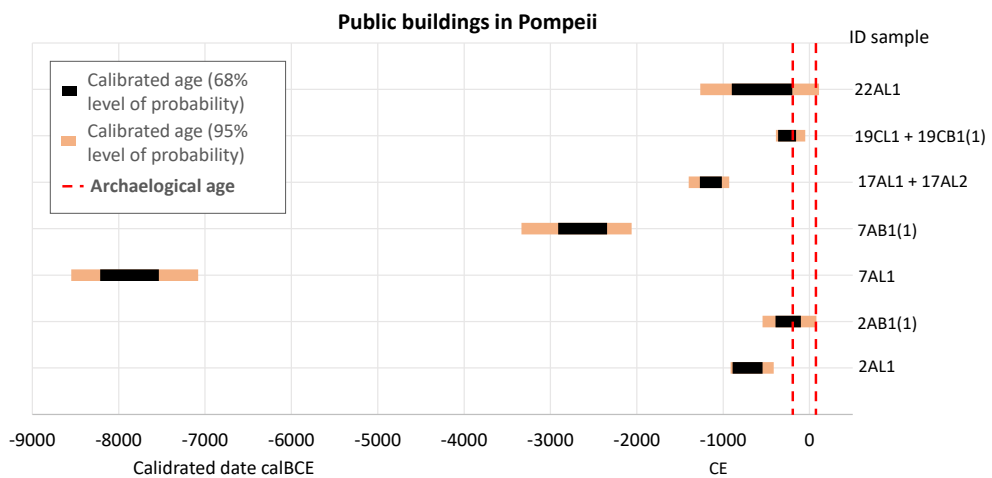


Figure 11.2 – Summary of calibration graphs of dating of mortar samples from public buildings in Pompeii.

In this work, we have also discussed the case when either mortars or plasters from a historical building are not suitable for radiocarbon dating: the case of the Church of St Philip in the archaeological site of Hierapolis. The reason for this is the state of preservation of the mortar binder and the raw materials used for its production. Thanks to the characterization we have found a datable part, the straw fragments. The straw pieces are very thin inclusions worked into the plaster. Plaster with straw addition was

used on various painted walls of the church. We selected these organic inclusions and, thanks to the optimized line for microsamples, we obtained satisfactory data that allowed us to identify the two construction phases of the church.

#### *Future perspective and advancements in mortar dating*

Based on our current findings and considerations, we establish guidelines for dating applications derived from initial characterization. The success of masonry dating depends on several factors, particularly on the availability of datable samples. Precision in dating can only be enhanced through the selection of multiple uncontaminated samples. There exists a delicate balance between accessing a wide range of data, employing low-invasive sampling techniques, and managing the costs and time required for applying the dating procedure to all samples. Under optimal conditions, wherein there are at least three samples from the same construction phase of masonry with consistent radiocarbon concentrations, the weighted averages of these concentrations yield precise measurements and reduce the error range of conventional radiocarbon ages (such as CT26).

The combination of additional parameters for evaluating the origins of calcite ( $\delta^{13}\text{C}$ , LIF, EPR), along with the optimization of  $\text{CO}_2$  extraction processes, has the potential to enhance precision in analyses, thereby improving the dating of binders in historical mortars. The identification of techniques for recognizing recrystallized calcite represents another aspect warranting further exploration.

From this perspective, the micro-Raman results encourage further investigation, coupled with crystal structure analyses. Technological advancements in spectroscopy-based instrumentation could enable in-situ measurements. The application of developed procedures could be expanded to new geographical areas, thereby enhancing understanding of construction techniques and the evolution of mortars across different regions and historical periods, as well as their feasibility for radiocarbon dating.

The characterization procedure could be extended to evaluate the carbonate origins of pigments and sediments in archaeological contexts. In addition, it could be used to study the transformation of the added calcite in ceramic pastes during the firing process.

## References

Abbate, E., & Sagri, M. (1970). The eugeosynclinal sequences. *Sedimentary Geology*, 4(3-4), 251-340.

ALESSANDRINI, G. (1985). Gli intonaci nell'edilizia storica: metodologie analitiche per la caratterizzazione chimica e fisica. In *Plasterwork: history, culture and technology*. 1985 Proceedings of the congress, Bressanone, 24-27 June. L'intonaco: storia, cultura e tecnologia. Atti del convegno di studi, Bressanone 24-27 giugno 1985, pp. 147-166.

Alvarez, J. I., Veiga, M. R., Martínez-Ramírez, S., Secco, M., Faria, P., Maravelaki, P. N., ... & Valek, J. (2021). RILEM TC 277-LHS REPORT. *Materials and Structures/Materiaux et Constructions*, 54.

Alvarez, J. I., Veiga, R., Martínez-Ramírez, S., Secco, M., Faria, P., Maravelaki, P. N., ... & Válek, J. (2021). RILEM TC 277-LHS report: a review on the mechanisms of setting and hardening of lime-based binding systems. *Materials and Structures*, 54(2), 63.

Amjad, A., Ullah, R., Khan, S., Bilal, M., & Khan, A. (2018). Raman spectroscopy based analysis of milk using random forest classification. *Vibrational Spectroscopy*, 99, 124-129.

Aquino, A., Lezzerini, M., Pecchioni, E., Giamello, M., Columbu, S., Cantisani, E., & FRATINI, F. (2019). Stones for the production of binding materials in Florence area (Tuscany, Italy). *JOURNAL OF THE GEOLOGICAL SOCIETY*.



Arizzi, A., & Cultrone, G. (2021). Mortars and plasters—how to characterise hydraulic mortars. *Archaeological and Anthropological Sciences*, 13(9), 144.

Artioli, G. (2010). *Scientific methods and cultural heritage: An introduction to the application of materials science to archaeometry and conservation science*. Oxford University Press.

Artioli, G., Secco, M., & Addis, A. (2019). *The Vitruvian legacy: Mortars and binders before and after the Roman world*.

Artioli, G., Barone, S., Fedi, M., Galli, A., Liccioli, L., Martini, M., ... & Terrasi, F. (2024). Characterization and selection of mortar samples for radiocarbon dating in the framework of the MODIS2 intercomparison: two compared procedures. *Radiocarbon*, 1-14.

Arrighetti, A. (2017). *Materials and building techniques in Mugello from the Late Middle Ages to the Early Modern Age; Materiali e tecniche costruttive del Mugello tra basso Medioevo e prima Età Moderna*.

Bakolas, A., Biscontin, G., Contardi, V., Franceschi, E., Moropoulou, A., Palazzi, D., & Zendri, E. (1995). Thermoanalytical research on traditional mortars in Venice. *Thermochimica Acta*, 269-270, 817–828.

Bensted, J. (1997). Workability of Portland Cement in Mortar and Concrete. *Industria Italiana del Cemento*, 56-74.

Bischoff, W. D., Sharma, S. K., & MacKenzie, F. T. (1985). Carbonate ion disorder in synthetic and biogenic magnesian calcites: a Raman spectral study. *American Mineralogist*, 70(5-6), 581-589.

Black, L., Breen, C., Yarwood, J., Garbev, K., Stemmermann, P., & Gasharova, B. (2007). Structural features of C–S–H (I) and its carbonation in air—a Raman spectroscopic study. Part II: carbonated phases. *Journal of the American Ceramic Society*, 90(3), 908-917.

- Boaretto, E. (2009). Dating materials in good archaeological contexts: The next challenge for radiocarbon analysis. *Radiocarbon*, 51(1), 275–281.
- Borromeo, L., Zimmermann, U., Andò, S., Coletti, G., Bersani, D., Basso, D., ... & Garzanti, E. (2017). Raman spectroscopy as a tool for magnesium estimation in Mg-calcite. *Journal of Raman Spectroscopy*, 48(7), 983-992.
- Borges, C., Santos Silva, A., Veiga, R. (2014). Durability of ancient lime mortars in humid environment. *Construction and Building Materials*, 66, 606-620.
- Bortolotti, V. (1962). Contributo alla conoscenza della stratigrafia della serie Pietraforte-Alberese. *Boll. Soc. Geol. It.*, 81(2), 225-314.
- Boynton, R. S. (1980). *Chemistry and technology of lime and limestone* (2nd ed.). New York, NY, USA: John Wiley & Sons. Inc.
- Brogiolo, G. P., & Cagnana, A. (2012). *Archeologia dell'architettura-metodi e interpretazioni* (Vol. 3). All'Insegna del Giglio.
- Barrett, G. T., Keaveney, E., Lindroos, A., Donnelly, C., Daugbjerg, T. S., Ringbom, Å., ... & Reimer, P. J. (2021). Ramped pyrooxidation: A new approach for radiocarbon dating of lime mortars. *Journal of Archaeological Science*, 129, 105366.
- Barrett, G. T., Allen, K., Reimer, P. J., Ringbom, Å., Olsen, J., & Lindroos, A. (2023). Ramped pyrolysis radiocarbon dating of lime lumps: Establishing the earliest mortar-based construction phase of Turku cathedral, Finland. *Journal of Cultural Heritage*, 61, 201-210.
- Calandra, S., Cantisani, E., Salvadori, B., Barone, S., Liccioli, L., Fedi, M., & Garzonio, C. A. (2022, April). Evaluation of ATR-FTIR spectroscopy for distinguishing anthropogenic and geogenic calcite. In *Journal of Physics: Conference Series* (Vol. 2204, No. 1, p. 012048). IOP Publishing.

Calandra, S., Salvatici, T., Centauro, I., Cantisani, E., & Garzonio, C. A. (2022a). The mortars of Florence riverbanks: raw materials and technologies of Lungarni historical masonry. *Applied Sciences*, 12(10), 5200.

Calandra, S., Cantisani, E., Vettori, S., Ricci, M., Agostini, B., & Garzonio, C. A. (2022b). The San Giovanni Baptistery in Florence (Italy): assessment of the state of conservation of surfaces and characterization of stone materials. *Applied Sciences*, 12(8), 4050.

Calandra, S., Conti, C., Centauro, I., & Cantisani, E. (2023). Non-destructive distinction between geogenic and anthropogenic calcite by Raman spectroscopy combined with machine learning workflow. *Analyst*.

Caggia M. P. (2022). Il terrazzo mediano del Santuario di San Filippo: dalla Chiesa all'occupazione selgiuchide. In: D'Andria F, Caggia MP, Ismaelli T, editors, Hierapolis di Frigia XV. Le attività delle campagne di scavo e restauro 2012–2015. Istanbul. p. 675–713.

Caggia M. P. (2018). Mosaic and opus sectile pavements in the Church of St. Philip in Hierapolis. In: Şimşek C, Kaçar T, editors. The Lykos Valley and neighborhood in Late Antiquity. 2nd International Symposium on Archaeological Practices, Laodikeia. Istanbul. p. 309–323.

Caggia, M. P. (2016). The marbles of the Church of St Philip in Hierapolis. Phases of construction and opus sectile flooring. Ancient quarries and building sites in Asia Minor. Research on Hierapolis in Phrygia and other cities in south-western Anatolia: archaeology. *Archaeometry*, 473-488.

Cantisani, E., Calandra, S., Barone, S., Caciagli, S., Fedi, M., Garzonio, C. A., ... & Vettori, S. (2021). The mortars of Giotto's Bell Tower (Florence, Italy): raw materials and technologies. *Construction and Building Materials*, 267, 120801.

Cantisani, E., Centauro, I., Grandin, C., Salvini, A., & Vettori, S. (2017). The influence of natural organic materials on the properties of traditional lime-based mortars. *International Journal of Architectural Heritage*, 11(5), 670-684.

Cantisani, E., Falabella, A., Fratini, F., Pecchioni, E., Vettori, S., Antonelli, F., ... & Lezzerini, M. (2018). Production of the Roman Cement in Italy: Characterization of a raw material used in Tuscany between 19th and 20th century and its comparison with a commercialized French stone material. *International Journal of Architectural Heritage*, 12(6), 1038-1050.

Cantisani, E., Fratini, F., & Pecchioni, E. (2021). Optical and electronic microscope for minero-petrographic and microchemical studies of lime binders of ancient mortars. *Minerals*, 12(1), 41.

Cantisani, E. M. M. A., Cecchi, A., Chiaverini, I., Fratini, F. A. B. I. O., Manganelli Del Fá, C., Pecchioni, E., & Rescic, S. (2002). The binder of the Roman concrete of the Ponte di Augusto at Narni (Italy). *Periodico di Mineralogia*, 71, 113-123.

Cantisani, E., Vettori, S., Ismaelli, T., & Scardozi, G. (2016). Imperial age mortars at Hierapolis: Raw materials and technologies. *Ancient Quarries and Building Sites in Asia Minor. Research on Hierapolis in Phrygia and other Cities in South-Western Anatolia: Archaeology, Archaeometry, Conservation*, 589-608.

Cantisani, E., Fratini, F., & Pecchioni, E. (2021). Optical and electronic microscope for minero-petrographic and microchemical studies of lime binders of ancient mortars. *Minerals*, 12(1), 41.

Cantisani, E., Salvatici, T., Centauro, I., Caggia, M. P., Garzonio, C. A., & Grandin, C. (2020). Technological knowledge and conservation issues: the Roman cements of Santa Reparata Cathedral in Florence. *Journal of Cultural Heritage*, 46, 154-161.

Centauro, I., Cantisani, E., Grandin, C., Salvini, A., & Vettori, S. (2017). The influence of natural organic materials on the properties of traditional lime-based mortars. *International Journal of Architectural Heritage*, 11(5), 670-684.

Centauro, I., Vitale, J. G., Calandra, S., Salvatici, T., Natali, C., Coppola, M., ... & Garzonio, C. A. (2022). A Multidisciplinary methodology for technological knowledge, characterization and diagnostics: sandstone facades in florentine architectural heritage. *Applied Sciences*, 12(9), 4266.

Chu, V., Regev, L., Weiner, S., & Boaretto, E. (2008). Differentiating between anthropogenic calcite in plaster, ash and natural calcite using infrared spectroscopy: implications in archaeology. *Journal of Archaeological Science*, 35(4), 905-911.

Colleparidi, M. (1990). Degradation and restoration of masonry walls of historical buildings. *Materials and Structures*, 23, 81–102.

Cotte, M., Gonzalez, V., Vanmeert, F., Monico, L., Dejoie, C., Burghammer, M., ... & Susini, J. (2022). The “historical materials BAG”: A new facilitated access to synchrotron X-ray diffraction analyses for cultural heritage materials at the European synchrotron radiation facility. *Molecules*, 27(6), 1997.

Couronné, R., Probst, P., & Boulesteix, A. L. (2018). Random forest versus logistic regression: a large-scale benchmark experiment. *BMC bioinformatics*, 19, 1-14.

Cizer, Ö., Rodriguez-Navarro, C., Ruiz-Agudo, E., Elsen, J., Van Gemert, D., & Van Balen, K. (2012). Phase and morphology evolution of calcium carbonate precipitated by carbonation of hydrated lime. *Journal of Materials Science*, 47(16), 6151-6165.

De Luca, R., Miriello, D., Pecci, A., Domínguez-Bella, S., Bernal-Casasola, D., Bloise, A., & Crisci, G. M. (2015). Archaeometric study of mortars from the Garum shop at Pompeii, Campania, Italy. *Geoarchaeology*, 30(4), 330–351.

Dilaria, S., Previato, C., Secco, M., Busana, M. S., Bonetto, J., Cappellato, J., ... & Tan, P. (2022). Phasing the history of ancient buildings through PCA on mortars'

mineralogical profiles: the example of the Sarno Baths (Pompeii). *Archaeometry*, 64(4), 866-882.

Demauro, T. (2020). Lo studio delle malte. Strumento di verifica. In T. Demauro (Ed.), *Restauri a Pompei (1748– 1860). Studi e Ricerche del Parco Archeologico di Pompei* 44. (pp. 143–161). «L’Erma» di Bretschneider.

De Bonis, A., Febraro, S., Germinario, C., Giampaola, D., Grifa, C., Guarino, V., ... & Morra, V. (2016). Distinctive volcanic material for the production of Campana A Ware: The workshop area of Neapolis at the Duomo Metro Station in Naples, Italy. *Geoarchaeology*, 31(6), 437-466.

Davey, N. (1961). *A History of Building Materials* (London: Phoenix House), 260.

Daugbjerg, T. S., Lindroos, A., Hajdas, I., Ringbom, Å., & Olsen, J. (2021a). Comparison of thermal decomposition and sequential dissolution—Two sample preparation methods for radiocarbon dating of lime mortars. *Radiocarbon*, 63(2), 405-427.

Dodson, V. H. (1990). *Concrete admixtures*. Springer US.

Daugbjerg, T. S., et al. (2021b). A field guide to mortar sampling for radiocarbon dating. *Archaeometry*, 63(5), 1121-1140.

De Giorgi M. 2018. Divine liturgy and human skills in the architectural sculpture from the Church of the Apostle in Hierapolis (Phrygia). In: Şimşek C, Kaçar T, editors. *The Lykos Valley and neighbourhood in Late Antiquity*. 2nd International Symposium on Archaeological Practises, Laodikeia. Istanbul. p. 291–307.

Elert, K., Rodriguez-Navarro, C., Pardo, E. S., Hansen, E., & Cazalla, O. (2002). Lime mortars for the conservation of historic buildings. *Studies in Conservation*, 47(3), 177-188.

- Elsen, J. (2006). Microscopy of historic mortars—a review. *Cement and Concrete Research*, 36, 1416-1424
- Fedi, M. (2009). Accelerator mass spectrometry for <sup>14</sup>C dating. In *Organic Mass Spectrometry in Art and Archaeology* (pp. 459).
- Folk, R., & Valastro, S. (1976). Successful technique for dating of lime mortar by carbon-14. *Journal of Field Archaeology*.
- Farmer, V. C. (1974). The Infrared Spectra of Minerals. Mineralogical society monograph, 4, 331-363.
- Frankeová, D., & Koudelková, V. (2020). Influence of ageing conditions on the mineralogical micro-character of natural hydraulic lime mortars. *Construction and Building Materials*, 264, 120205.
- Fiori, C., Vandini, M., Prati, S., & Chiavari, G. (2009). Vaterite in the mortars of a mosaic in the Saint Peter basilica, Vatican (Rome). *Journal of Cultural Heritage*, 10(2), 248-257.
- Fan, X., Ming, W., Zeng, H., Zhang, Z., & Lu, H. (2019). Deep learning-based component identification for the Raman spectra of mixtures. *Analyst*, 144(5), 1789-1798.
- Fedi, M. E., Cartocci, A., Manetti, M., Taccetti, F., & Mandò, P. A. (2007). The <sup>14</sup>C AMS facility at LABEC, Florence. *Nuclear Instruments and Methods in Physics Research Section B: Beam Interactions with Materials and Atoms*, 259(1), 18-22.
- Fedi, M., Barone, S., Barile, F., Liccioli, L., Manetti, M., & Schiavulli, L. (2020). Towards micro-samples radiocarbon dating at INFN-LABEC, Florence. *Nuclear Instruments and Methods in Physics Research Section B: Beam Interactions with Materials and Atoms*, 465, 19-23.

Goedicke, C. (2003). Dating historical calcite mortar by blue OSL: results from known age samples. *Radiation Measurements*, 37(4-5), 409-415.

Goedicke, C. (2011). Dating mortar by optically stimulated luminescence: a feasibility study. *Geochronometria*, 38(1), 42-49.

Gueli, A. M., Stella, G., Troja, S. O., Burrafato, G., Fontana, D., Ristuccia, G., & Zuccarello, A. R. (2010). Historical buildings: Luminescence dating of fine grains from bricks and mortar. *Il Nuovo Cimento B*, 125(5-6), 719-729.

Hajdas, I., Lindroos, A., Heinemeier, J., Ringbom, Å., Marzaioli, F., Terrasi, F., ... & Guibert, P. (2017). Preparation and dating of mortar samples—Mortar Dating Inter-comparison Study (MODIS). *Radiocarbon*, 59(6), 1845-1858.

Hao, J., & Ho, T. K. (2019). Machine learning made easy: a review of scikit-learn package in python programming language. *Journal of Educational and Behavioral Statistics*, 44(3), 348-361.

Hobbs, L. W., & Siddall, R. (2011). Cementitious materials of the ancient world. *Commentationes Humanarum Litterarum*, 128, 35-60.

Hayen, R., et al. (2017). Mortar dating methodology: assessing recurrent issues and needs for further research. *Radiocarbon*, 59(6), 1859-1871.

Heaton, T. J., et al. (2020). Marine20 - The marine Radiocarbon age calibration curve (0-55000 CAL BP). *Radiocarbon*.

Heinemeier, J., et al. (1997). AMS 14C dating of lime mortar. *Nuclear Instruments and Methods in Physics Research Section B: Beam Interactions with Materials and Atoms*, 123(1-4), 487-495.

Heinemeier, J., et al. (2010). Successful AMS C-14 dating of non-hydraulic lime mortars from the medieval churches of the Aland Islands, Finland. *Radiocarbon*, 52(1), 171-204.



Heinemeier, J., Jungner, H., Lindroos, A., Ringbom, Å., von Konow, T., & Rud, N. (1997). AMS 14C dating of lime mortar. *Nuclear Instruments and Methods in Physics Research Section B: Beam Interactions with Materials and Atoms*, 123(1-4), 487-495.

Izzo, F., Grifa, C., Germinario, C., Mercurio, M., De Bonis, A., Tomay, L., ... & Langella, A. (2018). Production technology of mortar-based building materials from the Arch of Trajan and the Roman Theatre in Benevento, Italy. *The European Physical Journal Plus*, 133(8), 363.

Jackson, M. D., Moon, J., Gotti, E., Taylor, R., Chae, S. R., Kunz, M., ... & Monteiro, P. J. (2013). Material and elastic properties of Al-tobermorite in ancient Roman seawater concrete. *Journal of the American Ceramic Society*, 96(8), 2598-2606.

Jain, M., Bøtter-Jensen, L., S. Murray, A., & Jungner, H. (2002). Retrospective dosimetry: dose evaluation using unheated and heated quartz from a radioactive waste storage building. *Radiation protection dosimetry*, 101(1-4), 525-530.

Jain, M., Thomsen, K. J., Bøtter-Jensen, L., & Murray, A. S. (2004). Thermal transfer and apparent-dose distributions in poorly bleached mortar samples: results from single grains and small aliquots of quartz. *Radiation Measurements*, 38(1), 101-109.

Joosten, I. (1999). Die Analyse der Mörtel im Steinfachwerk von Pompeji. In K. Peterse (Ed.), *Steinfachwerk in Pompeji Bautechnik und Architektur* (pp. 77–106). J.C. Gießen Publisher.

Keaveney, E. M., Barrett, G. T., Allen, K., & Reimer, P. J. (2021). A new ramped pyrooxidation/combustion facility at 14CHRONO, Belfast: setup description and initial results. *Radiocarbon*, 63(4), 1273-1286.

Kuckova, S., Hynek, R., & Kodicek, M. (2009). Application of peptide mass mapping on proteins in historical mortars. *Journal of Cultural Heritage*, 10(2), 244-247.

Kutschera, W. (2013). Applications of Accelerator Mass Spectrometry. *International Journal of Mass Spectrometry*.

Lanas, J., Bernal, J. P., Bello, M. A., & Galindo, J. A. (2004). Mechanical properties of natural hydraulic lime-based mortars. *Cement and Concrete Research*, 34(12), 2191-2201.

Lezzerini, M., Ramacciotti, M., Cantini, F., Fatighenti, B., Antonelli, F., Pecchioni, E., ... & Giamello, M. (2017). Archaeometric study of natural hydraulic mortars: the case of the Late Roman Villa dell'Oratorio (Florence, Italy). *Archaeological and Anthropological Sciences*, 9, 603-615.

Libby, W. (1964). Radiocarbon Dating. Nobel lectures, Chemistry 1942-1962.

Lichtenberger, A., Lindroos, A., Raja, R., & Heinemeier, J. (2015). Radiocarbon analysis of mortar from Roman and Byzantine water management installations in the northwest quarter of Jerash, Jordan. *Journal of Archaeological Science Reports*, 2, 114–121.

Liu, G. L., Kazarian, S. G. (2022). Recent advances and applications to cultural heritage using ATR-FTIR spectroscopy and ATR-FTIR spectroscopic imaging. *Analyst*, 147(9), 1777-1797.

Lindroos, A. (2005). Carbonate phase in historical lime mortars and pozzolana concrete: implications for <sup>14</sup>C dating. Department of Geology and Mineralogy, Abo Akademi University.

Lindroos, A., Heinemeier, J., Ringbom, Å., Braskén, M., & Sveinbjörnsdóttir, Á. (2007). Mortar dating using AMS <sup>14</sup>C and sequential dissolution: examples from medieval, non-hydraulic lime mortars from the Åland Islands, SW Finland. *Radiocarbon*, 49(1), 47-67.

Lindroos, A., Heinemeier, J., Ringbom, Å., Brock, F., Sonck-Koota, P., Pehkonen, M., & Suksi, J. (2011). Problems in radiocarbon dating of Roman pozzolana mortars.

Building Roma Aeterna. Current Research On Roman Mortar and Concrete. 214-230.

Lubritto, C., Ricci, P., Germinario, C., Izzo, F., Mercurio, M., Langella, A., ... & Grifa, C. (2018). Radiocarbon dating of mortars: Contamination effects and sample characterisation. The case-study of Andalusian medieval castles (Jaén, Spain). *Measurement*, 118, 362-371.

Maragh, J. M., Weaver, J. C., & Masic, A. (2019). Large-scale micron-order 3D surface correlative chemical imaging of ancient Roman concrete. *PloS one*, 14(2), e0210710.

Maravelaki-Kalaitzaki, P., Bakolas, A., & Moropoulou, A. (2003). Physico-chemical study of Cretan ancient mortars. *Cement and Concrete Research*, 33(5), 651-661.

Mariani, E. (1976). *Leganti: Aerei e idraulici*. Casa editrice ambrosiana, Milano.

Martini, M., Castellano, A., & Sibilìa, E. (2002). *Elementi di archeometria: metodi fisici per i beni culturali*. Milano: EGEA. pp 26-63.

Marshall, J. D. (1991). *Cathodoluminescence of geological materials* by DJ Marshall, Unwin Hyman, 1988. ISBN 004 5520267.

Martinet, G., & Quenée, B. (2000). Proposal for a useful methodology for the study of ancient mortars. In P. Bartos, C. Groot, & J. J. Hughes (Eds.), *Historic Mortars: Characteristics and Tests* (pp. 81–91). Chapman & Hall.

Marzaioli, F., et al. (2011). Mortar radiocarbon dating: preliminary accuracy evaluation of a novel methodology. *Analytical Chemistry*, 83(6), 2038-2045.

Massazza, F. (1998). Pozzolana and pozzolanic cements. In *Lea's Chemistry of Cement and Concrete* (4th Ed.) (P.C. Hewlett, Ed.), pp. 471-635. Oxford, UK: Butterworth-Heimann.

Massazza, F. (2003). Pozzolana and Pozzolanic cements. In P. C. Hewlett (Ed.), *Lea's chemistry of cement and concrete* (pp. 471–635). Butterworth-Heinemann.

Megna, B., Rizzo, G., & Ercoli, L. (2010). The mortars and plasters under the mosaics and the wall paintings of the Roman villa at Piazza Armerina, Sicily. In Proceedings of the 2nd Conference on Historic Mortars - HMC 2010 and RILEM TC 203-RHM final workshop (pp. 275-283).

Menicali, U. (1992). I materiali dell'edilizia storica: tecnologia e impiego dei materiali tradizionali.

Michalska, D., & Czernik, J. (2015). Carbonates in leaching reactions in context of <sup>14</sup>C dating. Nuclear Instruments and Methods in Physics Research Section B: Beam Interactions with Materials and Atoms, 361, 431-439.

Michalska, D., & Mrozek-Wysocka, M. (2020). Radiocarbon dating of mortars and charcoals from novae bath complex: sequential dissolution of historical and experimental mortar samples with pozzolanic admixture. Radiocarbon, 62(3), 579-590.

Michalska, D., Czernik, J., & Goslar, T. (2017). Methodological aspects of mortars dating (Poznań, Poland, MODIS). Radiocarbon, 59(6), 1891-1906.

Miriello, D., Barca, D., Bloise, A., Ciarallo, A., Crisci, G. M., De Rose, T., ... & La Russa, M. F. (2010). Characterisation of archaeological mortars from Pompeii (Campania, Italy) and identification of construction phases by compositional data analysis. Journal of Archaeological Science, 37(9), 2207-2223.

Miriello, D., Bloise, A., Crisci, G. M., De Luca, R., De Nigris, B., Martellone, A., Osanna, M., Pace, R., Pecci, A., & Ruggieri, N. (2018). New compositional data on ancient mortars and plasters from Pompeii (Campania— Southern Italy): Archaeometric results and considerations about their time evolution. Materials Characterization, 146, 189–203.

Miyata, S., 1983. Anion-exchange properties of hydrotalcite-like compounds. Clays and Clay Minerals 31, 305-311.

Moropoulou, A., Bakolas, A., Anagnostopoulou, S. (2005). Composite materials in ancient structures. *Cement and Concrete Composites*, 27, 295-300.

Moropoulou, A., Bakolas, A., & Bisbikou, K. (1995). Characterization of ancient, Byzantine and later historic mortars by thermal and X-ray diffraction techniques. *Thermochimica Acta*, 269-270, 779–795.

Morra, V., DE BONIS, A., Grifa, C., Langella, A., Cavassa, L., & Piovesan, R. (2013). Minerograpic study of cooking ware and Pompeian red ware (Rosso Pompeiano) from Cuma (Southern Italy). *Archaeometry*, 55(5), 852-879.

Murakami, T., Hodgins, G., & Simon, A. W. (2013). Characterization of lime carbonates in plasters from Teotihuacan, Mexico: preliminary results of cathodoluminescence and carbon isotope analyses. *Journal of Archaeological Science*, 40(2), 960-970.

Nawrocka, D., Czernik, J., & Goslar, T. (2009). <sup>14</sup>C dating of carbonate mortars from Polish and Israeli sites. *Radiocarbon*, 51(2), 857-866.

Nonni, S. (2014). An innovative method to select a suitable fraction for mortar <sup>14</sup>C dating: the Cryo2Sonic protocol. PhD Thesis.

Nonni, S., Marzaioli, F., Mignardi, S., Passariello, I., Capano, M., & Terrasi, F. (2018). Radiocarbon dating of mortars with a Pozzolana aggregate using the Cryo2Sonic protocol to isolate the binder. *Radiocarbon*, 60(2), 617-637.

NORMA UNI (Ente Nazionale Italiano Unificazione). (2001). EN 10924 - Malte per elementi costruttivi e decorativi – Classificazione e terminologia. Milano.

NORMA UNI 11176, 2006 – Descrizione petrografica di una malta. Ed. UNI (Ente Nazionale Italiano Unificazione) Milano.

NORMA UNI EN 14630, 2007. Prodotti e sistemi per la protezione e la riparazione delle e la riparazione delle strutture di calcestruzzo. Metodi di prova.

Determinazione della profondità di carbonatazione di un calcestruzzo indurito con il metodo della fenolftaleina. Milano: Ed. UNI (Ente Nazionale Italiano Unificazione).

Oleson, J. P., Brandon, C., Cramer, S. M., Cucitore, R., Gotti, E., & Hohlfelder, R. L. (2004). The ROMACONS project: a contribution to the historical and engineering analysis of hydraulic concrete in Roman maritime structures. *International Journal of Nautical Archaeology*, 33(2), 199–299.

Olsson, I. (1968). Modern aspects of radiocarbon datings. *Earth-Science Reviews*.

Ortega, L. A., Zuluaga, M. C., Alonso-Olazabal, A., Murelaga, X., Insausti, M., & Ibañez-Etxeberria, A. (2012). Historic lime-mortar 14C dating of Santa Maria la Real (Zarautz, northern Spain): extraction of suitable grain size for reliable 14C dating. *Radiocarbon*, 54(1), 23-36.

Panzeri, L., Caroselli, M., Galli, A., Lugli, S., Martini, M., & Sibilìa, E. (2019). Mortar OSL and brick TL dating: The case study of the UNESCO world heritage site of Modena. *Quaternary Geochronology*, 49, 236-241.

Palma-Ruiz, J. M., Torres-Toukoumidis, A., González-Moreno, S. E., & Valles-Baca, H. G. (2022). An overview of the gaming industry across nations: using analytics with power BI to forecast and identify key influencers. *Heliyon*.

Pecchioni, E., Malesani, P., Bellucci, B., & Fratini, F. (2005). Artificial stones utilised in Florence historical palaces between the XIX and XX centuries. *Journal of Cultural Heritage*, 6(3), 227-233.

Pecchioni, E., Fratini, F., Cantisani, E. (2018). *Le malte antiche e moderne: tra tradizione ed innovazione*. Pàtron.

Pecchioni, E., Fratini, F., & Cantisani, E. (2020). *Atlas of the Ancient Mortars in Thin Section under Optical Microscope* (2nd ed.). Nardini, Florence, Italy.

Perrin, J., Vielzeuf, D., Laporte, D., Ricolleau, A., Rossman, G. R., & Floquet, N. (2016). Raman characterization of synthetic magnesian calcites. *American Mineralogist*, 101(11), 2525-2538.

Pesce, G., et al. (2009). Radiocarbon dating of lumps from aerial lime mortars and plasters: methodological issues and results from S. Nicolò of Capodimonte Church (Camogli, Genoa-Italy). *Radiocarbon*, 51, 867-872.

Pesce, G., et al. (2012). Identification, extraction, and preparation of reliable lime sample for <sup>14</sup>C dating of plasters and mortars with the “pure lime lumps” technique. *Proceedings of the 6th International Radiocarbon and Archaeology Symposium*. *Radiocarbon*, 54(3-4), 933-942.

Poduska, K. M., Regev, L., Boaretto, E., Addadi, L., Weiner, S., Kronik, L., & Curtarolo, S. (2011). Decoupling local disorder and optical effects in infrared spectra: differentiating between calcites with different origins. *Advanced Materials*, 23(4), 550-554.

Ponce-Antón, G., Ortega, L. A., Zuluaga, M. C., Alonso-Olazabal, A., & Solaun, J. L. (2018). Hydrotalcite and hydrocalumite in mortar binders from the medieval castle of portilla (Álava, north Spain): Accurate mineralogical control to achieve more reliable chronological ages. *Minerals*, 8(8), 326.

Principi, G., Bortolotti, V., Sani, F., Mannori, G., Babbini, A., Corti, S., & Tanini, A. (2008). Carta Geologica d'Italia alla scala 1: 50.000. Foglio 278-Pieve S. Stefano. - Servizio Geologico d'Italia.

Regev, L., Poduska, K. M., Addadi, L., Weiner, S., & Boaretto, E. (2010). Distinguishing between calcites formed by different mechanisms using infrared spectrometry: archaeological applications. *Journal of Archaeological Science*, 37(12), 3022-3029.

Reimer, P. J., et al. (2020). The IntCal20 Northern Hemisphere radiocarbon age calibration curve (0-55 kcal BP). *Radiocarbon*.

Riccardi, M. P., Lezzerini, M., Car, F., Franzini, M., & Messiga, B. (2007). Microtextural and microchemical studies of hydraulic ancient mortars: two analytical approaches to understand pre-industrial technology processes. *Journal of Cultural Heritage*, 8, 350-360.

Ricci, G., Secco, M., Artioli, G., Marzaioli, F., Passariello, I., & Valluzzi, M. R. (2020, October). The contribution of archaeometric analyses to the multi-disciplinary research in Hierapolis of Phrygia, Turkey. In *Proceedings of IMEKO TC-4 MetroArchaeo 2020-International Conference on Metrology for Archaeology and Cultural Heritage*. Trento, Italy (pp. 22-24).

Ricci, G., Secco, M., Marzaioli, F., Terrasi, F., Passariello, I., Addis, A., ... & Artioli, G. (2020). The Cannero Castle (Italy): Development of radiocarbon dating methodologies in the framework of the layered double hydroxide mortars. *Radiocarbon*, 62(3), 617-631.

Ricci, G., Secco, M., Addis, A., Pistilli, A., Preto, N., Brogiolo, G. P., ... & Artioli, G. (2022). Integrated multi-analytical screening approach for reliable radiocarbon dating of ancient mortars. *Scientific Reports*, 12(1), 3339.

Richter, D. K., Götze, T., Götze, J., & Neuser, R. D. (2003). Progress in application of cathodoluminescence (CL) in sedimentary petrology. *Mineralogy and Petrology*, 79, 127-166.

Ringbom, Å., et al. (2014). 19 years of mortar dating: Learning from experience. *Radiocarbon*, 56(2), 619–635.

Rispoli, C., De Bonis, A., Guarino, V., Graziano, S. F., Di Benedetto, C., Esposito, R., ... & Cappelletti, P. (2019). The ancient pozzolanic mortars of the Thermal complex of Baia (Campi Flegrei, Italy). *Journal of Cultural Heritage*, 40, 143-154.



Rispoli, C., Graziano, S. F., Di Benedetto, C., De Bonis, A., Guarino, V., Esposito, R., ... & Cappelletti, P. (2019). New insights of historical mortars beyond pompeii: The example of Villa del Pezzolo, Sorrento Peninsula. *Minerals*, 9(10), 575.

Rodriguez-Navarro, C., Ruiz-Agudo, E., Luque, A., Rodriguez-Navarro, A. B., & Ortega-Huertas, M. (2009). Thermal decomposition of calcite: Mechanisms of formation and textural evolution of CaO nanocrystals. *American Mineralogist*, 94(4), 578-593.

Rodriguez-Navarro, C., Kudłacz, K., Cizer, Ö., & Ruiz-Agudo, E. (2015). Formation of amorphous calcium carbonate and its transformation into mesostructured calcite. *CrystEngComm*, 17(1), 58-72

Sabbioni, C., Zappia, G., Riontino, C., Blanco-Varela, M. T., Aguilera, J., Puertas, F., ... & Toumbakari, E. E. (2001). Atmospheric deterioration of ancient and modern hydraulic mortars. *Atmospheric Environment*, 35(3), 539-548.

Sartori, R. Alberese: Zone di estrazione, suoi impieghi nel passato e sue varietà. *Boll. Ing.* 2007, 12, 15–18

Secco, M., Valentini, L., & Addis, A. (2019). Ancient and modern binders: naturally nanostructured materials. In *Nanotechnologies and Nanomaterials for Diagnostic, Conservation and Restoration of Cultural Heritage* (pp. 205-237). Elsevier.

Seymour, L. M., Keenan-Jones, D., Zanzi, G. L., & Masic, A. (2021). Reactive Synthetic Pozzolans in Mortars from Ancient Water Infrastructure Serving Rome and Pompeii. Available at SSRN 3885241.

Seymour, L. M., Maragh, J., Sabatini, P., Di Tommaso, M., Weaver, J. C., & Masic, A. (2023). Hot mixing: Mechanistic insights into the durability of ancient Roman concrete. *Science Advances*, 9(1), eadd1602.

Siddall, R. (2000). The use of volcanoclastic material in Roman hydraulic concretes: a brief review. Geological Society, London, Special Publications, 171(1), 339-344.

- Sufi, F. K. (2022). AI-GlobalEvents: A Software for analyzing, identifying and explaining global events with Artificial Intelligence. *Software Impacts*, 11, 100218.
- Surovell, T. A., & Stiner, M. C. (2001). Standardizing infrared measures of bone mineral crystallinity: an experimental approach. *Journal of Archaeological science*, 28(6), 633-642.
- Schiele, E., & Berens, L. W. (1976). *La calce: calcare, calce viva, idrato di calcio, fabbricazione, caratteristiche, impieghi*. Milano: Edizioni Tecniche ET.
- Toffolo, M. B., Regev, L., Mintz, E., Poduska, K. M., Shahack-Gross, R., Berthold, C., ... & Boaretto, E. (2017). Accurate radiocarbon dating of archaeological ash using pyrogenic aragonite. *Radiocarbon*, 59(1), 231-249.
- Toffolo, M. B., Ricci, G., Caneve, L., & Kaplan-Ashiri, I. (2019). Luminescence reveals variations in local structural order of calcium carbonate polymorphs formed by different mechanisms. *Scientific Reports*, 9(1), 16170.
- Toffolo, M. B., Regev, L., Mintz, E., Kaplan-Ashiri, I., Berna, F., Dubernet, S., ... & Boaretto, E. (2020). Structural characterization and thermal decomposition of lime binders allow accurate radiocarbon age determinations of aerial lime plaster. *Radiocarbon*, 62(3), 633-655.
- Toffolo, M. B., Ricci, G., Chapoulie, R., Caneve, L., & Kaplan-Ashiri, I. (2020). Cathodoluminescence and laser-induced fluorescence of calcium carbonate: a review of screening methods for radiocarbon dating of ancient lime mortars. *Radiocarbon*, 62(3), 545-564.
- Toffolo, M. B., Pinkas, I., Gallo, A. Á., & Boaretto, E. (2023). Crystallinity assessment of anthropogenic calcites using Raman micro-spectroscopy. *Scientific Reports*, 13(1), 12971.
- Tuniz, C. (2001). Accelerator mass spectrometry: ultra-sensitive analysis for global science. *Radiation Physics and Chemistry*, 61(3-6), 317-322.

- Van Strydonck, M., Dupas, M., & Dauchot-Dehon, M. (1983). Radiocarbon dating of old mortars. *PACT Journal*, 8, 337–343.
- Van Strydonck, M., et al. (1992). Radiocarbon dating of lime fractions and material from buildings. *Radiocarbon*, 34(3), 873–9.
- Veiga, M. R., Velosa, A., & Magalhaes, A. (2009). Experimental applications of mortars with pozzolanic additions: Characterization and performance evaluation. *Construction and building materials*, 23(1), 318-327.
- Ventolà, L., Vendrell, M., Giraldez, P., & Merino, L. (2011). Traditional organic additives improve lime mortars: New old materials for restoration and building natural stone fabrics. *Construction and Building Materials*, 25(8), 3313-3318.
- Vettori, S., Cabassi, J., Cantisani, E., & Riminesi, C. (2019). Environmental impact assessment on the stone decay in the archaeological site of Hierapolis (Denizli, Turkey). *Science of the Total Environment*, 650, 2962-2973.
- Wang, Q., Allred, D. D., & Knight, L. V. (1995). Deconvolution of the Raman spectrum of amorphous carbon. *Journal of Raman Spectroscopy*, 26(12), 1039-1043.
- Wang, D., Xiong, C., Li, W., & Chang, J. (2020). Growth of calcium carbonate induced by accelerated carbonation of tricalcium silicate. *ACS Sustainable Chemistry & Engineering*, 8(39), 14718-14731.
- Wehrmeister, U., Jacob, D. E., Soldati, A. L., Loges, N., Häger, T., & Hofmeister, W. (2011). Amorphous, nanocrystalline and crystalline calcium carbonates in biological materials. *Journal of Raman Spectroscopy*, 42(5), 926-935.
- Weiner, S. (2010). *Microarchaeology. Beyond the visible archaeological record.* Cambridge University Press.
- Whitney, D. L., & Evans, B. W. (2010). Abbreviations for names of rock-forming minerals. *American mineralogist*, 95(1), 185-187.

Xu, B., & Poduska, K. M. (2014). Linking crystal structure with temperature-sensitive vibrational modes in calcium carbonate minerals. *Physical Chemistry Chemical Physics*, 16(33), 17634-17639.

Xu, B., Toffolo, M. B., Regev, L., Boaretto, E., & Poduska, K. M. (2015). Structural differences in archaeologically relevant calcite. *Analytical Methods*, 7(22), 9304-9309.

Zolotoyabko, E., Caspi, E. N., Fieramosca, J. S., Von Dreele, R. B., Marin, F., Mor, G., ... & Politi, Y. (2010). Differences between bond lengths in biogenic and geological calcite. *Crystal Growth & Design*, 10(3), 1207-1214.

Zhang, D., Zhao, J., Wang, D., Xu, C., Zhai, M., & Ma, X. (2018). Comparative study on the properties of three hydraulic lime mortar systems: Natural hydraulic lime mortar, cement-aerial lime-based mortar and slag-aerial lime-based mortar. *Construction and Building Materials*, 186, 42-52.

Zhu, C., Idemudia, C. U., & Feng, W. (2019). Improved logistic regression model for diabetes prediction by integrating PCA and K-means techniques. *Informatics in Medicine Unlocked*, 17, 100179.

Zhu, J., Ding, J., Zhang, P., Dong, W., Zhao, X., Camaiti, M., & Li, X. (2021). In-situ growth synthesis of nanolime/kaolin nanocomposite for strongly consolidating highly porous dinosaur fossil. *Construction and Building Materials*, 300, 124312.

## Acknowledgements

I would like to thank my Supervisor and Co-Supervisor for their scientific and emotional support, as well as to my colleagues at the LAM-DST-UNIFI laboratory, particularly Elena Pecchioni, Teresa Salvatici, and Irene Centauro; Giacomo Casa and Matteo Maria Niccolò Franceschini (for Pompeian activity), the researchers Claudia Conti, Fabio Fratini, Barbara Salvadori and Tommaso Ismaelli (ISPC-CNR), Lucia Liccioli and Serena Barone (INFN-LABEC in Florence).

Additionally, appreciation is extended to Laura Chiarantini and Tiziano Catalani (Centro di Servizi M.E.M.A.) for their technical assistance in the SEM-EDS analysis, Celestino Grifa (DST, UniSannio) for analysis support of Pompeian mortars, well as to Silvia Danise (DST-UNIFI) for providing access to OM-CL instrumentation.

## Appendix 1: The instrumentation and specific analytical methodology

### Carbonation test

The phenolphthalein test (standardized by UNI EN 14630, 2007) is carried out using a 1% solution of phenolphthalein in ethyl alcohol. Applied to the surface of the freshly cut sample.

### Optical microscope

The Axioscope A.1 Zeiss transmitted light polarizing optical microscope, connected to a digital video camera, allowed for the acquisition of sample images in thin sections, which were processed using AxioVision software. Microscopes were used in the laboratories of ISPC-CNR (Institute of Heritage Science in Sesto Fiorentino), and UNIFI-DST-LAM (Department of Earth Sciences in Florence), Italy. The acquired images were further analyzed to obtain information on the morphological and morphometric characteristics of the samples using the ImageJ program.

### Scanning Electron Microscopy with Energy-Dispersive X-ray Spectroscopy (SEM-EDS)

The ZEISS EVO MA 15 SEM-EDS with a tungsten filament and an energy-dispersive X-ray spectroscopy (EDS) analytical system, Oxford Ultimex 40 (with a resolution of 127 eV @5.9 keV and an area of 40 mm<sup>2</sup>), was utilized for semi-quantitative microchemical and morphological analyses. These analyses were conducted on thin sections (prepared after carbon-metallized pre-treatment) taken from both the binder and lumps areas, as well as from powder samples. The operational settings were as follows: an acceleration potential of 15 kV, a beam current of 500 pA, a working distance of 9–8.5 mm, a live time of 20 s to achieve an acquisition rate of at least 600,000 counts using Co standard, a process time of 4 for point analyses, and a pixel dwell time of 500 μs for map acquisition with a resolution of 1024 × 768 pixels. The microanalysis employed the Aztec 5.0 SP1 software, implementing the XPP matrix correction scheme. This process utilized

purchased standard elements for calculations, enabling "standard-less" quantitative analysis. Constant analytical conditions, such as filament emission, were monitored through numerous analyses of a Co metallic standard. Microscope was used in laboratory of UNIFI-DST-MEMA (Centro di Servizi di Microscopia Elettronica e Microanalisi) in Florence, Italy.

#### X-ray powder diffraction

The mineralogical composition was analyzed using a Philips X'Pert PRO X-ray powder diffractometer (XRPD) with a Cu anticathode (wavelength  $\lambda = 1.54 \text{ \AA}$ ). The instrument operated at a current intensity of 30 mA and a voltage of 40 kV. The  $2\theta$  range explored was between 3 and  $70^\circ$  with a step size of  $0.02^\circ$  and a time to step of 50 s. XRPD analyses were conducted on both powder bulk samples and specific lumps. Instrument was used in the laboratory of ISPC-CNR (Institute of Heritage Science in Sesto Fiorentino), Italy.

#### Thermo-gravimetric analysis

Thermogravimetric analyses (TGA) were carried out on historical mortar samples using two different systems: a Perkin Elmer Pyris 6 system and Netzsch TG 209 F3 Tarsus (instruments used in laboratories of ISPC-CNR (Institute of Heritage Science in Sesto Fiorentino) and UNISANNIO-DST (Department of Science and Technology, University of Sannio in Benevento), Italy). Fragments from each sample were mechanically broken down using a porcelain pestle, and the portion passing through a sieve with  $63 \mu\text{m}$  openings (ISO R 565 Series) was selected as a binder-enriched specimen. About 5 mg of the sample was used for TGA, and the analysis was conducted within the temperature range of  $110\text{--}1000^\circ\text{C}$ . The samples were dried using silica gel as a desiccant at room temperature for a minimum of one week. The TGA experiments were performed in open alumina crucibles, with a heating rate of  $10^\circ\text{C}/\text{min}$ , and a nitrogen gas flow of  $30 \text{ mL}/\text{min}$ .

### Fourier transform infrared spectroscopy

FTIR ALPHA Bruker was used in transmission mode and equipped with an ATR system. The spectra obtained from the analysis of the powdered sample were acquired and processed using OPUS 7.2 software (Bruker Optics GmbH, Ettlingen, Germany) and Spectragryph 1.2.15.. The acquisition was carried out in the spectral range between 4000 and 400  $\text{cm}^{-1}$ , with a resolution of 4  $\text{cm}^{-1}$  for 24 scans. Instrument was used in the laboratory of ISPC-CNR (Institute of Heritage Science in Sesto Fiorentino), Italy.

### Cathodoluminescence

Optical cathodoluminescence (CL) analysis was conducted using the CL8100 MK5 model by Cambridge Image Technology Ltd., coupled with a Leica DM2700P polarization optical microscope. The microscope is equipped with a high-sensitivity 12 MP Leica Flexcam C1 camera and dedicated LAS X software, enabling the acquisition of digital images in various formats. Instrument was used in the laboratory of UNIFI-DST (Department of Earth Sciences in Florence), Italy.

### FPA spectroscopy

A Bruker LUMOS II micro-FTIR (Bruker Optics GmbH, Ettlingen, Germany), equipped with a 32x32 element cooled liquid nitrogen Focal Plane Array (FPA) detector, was utilized for chemical imaging. The FPA-FTIR images were acquired in Reflection mode within a spectral range of 4000–750  $\text{cm}^{-1}$ . Each FPA-FTIR image consisted of 1024 spectra, covering a sampling area of approximately 150 x 150  $\text{mm}^2$ , with a resolution of 4  $\text{cm}^{-1}$  and 128 scans. A single spectrum in each FTIR image represents molecular information acquired from an area of about 5 x 5  $\mu\text{m}^2$  on the sample surface. The background was acquired on a gold mirror prior to measurements. The collected FTIR spectra were processed using OPUS 8.2 software. Instrument was used in the laboratory of ISPC-CNR (Institute of Heritage Science in Sesto Fiorentino), Italy.



## ID13 beamline at the European Synchrotron Radiation Facility (ESRF) ( $\mu$ XRPD)

Experiments in X-ray microdiffraction were conducted at the ID13 beamline situated in the European Synchrotron Radiation Facility–Grenoble. ID13 is a specialized ESRF undulator beamline dedicated to high-lateral-resolution diffraction and scattering studies utilizing focused monochromatic X-ray beams. A micro-branch with a beam size of approximately  $2 \times 2 \mu\text{m}^2$  was utilized. Samples were mounted in a vertical orientation, perpendicular to the X-ray beam. The incident beam's energy was set at approximately 13.0 keV. The energy was carefully selected to slightly excite Pb L3-edge XRF, without saturating the XRF detector or significantly attenuating the beam's transmission through the material and, consequently, the XRPD intensity. The beam was focused to about  $2 \times 2 \mu\text{m}^2$  (with a flux of approximately  $2 \times 10^{12}$  ph/s, at  $I = 128$  mA electron beam current) using a compound refractive lens set-up (CRL) mounted in a transfocator. XRPD maps were generated by raster-scanning the samples and capturing 2D XRPD patterns in transmission. A Dectris EIGER 4 M single photon counting detector with  $2070 \times 2167$  pixels (pixel size of  $75 \times 75 \mu\text{m}^2$ ) was employed, achieving a frame acquisition rate of up to 750 Hz. A dwell time of 10 ms was typically adequate to detect most crystalline phases while minimizing the risk of beam damage.

## Raman spectroscopy

A Renishaw InVia Raman spectrometer, characterized by high resolution, was utilized in combination with a Leica DMLM microscope. The experiments involved employing a 785 nm excitation line, a 50x long working distance objective (NA 0.5), a spectral resolution better than  $1 \text{ cm}^{-1}$ , and a theoretical laser spot diameter of  $1.9 \mu\text{m}$ . The laser operated at a power of 80 mW, and each spectrum was acquired over a period of 5 s. Our focus was primarily on the low-to-medium region of the spectral range, specifically collecting data within the range of  $100\text{-}1400 \text{ cm}^{-1}$ . Instrument was used in the laboratory of ISPC-CNR (Institute of Heritage Science in Milan), Italy.

## Statistical methods

Two technologies, Microsoft PowerBI and Python, have been used to build a data analysis workflow, aimed to distinguish groups of the spectral data acquired for the different calcite samples and to identify their characteristic Raman spectral features. Another objective of the data analysis was to evaluate the accuracy to identify geogenic and anthropogenic calcite from spectral data through a comparison between machine learning models. Raman spectra data are stored in a dataframe: each parameter collected from Raman spectra is called "feature" (or "variable"); the 2 possible classes of the target variable are geogenic or anthropogenic calcite. For each variable, outliers are detected and removed by the Interquartile Range (IQR) method, calculated in Python.

Then, visual inspection is carried out in PowerBI, directly connected to the dataframe, through the Key Influence Factor (KIF) visual, that performs ML.NET SDCA regression implementation.

According to the second step, PCA was performed in Python, using the `sklearn.decomposition.PCA` function. Before applying PCA, data is standardized using `StandardScaler`, a function implemented in `scikit-learn` package, so that all features are at the same scale. From the transformed dataframe after PCA, K-means Clustering in PowerBI Clustering visual is performed. Then, the dataframe has been randomly divided into a training set and testing set (with a 70:30 split ratio) in Python. A comparison between Logistic Regression and Random Forest models, is performed in Python, with `scikit-learn` function `LogisticRegression` and `RandomForestClassifier`, on the PCA components, setting up a repeated K-fold Cross Validation with `scikit-learn` function `KFold` on the training set, in order to find the best fit to describe the relationship between the target variable and the predictor variables.

## Appendix 2 Supplementary information

*Table 1 Petrographic description of mortar and plaster samples from Trebbio Castle (B/A = binder/aggregate ratio).*

ID sample	Binder	Aggregate	B/A	Macroporosity
CT1	Natural hydraulic lime with homogeneous structure and micritic texture. Recrystallized binder Presence of unburned lumps	Composition: fragments of serpentinitic rocks, sandstone, micritic limestone, sparitic calcite, quartz, plagioclase, micas. Well-selected and bimodal grain size Grain size: 400-600 µm, 1-1.5 mm Shape: subrounded-subangular	1/3	Low amount due to pores of irregular shape and shrinkage fractures
CT2	Natural hydraulic lime with homogeneous structure and micritic texture. Presence of unburned lumps	Composition: fragments of serpentinitic rocks, sandstone, micritic limestone, sparitic calcite, quartz, plagioclase, micas. Well-selected and bimodal grain size Grain size: 400-600 µm, 1-1.5 mm Shape: subrounded-subangular	1/3	Low amount due to pores of irregular shape and shrinkage fractures
CT3	Natural hydraulic lime with homogeneous structure and micritic texture. Recrystallized binder Presence of unburned lumps	Composition: fragments of serpentinitic rocks, sandstone, micritic limestone, sparitic calcite, quartz, plagioclase, micas. Well-selected and bimodal grain size Grain size: 400-600 µm, 2-2.5 mm Shape: subrounded-subangular	1/3	Low amount due to pores of irregular shape and shrinkage fractures
CT4	Natural hydraulic lime with homogeneous structure and micritic texture. Recrystallized binder Presence of unburned lumps	Composition: quartz, plagioclase, sparitic calcite, fragments of serpentinitic rocks, sandstone, micritic limestone, cocchiopesto. Well-selected and bimodal grain size Grain size: 300-500 µm, 1-1.5 mm	1/3- 1/4	Low amount due to pores of irregular shape

		Shape: subrounded-subangular		
CT5	Natural hydraulic lime with homogeneous structure and micritic texture. Recrystallized binder Numerous lumps (unmixed lime, unburned rock)	Composition: quartz, feldspars, sparitic calcite, fragments of serpentinitic rocks, sandstone, micritic limestone. Bimodal grain size distribution Grain size: 150-300 $\mu\text{m}$ , 0.6-1 mm Shape: subrounded-subangular	1/2-1/3	Low amount due to shrinkage fractures
CT6	Natural hydraulic lime with homogeneous structure and micritic texture. Recrystallized binder Numerous lumps (mainly unmixed lime)	Composition: single crystals of quartz and feldspars, sparitic calcite, sandstone fragments and rare granules of cocchiopesto. Unimodal grain size distribution Grain size: 100-200 $\mu\text{m}$ Shape: subrounded-subangular	1/1-1/2	Low amount due to shrinkage fractures
CT7	Natural hydraulic lime with homogeneous structure and micritic texture. Recrystallized binder Numerous lumps (mainly unmixed lime)	Composition: single crystals of quartz and feldspars, sparitic calcite, sandstone fragments and rare granules of cocchiopesto. Unimodal grain size distribution Grain size: 100-300 $\mu\text{m}$ Shape: subrounded-subangular	1/1-1/2	Low amount due to shrinkage fractures
CT8	Natural hydraulic lime with homogeneous structure and micritic texture. Recrystallized binder Numerous lumps (mainly unmixed lime)	Composition: single crystals of quartz and plagioclase, sparitic calcite, sandstone fragments and rare granules of cocchiopesto. Unimodal grain size distribution Grain size: 100-300 $\mu\text{m}$ Shape: subrounded-subangular	1/1-1/2	Low amount due to shrinkage fractures
CT9	Natural hydraulic lime with homogeneous structure and micritic texture. Numerous lumps (mainly unburned rock)	Composition: single crystals of quartz and plagioclase, sparitic calcite, sandstone fragments and rare granules of cocchiopesto. Unimodal grain size distribution Grain size: 150-400 $\mu\text{m}$ Shape: subangular	1/3	Low amount due to shrinkage fractures

CT10	Natural hydraulic lime with homogeneous structure and micritic texture. Recrystallized binder Numerous lumps (mainly unmixed lime)	Composition: single crystals of quartz and plagioclase, less presence: sparitic calcite, sandstone fragments and rare granules of cocchiopesto. Unimodal grain size distribution Grain size: 200-300 µm Shape: subangular	1/1- 1/2	Low amount, due to shrinkage fractures
CT11	Natural hydraulic lime with homogeneous structure and micritic texture. Numerous lumps (mainly unmixed lime)	Composition: single crystals of quartz and plagioclase, less presence: sparitic calcite, sandstone fragments and rare granules of cocchiopesto. Unimodal grain size distribution Grain size: 150-250 µm Shape: subangular	3/1	Low amount, due to shrinkage fractures
CT12	Natural hydraulic lime with homogeneous structure and microsparitic texture with small dark inclusions. Numerous lumps (mainly unmixed lime)	Composition: single crystals of quartz and plagioclase, less presence: sparitic calcite, sandstone fragments and rare granules of cocchiopesto. Unimodal grain size distribution Grain size: 400-600 µm Shape: subangular	1/2	Low amount, due to shrinkage fractures
CT13	Natural hydraulic lime with homogeneous structure and microsparitic/sparitic texture with small dark inclusions. Recrystallized binder One unburned lump	Composition: fragments of sandstone and micritic limestone, from single crystals of quartz and feldspars, secondarily sparitic calcite and rare granules of cocchiopesto. Bimodal grain size distribution Grain size: 400-600 µm, 1-1.5 mm Shape: subrounded-subangular	1/2	Low amount, due to shrinkage fractures
CT14	Natural hydraulic lime with homogeneous structure and microsparitic/sparitic texture with small dark inclusions. Recrystallized binder One unburned lump	Composition: fragments of sandstone and micritic limestone, from single crystals of quartz and feldspars, secondarily sparitic calcite and rare granules of cocchiopesto. Bimodal grain size distribution Grain size: 400-600 µm, 1-1.5 mm Shape: subrounded-subangular	1/2	Low amount, due to shrinkage fractures
CT15	Natural hydraulic lime with homogeneous structure and microsparitic texture.	Composition: single crystals of quartz and feldspars, less presence: sandstone	1/1	Low amount, due to shrinkage fractures

		fragments and rare granules of cocchiopesto. Unimodal grain size distribution Grain size: 350-600 $\mu\text{m}$ Shape: subrounded-subangular		
CT16	Natural hydraulic lime with homogeneous structure and microsparitic texture with small dark inclusions. Recrystallized binder. Rare lumps	Composition: fragments of sandstone and micritic limestone, from single crystals of quartz and plagioclase, secondarily sparitic calcite and rare granules of cocchiopesto. Unimodal grain size distribution Grain size: 400-600 $\mu\text{m}$ Shape: subangular	1/2	Low amount, due to shrinkage fractures
CT17	Natural hydraulic lime with homogeneous structure and micritic texture with small dark inclusions. Numerous lumps (unmixed lime, unburned rock)	Composition: fragments of sandstone and micritic limestone, from single crystals of quartz and plagioclase, secondarily sparitic calcite and rare serpentinitic fragments. Unimodal grain size distribution Grain size: 400-600 $\mu\text{m}$ , 0.6-1 mm Shape: subrounded-subangular	1/1- 1/2	Low amount due to shrinkage fractures
CT18	Natural hydraulic lime with homogeneous structure and microsparitic texture with small dark inclusions. Recrystallized binder. Rare lumps	Composition: fragments of sandstone and micritic limestone, from single crystals of quartz and plagioclase, secondarily calcite spatia and rare granules of cocchiopesto. Unimodal grain size distribution Grain size: 400-700 $\mu\text{m}$ Shape: subangular	1/3	Low amount, due to shrinkage fractures
CT19	Natural hydraulic lime with homogeneous structure and micritic texture with small dark inclusions. Numerous lumps (unmixed lime)	Composition: fragments of sandstone and micritic limestone, single crystals of quartz and plagioclase, secondarily sparitic calcite and rare serpentinitic fragments. Unimodal grain size distribution Grain size: 400-600 $\mu\text{m}$ Shape: subangular	1/2- 1/3	Low amount due to shrinkage fractures
CT20	Natural hydraulic lime with homogeneous structure and	Composition: fragments of sandstone and micritic limestone, single crystals of	1/2- 1/3	Low amount due to shrinkage fractures

	micritic texture with small dark inclusions. Numerous lumps (unmixed lime, unburned rock)	quartz and plagioclase, secondarily sparitic calcite and rare serpentinitic fragments. Unimodal grain size distribution Grain size: 400-600 µm Shape: subrounded-subangular		
CT21	Natural hydraulic lime with homogeneous structure and microsparitic texture with small dark inclusions. Recrystallized binder. Numerous lumps (unmixed lime, unburned rock)	Composition: fragments of sandstone and micritic limestone, from single crystals of quartz and plagioclase, secondarily sparitic calcite and rare granules of cocciopesto. Unimodal grain size distribution Grain size: 400-800 µm Shape: subangular	1/3	Low amount, due to shrinkage fractures
CT22	Natural hydraulic lime with homogeneous structure and microsparitic texture with small dark inclusions. Recrystallized binder. Numerous lumps (unmixed lime)	Composition: fragments of sandstone and micritic limestone, from single crystals of quartz and plagioclase, secondarily sparitic calcite and rare serpentinitic fragments. Unimodal grain size distribution Grain size: 400-700 µm Shape: subangular	1/2	Low amount, due to shrinkage fractures
CT23	Natural hydraulic lime with homogeneous structure and micritic texture with small dark inclusions. Numerous lumps (unmixed lime)	Composition: fragments of sandstone and micritic limestone, single crystals of quartz and plagioclase, secondarily sparitic calcite and rare serpentinitic fragments. Unimodal grain size distribution Grain size: 400-700 µm Shape: subangular	1/2-1/3	Low amount due to shrinkage fractures
CT24	Natural hydraulic lime with homogeneous structure and micritic texture with small dark inclusions. Numerous lumps (unmixed lime, unburned rock)	Composition: fragments of sandstone and micritic limestone, single crystals of quartz and plagioclase, secondarily sparitic calcite and rare serpentinitic fragments. Unimodal grain size distribution Grain size: 300-600 µm Shape: subangular	1/2	Low amount due to shrinkage fractures
CT25	Natural hydraulic lime with homogeneous structure and micritic texture with small dark inclusions.	Composition: fragments of sandstone and micritic limestone, single crystals of quartz and plagioclase,	1/2	Low amount due to shrinkage fractures

	Numerous lumps (unmixed lime, unburned rock)	secondarily sparitic calcite and rare serpentinitic fragments. Unimodal grain size distribution Grain size: 300-600 $\mu\text{m}$ Shape: subangular		
CT26	Natural hydraulic lime with homogeneous structure and micritic texture with small dark inclusions. Numerous lumps (unmixed lime, unburned rock)	Composition: fragments of sandstone and micritic limestone, single crystals of quartz and plagioclase, secondarily sparitic calcite and rare serpentinitic fragments. Bimodal grain size distribution Grain size: 200-300 $\mu\text{m}$ , 700-800 $\mu\text{m}$ Shape: subangular	1/3	Low amount due to shrinkage fractures
CT27	Natural hydraulic lime with homogeneous structure and micritic texture with small dark inclusions. Numerous lumps (unmixed lime, unburned rock)	Composition: fragments of sandstone and micritic limestone, single crystals of quartz and plagioclase, secondarily sparitic calcite and rare serpentinitic fragments. Bimodal grain size distribution Grain size: 200-300 $\mu\text{m}$ , 0.7-1 mm Shape: subangular	1/2	Low amount due to shrinkage fractures

Table 2 Petrographic description of mortar samples from S. Felicita Church (B/A = binder/aggregate ratio).

ID sample	Binder	Aggregate	B/A	Macroporosity
SFC1	Natural hydraulic lime with heterogeneous structure and micritic/microsparitic texture with small dark inclusions. Numerous lumps (mainly unmixed lime)	Composition: fragments of sandstone, mono and polycrystalline quartz, feldspars, micas, fragments of carbonate rocks, siltitis and few granules of cocchiopesto. Well-selected and unimodal grain size Grain size: 200-400 $\mu\text{m}$ , 1-1.5 mm Shape: subrounded-subangular	1/2	Low amount, due to pores of irregular shape
SFC2	Natural hydraulic/aerial lime with heterogeneous structure and micritic/microsparitic texture. Superficial layer	Composition: mono and polycrystalline quartz, feldspars, micas, fragments of sandstone, carbonate rocks and few granules of cocchiopesto.	1/3-1/4	Medium amount due to pores of subrounded shape



	No lumps	Well-selected and seriate grain size Grain size: 100-600 $\mu\text{m}$ Shape: subrounded-subangular		
SFC3	Hydraulic lime binder hydraulicized with pozzolanic fragments and with a microsparitic texture. Recrystallized binder No lumps	Composition: quartz, feldspars, spirititic calcite, micas and fragments of sandstone and limestone. Not selected and unimodal grain size Grain size: 100-700 $\mu\text{m}$ , (100-500 $\mu\text{m}$ pozzolanic fragments) Shape: subrounded-subangular	1/3-1/4	Medium amount due to pores of subrounded shape
SFC4	Natural hydraulic/aerial lime with heterogeneous structure and micritic/microsparitic texture. No lumps	Composition: mono and polycrystalline quartz, feldspars, micas, fragments of sandstone, carbonate rocks and few granules of cocciopesto. Not selected and seriate grain size Grain size: 100-600 $\mu\text{m}$ Shape: subrounded-subangular	1/4	Medium amount due to pores of subrounded and irregular shape
SFC5	Natural hydraulic lime with homogeneous structure and micritic/microsparitic texture with small dark inclusions. Some lumps (mainly unmixed lime)	Composition: single crystals of quartz and feldspars, less presence: sandstone fragments and rare granules of cocciopesto. Well-selected and unimodal grain size distribution Grain size: 150-400 $\mu\text{m}$ Shape: subrounded-subangular	1/1	Low amount due to pores of irregular shape
SFC8	Natural hydraulic lime with homogeneous structure and microsparitic texture. Recrystallized binder Some lumps (mainly unmixed lime)	Composition: single crystals of quartz and feldspars, micas, less presence: fragments of carbonate rocks, sandstone, siltitis and rare granules of cocciopesto. Well-selected and unimodal grain size distribution Grain size: 100-500 $\mu\text{m}$ Shape: subrounded-subangular	1/3	Low amount due to pores of irregular shape
SFC9	Hydraulic lime binder hydraulicized with pozzolanic fragments and with a microsparitic texture. Recrystallized binder	Composition: quartz, feldspars, spirititic calcite, micas and fragments of sandstone and limestone.	1/3-1/4	Medium amount due to pores of subrounded shape

	No lumps	Not selected and unimodal grain size Grain size: 100-700 µm, (also pozzolanic fragments) Shape: subrounded-subangular		
SFC10	Natural hydraulic lime with homogeneous structure and microsparitic texture. Recrystallized binder Some lumps (mainly unmixed lime)	Composition: single crystals of quartz and feldspars, micas, less presence: fragments of carbonate rocks, sandstone, siltitis and rare granules of cocchiopesto. Well-selected and unimodal grain size distribution Grain size: 100-500 µm Shape: subrounded-subangular	1/3	Low amount due to pores of irregular shape

*Table 3 Petrographic description of mortar and plaster samples from Medici Riccardi Palace (B/A = binder/aggregate ratio).*

ID sample	Binder	Aggregate	B/A	Macroporosity
PMRC1(13-15)cm	Natural hydraulic lime with homogeneous structure and micritic texture with small dark inclusions. Some lumps (mainly unburned rock)	Composition: single crystals of quartz plagioclase, k feldspar, less presence: sparitic calcite, sandstone fragments, siltitis and iron oxides. Well-selected and homogeneous grain size distribution, bimodal Grain size: 250-300 µm, 650-700 µm Shape: subangular	1/2	Low amount, due to subrounded shape
PMRC1(58-63)cm	Natural hydraulic lime with heterogeneous structure, micritic texture with small dark inclusions. Partial carbonation Some lumps (mainly unburned rock)	Composition: single crystals of quartz plagioclase, k feldspar, less presence: sparitic calcite, sandstone fragments, siltitis and iron oxides. Well-selected and homogeneous grain size distribution, bimodal Grain size: 250-300 µm, 650-700 µm Shape: subangular	1/2	Low amount, due to subrounded shape
PMRC3(40-41)cm	Natural hydraulic lime with heterogeneous structure,	Composition: mono and poly-crystalline quartz,	1/3-1/4	Medium amount due to pores of

	micritic texture with small dark inclusions. Partial carbonation Numerous lumps	plagioclases, micas, fragments of sparitic calcite, and carbonate rocks (calcarenites, fossiliferous rocks), sandstone, cocchiopesto. Not selected grain size Grain size: 200-500 µm up to 1mm Shape: subangular		subrounded shape
PMRC3(55-56)cm	Natural hydraulic/aerial lime with heterogeneous structure and micritic texture with small dark inclusions. Partial carbonation Numerous lumps	Composition: mono and polycrystalline quartz, plagioclases, micas, fragments of sparitic calcite, and carbonate rocks (calcarenites, fossiliferous rocks), sandstones, cocchiopesto. Not selected grain size Grain size: 200-500 µm up to 1mm Shape: subangular	1/3-1/4	Medium amount due to pores of subrounded
PMRC4(20-21)cm	Natural hydraulic lime with homogeneous structure and micritic texture with small dark inclusions. Some lumps (mainly unmixed lime)	Composition: mono and polycrystalline quartz, sparitic calcite, micas, plagioclases, fragments of carbonate rocks (calcarenites, fossiliferous rocks), sandstones, siltitis, cocchiopesto. Not selected grain size Grain size: 300-500 µm up to 1mm Shape: subangular	1/3-1/4	Low amount due to pores of irregular shape
PMRC4(53-54)cm	Natural hydraulic lime with homogeneous structure and micritic texture with small dark inclusions. Partial carbonation Numerous lumps (unmixed lime, unburned rock)	Composition: mono and polycrystalline quartz, sparitic calcite, micas, plagioclases, fragments of carbonate rocks (calcarenites, fossiliferous rocks), sandstones, siltitis, cocchiopesto. Not selected grain size Grain size: 300-500 µm up to 1mm Shape: subangular	1/3-1/4	Medium-low amount due to pores of irregular shape and shrinkage fractures
PMRC5(17-20)cm	Natural hydraulic lime with homogeneous structure and micritic texture with small dark inclusions. Some lumps (unmixed lime, unburned rock)	Composition: single crystals of quartz plagioclase, k feldspar, less presence: sparitic calcite, sandstone fragments, siltitis and iron oxides.	1/2-1/3	Low amount, due to subrounded shape

		Well-selected and homogeneous grain size distribution, bimodal Grain size: 250-300 $\mu\text{m}$ , 650-700 $\mu\text{m}$ Shape: subangular		
PMRC5(45-47)cm	Natural hydraulic lime with homogeneous structure and micritic texture with small dark inclusions. Numerous lumps (unmixed lime, unburned rock)	Composition: single crystals of quartz plagioclase, k feldspar, less presence: sparitic calcite, sandstone fragments, siltitis and iron oxides. Well-selected and homogeneous grain size distribution, bimodal Grain size: 250-300 $\mu\text{m}$ , 650-700 $\mu\text{m}$ Shape: subangular	1/2	Medium-high amount, due to subrounded shape and shrinkage fractures
PMRC6(16-17)cm	Natural hydraulic lime with homogeneous structure and micritic texture with small dark inclusions. Numerous lumps (unmixed lime, unburned rock)	Composition: mono and polycrystalline quartz, sparitic calcite, micas, plagioclases, fragments of carbonate rocks (calcarenites, fossiliferous rocks), sandstones, siltitis, cocchiopesto and iron oxides. Not selected grain size Grain size: 300-500 $\mu\text{m}$ up to 1 mm Shape: subangular	1/3	Low amount due to pores of irregular shape and shrinkage fractures
PMRC6(31-32)cm	Natural hydraulic lime with homogeneous structure and micritic texture with small dark inclusions. Numerous lumps (unmixed lime, unburned rock)	Composition: mono and polycrystalline quartz, plagioclase, micas, sparitic calcite, fragments of carbonate rocks (calcarenites, fossiliferous rocks), sandstones, siltitis, cocchiopesto and iron oxides. Not selected grain size Grain size: 300-500 $\mu\text{m}$ up to 1 mm Shape: subangular	1/3	Medium-low amount, due to subrounded shape and shrinkage fractures
PMRC7(17-18)cm	Natural hydraulic lime with homogeneous structure and micritic texture with small dark inclusions. Numerous lumps (unmixed lime, unburned rock)	Composition: single crystals of quartz plagioclase, k feldspar, less presence: sparitic calcite, sandstone fragments, siltitis and iron oxides. Well-selected and homogeneous grain size distribution, bimodal	1/2	Low amount, due to subrounded shape

		Grain size: 200-300 µm, 600-700 µm Shape: subangular		
PMRC7(49-51)cm	Natural hydraulic lime with homogeneous structure and micritic texture with small dark inclusions. Numerous lumps (unmixed lime, unburned rock)	Composition: single crystals of quartz plagioclase, k feldspar, less presence: sparitic calcite, sandstone fragments, siltitis and iron oxides. Well-selected and homogeneous grain size distribution, bimodal Grain size: 250-300 µm, 650-700 µm Shape: subangular	1/2	Medium-low amount, due to subrounded shape and shrinkage fractures

Table 4 Petrographic description of mortar and plaster samples from S. Giovanni Baptistery (B/A = binder/aggregate ratio).

ID sample	Binder	Aggregate	B/A	Macroporosity
BG1(10-15)cm	Natural hydraulic lime with heterogeneous structure and micritic/microsparitic texture. Recrystallized binder Numerous lumps	Composition: quartz (monocrystalline), feldspars, rock fragments (quartzite, arenaceous, calcarenite, micritic carbonate) and few <i>cocciopesto</i> grains Homogeneous grain size distribution Grain size: 100 µm-700 µm Shape: sub rounded	1/3-1/4	Medium amount due to pores of irregular shape
BG2(9-14)cm	Natural hydraulic lime with heterogeneous structure and micritic/microsparitic texture. Recrystallized binder Numerous lumps	Composition: quartz (monocrystalline), feldspars, spatic calcite, rock fragments (quartzite, arenaceous, calcarenite, micritic calcite) Homogeneous grain size distribution Grain size 100 µm- >1 mm Shape: sub angular/ sub rounded	1/3-1/4	Medium amount due to pores of irregular shape
BG3(9-25)cm	Natural hydraulic lime with homogeneous structure and micritic texture. Recrystallized binder Some lumps	Composition: quartz (monocrystalline), feldspars, spatic calcite, quartzite, few carbonates rock fragments and <i>cocciopesto</i> Homogeneous grain size distribution	1/3	Medium amount due to pores elongated and sub rounded shape

BG3(25–30)cm	Natural hydraulic lime with homogeneous structure and micritic texture. Recrystallized binder Numerous lumps	Mean grain size 150-200 µm, few mm grains Shape: sub angular Composition: quartz (monocrystalline), feldspars, rock fragments (quartzite, calcarenite, micritic carbonate, flint) and few <i>cocciopesto</i> grains Homogeneous grain size distribution Grain size 100 µm- >1 mm Shape: sub angular	1/3	Medium amount due to pores of sub rounded shape
BG4(4–20)cm	Natural hydraulic lime with heterogeneous structure and micritic/microsparitic texture. Slight recrystallized binder Some lumps	Composition: quartz (monocrystalline), feldspars, rock fragments (quartzite, arenaceous, calcarenite, micritic carbonate) and few <i>cocciopesto</i> grains Homogeneous grain size distribution Grain size: 100 µm-700 µm Shape: sub angular	1/3	Medium amount due to microcracks and pores of sub rounded shape
BG4(20–35)cm	Natural hydraulic lime with heterogeneous structure and micritic/microsparitic texture. Recrystallized binder Some lumps	Composition: quartz (monocrystalline), feldspars, rock fragments (quartzite, arenaceous, calcarenite, micritic carbonate) and few <i>cocciopesto</i> grains Homogeneous grain size distribution Grain size 100 µm-1 mm Shape: sub angular/ sub rounded	1/2-1/3	Medium-high amount due to pores of irregular and sub rounded shape
BG5(7–12)cm	Natural hydraulic lime with heterogeneous structure and micritic/microsparitic texture. Recrystallized binder Numerous lumps	Composition: quartz (monocrystalline), feldspars, rock fragments (quartzite, arenaceous, micritic carbonate) Heterogeneous grain size distribution Grain size 100 µm - 600 µm Shape: sub angular/ sub rounded	1/3	Medium amount due to microcracks and pores of irregular shape
BG5(12–26)cm	Natural hydraulic lime with heterogeneous structure and micritic texture. Recrystallized binder. Numerous lumps	Composition: quartz (monocrystalline), feldspars, several fragments of carbonate rocks and quartzite, arenaceous rocks Homogeneous grain size distribution Grain size 100 µm - 600 µm	1/2-1/3	Medium amount due to pores of irregular and sub rounded shape

BG5(26–38)cm	Natural hydraulic lime with heterogeneous structure and micritic/microsparitic texture. Recrystallized binder Numerous lumps	Shape: sub angular/ sub rounded Composition: quartz (monocrystalline), feldspars, rock fragments (quartzite, calcarenite, micritic carbonate, marble) and few <i>cocciopesto</i> grains Homogeneous grain size distribution Grain size 100 µm - 600 µm Shape: sub angular/ sub rounded	1/2-1/3	Medium amount due to microcracks and pores of sub rounded and irregular shape
BG6(0–10)cm	Natural hydraulic lime with heterogeneous structure and micritic/microsparitic texture. Recrystallized binder Some lumps	Composition: quartz (monocrystalline), feldspars, abundant fragments of carbonate rocks Homogeneous grain size distribution Grain size 100 µm – 1 mm Shape: sub angular/ sub rounded	1/3-1/4	High amount due to pores of irregular
BG6(10–32)cm	Natural hydraulic lime with heterogeneous structure and micritic/microsparitic texture. Recrystallized binder Some lumps	Composition: quartz (monocrystalline), feldspars, abundant fragments of carbonate rocks Homogeneous grain size distribution Grain size 100 µm – 1 mm Shape: sub angular/ sub rounded	1/3-1/4	High amount due to pores of irregular shape
BG7(0–11)cm	Natural hydraulic lime with heterogeneous structure and micritic/microsparitic texture. Recrystallized binder Some lumps	Composition: quartz (monocrystalline), feldspars, rock fragments (micritic carbonate, flint, quartzite, calcarenite) Homogeneous grain size distribution Grain size 100 µm – 1 mm Shape: sub angular/ sub rounded	1/3-1/4	High amount due to pores of irregular shape
BG7(11–32)cm	Natural hydraulic lime with heterogeneous structure and micritic/microsparitic texture. Some lumps	Composition: quartz (monocrystalline), feldspars, abundant fragments of carbonate rocks, fragments of arenaceous rocks Homogeneous grain size distribution Grain size 100 µm – 1 mm Shape: sub angular/ sub rounded	1/3-1/4	High amount due to pores of irregular shape

BG8(0–12)cm	Natural hydraulic lime with heterogeneous structure and micritic/microsparitic texture. Recrystallized binder Some lumps	Composition: quartz (monocrystalline), feldspars, quartzite, few fragments of carbonate rocks and flint Homogeneous grain size distribution Grain size 100 µm – 1 mm Shape: sub angular/ sub rounded	1/4	Medium/ high amount due to pores of irregular shape
BG8(12–38)cm	Natural hydraulic lime with heterogeneous structure and micritic/microsparitic texture. Numerous lumps	Composition: quartz (monocrystalline), feldspars, quartzite, few fragments of carbonate rocks Homogeneous grain size distribution Grain size 100 µm – 1 mm Shape: sub angular/ sub rounded	1/3-1/4	Low amount due to pores of irregular shape
BG9(0–11)cm	Natural hydraulic lime with heterogeneous structure and micritic/microsparitic texture. Recrystallized binder Some lumps	Composition: quartz (monocrystalline), feldspars, mica, quartzite, few fragments of carbonate rocks Homogeneous grain size distribution Grain size 100 µm – 500 µm Shape: sub angular/ sub rounded	1/3-1/4	High amount due to pores of irregular shape
BG9(11–21)cm	Natural hydraulic lime with heterogeneous structure and micritic/microsparitic texture. Recrystallized binder Some lumps	Composition: quartz (monocrystalline), feldspars, mica, quartzite, few fragments of carbonate rocks and <i>cocciopesto</i> Homogeneous grain size distribution Grain size 100 µm – 700 µm Shape: sub angular/ sub rounded	1/3-1/4	High amount due to pores of irregular shape
BG9(21–38)cm	Natural hydraulic lime with heterogeneous structure and micritic/microsparitic texture. Recrystallized binder. Some lumps	Composition: quartz (monocrystalline), feldspars, mica, quartzite, few fragments of carbonate rocks (with fossil, calcarenite) Homogeneous grain size distribution Grain size 100 µm – 500 µm Shape: sub angular/ sub rounded	1/3	High amount due to pores of irregular shape
BG10(0–15)cm	Natural hydraulic lime with heterogeneous structure and micritic/microsparitic texture. Recrystallized binder	Composition: quartz (monocrystalline), feldspars, mica, quartzite, large fragments of carbonate rocks (with fossil, calcarenite)	1/3	High amount due to pores of irregular shape



BG10(15–38)cm	Some lumps	Heterogeneous grain size distribution Grain size 100 µm – 700 µm Shape: sub angular	1/3	High amount due to pores of irregular shape
	Natural hydraulic lime with heterogeneous structure and micritic/microsparitic texture. Recrystallized binder Few lumps	Composition: quartz (monocrystalline), feldspars, mica, quartzite, calcite, abundant fragments of carbonate rocks (with fossil, calcarenite) and fragments of <i>cocciopesto</i> Heterogeneous grain size distribution Grain size 100 µm – 700 µm Shape: sub angular		
BG11(0–5)cm	Natural hydraulic lime with heterogeneous structure and micritic/microsparitic texture. Recrystallized binder Few lumps	Composition: quartz (monocrystalline), feldspars, rock fragments (micritic carbonate, flint, quartzite, marble) and few fragments of <i>cocciopesto</i> Homogeneous grain size distribution Grain size 100 µm – 800 µm Shape: sub angular	1/3-1/4	High amount due to pores of irregular shape
	Lime hydraulicized with crushed ceramics and heterogeneous structure and micritic/ microsparitic texture. Recrystallized binder	Composition: <i>cocciopesto</i> , calcite, carbonate fragments and some fragments of arenaceous rocks Heterogeneous grain size distribution (bimodal) Grain size 50 µm – 1 mm Shape: sub angular/ sub rounded	1/2-1/3	Medium amount due to pores of irregular shape
BG13(0–5)cm	Natural hydraulic lime with homogeneous structure and microsparitic texture. Recrystallized binder Some lumps	Composition: quartz (monocrystalline), feldspars, rock fragments (micritic carbonate, quartzite) and few fragments of <i>cocciopesto</i> Heterogeneous grain size distribution Grain size 100 µm – 800 µm Shape: sub angular	1/2	High amount due to pores of irregular shape
	Natural hydraulic lime with homogeneous structure and micritic texture. Recrystallized binder Some lumps	Composition: quartz (monocrystalline), feldspars, arenaceous rocks few fragments of carbonate and rare fragments of <i>cocciopesto</i> Homogeneous grain size distribution Grain size 100 µm – 500 µm Shape: sub angular	1/1-1/2	Medium amount due to pores of irregular shape

BG15(0–2)cm	Natural hydraulic lime with heterogeneous structure and micritic/microsparitic texture. Recrystallized binder Some lumps	Composition: quartz (monocrystalline), feldspars, few fragments of carbonate rocks and <i>cocciopesto</i> Homogeneous grain size distribution Grain size 100 µm – 500 µm Shape: sub angular/ sub rounded	1/3	High amount due to pores of irregular shape
BG16(4–12)cm	Natural hydraulic lime with heterogeneous structure and micritic/microsparitic texture. Recrystallized binder Some lumps	Composition: quartz (monocrystalline), feldspars, fragments of arenaceous rocks, few fragments of carbonate rocks and <i>cocciopesto</i> Homogeneous grain size distribution Grain size 100 µm – 500 µm Shape: sub angular	1/3-1/4	Medium amount due to pores of irregular shape
BG17(0–2)cm	Natural hydraulic lime with heterogeneous structure and micritic/microsparitic texture. Recrystallized binder Some lumps	Composition: quartz (monocrystalline), feldspars, few fragments of carbonate rocks and <i>cocciopesto</i> Homogeneous grain size distribution Grain size 100 µm – 800 µm Shape: sub angular	1/3	High amount due to pores of irregular shape

Table 5 Petrographic description of mortar and plaster samples from Pompeii (B/A = binder/aggregate ratio). The composition is in order of abundance. Abbreviations for names of rock-forming minerals in Whitney and Evans, 2010.

ID SAMPLE	Binder	Aggregate	B/A	Macroporosity
C01A EUMACHIA	Hydraulic lime (lime binder and pozzolan fragments) with heterogeneous structure and micritic/microsparitic texture. Rare lumps in millimetres	Composition: cryptocrystalline and hyaline lavas, pumice and scoriae, Cpx, Fds, Lct/Anl, Bt. Seriatic grain size Grain size: 200 µm up to pluri-mm (max size 9 mm) Shape: sub-angular - sub-rounded	1/3	Medium-low amount, due to pores of sub-spherical shape
C01C EUMACHIA	Hydraulic lime (lime binder and pozzolan fragments) with heterogeneous structure and micritic/microsparitic texture. Rare lumps in millimetres	Composition: microcrystalline and hyaline lavas, pumice and scoriae, Fds (Kfs, Pl), Cpx, Lct/Anl and Ol. Seriatic grain size Grain size: 200 µm up to pluri-mm (max size 5.1 mm) Shape: sub-angular - sub-rounded	1/3	Medium-low amount, due to pores of sub-spherical shape

C01D EUMACHIA	Hydraulic lime (lime binder and pozzolan fragments) with homogeneous structure and micritic texture. Numerous lumps (unmixed lime, unburned rock)	Composition: Cpx, marble, pumice, hyaline lavas, Pl, limestone, sandstone, Cal, Lct/Anl, Qtz. Seriatic grain size Grain size: <250 µm up to 4 mm Shape: sub-angular	1/4	Medium-low amount due to pores of irregular shape
C01E EUMACHIA	Hydraulic lime (lime binder and pozzolan fragments) with heterogeneous structure and microsparitic texture. Numerous reaction rims Recrystallized binder Numerous lumps (unmixed lime, unburned rock)	Composition: microcrystalline lavas, pumice, Cpx, Fds, scoriae, Bt and Lct/Anl. Unimodal grain size Grain size: 70-500 µm, (max size 2.5 mm) Shape: sub-rounded	1/3	Medium-low amount, due to pores of sub-spherical shape
C02A EUMACHIA	Hydraulic lime (lime binder and pozzolan fragments) with homogeneous structure and micritic texture. Numerous lumps (unmixed lime, unburned rock)	Composition: Cpx, scoriae, pumice, hyaline lavas, Pl, Ol and Lct/Anl, shards, limestone fragments. Unimodal grain size Grain size: 70-600 µm, rare 0.7-3 mm Shape: sub-rounded - sub-angular	1/2	Low amount, due to pores of sub-spherical shape
C02C EUMACHIA	Hydraulic lime (lime binder and pozzolan fragments) with heterogeneous structure and micritic/microsparitic texture. Numerous reaction rims Recrystallized/decay binder Some lumps	Composition: scoriae, pumice, hyaline lavas, Cpx, Pl, shards, Ol Unimodal grain size Grain size: 70-500 µm, rare up to 2.2 mm (max size 7 mm) Shape: sub-rounded	1/2	High amount, due to pores of sub-spherical shape and shrinkage fractures
C03A EUMACHIA	Hydraulic lime (lime binder and pozzolan fragments) with heterogeneous structure and micritic/microsparitic texture. Numerous reaction rims Recrystallized/decay binder Some lumps (also dark nodules)	Composition: scoriae, hyaline lava fragments, Cpx, Pl, Lct/Anl, pumice, Ol, shards Unimodal tends to skewed grain size Grain size: 100-500 µm, frequent 1mm up to 3 mm Shape: sub-angular – angular	1/2	Medium amount, due to pores of sub-spherical shape
C03C EUMACHIA	Hydraulic lime (lime binder and pozzolan fragments) with heterogeneous structure and microsparitic/sparitic texture. Recrystallized/decay binder Rare lumps	Composition: pumice, scoriae, Cpx and Fds (Kfs, Pl), Lct/Anl, microcrystalline lavas, Ol, Bt Unimodal grain size Grain size: 100-500 µm, rare grains up to 3 mm Shape: sub-rounded	1/3	Medium-high amount, due to pores of sub-spherical shape

C04A EUMACHIA	Hydraulic lime (lime binder and pozzolan fragments) with heterogeneous structure and micritic/microsparitic texture. Numerous reaction rims Recrystallized/decay binder Numerous lumps (also dark nodules)	Composition: microcrystalline lavas, pumice and scoriae, Fds (Kfs, Pl), Cpx, Lct/Anl, Ol Seriata grain size Grain size: 100 µm up to pluri-mm (max size 1.1 cm) Shape: angular	1/2	Medium amount, due to pores of sub-spherical shape
C04C EUMACHIA	Hydraulic lime (lime binder and pozzolan fragments) with heterogeneous structure and microsparitic texture. Numerous reaction rims Recrystallized binder Unburned lump (centimetre size)	Composition: lavas, scoriae (and lapilli), Fds (Pl, Kfs), Cpx, Lct/Anl, fragments of limestone, Ol Seriata grain size Grain size: 100 µm up to pluri-mm Shape: sub-rounded	1/2	Medium amount, due to pores of sub-spherical shape
C05 EUMACHIA	Hydraulic lime (lime binder and pozzolan fragments) with heterogeneous structure and micritic texture. Numerous reaction rims Recrystallized/decay binder Small recrystallized lumps	Composition: scoriae, pumice, hyaline and microcrystalline lavas, Pl, Cpx, Lct/Anl, shards, Ol Seriata grain size Grain size: 100 µm, up to pluri-mm (max size 9 mm) Shape: sub-rounded - sub-angular	1/1- 1/2	Low amount, due to shrinkage fractures
C06A GENIUS AUGUSTI	Hydraulic lime (lime binder and pozzolan fragments) with heterogeneous structure and micritic/microsparitic texture. Numerous reaction rims Recrystallized binder Numerous lumps (millimetre size, different types)	Composition: pumice, microcrystalline lavas, Cpx, Fds (Kfs, Pl), Ol and Lct/Anl. Seriata grain size Grain size: <200 µm up to 6 mm Shape: sub-rounded - sub-angular	1/3	Medium-high amount, due to pores of sub-spherical shape and shrinkage fractures
C07A GENIUS AUGUSTI	Hydraulic lime (lime binder and pozzolan fragments) with heterogeneous structure and micritic/microsparitic texture. Numerous reaction rims Numerous lumps (millimetre size, different types)	Composition: pumice, hyaline lava fragments, Fds (Pl), Cpx, <u>Ol</u> Grain size: n.d. (max size 1.3 mm) Shape: sub-rounded	n.d.	Medium-high amount, due to pores of sub-spherical shape and shrinkage fractures
C09 LARI PUBBLICI	Hydraulic lime (lime binder and pozzolan fragments) with heterogeneous structure and micritic texture. Some reaction rims	Composition: microcrystalline lavas, Fds, scoriae and pumice, Cpx, Bt and Grt. Unimodal grain size Grain size: 70-500 µm, rare 800 µm -1.2 mm	1/1	High amount, due to shrinkage fractures and pores of sub-spherical shape

Numerous lumps  
(unburned rock)

Shape: sub-rounded

C10A LARI PUBBLICI	Hydraulic lime (lime binder and pozzolan fragments) with heterogeneous structure and micritic/microsparitic texture. Some reaction rims Some recrystallized lumps	Composition: scoriae, hyaline and microcrystalline lavas, pumice, Cpx, Fds (Kfs, Pl), Lct/Anl, Bt and Ol Unimodal (skewed) grain size Grain size: 100-500 µm, rare up to pluri-mm (max size 4.2 mm) Shape: sub-rounded	1/2- 1/3	Medium-high amount, due to pores of sub-spherical shape
C10C LARI PUBBLICI	Hydraulic lime (lime binder and pozzolan fragments) with heterogeneous structure and micritic texture. Some reaction rims Numerous lumps (pluri-millimetre size and porous)	Composition: pumice, scoriae, cryptocrystalline and microcrystalline lavas (rare holocrystalline), Fds (Kfs, Pl), Cpx and Bt. Unimodal grain size Grain size: 100-500 µm, rare grains between 0.8-3 mm Shape: sub-rounded	1/2- 1/3	Medium amount, due to pores of irregular-sub-spherical shape
C11A LARI PUBBLICI	Hydraulic lime (lime binder and pozzolan fragments) with heterogeneous structure and microsparitic texture. Numerous reaction rims Recrystallized/decay binder Rare lumps	Composition: scoriae (analcime/leucite rich), pumice, lavas hyaline, Cpx, Fds, Lct/Anl and Bt. Unimodal grain size Grain size: 100-500 µm, max grains size 1.6 mm (rare between 0.6-1.6 mm) Shape: sub-rounded	1/2	Medium amount, due to pores of irregular-sub-spherical shape
C11C LARI PUBBLICI	Hydraulic lime (lime binder and pozzolan fragments) with heterogeneous structure and microsparitic texture. Some reaction rims Recrystallized/decay binder Rare lumps	Composition: pumice, scoriae, microcrystalline and hyaline lavas, Fds, Cpx, Lct/Anl and Bt. Unimodal grain size Grain size: 100-500 µm, rare grains between 0.8 - 2 mm Shape: sub-rounded	1/1	Medium amount, due to pores of irregular-sub-spherical shape
C11D LARI PUBBLICI	Hydraulic lime (lime binder and pozzolan fragments) with heterogeneous structure and microsparitic texture. Numerous reaction rims Recrystallized/decay binder Rare lumps	Composition: scoriae, hyaline lavas, pumice, Fds, Cpx, Bt. Unimodal grain size Grain size: 100-500 µm, rare 0.6-1.8 mm Shape: sub-rounded	1/2- 1/3	Medium-high amount, due to pores of sub-spherical shape

C12A MACELLUM	Hydraulic lime (lime binder and pozzolan fragments) with heterogeneous structure and microsparitic texture. Numerous reaction rims Recrystallized binder Some lumps (mm size and different types)	Composition: scoriae, pumice, Cpx, Fds (Kfs, Pl), hyaline and microcrystalline lavas Unimodal grain size Grain size: 60-400 µm, rare grains up to 1 mm. Shape: sub-rounded	1/1	Medium amount, due to shrinkage fractures
C12C MACELLUM	Hydraulic lime (lime binder and pozzolan fragments) with heterogeneous structure and microsparitic texture. n.d.	N.d Shape: sub-rounded.	n.d.	n.d.
C13A MACELLUM	Hydraulic lime (lime binder and pozzolan fragments) with heterogeneous structure and microsparitic texture. Numerous reaction rims Recrystallized binder Some lumps (unburned rock)	Composition: microcrystalline lavas, scoriae, pumice, Cpx, Fds (Kfs, Pl), Ol, Lct/Anl and Bt, shards. Unimodal grain size Grain size: 100-600 µm, rare between 1 - 2.5 mm Shape: sub-rounded - sub-angular	1/3	Medium amount, due to pores of irregular-sub-spherical shape
C13B MACELLUM	Hydraulic lime (lime binder and pozzolan fragments) with heterogeneous structure and micritic/microsparitic texture. Numerous reaction rims Recrystallized/decay binder Numerous lumps (unburned rock, unmixed binder and dark nodules)	Composition: hyaline and microcrystalline lavas, pumice, scoriae, Cpx, Fds (Pl, Kfs), Lct/Anl, shards. Seriate grain size Grain size: 150 µm, up to pluri-mm (max size 4.6 mm) Shape: sub-angular	1/3	Medium-high amount, due to pores of sub-spherical shape
C13C MACELLUM	Hydraulic lime (lime binder and pozzolan fragments) with heterogeneous structure and micritic/microsparitic texture. Numerous reaction rims Recrystallized binder Numerous lumps (unburned rock, unmixed binder and dark nodules)	Composition: (from hyaline to holocrystalline) lavas, Fds (Pl, Kfs), scoriae, Lct/Anl, Cpx, pumice, Ol. Seriated grain size Grain size: 70 µm, up to 4 mm Shape: sub-angular - sub-rounded	1/3	Medium amount, due to pores of sub-spherical shape
C13D MACELLUM	Hydraulic lime (lime binder and pozzolan fragments) with heterogeneous structure and micritic texture. Some reaction rims Numerous lumps (mm size of unmixed binder and dark nodules)	Composition: from hyaline to holocrystalline lavas, scoriae, pumice, Cpx, Pl, Lct/Anl, Bt and Ol, shards, limestone fragments. Seriated grain size Grain size: from 70 µm to 4.5 mm	1/3	Medium-high amount, due to pores of sub-spherical shape

			Shape: sub-angular – angular	
C14A MACELLUM	Hydraulic lime (lime binder and pozzolan fragments) with heterogeneous structure and micritic/microsparitic texture. Some reaction rims Recrystallized/decay binder Numerous lumps (unburned rock, unmixed binder and dark nodules)	Composition: microcrystalline lavas, scoriae, Cpx, Lct/Anl, pumices, Fds (Pl, Kfs), Ol and Grt. Seriated grain size Grain size: 100 µm up to 3.7 mm Shape: sub-rounded – angular	1/3	Medium-high amount, due to pores of sub-spherical shape
C14B MACELLUM	Hydraulic lime (lime binder and pozzolan fragments) with heterogeneous structure and micritic texture. Some reaction rims Numerous lumps (unmixed binder)	Composition: microcrystalline and hyaline lavas, scoriae, Cpx, pumices, Fds, Lct/Anl, Ol and Bt. Seriate grain size Grain size: 100 µm, up to pluri-mm (max size 6.9 mm) Shape: sub-rounded-angular	1/3	Medium-high amount, due to pores of sub-spherical shape
C14C MACELLUM	Hydraulic lime (lime binder and pozzolan fragments) with heterogeneous structure and micritic texture. Some reaction rims Rare lumps (unburned rock)	Composition: scoriae, hyaline and microcrystalline lavas, Fds (Pl, Kfs) and pumices, Cpx, Lct/Anl. Seriate grain size Grain size: 100 µm, up to pluri-mm (max size 6 mm) Shape: sub-rounded- sub-angular	1/2	Medium-high amount, due to pores of sub-spherical shape
C14F MACELLUM	Hydraulic lime (lime binder and pozzolan fragments) with heterogeneous structure and micritic texture. Some reaction rims Numerous lumps (unmixed binder and dark nodules)	Composition: hyaline and microcrystalline lavas, pumice, scoriae, Fds (Pl, Kfs), Cpx, Ol and Lct/Anl, dolomite fragment. Seriate grain size Grain size: 100 µm, up to pluri-mm (max size 5 mm) Shape: sub-rounded-angular	1/2	Medium-high amount, due to pores of sub-spherical shape
C15A TEMPLE OF JUPITER	Hydraulic lime (lime binder and pozzolan fragments) with heterogeneous structure and microsparitic texture. Recrystallized/decay binder Numerous lumps (unmixed binder and dark nodules)	Composition: scoriae, hyaline lavas, Fds, Cpx, pumice, Lct/Anl, shards, Bt and Ol. Tendentially Unimodal grain size Grain size: 100-500 µm, rare grains up to 2.5 mm Shape: sub-angular	1/3	Medium-high amount, due to pores of sub-spherical shape

C15C TEMPLE OF JUPITER	Hydraulic lime (lime binder and pozzolan fragments) with heterogeneous structure and micritic texture. Some reaction rims Numerous lumps (unmixed binder and dark nodules)	Composition: Cpx, scoriae, Fds (Pl, Kfs) and Lct/Anl, Ol, pumice, shards. Skewed grain size Grain size: 150-300 $\mu$ m, 0.8-2 mm Shape: sub-angular	1/1	Low amount
C16A ARCO GERMANICO	Hydraulic lime (lime binder and pozzolan fragments) with heterogeneous structure and microsparitic texture. Numerous reaction rims Recrystallized binder Some lumps (unburned rock)	Composition: microcrystalline and hyaline lavas, scoriae and pumice ( <u>and lapilli</u> ), Fds (Kfs, Pl), fictile fragments, Cpx, Ol. Seriate grain size Grain size: 150 $\mu$ m, up to pluri-mm (max size 3.8 mm) Shape: sub-rounded	1/2	Medium-high amount, due to pores of sub-spherical shape
C16B ARCO GERMANICO	Hydraulic lime (lime binder and pozzolan fragments) with heterogeneous structure and microsparitic texture. Some reaction rims Recrystallized binder Numerous lumps (unmixed binder and unburned rock)	Composition: microcrystalline and hyaline lavas, scoriae, Fds, pumice, fictile fragments, Cpx, Bt. Seriate grain size Grain size: 150 $\mu$ m, up to 2.5mm Shape: sub-rounded	1/3	High amount, due to pores of sub-spherical shape
C17A TEMPLE OF APOLLO	Hydraulic lime (lime binder and pozzolan fragments) with heterogeneous structure and micritic texture. Reuse mortar fragment Some reaction rims Numerous lumps (unmixed binder)	Composition: scoriae, reused mortar, hyaline lava fragments, pumice, Cpx, Fds (Kfs, Pl), fictile fragments, Lct/Anl and Ol, <u>Qtz</u> , shards. Seriated grain size Grain size: from 100 $\mu$ m to 3 mm Shape: sub-angular – angular	1/2	Low amount, due to pores of sub-spherical shape
C18A TEMPLE OF APOLLO	Hydraulic lime (lime binder and pozzolan fragments) with strong heterogeneous structure and micritic/microsparitic texture. Numerous reaction rims Recrystallized/decay binder Numerous lumps (unmixed binder and dark nodules)	Composition: scoriae, pumice, Fds (Pl, Kfs), Cpx, microcrystalline and hyaline lava fragments, Lct/Anl and Ol. Unimodal grain size Grain size: 100-500 $\mu$ m, very rare grains up to 1-2.9 mm Shape: sub-rounded	1/3	Medium amount, due to pores of irregular-sub-spherical shape



C18B TEMPLE OF APOLLO	Hydraulic lime (lime binder and pozzolan fragments) with strong heterogeneous structure and micritic texture. Numerous reaction rims Recrystallized/decay binder Numerous lumps (unmixed binder of mm size)	Composition: microcrystalline lavas, fctile fragments, scoriae, Fds, Cpx, pumice, Ol. Unimodal, tendentially skewed grain size Grain size: 100-400 $\mu\text{m}$ , and rare 1-4.7 mm Shape: sub-rounded	1/1	Medium-high amount, due to pores of irregular shape
C19C TEMPLE OF APOLLO	Hydraulic lime (lime binder and pozzolan fragments) with strong heterogeneous structure and micritic texture. Numerous reaction rims Numerous lumps (unmixed binder of mm size)	Composition: <u>scoriae</u> , hyaline lavas, pumice, Cpx, Fds. Tendentially unimodal grain size Grain size: 100-600 $\mu\text{m}$ , rare 1-1.5 mm, present single big scoriae 8 mm. Shape: sub-rounded	1/2	High amount, due to pores of sub-spherical shape
C20 BASILICA	Hydraulic lime (lime binder and pozzolan fragments) with heterogeneous structure and micritic texture. Numerous reaction rims Numerous lumps (unmixed binder of mm size and dark nodules)	Composition: hyaline and microcrystalline lavas (rare holocrystalline), Cpx, scoriae, Fds (Pl, Kfs), pumice, Lct/Anl, Ol, limestone fragments, shards. Skewed grain size Grain size: 100-300 $\mu\text{m}$ , 0.8-3.6 mm Shape: sub-angular	1/1- 1/2	Low amount, due to pores of sub-spherical shape
C21A DUOVIRI BUILDING	Hydraulic lime (lime binder and pozzolan and cocchiopesto fragments) with heterogeneous structure and microsparitic texture. Numerous reaction rims Recrystallized/decay binder Some lumps (unburned rock, dark nodules)	Composition: pumice and scoriae, cryptocrystalline and microcrystalline lavas, Fds (Pl), Bt, Cpx, Bt, Lct/Anl. Seriatic grain size Grain size: 150 $\mu\text{m}$ , up to 2.5 mm Shape: sub-angular	1/1	Medium-high amount, due to pores of irregular shape
C21B DUOVIRI BUILDING	Hydraulic lime (lime binder and pozzolan fragments) with heterogeneous structure and microsparitic texture. Numerous reaction rims Recrystallized/decay binder Rare lumps	Composition: lavas, pumice, scoriae, fctile fragments, Fds (Pl, Kfs), Cpx, Bt. Unimodal grain size Grain size: 100-500 $\mu\text{m}$ , rare >600 $\mu\text{m}$ up to 4 mm Shape: sub-rounded – subangular	1/1- 1/2	Medium-high amount, due to pores of irregular shape

C22A TABULARIUM	Hydraulic lime (lime binder and pozzolan fragments) with heterogeneous structure and micritic texture. Some reaction rims Numerous lumps (unmixed binder, unburned rock of mm size)	Composition: microcrystalline and hyaline lavas, scoriae, pumice, Cpx, Fds (Pl, Kfs), Ol, Lct/Anl Seriate grain size Grain size: 200 µm, up to pluri-mm (max size 6.5 mm) Shape: sub-angular	1/2- 1/3	Low amount, due to pores of sub-spherical shape
C23A CURIA	Hydraulic lime (lime binder and pozzolan fragments) with heterogeneous structure and micritic/microsparitic texture. Some reaction rims Rare lumps	Composition: pumice, scoriae, hyaline lavas (rare holocrystalline), Cpx, Fds (Pl, Kfs), Ol and <u>Grt</u> Seriate grain size Grain size: 150 µm, up to pluri-mm (max 2.5 mm) Shape: sub-rounded- sub-angular	1/1- 1/2	Medium-low amount, due to pores of irregular-sub-spherical shape
C23B CURIA	Hydraulic lime (lime binder and pozzolan fragments) with heterogeneous structure and micritic/microsparitic texture. Some reaction rims Rare lumps	Composition: scoriae, hyaline lavas (rare holocrystalline), pumice, CPx/Bt, Fds (Pl, Kfs), fictile fragments, Ol, limestone fragments. Seriate grain size Grain size: 150 µm, up to pluri-mm Shape: sub-angular	1/1- 1/2	Low amount, due to pores of sub-spherical shape
C25A TEMPLE OF FORTUNA AUGUSTA	Hydraulic lime (lime binder and pozzolan fragments) with heterogeneous structure and microsparitic texture. Numerous reaction rims Recrystallized binder Numerous lumps (unmixed binder, unburned rock of mm size)	Composition: Cpx, hyaline lavas, scoriae and pumice, Fds (Pl, Kfs), Ol, Lct/Anl Seriate grain size Grain size: 150 µm, up to 3.5 mm Shape: sub-rounded – sub-angular	1/3	Low amount, due to shrinkage fractures
C25B TEMPLE OF FORTUNA AUGUSTA	Hydraulic lime (lime binder and pozzolan fragments) with heterogeneous structure and micritic texture. Mainly composed by lumps (unburned rock, dark nodules)	Composition: pumice, scoriae, fictile fragments, Fds Cpx and <u>Qtz</u> Unimodal grain size Grain size: 100-600 µm, rare between 1-2.4 mm Shape: sub-rounded	3/1	Medium amount, due to pores of irregular-sub-spherical shape
C25C TEMPLE OF FORTUNA AUGUSTA	Hydraulic lime (lime binder and pozzolan fragments) with heterogeneous structure and micritic/microsparitic texture. Some reaction rims Recrystallized binder Rare lumps	Composition: scoriae, Fds (Kfs, Pl), Cpx, pumice, hyaline lavas, shards, Lct/Anl and Ol Unimodal grain size Grain size: 100-400 µm, rare > 600 µm up to 3 mm Shape: sub-angular - sub-rounded	1/2	Medium amount, due to pores of irregular-sub-spherical shape

C25E TEMPLE OF FORTUNA AUGUSTA	Hydraulic lime (lime binder and pozzolan fragments) with heterogeneous structure and micritic texture. Some lumps (unmixed binder and dark nodules)	Composition: scoriae, pumice, Lct/Anl, hyaline lavas, Fds (Pl, Kfs), Cpx, Bt Unimodal tends to skewed grain size Grain size: 50-500 $\mu\text{m}$ , present grains between 0.8-2.3 mm (max size 6.1 mm) Shape: sub-angular-sub-rounded	1/2	Medium-low amount, due to pores of irregular shape
C26A ODEION	Hydraulic lime (lime binder and pozzolan fragments) with heterogeneous structure and micritic texture. Numerous lumps (unmixed binder, unburned rock and dark nodules)	Composition: microcrystalline lavas, scoriae, Cpx, Fds (Pl, Kfs), pumice, Lct/Anl, shards, Bt Unimodal grain size Grain size: 100-400 $\mu\text{m}$ , rare grains between 1-2.5 mm (max size 3.2 mm) Shape: sub-angular	1/1	Low amount, due to pores of sub-spherical shape
C27A THEATER	Hydraulic lime (lime binder and pozzolan fragments) with homogeneous structure and micritic texture. Some reaction rims Numerous lumps (unmixed binder, unburned rock)	Composition: microcrystalline and hyaline lavas, Cpx, scoriae (analcime/leucite rich), Fds (Kfs, Pl), pumice, shards, Ol, Lct/Anl. Seriaded grain size Grain size: 150-300 $\mu\text{m}$ , 500-600 $\mu\text{m}$ (max size 7.3mm) Shape: sub-angular – angular	1/1	Low amount, due to pores of sub-spherical shape
C27B THEATER	Hydraulic lime (lime binder and pozzolan fragments) with heterogeneous structure and micritic/microsparitic texture. Some reaction rims Recrystallized binder Numerous lumps (unburned rock)	Composition: microcrystalline and hyaline lavas, scoriae, Cpx, Fds (Pl, Kfs), pumice, Lct/Anl, shards, limestone fragments, Bt and Ol Unimodal grain size Grain size: 50-400 $\mu\text{m}$ , rare grains between 1-2 mm (max size 3.3 mm) Shape: sub-angular	1/1	Medium amount, due to pores of irregular-sub-spherical shape
C28A TRIANGULAR FORUM	Hydraulic lime (lime binder and pozzolan fragments) with heterogeneous structure and micritic texture. Numerous lumps (unmixed binder, unburned rock and dark nodules)	Composition: scoriae, pumice, microcrystalline lavas, Cpx, Fds, sedimentary rocks, Bt and Lct/Anl Unimodal grain size Grain size: 100-500 $\mu\text{m}$ , (max size 1.3 mm) Shape: sub-rounded – sub-angular	2/1	Medium amount, due to pores of irregular-sub-spherical shape

C29A  
TEMPLE OF  
ISIDE

Hydraulic lime (lime binder and pozzolan fragments) with heterogeneous structure and micritic/microsparitic texture.  
Some reaction rims  
Recrystallized binder  
Rare lumps

Composition: scoriae, Cpx, Fds (Pl, Kfs), hyaline lavas, pumice, Ol and Lct/Anl  
Skewed (tententially seriated) grain size  
Grain size: 100 $\mu$ m, up to 9 mm  
Shape: sub-angular – angular

1/2

Medium amount, due to pores of irregular-sub-spherical shape

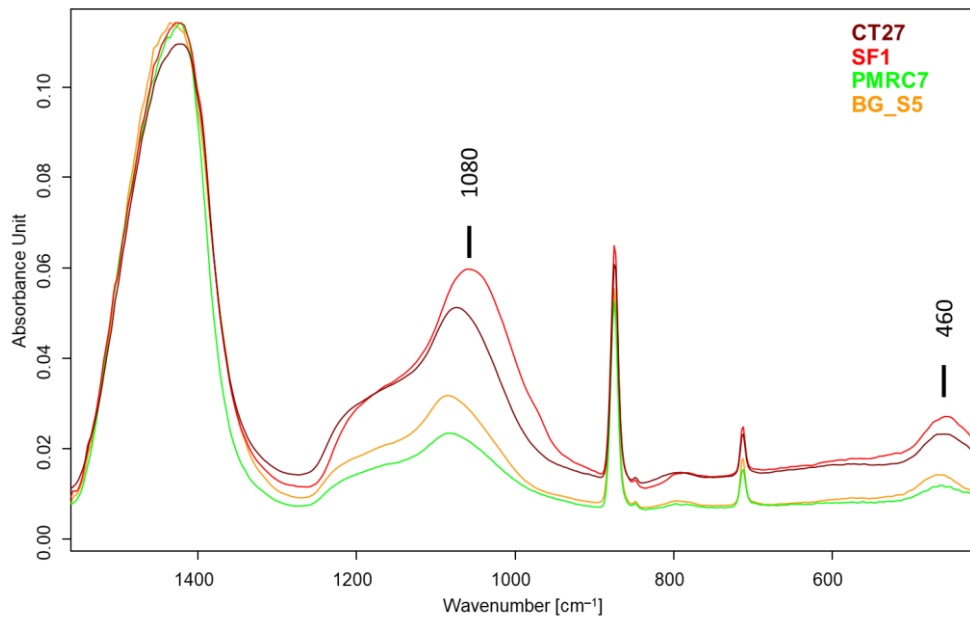


Figure 1 – Detail of the FTIR spectrum of lump (interesting range 1500– 400  $\text{cm}^{-1}$ ) of lump samples from the historical buildings in Florence.

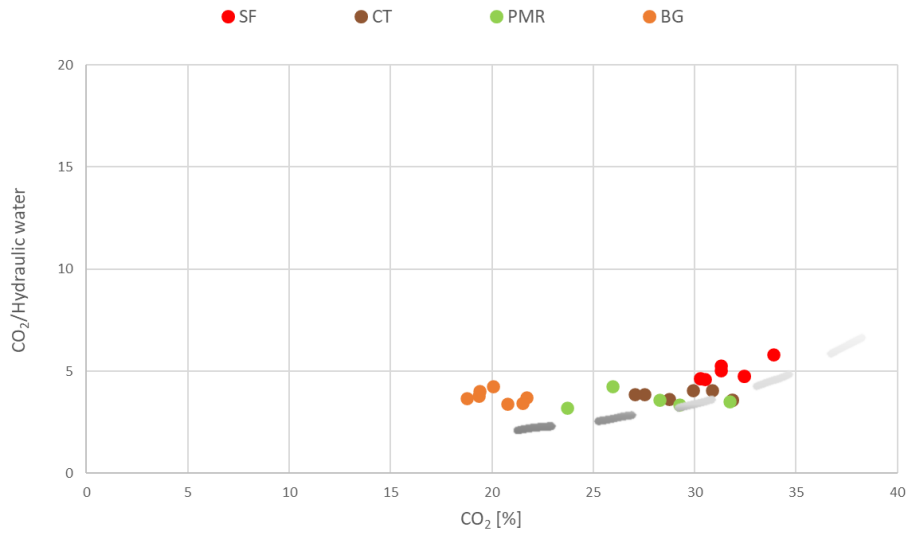


Figure 2 – Comparison between TGA results of study cases. Diagram of CO<sub>2</sub> vs CO<sub>2</sub>/hydraulic water with the theoretical curve of binders obtained burning Alberese limestone is reported (modified from (Lezzerini et al., 2017)).

## Appendix 3: Published work on PhD topics

[1] Calandra, S.; Barone, S.; Cantisani, E.; Caggia M. P.; Liccioli, L.; Vettori, S.; Fedi, M. Radiocarbon dating of straw fragments in the plasters of St Philip Church in archaeological site Hierapolis of Phrygia (Denizli, Turkey), Radiocarbon 2023, 65(2), 323-334. DOI: [10.1017/RDC.2023.20](https://doi.org/10.1017/RDC.2023.20)

[2] Calandra, S.; Conti, C.; Centauro, I.; Cantisani, E. Non-destructive distinction between geogenic and anthropogenic calcite by Raman spectroscopy combined with machine learning workflow. Analyst, 2023. DOI: [10.1039/D3AN00441D](https://doi.org/10.1039/D3AN00441D)

[3] Calandra, S.; Salvatici, T.; Pecchioni, E.; Centauro, I.; Garzonio, C. A.. Mortar Characterization of Historical Masonry Damaged by Riverbank Failure: The Case of Lungarno Torrigiani (Florence). Heritage, 6.5: 3820-3834. DOI: [10.3390/heritage6050203](https://doi.org/10.3390/heritage6050203)

[4] Calandra, S.; Salvatici, T.; Centauro, I.; Cantisani, E.; Garzonio, C. A. The Mortars of Florence Riverbanks: Raw Materials and Technologies of Lungarni Historical Masonry. Applied Sciences 2022, 12(10), 5200. DOI: [10.3390/app12105200](https://doi.org/10.3390/app12105200)

[5] Di Bilio, L. et al. Palazzo Medici Riccardi: Diagnostic Experimental Site for the Pietraforte Façades. In: Furferi, R., Governi, L., Volpe, Y., Gherardini, F., Seymour, K. (eds) The Future of Heritage Science and Technologies. Florence Heri-Tech 2022. Lecture Notes in Mechanical Engineering. Springer, Cham. DOI: [10.1007/978-3-031-17594-7\\_23](https://doi.org/10.1007/978-3-031-17594-7_23)

[6] Centauro, I.; Vitale, J. G.; Calandra, S.; Salvatici, T., Natali, C., Coppola, M., Intriери, E., Garzonio, C. A. A multidisciplinary methodology for technological knowledge, characterization and diagnostics: sandstone facades in Florentine Architectural Heritage. Applied Sciences, 2022, 12(7). DOI: [10.3390/app12094266](https://doi.org/10.3390/app12094266)

[7] Calandra, S.; Cantisani, E.; Vettori, S.; Ricci, M.; Agostini, B.; Garzonio, C. A. The San Giovanni Baptistery in Florence (Italy): assessment of the state of conservation of surfaces and characterization of stone materials. Applied Sciences, 2022, 12(7). DOI: [10.3390/app12084050](https://doi.org/10.3390/app12084050)

[8] Calandra, S.; Cantisani, E.; Salvadori, S.; Barone, S.; Liccioli, L.; Mariaelena Fedi, M.; Garzonio, C. A. Evaluation of ATR-FTIR spectroscopy for distinguishing anthropogenic and geogenic calcite. Journal of Physics: Conference Series 2022, 2204(1), 012048. IOP Publishing. DOI: [10.1088/1742-6596/2204/1/012048](https://doi.org/10.1088/1742-6596/2204/1/012048)

[9] Cantisani, E.; Calandra, S.; Caciagli, S.; Barone, S.; Fedi, M.; Garzonio, C. A.; Liccioli, L.; Salvadori, B.; Salvatici, T.; Vettori, S. The mortars of Giotto's Bell Tower (Florence, Italy): raw materials and technologies. *Constr. Build. Mater.* 2021, 267, 120801. DOI: [10.1016/j.conbuildmat.2020.120801](https://doi.org/10.1016/j.conbuildmat.2020.120801)

## Appendix 4: Published work on topics different from the PhD project

[1] Lanteri, L., Calandra, S., Briani, F., Germinario, C., Izzo, F., Pagano, S., ... & Santo, A. P. (2023). 3D Photogrammetric Survey, Raking Light Photography and Mapping of Degradation Phenomena of the Early Renaissance Wall Paintings by Saturnino Gatti—Case Study of the St. Panfilo Church in Tornimparte (L’Aquila, Italy). *Applied Sciences*, 13(9), 5689. DOI: [10.3390/ app13095689](https://doi.org/10.3390/app13095689)

[2] Calandra, S., Centauro, I., Laureti, S., Ricci, M., Salvatici, T., & Sfarra, S. (2023). Application of Sonic, Hygrometric Tests and Infrared Thermography for Diagnostic Investigations of Wall Paintings in St. Panfilo’s Church. *Applied Sciences*, 13(12), 7026. DOI: [10.3390/ app13127026](https://doi.org/10.3390/app13127026)

[3] Salvatici, T., Centauro, I., Calandra, S., Segabinazzi, E., Intrieri, E., & Garzonio, C. A. (2023). Non-destructive methods applied for in situ mechanical diagnosis: Florentine historical buildings in Pietra Serena. *Heritage Science*, 11(1), 1-11. DOI: [10.1186/s40494-023-00959-8](https://doi.org/10.1186/s40494-023-00959-8)

[4] Calandra, S.; Centauro, I.; Salvatici, T.; Pecchioni, E.; Garzonio, C.A. Monitoring and Evaluation of Pietra Serena Decay Adopting NDT Techniques: Application on Building Stones in Situ. In: Furferi, R., Governi, L., Volpe, Y., Gherardini, F., Seymour, K. (eds) *The Future of Heritage Science and Technologies*. Florence Heri-Tech 2022. Lecture Notes in Mechanical Engineering. Springer, Cham. DOI: [10.1007/978-3-031-17594-7\\_22](https://doi.org/10.1007/978-3-031-17594-7_22)

[5] Salvatici, T.; Garzonio, C.A.; Calandra, S.; Pecchioni, E.; Santo, A.P. A Diagnostic Method for the Pavement Conservation of the Great Synagogue of Florence (Italy). In: Furferi, R.; Governi, L.; Volpe, Y.; Gherardini, F., Seymour, K. (eds). *The Future of Heritage Science and Technologies*. Florence Heri-Tech 2022. Lecture Notes in Mechanical Engineering. Springer, Cham. DOI: [10.1007/978-3-031-17594-7\\_25](https://doi.org/10.1007/978-3-031-17594-7_25)

[6] Centauro, I.; Calandra, S.; Salvatici, T.; Garzonio, C.A. System Integration for Masonry Quality Assessment: A Complete Solution Applied to Sonic Velocity Test on Historic Buildings. In: Furferi, R.; Giorgi, R.; Seymour, K.; Pelagotti, A. (eds). *The Future of Heritage Science and Technologies*. Florence Heri-Tech 2022. *Advanced Structured Materials*, vol 179. Springer, Cham. DOI: [10.1007/978-3-031-15676-2\\_15](https://doi.org/10.1007/978-3-031-15676-2_15)

[7] Pecchioni, E.; Pallecchi, P.; Giachi, G.; Calandra, S.; Santo, A. P. The Preparatory Layers in the Etruscan Paintings of the Tomba dei Demoni Alati in the Sovana Necropolis



(Southern Tuscany, Italy). Applied Sciences 2022, 12(7), 3542. DOI: [10.3390/app12073542](https://doi.org/10.3390/app12073542)

[8] Salvatici, T.; Calandra, S.; Centauro, I.; Pecchioni, E.; Intrieri, E.; Garzonio, C. A. Monitoring and evaluation of sandstone decay adopting Non-Destructive Techniques: on-site application on building stones. Heritage, 2020, 3(4), 1287-1301 DOI: [10.3390/heritage3040071](https://doi.org/10.3390/heritage3040071)